PhD THESIS Experimental Characterization, Modeling and Simulation of Magneto-Rheological Elastomers

Tobias Pössinger

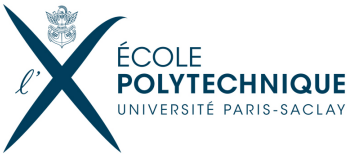

PhD THESIS

OF

ECOLE POLYTECHNIQUE

Submitted by:

Tobias PöSSINGER

in Partial Fulfillment of the Requirements for the Degree of

DOCTOR OF PHILOSOPHY

SPECIALTY: Mechanics

Experimental Characterization, Modeling and Simulation of Magneto-Rheological Elastomers

Prepared at the

Sensorial and Ambient Interfaces Laboratory, CEA LIST,

and at the

Solid Mechanics Laboratory, LMS

Defended on the 22th of June 2015

Before the Committee:

Mr. Krishnaswamy RAVI-CHANDAR	Professor	University of Texas at Austin	Rapporteur
Mr. Jean-Claude MICHEL	Research Director	LMA, Marseille	Rapporteur
Mr. Habibou MAITOURNAM	Professor	ENSTA Paristech, Palaiseau	Head of the Commitee
Mr. Pedro PONTE CASTAñEDA	Professor	University of Pennsylvania	Examiner
Mr. Olivier HUBERT	Professor	LMT, Cachan	Examiner
Ms. Laurence BODELOT	Assistant Professor	Ecole Polytechnique, Palaiseau	Examiner
Mr. Nicolas TRIANTAFYLLIDIS	Research Director	LMS, Palaiseau	Advisor
Mr. Christian BOLZMACHER	Research Engineer	CEA LIST	Co-Advisor
Mr. Kostantinos DANAS	Research Scientist	LMS, Palaiseau	Invited

Abstract

In this thesis, we study a class of active materials named Magneto-Rheological Elastomers (MREs) with a main focus on their coupled magneto-mechanical response up to large strains and up to high magnetic fields. With the purpose of achieving a coupled characterization of MREs behavior for the design of haptic interface devices, this work encompasses experimental, theoretical and numerical developments.

The first part of this work is dedicated to aspects pertaining to sample fabrication. Isotropic and magnetic field-cured MREs, composed of soft silicone rubber and micrometric carbonyl iron powder, are manufactured using a reliable and repeatable process. A special sample geometry is designed in order to obtain both homogeneous mechanical and magnetic fields during the coupled-field characterization. The interfacial adhesion between the iron fillers and the silicone matrix in MREs submitted to large deformations is investigated and a critical strain threshold is identified beyond which a primer treatment of the particles is needed to prevent debonding between the particles and the matrix.

The second part of this thesis focuses on the coupled magneto-mechanical characterization of MREs and involves both theoretical and experimental developments. Based on the general theoretical framework for transversely isotropic magneto-elastic continua proposed by Kankanala, Danas and Triantafyllidis [Kan04, Dan12, Dan14], the coupled magneto-mechanical constitutive laws for both isotropic and anisotropic MREs are used to determine experimentally the corresponding constitutive model's material parameters. The actual characterization of MREs is conducted thanks to a specially designed and novel experimental setup allowing tensile tests up to large strains and under high magnetic fields. The experimental data thus obtained provide the constitutive models for the isotropic and anisotropic MREs needed as input for the subsequent numerical simulations.

The third part of this work pertains to the experiments, modeling and numerical calculations for boundary value problems corresponding to the design of a haptic interface prototype. A coupled variational formulation for a non-uniform applied magnetic field, using displacement, magnetic vector potential and magnetization as independent variables, is proposed and subsequently applied to the solution of the boundary value problem of an MRE layer subjected to the spatially localized magnetic field produced by an electromagnetic coil. The axisymmetric problem is solved numerically using finite element analysis. The device has been built and experimental results are compared to numerical simulations, thus providing a benchmark for the validation of the axisymmetric simulations as well as a proof of concept for the design of haptic interface applications.

Acknowledgment

I would like to express my deep sense of gratitude to my supervisors at the LMS: Professor Nicolas Triantafyllidis, who indicated the right directions and helped me with his immense theoretical background in this for me new field of continuum mechanics. Professor Laurence Bodelot, who always was there for any questions with her accurate help and guidance during the three years of my doctoral thesis. It was a great pleasure to develop together all the experimental facility from scratch. Professor Kostas Danas, who introduced and guided me through the formulation of the FEM methodology and who was there with his exceptional knowledge on MREs if I had questions. I would also like to mention and thank Professor Patrick Le Tallec, head of the lab, who always showed an honest interest on the work of all the PhD students at the LMS.

In the same way, I would like to express my deep sense of gratitude to my supervisors at the CEA LISA: Dr. Christian Bolzmacher, who always supported me during this work with his great knowledge on smart materials and to keep in mind the technological application of MREs. I am especially indebted to the head of the lab (CEA LISA) and director of research at the CEA, Dr. Moustapha Hafez, for the generous funding I received, which was fundamental for my PhD studies.

I would also like to mention the very interesting weekly seminars at the LMS, the excellent courses at the Ecole Polytechnique and the well organized on-site assistance and courses of the doctoral school EDX and thank the people responsible therefore.

Next, I would like to thank all engineers and technicians, who generously offered their great expertise and technical support: the mechatronic engineers Vincent De Greef, especially, and Jean-Christophe Eytard at the LMS, Laurent Eck at the CEA. The technicians from the machine shop François Lelong and Antoine Soler, the designing engineer Erik Guimbretiere and the research engineers and specialists in Scanning Electron Microscopy Alexandre Tanguy and Eva Héripré at the LMS. The research engineer and specialist in 3D printing Gwenaël Changeon at the CEA.

I would also like to thank the doctoral students and employees at the LMS and the CEA LISA for the helpful and friendly working atmosphere at both laboratories. Particular thanks to Annick Latare and Alexandra Joly for their help on administration procedures, as well as to René, Harald, Hakim and the LMS soccer team.

I am very thankful to Professor Krishnaswamy Ravi-Chandar and research director Jean-Claude Michel that they generously took the time to report on my work, to Professor Habibou Maitournam chairing as well as to Professor Pedro Ponte Castañeda and Professor Olivier Hubert completing an exceptional PhD committee.

Finally, I am so thankful to my family, especially my mother Birgit, my father Josef, my brothers Maxi and Christian, and my wife Eva, who enormously enrich my life. And a big thank you to my friends in Germany and France.

Contents

Chapter 1

Introduction

Magneto-rheological elastomers (MREs) are smart materials composed of an elastomeric matrix filled with magnetic particles. The viscoelastic characteristics of the matrix combined with the magnetic properties of the particles allow these flexible composites to deform in response to a relatively low externally applied magnetic field. The rapid response, the high level of deformations and the possibility to control these deformations by adjusting the field make these materials of special interest in modern engineering [Bus07]. Due to their unique properties, a variety of technological applications in smart structures based on MREs can be envisioned: novel actuators, smart sensors, artificial muscles, sound control, shape control, product health or lifetime monitoring, etc. (see the review by [Har06]). Yet, no full characterization of the magneto-mechanical properties for finite strains and high magnetic fields has been undertaken so far, thus limiting the efficient design of such MRE-based devices.

In this chapter, after introducing MREs and where they stand among smart materials in Section 1.1, a sorting in the class of MRE is proposed in Section 1.2 and the main research topics, as well as some examples of applications, are presented in Section 1.3. Next, physical phenomena involved in the behavior of MREs are discussed in more detail in Section 1.4, from general aspects of the behavior of filled composites to the behavior of MREs under magnetic field. Then we briefly review the different modeling approaches in Section 1.5, as one can find either microscopic-based models or phenomenological continuum descriptions. The latter approach is the theoretical basis for the developments done in this thesis and requires a careful experimental characterization of magneto-elastic material properties. Thus, we also analyze what has been done previously experimentally on this topic in Section 1.6. Finally, the scope of the present work is presented and the organization of the manuscript is detailed to guide the reader through the following chapters in Section 1.7.

1.1 MREs among smart materials

Different stimuli cause some materials called “smart”, “intelligent” or “active” to respond to their environment in a reversible manner, thus producing a useful effect. Common materials that formally have the label of being smart include piezo-electric materials, electro-strictive materials, magneto-strictive materials, electro-rheological materials, magneto-rheological materials, thermo-responsive materials and shape memory alloys. The applied driving forces for field-driven smart materials then can be broadly identified as mechanical fields, electrical fields, magnetic fields and thermal fields. Therefore, an important feature related to smart materials is that they encompass almost all fields of science and engineering.

While electro-active materials usually require high voltages for activation, economically generated magnetic fields (permanent magnets, solenoids) can be used to stimulate magneto-active materials. As a branch of this kind of active materials, electro- and magneto-rheological materials consist of an insulating or non-magnetic matrix (either a fluid, a foam or an elastomer) into which electrically or magnetically polarizable particles are mixed, respectively [Har06].

The first explored [Rab48] and most common magneto-rheological (MR) materials have a fluid matrix. In these MR fluids, the interaction between dipoles, induced by an external magnetic field, causes the particles to form columnar structures parallel to the uni-axially applied field. As the external magnetic field increases, the mechanical energy needed to yield these chain-like structures increases since it becomes more and more difficult for the fluid to flow through these formed structures. The obtained field-dependent yield stress, which can be rapidly and reversibly controlled, has been exploited in a variety of vibration control or torque transfer devices [Car01, Ber12]. However, the drawback of MR fluids is the settling of their particles and the fact that the devices need to be enclosed. As a solution to this, magneto-rheological foams have been developed, in which the controllable fluid is contained in an absorbent porous matrix. Fluids in these smart devices are thus more resistant to gravitational settling. Additionally, no seals or bearings are required and a smaller quantity of fluid is needed [Car00].

A definite answer to the particles settling was the use of an elastomer as the matrix. The magnetic particles are mixed into the fluid-like polymer blend but remain locked in place within the cross-linked network of the cured elastomer. Hence, these composite materials are often considered as the solid analogs of magneto-rheological

fluids. The first researchers who conducted preliminary tests on these so-called magneto-rheological elastomers[1] are Rigbi and Jilken [Rig83]. They studied the behavior of a ferrite elastomer composite under the combined influence of changing elastic stresses and magnetic fields and described the previously unknown magneto-mechanical effects[2].

1.2 Classification within MREs

If magnetic fields are applied to the elastomer composite during processing, special anisotropic properties can be imparted to these materials. They are then called field-structured MREs and it has been observed that they are anisotropic in terms of mechanical, magnetic, electrical, and thermal properties [Car00]. More particularly, an applied uni-axial magnetic field produces chain-like particle structures[3]: at low particle concentrations the particles initially form chains that slowly coalesce into columns, as shown in Figure 1.1, while at high concentrations the morphology becomes slightly more complex, with possible branching between columns and a slight loss in anisotropy [Mar98, Boc12]. A bi-axial (e.g. rotating) field produces sheet-like particle structures [Mar00]. Finally, with the generation of triaxial magnetic fields during processing, a variety of isotropic and anisotropic particle structures can be created [Mar04].

MREs can be further classified according to their main constituents, i.e. the non-magnetic matrix and the magnetic filler particles as well as their inherent properties. They usually are composed of a solid, electrically insulating[4] matrix, such as silicone rubber, natural rubber, polyurethane or thermoplastic elastomers [Kal05, Hu05, Che07, Wei10, Kal11]. In fact, a great variety of matrix materials covering a wide range of properties in modulus, tensile strength or viscosity can be found on the market and in the literature. Within all these materials however, MREs based

[1] They are also often named magneto-active elastomers [Bus10] or magneto-sensitive elastomers [Kar13]. Respecting the rule of anteriority, we will use magneto-rheological elastomers (MREs) as defined by Carlson and Jolly [Car00].

[2] The reader interested in a historical overview is referred to the thesis of Schubert [Schu14], who presented a thorough summary in graphical form.

[3] In the following, MREs structured by an externally applied, uni-axial magnetic field are termed field-structured, aligned or transversely isotropic whereas (isotropic) MREs designate composites with a random distribution of particles since no structuring field is applied during fabrication in this case.

[4] We will neither consider conductive or graphite-particle-doped MR elastomers nor the phenomenon of magneto-electrical resistance within the scope of this thesis. The interested reader is referred to the papers of Bica [Bic11] and Ausanio et al. [Aus14], for example.

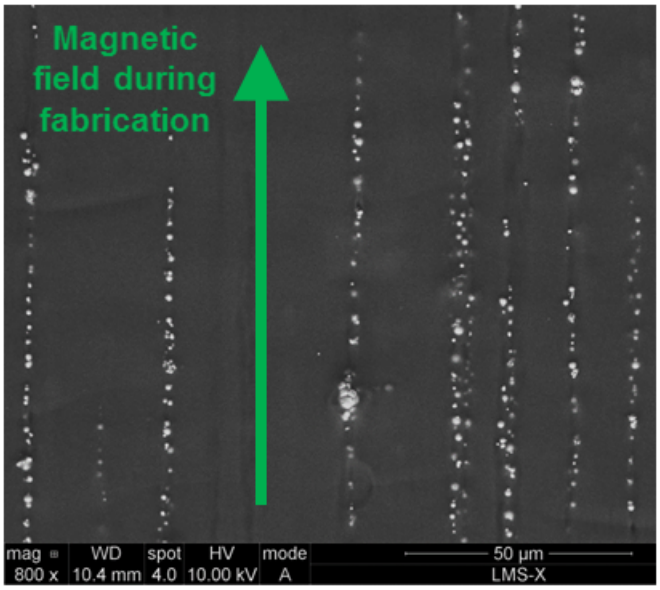

Figure 1.1: Scanning electron micrograph of a field-structured MRE with low particle concentration. The particles appear as white dots aligned by the externally applied magnetic field in the elastomeric matrix appearing as the black background.

on silicone rubber enjoy much popularity due to their excellent processability, to the good compromise between mechanical, thermal and aging properties, as well as to their widespread use in industrial applications. Furthermore, relatively soft matrices with low elastic moduli are achievable in silicon rubbers and tend to ease the magneto-mechanical interaction [Kal05, Gon07, Dig10, Schu14]. Let's note also that the individual class of "soft magneto-rheological elastomers" has been claimed, which covers MREs whose matrix is elastically soft. This class includes magnetic gels consisting of magnetic particles dispersed in a gel-like polymeric matrix. Gel materials (fluid within a three-dimensional weakly cross-linked network) can indeed be much softer than classical elastomers. However, they usually have a wet and sticky consistency, and when agitated, these materials start to flow (thixotropy), thereby resulting in poor mechanical properties [Zri97, Rai08, Zub12].

Different types of magnetic filler particles have been used in MREs: magneto-strictive or magnetic shape memory particles, as well as hard or soft magnetic particles. A number of researchers employed highly magneto-strictive particles, usually Terfenol-D [Due00]. This alloy of rare earth crystals is the most effective but a cost intensive magneto-strictive material, capable of showing reversible strains in the order of 10^{-3} in response to an applied magnetic field [Guy94]. Particles with

magnetic shape memory have also been used [Sche07] yielding both temperature and magnetic field-driven MRE composites. The dispersion of hard magnetic particles in an elastomeric matrix, magnetized during fabrication, produces anisotropic, magnetically-poled MREs similar to a flexible permanent magnet [Koo12]. However, the most commonly used particles are made of soft ferromagnetic materials such as nickel, cobalt or iron and their alloys [Aus11, Ant11]. In particular, carbonyl iron powder (CIP) with spherical particles has been widely preferred in MREs fabrication [Kal05, Boes07, Dig10, Schu14]. Iron has indeed a high magnetic susceptibility and saturation magnetization, providing high inter-particle interaction forces, as well as a low remanent magnetization required in order to obtain quick and reversible control by the magnetic field in MRE applications. The size of the magnetic particles further distinguishes MREs from ferro-elastomers or ferro-gels[5]. Standard ferrogels (as well as ferro-fluids) tend to include nano-sized particles which are magnetic mono-domains. They agglomerate easily and cannot be separated again once they have agglomerated. Following the definition in the review by Carlson and Jolly [Car00], MREs rather embed micron-sized particles possessing a high number of magnetic domains that, overall, are harder to magnetize [Car00, Mar06].

1.3 Main MRE research topics and applications

Considering the large amount of possible matrix-filler combinations in the literature, many of the early experiments but also current research have been dedicated to the composition and processing of MREs together with the investigation of the obtained microstructures by optical microscopy [Far04a], scanning electron microscopy [Gon05, Chen07] or X-ray microtomography [Bor12]. The processing conditions and (field-)curing mechanisms are crucial parameters for the manufacturing in a laboratory environment. More specifically, the mixed viscosity – a measure of the thickness of the blended composite constituents –, the temperature and the magnetic field will determine the competition between gravitational settling and the alignment of the particles during curing [Als07, Gue12]. The final structure of the MRE is therefore specific to each of these parameters, which complicates the comparison of experimental results in the literature.

Furthermore, extensive studies have been conducted to investigate the dynamic small strain behavior of MREs, especially the influence of an external magnetic

[5]They are sometimes denoted as MREs (see [Mor09]).

field on mechanical properties such as storage, loss and viscoelastic moduli [Shi95, Jol96, Gin00, Lok04, Kal05, Fan11, Kar13]. Since MREs have been shown to alter their dynamic moduli in response to the field, their performance as tunable vibration absorbers and tunable stiffness devices has been widely studied and prototype applications have been developed [Eli02, Far04b, Cri09, Mar13, Kim14], such as a prosthetic foot [Tho13] shown in Figure 1.2.

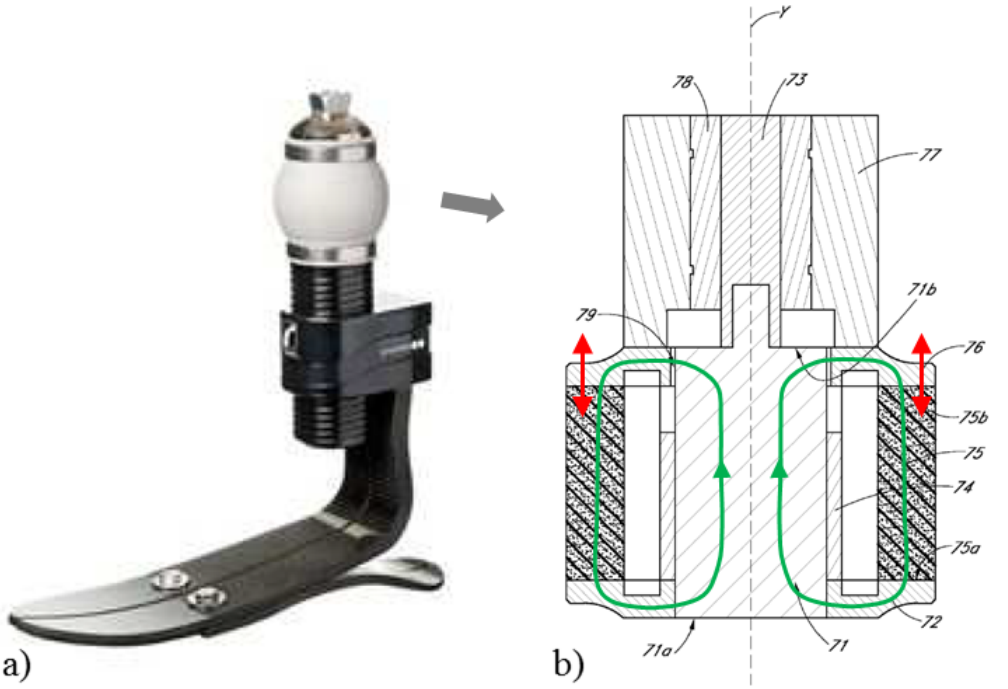

Figure 1.2: a) Picture of a smart prosthetic foot device and b) cross-section of the integrated tunable MRE spring [Tho13]. The motion (red arrows) resistance of the MRE spring (75) can be adjusted by the magnetic flux (green circuit) generated by the coil (74).

In parallel, a large body of research has been devoted to the investigation of the deformation of MRE materials exposed to a magnetic field. The attraction of magnetically soft and mechanically flexible MREs by magnetic field gradients has been discovered early [Zri96] and the use of this effect in smart high-strain actuators has been proposed [Boes12, Bro12]. Figure 1.3 shows the example of an MRE device enabling flow control [Ste13]. The deformations induced by a uniform magnetic field have also been studied early [Gin02] but the results are still rather contradictory up to now and cannot yet be explained clearly. We will come back to these aspects in the next section.

Finally, an important part of the literature on MREs is concerned with the mod-

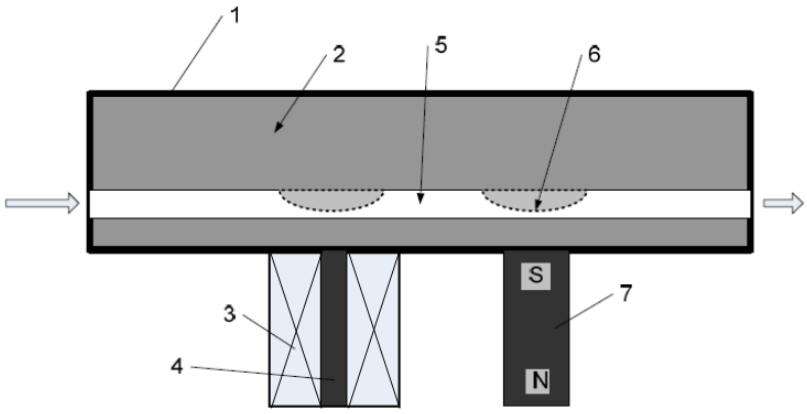

Figure 1.3: Schematic of a smart fluid valve [Ste13]. The flow (large arrows) of the medium inside a channel (5) can be adjusted by attracting (6) the MRE material (2) by means of an electromagnet (3,4) or a permanent magnet (7).

eling of these materials. The approaches therein can basically be partitioned in micro-mechanical or structural models on the one hand and continuum or phenomenological models on the other hand. In the continuum approach that is the theoretical basis for what has been done in this thesis, the material constitutive behavior needs to be characterized with the help of magneto-mechanical experiments. In Section 1.6, a review on the available experimental data will show that the magneto-elastic coupled behavior up to high strain and high magnetic fields has not been well explored yet. Hence the design of smart devices capable of high deformations has been limited so far and very few applications allow the MRE material to deform up to 20 percent [Cri09, Tho13, Ste13].

1.4 Physical phenomena in MRE behavior

In this section, selected physical phenomena involved in MREs behavior are discussed in more detail, mainly from an experimental point of view. To remain within the scope of this work, the focus is especially set on the quasi-static or low-frequency behavior of these materials while accounting for large strains and high magnetic fields.

1.4.1 Mechanical behavior of MREs as particle-filled composites

Some purely mechanical phenomena characteristic of particle-filled composites have to be clarified when investigating MREs, even before considering magneto-mechanical

aspects. It is well known that the highly nonlinear macroscopic behavior of filled polymers in response to a mechanical load is affected by matrix-filler and filler-filler interactions. Different phenomena have been experimentally observed[6] and can be linked to changes in the microstructure.

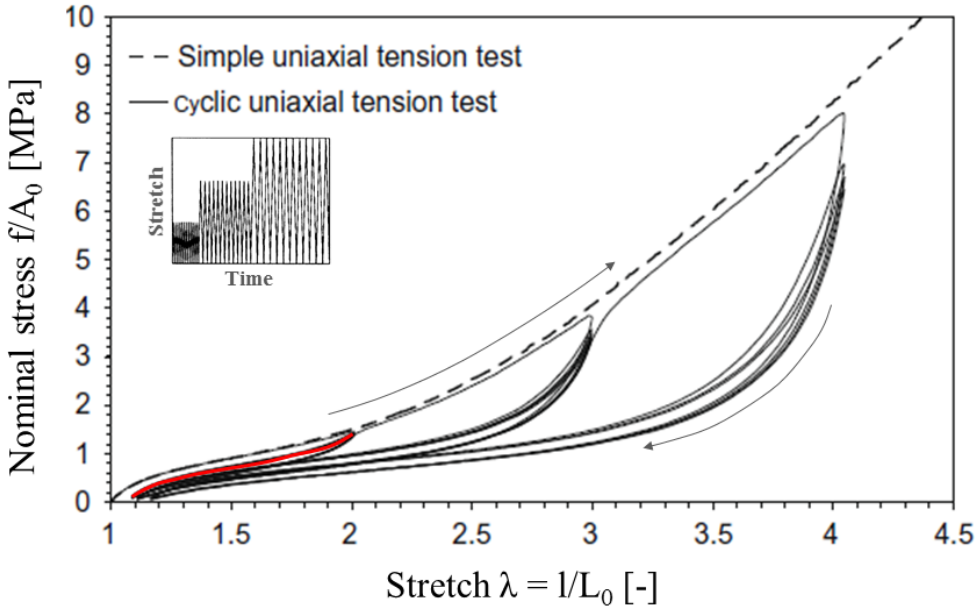

Figure 1.4: Illustration of the Mullins effect for a carbon black filled rubber (particle volume fraction $\Phi_{vol} \sim 0.2$) from [Mie00, Dor04]. Two virgin samples are either uni-axially stretched directly up to high strain (dashed line) or cycled by increasing the strain amplitude after each set of cycles (solid lines). The stable upload curve for the set of cycles of lowest strain amplitude is highlighted in red.

Under large deformations, a softening (characterized by a lower resulting stress for the same applied strain) and a permanent deformation between first and subsequent load cycles can be observed in filled rubbers and MREs. This phenomenon depends on the maximum strain applied and is called "Mullins effect" [Mul57, Mie00, Dor04, Coq06a, Dia09]. It is illustrated in Figure 1.4. The highest softening occurs after the first load cycle and leads to a stable response after few cycles (c.f. Figure 1.4, stable upload curve in red), aside from a smaller fatigue effect [Schu14]. The propensity of the Mullins effect, as well as the composite stiffness are increased with a higher

[6]The large strain constitutive behavior is described by stress-strain curves: usually, the applied force f divided by the initial cross-section A_0 is plotted versus the measured stretch λ or engineering strain $e = \lambda - 1$. Since this response can be highly nonlinear, different stiffness measures are introduced in the literature. The static or elastic modulus is defined as the ratio of the stress and the corresponding strain, whereas the differential or tangent modulus is defined as the slope of the curve at the considered point.

filler content (see Figure 1.5). Let's note here that, in the MRE literature, the filler content is (with a small number of exceptions, e.g. [Als07]) expressed in terms of the particle volume fraction Φ_{vol}.

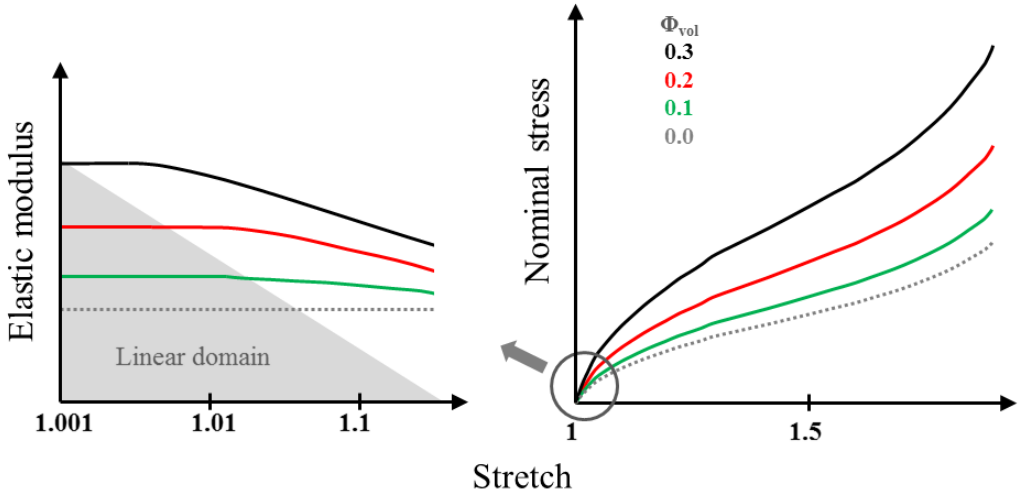

Figure 1.5: Qualitative summary of MREs elastic modulus E in the small strain region on the left (from [Boeh01, Bel02]) and stable stress-strain behavior up to high strain on the right (from [Schu14]) for different particle volume fractions Φ_{vol}.

Along with the particle content, the particle size and shape have a significant influence on the composite mechanical behavior. Below a critical particle size, usually in the nano-scale, the stiffness can be greatly enhanced whereas for a large particle size, above 10 microns, the filler influence can even be degrading [Leb02, Ram04]. Irregular and elongated particles can as well change the mechanical stress transfer throughout the material and thus the material stiffness, depending on their orientation within the host matrix [Fu08].

Another important aspect mainly influencing the mechanical strength is the interfacial adhesion between the filler particles and the matrix [Dek83, Coq04, Fu08]. Indeed, at a critical stress level, debonding acts as a distinct failure phenomenon in a polymer containing rigid inclusions due to stress concentrations at the weak particle-matrix interface [Gen84, Cre01], which could be of great influence on the magneto-mechanical coupling in soft MREs.

Finally, filler networks such as the particle chains in field-structured MREs, as well as possible aggregates and agglomerates due to the fabrication process, further affect the composite mechanical behavior. Some amount of rubber can indeed get trapped inside the particle networks, leading to an increase of the effective filler

volume fraction and hence of the stiffness, as long as the filler network is not broken down [Wan99, Yat01, Leb02]. Field-structured MREs also exhibit the highest mechanical stiffness when the load is applied in the direction of the particle alignment [Bel02, Var05, Schu14], similar to what is classically observed in uni-directional fiber-reinforced composites [Cam10].

1.4.2 Magnetic response of MREs

Before investigating the macroscopic magnetic properties of MREs, important variables, commonly used in the magnetics-related literature, will be reviewed for clarity. In vacuum, the magnetic field $\mathbf{b}_0 = \mu_0 \mathbf{h}_0$ is proportionally related to the magnetic permeability of free space $\mu_0 = 4\pi 10^{-7}$ $[N/A^2]$ multiplied by the externally applied field $\mathbf{h}_0$. If a finite ferromagnetic[7] body is now exposed to this excitation field $\mathbf{h}_0$, the body becomes magnetized and itself provokes a perturbation field $\mathbf{h}_1$, also known as demagnetizing field or stray field [Guy94, Kan04]. The macroscopic magnetic constitutive relation then can be defined following the SI (Système International d'Unités) system of measurement as:

$$\mathbf{b} = \mu_0 \left(\mathbf{h}_0 + \mathbf{h}_1 + \mathbf{m}\right) = \mu_0 \left(\mathbf{h} + \mathbf{m}\right), \tag{1.1}$$

where $\mathbf{b} = \mathbf{b}_0 + \mathbf{b}_1$ is the total magnetic field, also called magnetic induction or magnetic flux density and expressed in Tesla $[T = N/Am]$ and $\mathbf{b}_1 = \mu_0 \left(\mathbf{h}_1 + \mathbf{m}\right)$ is the magnetic perturbation field. $\mathbf{h} = \mathbf{h}_0 + \mathbf{h}_1$ is the total $\mathbf{h}$-field, also called magnetic field intensity or magnetic field strength, expressed in $[A/m]$. The state of magnetic polarization within the body is described by the magnetization field $\mathbf{m}$ $[A/m]$. The nonlinear relation between $\mathbf{h}$ and $\mathbf{m}$ for a ferromagnetic material can be determined experimentally and usually takes the form of a hysteresis loop (see Figure 1.6a).

Hard magnetic particles and nano-scale soft ferro-particles can show an important hysteretic behavior [Lan04, Har06]. In the case of carbonyl iron particles (CIP) however, remanence magnetization and coercitive field are small (in the order of

[7] Within the many classifications for magnetic materials, three major groups can be distinguished, namely diamagnetic (e.g. copper, $\chi \sim -10^{-5}$), paramagnetic (e.g. aluminum, $\chi \sim 10^{-5}$) and ferromagnetic (e.g. iron, $\chi \gg 1$) materials [Guy94]. Compared to the MRE filler particles, the elastomeric matrix, the surrounding air, etc. will be considered as non-magnetic for practical purposes, but probably exhibit some very small paramagnetic or diamagnetic behavior. χ denotes the magnetic susceptibility of the material and will be defined in what follows.

$10^{-3}\,T$, see definition in Figure 1.6a) and magnetic hysteresis is usually neglected [Mar00]. The dimensionless volume susceptibility χ $[-]$ corresponding to the initial slope of the $\mathbf{m} - \mathbf{h}$ curve can then be introduced, as well as the following linear constitutive relations:

$$\mathbf{m} = \chi \mathbf{h}, \quad \mathbf{b} = \mu_0 (1 + \chi) \mathbf{h} = \mu_0 \mu_r \mathbf{h} = \mu \mathbf{h}, \tag{1.2}$$

where μ_r and μ are the relative and magnetic permeability of the body, respectively.

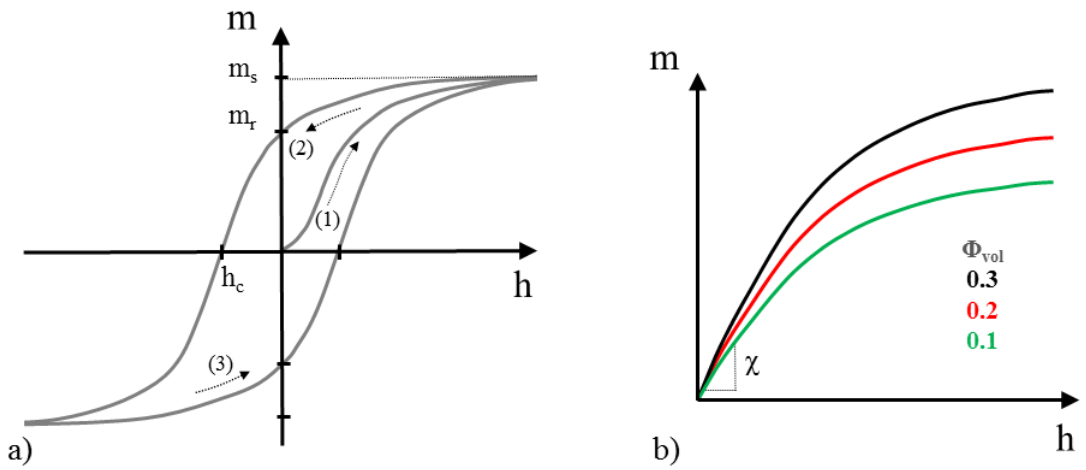

Figure 1.6: a) Magnetic hysteresis loop for a ferromagnetic material (from [Dig10]): the virgin sample is magnetized upon the application of the **h**-field (1) and asymptotically approaches the saturation magnetization $\mathbf{m}_s$ for high fields; decreasing the **h**-field (2) to zero results in a non-zero magnetization called remanent magnetization $\mathbf{m}_r$; the application of the field in opposite direction then leads to zero magnetization for the coercitive field $\mathbf{h}_c$ and the further decrease again saturates the material. b) Qualitative summary of MREs magnetic properties for different Φ_{vol} (first quadrant, no hysteretic effects, from [Mar00]).

Standard approaches in the field of magnetics such as the superconducting quantum interference device (SQUID) magnetometer [Mar00, Kal05], the Faraday balance method [Vic02, Dig10], vibrating sample magnetometry [Lan04, Abr07], induction coil [Bos01, Dan12] and Hall effect measurements [Schu14] have been used to determine the magnetic response in MREs. It has been shown that the susceptibility of MRE composites is small compared to the bulk values of iron (see Figure 4.4 on page 40 in [Schu14]). Moreover, it has been observed, that the initial susceptibil-

ity as well as the saturation magnetization increase with increasing particle volume fraction (see Figure 1.6b). The latter is often assumed to be a linear function of the particle volume fraction and the saturation magnetization of the bulk particle material [Mar06, Dig10, Schu14]. The alignment of the particles in field-structured MREs further enhances the magnetic susceptibility of the material, when the magnetic field is applied in the particle chain direction [Dan12]. Finally, we note that in the few investigations of MRE magnetic properties during mechanical loading, a decrease of the magnetic susceptibility with the strain has been reported [Bos01, Lan03].

1.4.3 Magnetic field-dependent modulus

Under the influence of an applied magnetic field, MREs display a change of stiffness. This corresponds to the so-called magneto-rheological (MR) effect introduced by many researchers as the field induced change of modulus[8]. A lot of different results are reported about the relative MR effect: from as low as a few percent [Boc12] up to more than a thousand percent [Ste07]. Due to the great variety of investigated materials, manufacturing techniques and testing conditions, it is difficult to compare objectively all these results. However, some tendencies regarding the field-dependent modulus can be outlined, that are closely related to the previously observed purely mechanical and magnetic phenomena:

- Generally speaking, the magneto-elastic interactions result from an overall competition between mechanical stiffness and magnetic interactions: the lower the composite's stiffness, the higher the possible magneto-elastic effects.
- The change in modulus usually increases with iron-filler content. An optimal proportion of particles resulting from a competition between the stiffening of the material and the magnetic interactions (linear regime) is estimated between 20% and 30% particle volume fraction [Dav99, Gal12] and observed by trend in some experimental studies [Kal05, Dig10].
- The MR effect increases with increasing magnetic field; however, it saturates above a certain level of the applied magnetic field [Gin02, Kal05].
- The modulus increase tends to be highest in the small-strain region $(0 - 5\%)$ while it tends to decrease in the mid-strain region ($\sim 15\%$) [Bos01, Bel02, Schu14].

[8] The absolute MR effect $[MPa]$ is defined as the difference between the modulus for an applied magnetic field and the modulus at zero field (either elastic or tangent) whereas the relative MR effect [%] is defined as the ratio between these two moduli.

- The MR effect can be further enhanced in field-structured MREs [Bel02, Kal05, Var05].

1.4.4 Deformation under magnetic field

The coupled magneto-mechanical behavior can also be approached from another point of view, closely related to the field-dependent modulus and attributed to the very same mechanisms. The deformation exclusively due to an externally applied magnetic field can be defined as the free deformation of the MRE material. If such a deformation is restricted by imposed mechanical boundary conditions, additional work has to be expended to act upon the material, thus leading to a field-induced increase in stiffness. Experimental studies demonstrate deformations in the order of 10^{-4} [Gua08] up to 10^{-1} [Dig10], and report either stretching or contracting of MREs along the uniform applied field [Mar06, Dan12]. This deformation due to the magnetic field is often referred to as magnetostriction. However, the term magnetostriction is rather ambiguous since it is also used in physics to describe another phenomenon, and the underlying mechanisms of such deformations have to be clarified. Henceforward, we will suppose that the applied magnetic field is static and will not consider phenomena due to time-dependent magnetic fields or deformations.

Influence of the field homogeneity on the material behavior

When characterizing MREs, a uniform field distribution within the sample should be achieved since field gradients can have an important influence on the behavior of MREs. If a magnetic material is placed in a non-uniform magnetic field, the material experiences a magnetic body force to decrease its interaction energy with the magnetic field. When a MRE composite is placed in a gradient of external magnetic field, these forces act on the filler particles. The (magnetically soft) particles together with the polymer network are therefore displaced towards a higher amplitude of the field. Depending on the geometrical arrangement, elongation, contraction, bending or rotation can be achieved and used to create motion [Zri96], for example in smart actuators [Ste13]. In experimental MRE characterization in contrast, one has to keep in mind that these parasite field gradients can lead to additional deformation of the material on top of the original MR effect. On the one hand, it is not trivial to generate uniform, external excitation fields (see Section 1.6).

On the other hand, even if we suppose that the externally applied field $\mathbf{h}_0$ is perfectly uniform, the magnetized MRE sample can further create field gradients within the specimen[9]. Magneto-static field equations and the corresponding boundary conditions (see Chapter 3, Section 3.1) indeed prescribe the field distribution within a body, which strongly depends on its geometry, as illustrated in Figure 1.7. Only for ellipsoids of revolution and, as a special subset, for the sphere (all being finite) is the magnetization $\mathbf{m}$ as well as the perturbation $\mathbf{h}_1$ and hence the total magnetic field $\mathbf{b}$ uniform within the body. Thus, such bodies can be used for precise investigations of magnetic materials [Osb45].

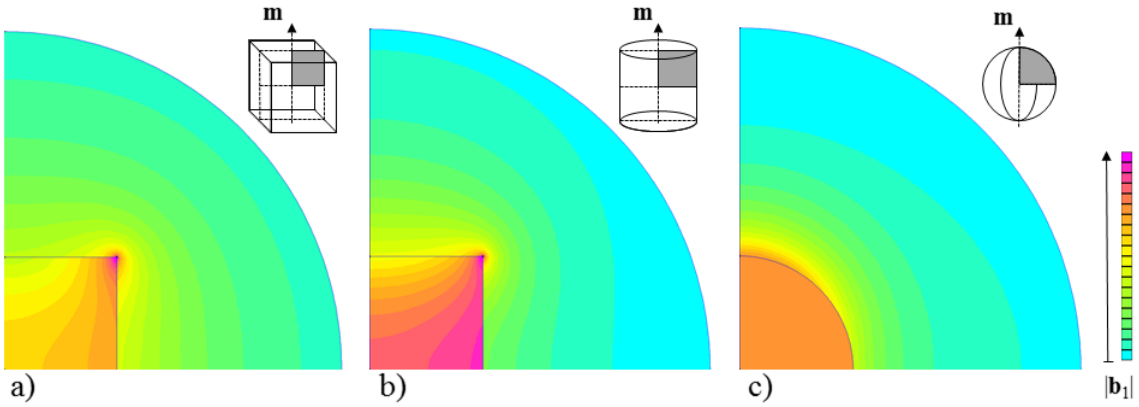

Figure 1.7: FEM simulation [FEMM] of the distribution of the magnitude of the magnetic perturbation field $|\mathbf{b}_1|$ in the first quadrant of the mid-symmetry plane of: a) a cube (2D plane), b) a cylinder (2D axisymmetric) and c) a sphere inclusion (2D axisymmetric) surrounded by air and magnetized bottom-up along the mid-axis.

Deformation behavior under uniform magnetic field

Since the 19th century, the term magnetostriction has been used in physics to designate the deformation caused by intra-granular spin-orbit interaction in crystalline ferro-magnets. A large piece of iron, for example, expands upon the application of a magnetic field though the saturation strain is in the order of 10^{-5} [Guy94]. This mechanism is inherently present in the ferromagnetic filler particles of MREs. However, the magnetostriction of the individual particles is several orders lower than the strains reported in MREs. Additionally, even if the applied field did create appreciable stresses in the stiff ferrous particles, these would not appreciably transmit

[9]Note that this will also influence the particle network when curing samples under magnetic field to obtain field-structured MREs.

through the soft polymer matrix. Therefore, this mechanism is usually neglected in investigations of standard MREs [Mar06, Sto11] and the word magnetostriction often used in the MRE literature designates the observed macroscopic effect.

Another mechanism that can arise at the microscopic scale is the rotation of the particles due to magnetic torques. Such torques apply predominantly to particles with an irregular, elongated shape and can produce strong magneto-elastic coupling. The particles indeed try to orient themselves parallel to the applied field, which tends to generate stretching of the sample in the field direction but can sometimes lead to an unstable configuration [Lan03, Lan04, Gal13a, Kar13]. Theoretically, because of their spherical shape, carbonyl iron particles cannot experience magnetic torques. However, particle aggregates can be present in MRE materials and are sometimes considered to contribute to the occurring deformations [Gua08, Sto11].

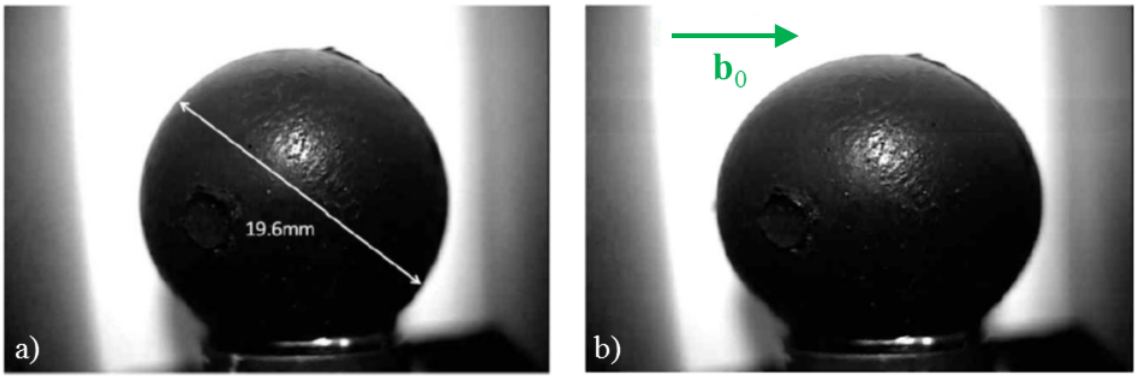

Figure 1.8: Photograph of an MRE sphere without a) and with b) an externally applied uniform field $\mathbf{b}_0 = \mu_0 \mathbf{h}_0 = 1.2\,T$ (green arrow). The applied field induces an elongation in the direction of the field of 4.8% at saturation ($E \approx 0.7\,MPa$) [Dig10].

The remaining physical mechanisms are the magneto-dipolar interactions between the particles. To summarize, these interactions try to enhance the overall magnetic susceptibility of the body by diminishing the magnetic part of its energy, in competition with the mechanical strain energy. The deformation of a MRE sample then seems to be the result of two contributions. On the one hand, determined by the overall geometry of the sample, the Maxwell stress at the discontinuity surface can induce an elongation of the MRE composite along the field. A significant strain of almost 5 percent for an MRE sphere has been reported ([Dig10], see Figure 1.8) and attributed to this so-called shape-effect, often described in terms of demagnetizing factors [Mar06, Mor09, Dig10, Zub12]. In the linear case of an ellipsoidal rigid body

(that has a uniform internal magnetic field **b**), if the material is isotropic or has its principal axes of magnetic anisotropy along the principal axes of the ellipsoid, the internal magnetic field **b** can be found analytically for a given externally applied uniform field $\mathbf{h}_0$. In this special case[10], the internal perturbation field $\mathbf{h}_1$ can be related to the uniform magnetization **m** with the help of the so-called demagnetizing factor D as $\mathbf{h}_1 = -D\mathbf{m}$ (see Figure 1.9).

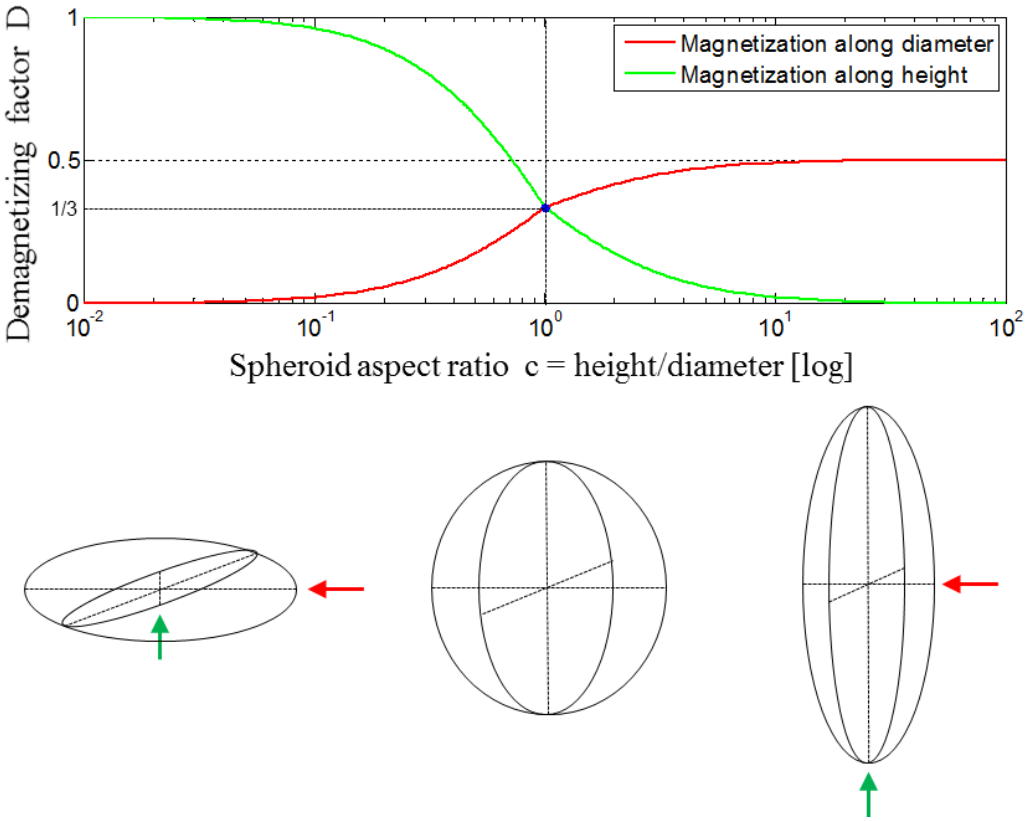

Figure 1.9: Demagnetizing factor D of the oblate spheroid ($0 < c < 1$), the sphere ($c = 1$) and the prolate spheroid ($1 < c$) depending on the spheroids aspect ratio and the direction of magnetization along the body's principal axes from [Osb45].

On the other hand, the sample can change its length in the direction of the field to enhance the magnetic susceptibility determined by the local position of the particles relative to one another. As described earlier in the context of magneto-rheological fluids [Lem91] and more recently in the context of MREs [Bor01], a restoring force between a pair of particles subjected to an externally applied magnetic field tends

[10]Note that average demagnetizing factors for other geometries, e.g. the rectangular rod or the cylinder, have also been derived [Sat89, Che91].

to align the particles with the field so that they form magnetic dipoles[11]. This contribution is characteristic for MREs (shape-independent material property) and theoretically can lead to either contraction or elongation of the sample:

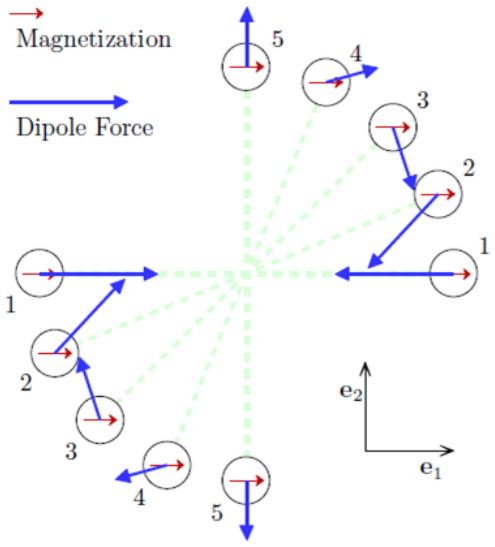

Figure 1.10: Schematic of the dipole interactions between a pair of particles for different angles magnetized along $\mathbf{e}_1$ [Gal14].

- In isotropic MREs, the tendency is for dipole pairs aligned with the applied field (pair 1 in Figure 1.10) to approach each other, causing a contraction of the sample along the field. Dipole pairs perpendicular to the field (pair 5 in Figure 1.10) typically push each other away, reinforcing the contraction along the field, since the material is almost incompressible [Kan04, Mar06]. However, the complicated nature of the particle interactions for random, three-dimensional micro-structures could give rise to different types of coupling, and this effect seems to generate strains in the order of 10^{-3}.
- In field-structured MREs, different possible magnetic and mechanical loading conditions further complicate the situation. If the magnetic field is applied parallel to the direction of particle chains, intuitively, there should be no or a very small deformational effect (due to possible shrinking during the fabrication process). The particles have reached their preferred arrangement during curing and have been trapped in the solid matrix. If an applied mechanical load disturbs this state of equilibrium and changes the inter-particle distances, the magnetic susceptibility decreases (as mentioned in Section 1.4.2).

[11]For simplicity, each particle magnetized along the applied field is treated as a dipole.

For an applied pre-tension, possibly up to a certain strain threshold, the magnetic interactions can try to restore the preferred state and the sample tends to be compressed [Coq04, Mar06, Dan12]. Conversely, for an applied pre-compression, the sample usually expands [Gin02, Dan12]. Typical values of strains in this case are in the order of 10^{-3}.

- If the magnetic field is applied transverse to the structuring direction, the deformational effect can even be higher. Due to the presence of the particle chains normal to the applied field, the particles tend to move more significantly in order to form dipole-pairs aligned with the applied field, typically leading to an overall extension of the sample [Gua08, Dan12]. Typical values of strains here are in the order of 10^{-2}.

Finally, note that under certain loading conditions, a uniform magnetic field can provoke extraordinary deformations of a MRE body, when a critical field is reached (onset of bifurcation). The instability of an elongated body subjected to a magnetic field transverse to its long axis can be interpreted as the well-known compass effect in magnetism [Moo68], whereby the body tends to align with the applied magnetic field (see Figure 1.11, [Rai08]). Instabilities due to a destabilizing torque are further favored when the sample's magnetic susceptibility in the direction of the applied field is lower than the susceptibility perpendicular to the field, for example due to a field-structured particle network [Mar06, Dan14].

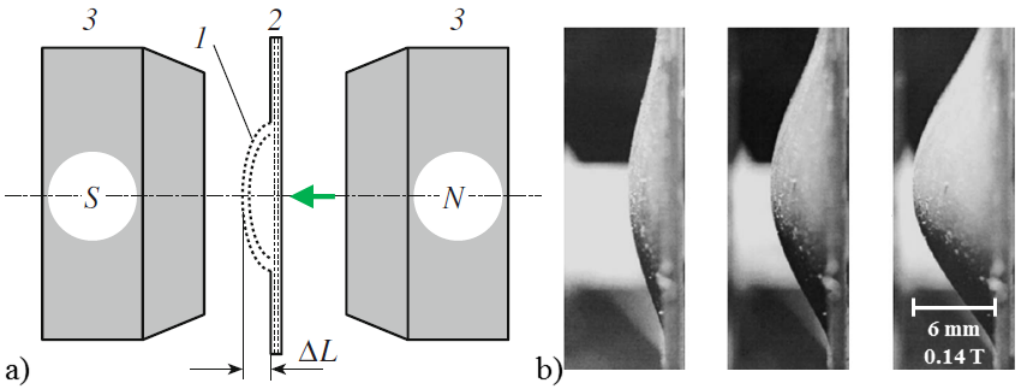

Figure 1.11: a) Schematic diagram and b) photographs of the deformation of a circular membrane (1), glued along the outer boundary to a fixating panel (2) and subjected to a uniform magnetic field (green arrow) [Rai08].

1.5 Approaches to the modeling of MREs

The above-described complexity of the magneto-mechanical coupled behavior of MREs makes their mathematical modeling a difficult task. Geometrical non-linearities are introduced in association with the large deformations that these elastomer-based materials are capable of developing. Additionally, constitutive non-linearities due to the hysteretic behavior of the viscoelastic matrix as well as a hysteretic, saturating magnetic response further complicate the modeling of such composites. The approaches in the modeling of these materials can basically be partitioned into micro-mechanical or structural models on the one hand and continuum or phenomenological models on the other hand. They are briefly reviewed in the following.

1.5.1 Micro-mechanically based modeling of MREs

The first kind of model provides a micro-mechanical description of MREs. Usually, the particles are considered as rigid spheres or spheroids distributed randomly [Bor01], or with a preferred alignment [Dav99, Yin06], within the elastomeric matrix. The magneto-mechanical interactions for a set of particles are then usually extrapolated in order to obtain the global expressions for a body. An interesting modeling approach is homogenization, that determines an effective macroscopic constitutive model for an MRE based on the properties of the constituent phases and their arrangement within the composite [Pon11]. The advantage of this type of models is that the mathematical expressions can provide insight into the underlying mechanisms responsible for the coupling in MREs. An important disadvantage that may be mentioned is the complexity of these expressions, even when a series of simplifications is usually adopted (linear mechanical or magnetic behavior; only the fields of closely neighboring particles or isolated evenly distributed particle chains affect each other).

1.5.2 Phenomenological continuum description

The second kind of models is continuum models, that do not have to describe all the microstructural phenomena to accurately capture the material's behavior. Since the magnetic particles are very small in comparison to the overall size of the investigated bodies, a continuous distribution of the particles or particle structures within the elastomer can be assumed. Some magneto-mechanical problems in MREs are solved in the framework of a relatively simple macroscopic theory, in which the

MRE composite is considered as a magnetizable elastic continuum, whose equations of magnetic and elastic state are uncoupled [Zri96, Rai08, Dig08]. Other models account for stress-induced changes in the magnetic behavior, but without a comprehensive field theory, they are limited to one-dimensional (small) deformations or to particular geometrical shapes [Mar06, Zub12, Kar13]. Fully coupled non-linear field theories for MREs have also been developed based on only one underlying continuum [Dor03, Kan04, Bus08, Ogd11, Sax13]. Global balances of linear and angular momentum, energy and entropy production, plus the Maxwell equations, are used in order to find a system of partial differential equations, from which the stress, the strain, the displacement and the magnetic fields can be obtained. At the heart of these theories, a free energy density function that depends in a coupled fashion on mechanical deformations and magnetic fields describes the materials constitutive behavior and is identified with the help of experimental data. Originally formulated for isotropic MRE materials, they have been recently expanded to describe field-structured magneto-elastic continua [Bus10, Dan12]. Once the material parameters of these models have been identified, they can be easily implemented numerically to handle boundary-value problems in complex geometries and loading conditions [Dor05, Dan14]. The main problem at the moment, however, is the lack of an accurate experimental characterization for finite strains and magnetic fields in order to propose realistic, mathematically consistent forms for the free energy function.

1.6 Previous experimental characterizations of magneto-elastic properties at finite strain

When characterizing MREs experimentally, the difficulty lies in the fact that (standard) mechanical testing methods of elastomers [Cha94, MSC10], accounting for uniform mechanical fields within a test specimen, have to be combined with externally applied magnetic loadings inducing a uniform field distribution inside the sample. Further complicating this task, mechanical tests up to high strain and under high magnetic fields have to be accomplished to completely capture the behavior of MREs. To account for the magneto-elastic coupling, the magnetic material parameters also have to be measured during sample deformation. Last but not least, different deformation modes should be evaluated to accurately identify the materials constitutive behavior. One can find in the literature a large number of tests (quasi-static, large strains, high magnetic field) for various MRE materials. The first

studies regarding MREs approached their behavior in a purely experimental fashion without the idea yet of a general constitutive description in mind. In what follows, the most significant studies are classified according to the magnetic field generation. Unless otherwise indicated in Section 1.4.2, measurements of the magnetic properties – if done at all – are performed separately from mechanical ones (i.e. no coupling). Additionally, "strains" implies nominal strain and "magnetic field" designates the excitation magnetic field $\mathbf{b}_0 = \mu_0 \mathbf{h}_0$ in $[T]$, if not otherwise specified.

1.6.1 Overview of experimental studies on MREs

Magnetic field created by permanent magnets

Probably the most simple way of applying an external magnetic field is through the use of permanent magnets. In such a setup, quasi-static double lap shear tests were performed by Shen et al. [She04] (strains up to 80%, magnetic fields up to 0.4 T), and quasi-static compression tests by Farshad et al. [Far04a, Far05] (strains up to 30%, magnetic fields up to 0.4 T). Schematics of these two experiments are presented in Figure 1.12a and b, respectively. Disadvantages that could be stated for this approach are that only fixed values of magnetic loads can be applied and that it is usually difficult to obtain a constant, homogenous field distribution with the help of these commonly rectangular-shaped permanent magnets.

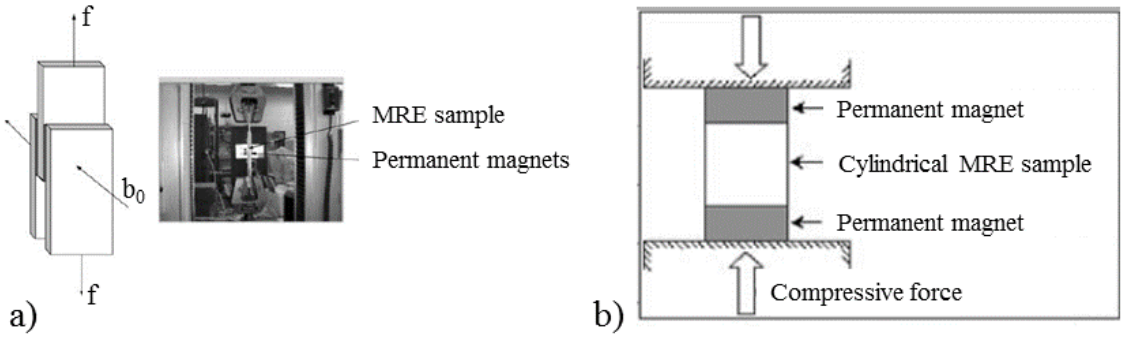

Figure 1.12: Schematics of setups in which MREs are subjected to a magnetic field generated by permanent magnets. a) Case of a double-lap shear test [She04]. b) Case of a compression test [Far04a].

Magnetic field created by solenoids

Static compression tests (up to 6.5% strain) under an externally applied magnetic field (up to 0.5 T) created with a ring-shaped solenoid around the MRE specimen were performed by Kallio [Kal05]. However, due to the small length of the solenoid and the asymmetrical positioning of the sample inside it (see Figure 1.13a), non-uniform magnetic fields influenced the measurements. Bossis et al. [Bos01, Bel02], as well as Coquelle [Coq04] (see Figure 1.13b), also placed their MRE sample within a solenoid (magnetic fields of up to 0.15 T). The elongated solenoid together with the central position of the long cylindrical sample ensured a uniform magnetic field in the region where the sample is placed. However, it blocked the access for experimental diagnostics that would be needed to extract the necessary strain data characterizing field-structured MREs. Hence, only one-dimensional tensile stress-strain measurements (up to 25% strain) were performed.

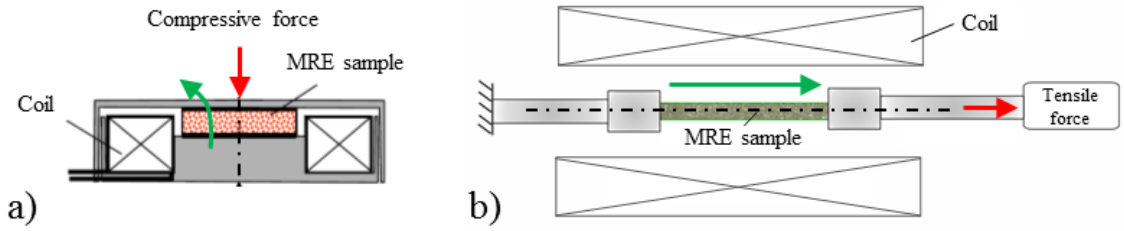

Figure 1.13: Schematics of setups in which MRE samples are placed within a solenoid-generated magnetic field (green arrow). a) Case of a compression test [Kal05]. b) Case of a tension test [Coq04].

Magnetic field created by Helmholtz coil systems

Martin et al. [Mar06] designed an interesting Helmholtz coil system for deformation measurements on MREs (see Figure 1.14). Two paired solenoids create a homogeneous magnetic field while providing access to the measurement region, despite being restricted to lower magnetic field values (up to 0.12 T). The rectangular-shaped MRE sample (non-uniform internal magnetic fields $\mathbf{b}$, $\mathbf{b}_1$ and mechanical fields) is suspended from a cantilever and centered within the two coils. By adding weights to the cantilever, a constant mechanical pre-stretch could be imposed (on the sample attached on the bottom end) and a one-dimensional deformation upon the application of the magnetic field was recorded by the help of an optical apparatus.

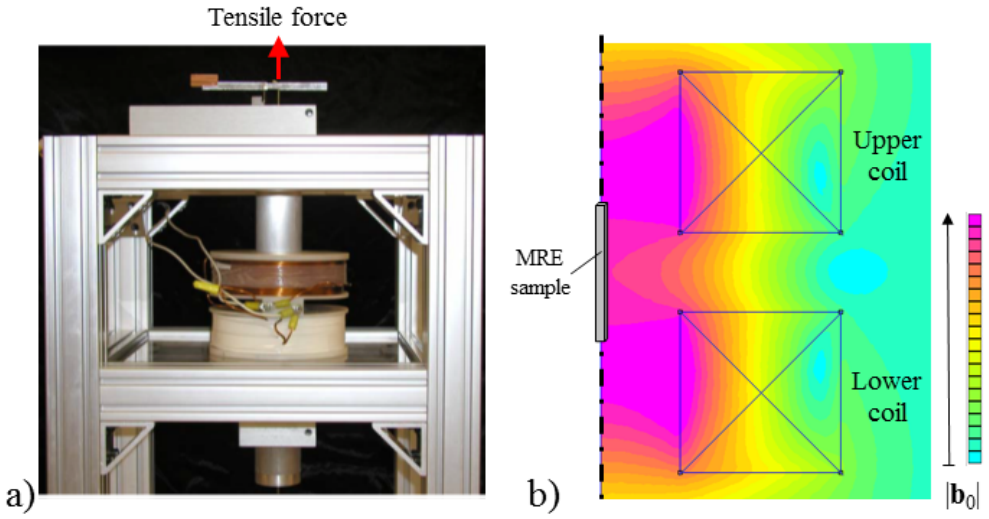

Figure 1.14: a) Schematics of the Helmholtz coil uniaxial tension system designed by Martin et al. [Mar06]. b) FEM visualization (2D axisymmetric, [FEMM]) of the distribution of the magnitude of the magnetic field $|\mathbf{b}_0|$ generated by the combination of both the upper and lower coils.

Magnetic field created by open magnetic circuits

Another common way to perform experiments on MREs is to place the sample between the two poles of an electromagnet. Commonly, tapered pole shapes guide the nearly uniform and elevated magnetic field (above 1 T), created by solenoids integrated in a high-susceptibility magnetic circuit, through an accessible air gap. In such a setup, double-lap shear tests (up to 10% strain, [Jol96, Gin99, Gin02, Kan07], see Figure 1.15), uniaxial deformation tests (up to 10% strain, [Kan07, Dig10]), and compression tests of an MRE cube (up to 10% strain, [Var05, Var06]) have been performed. Since this setting, adapted for uniaxial tensile tests, will be used in this study, a more detailed description of such an experimental setup can be found in Chapter 3.

1.6.2 Magneto-mechanical experimental characterization using continuum models

Just recently, some research groups have started working on a full magneto-mechanical experimental characterization for continuum models. During a PhD-thesis at the University of Glasgow, Schubert et al. [Schu13, Schu14] collected large-strain experimental data (up to 100% strain) for MREs under various deformation modes, both

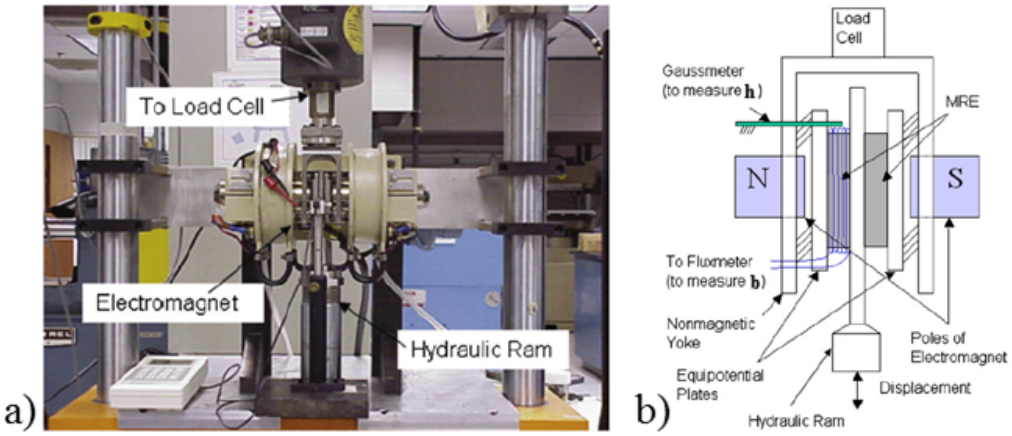

Figure 1.15: Double-lap shear setup with the MRE sample located between the two poles of an open electromagnetic circuit [Kan07]: a) photograph and b) schematic.

without and with the application of external magnetic fields. Isotropic and field-structured MREs were prepared and tested under uniaxial compression and tension, pure shear and equi-biaxial tension (see Figure 1.16). However, due to the use of permanent magnets, the applied magnetic fields (up to 0.3 T) were non-uniform and different in each setup. Furthermore, mechanical experimental issues were recorded (e.g. friction and buckling in compression tests and non-ideal deformation kinematics in pure shear). Tough the purely mechanical response of isotropic MREs could be described by a common constitutive model (Ogden), data fitting to several transversely isotropic models were not successful, even in the purely mechanical case. As a consequence, neither did they proceed to characterize magneto-mechanical constitutive models nor did they measure magnetic material properties depending on sample deformation.

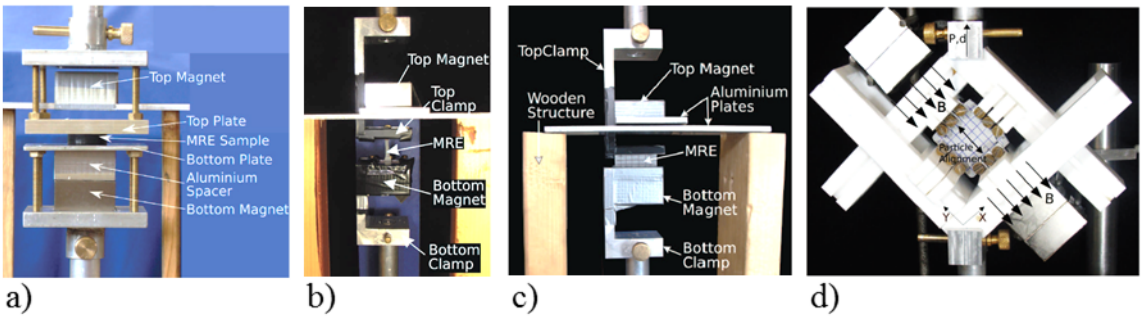

Figure 1.16: Photographs of MRE experimental setups for large strains under magnetic fields generated by permanent magnets: a) uniaxial compression, b) uniaxial tension, c) pure shear and d) equi-biaxial tension [Schu14].

Finally, in the framework of the European project MOCOPOLY[12] launched 2012 in Germany, one objective is the continuum physics modeling, testing and parameter identification of MREs at the macroscopic scale. Preliminary quasi-static and dynamic mechanical shear experiments for small deformations and low magnetic fields were conducted [Wal14] but no magneto-mechanical experimental results for finite strain have been published yet.

1.7 Scope and organization of the present work

The goal of the present work is to characterize the behavior of MREs with a main focus on their coupled magneto-mechanical response up to large strains and under high magnetic fields. Having in mind the design of smart devices capable of high deformations, the phenomenological material model proposed by Kankanala, Danas and Triantafyllidis [Kan04, Dan12, Dan14] needs to be accurately identified and implemented in numerical analysis. Indeed, a large out-of-plane deformation could be achieved in response to a spatially localized magnetic field and used in haptic devices such as a tactile interface [Vid07]. For example, patterns can be displayed on a surface by placing a matrix of solenoids or permanent magnets underneath a soft MRE surface (see Figure 1.17), as already achieved with magneto-rheological fluids [Jan10, Bol11, Lee11] or electro-rheological elastomers [Kyu12].

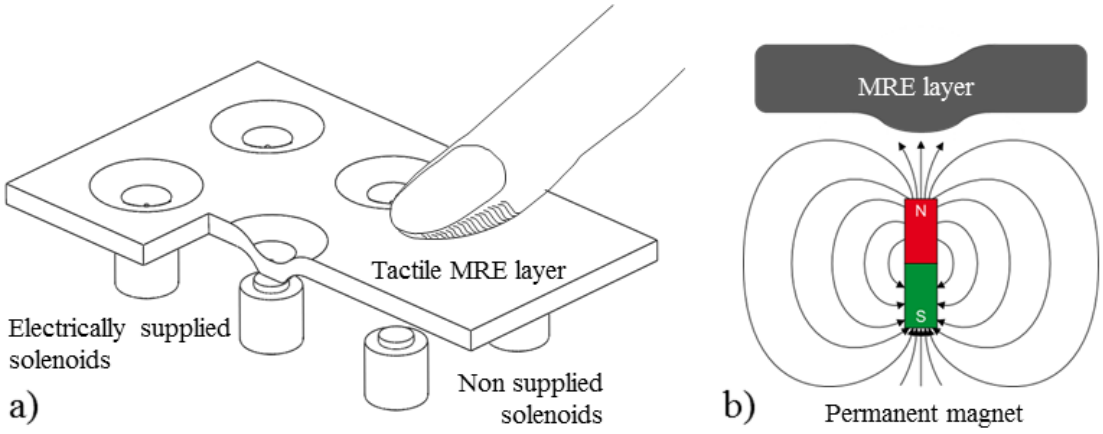

Figure 1.17: Schematics of the working principle for tactile interfaces with patterns created a) by a matrix of solenoids placed underneath a MRE layer or b) by a permanent magnet.

[12]Multi-scale, multi-physics modelling and computation of magneto-sensitive polymeric materials; ERC grant agreement n. 289049.

With the purpose of achieving a coupled magneto-mechanical characterization of MREs behavior for the development of a tactile interface, this work encompass experimental, theoretical and numerical developments. These topics are detailed in this manuscript as follows:

- In Chapter 2, aspects pertaining to the fabrication of MRE samples are presented. Material selection, fabrication process of isotropic and field-structured MREs, as well as sample design and particle/matrix compatibility are discussed.
- Chapter 3 covers the actual magneto-mechanical characterization. After introducing the general theoretical framework for transversely isotropic magneto-elastic continua, the coupled magneto-mechanical constitutive laws for both isotropic and field-structured MREs are derived in order to determine the sets of material parameters to be identified in each case. The second part of this chapter is dedicated to the experimental characterization of MREs thanks to a specially designed experimental setup allowing tensile tests up to large strains and up to high magnetic field.
- In Chapter 4, the identified MRE material models are integrated into a finite elements numerical analysis. The existing theoretical framework is extended to the axisymmetric case so as to predict the behavior of MRE layers subjected to a spatially localized magnetic field and the obtained numerical results are compared to an actual prototype device.
- Finally, Chapter 5 provides concluding remarks as well as perspectives for future work regarding the specific subjects treated in this thesis.

Chapter 2

Materials and samples

In this chapter, after a brief reminder of the state-of-the art in this domain in Section 2.1, all the aspects pertaining to the fabrication of the samples are covered. In Section 2.2, first the design of samples adapted to a coupled magneto-mechanical characterization is discussed. Material selection and general fabrication procedures are then presented in Section 2.3. Additionally, the interfacial adhesion between particles and matrix is investigated in detail in Section 2.4 in order to settle upon whether a pretreatment of the particles is needed in the rest of the study. The chapter is closed by a conclusion in Section 2.5.

2.1 Introduction

Magneto-rheological elastomers (MREs) are typically composed of micron-sized magnetizable particles dispersed in an elastomeric matrix. Within the class of elastomers, different stiffnesses can be targeted according to the intended use, from very soft silicone rubber for large-strain applications [Ber00] to relatively harder polybutadiene rubber [Sun08] for damping applications. Elastomers are made of macromolecular chains weakly bonded to each other. Their fabrication usually involves mixing two viscous liquids, the elastomeric non-bonded chains, often named Part A, and a catalyzer, named Part B, that triggers the cross-linking (also called vulcanization) of the macromolecular chains by creating bonds between them in order to obtain the final solid elastomer material. Depending on the elastomer formulation, cross-linking can be obtained via different chemical catalyzers (sulfur, platinum, ...) and can either happen at room temperature or require heating or even exposure to UV light during a specific curing time [Gen12].

The majority of fillers used in MREs are soft micrometric iron particles; magnetically "soft" meaning that they do not retain magnetization once the magnetic field is turned off. These particles are often spherical monodisperse carbonyl iron particles

(obtained by thermal decomposition of pentacarbonyl iron) of diameters ranging from 0.5 to 40 μm [Var06, Wan06, Boes09, Dan12], though the smaller end of the spectrum is favored to avoid degrading effects [Leb02, Ram04]. In MREs fabrication process, the micrometric particles are added to the uncured elastomer constituents and the obtained compound needs to be thoroughly mixed and degassed, before curing can be conducted in a mold of the desired shape.

Following the observation that particles arrange themselves in chain-like structures along the lines of the magnetic field in magneto-rheological fluids [Car00], researchers in the field of MREs have applied a homogeneous magnetic field to the elastomer composite during cross-linking. This also led to the formation of chain-like particle structures, which remained locked in place upon final curing [Car00, Kal05, Li08]. Hence the application or non-application of a magnetic field during curing gives the possibility to produce either transversely isotropic or isotropic samples, respectively.

As mentioned in the general introduction (Section 1.4.1), another important aspect influencing the strength of the composite material, especially under large deformations, is the interfacial adhesion between the filler particles and the matrix material [Dek83, Fu08]. Indeed, at a critical stress level, debonding acts as a distinct failure phenomenon in a polymer containing rigid inclusions due to stress concentrations at the weak particle-matrix interface [Gen84, Cre01]. In order to modify the particle-matrix interactions and more precisely to improve the interfacial adhesion for a given particle size, the modification of the surface properties of the system has been suggested [Zha07, Leg08]. Some studies showed the improved bond strength between primed metallic surfaces and addition-cured silicone elastomers [Pei04], and different kinds of silane coupling agents have already been used in MREs at moderate deformations [Coq04, Coq06b, Wan06, Fan10]. A silane coupling agent or primer typically consists of two different reactive groups located at either end of the active molecule, one compatible with the filler particles and the other one with the elastomer matrix. Applied in a thin, theoretically monomolecular layer, the primer serves as an adhesion promoter between the two initially non-bonding surfaces [Hab06]. Although the phenomenon of interfacial adhesion appears as a key property for the behavior of filler-soft elastomer composites, interfacial adhesion at high tensile deformations in soft MREs has rarely been investigated in detail.

Finally, due to the scarcity of coupled magneto-mechanical characterization existing in the literature, there has been so far, to our knowledge, no typical or ideal sample

specially devised for such a coupled characterization (see Section 1.6 in the general introduction). Indeed, particular attention to the sample shape was only mentioned in studies investigating the shape effect (see Section 1.4.4, [Dig10]) under purely magnetic loading. Considering that coupled magneto-mechanical characterization is the main goal of the present study, the crucial topic of the sample shape is addressed in the next section of this chapter.

2.2 Sample shape for coupled magneto-mechanical testing

In order to ensure reproducibility in material testing, norms provide guidelines for sample shape design depending on both the tested material and the type of loading. Behind a sample's shape for material properties evaluation lies the Saint Venant's principle according to which the difference between the effects of two different but statically equivalent loads becomes very small at sufficiently large distances from the load [Sai1855]. Practically, this means that for long tensile samples, the stress is homogeneous in the gage area of the sample far away from the clamping. If the sample is to be shorter, stress localization at the clamping needs to be attenuated by smooth root-corner radii from the sample's head to its gage area, hence yielding the well-known dog-bone (or dumbbell) samples for tensile testing. For elastomers tested in tension, the corresponding (equivalent) norms are the American ASTM D412[1] and its European counterpart ISO 37[2]. Some guidelines from the latter are reported in Figure 2.1, where the maximum recommended thickness is 3 mm for ISO 37-1 and 2.5 mm for ISO 37-2. Additionally, the cross-section of both samples is rectangular since in polymer testing, samples are often punched out of large sheets of the material of interest.

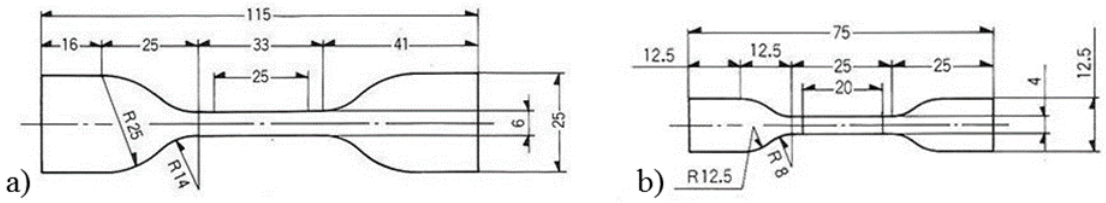

Figure 2.1: Sample shape design guidelines from [ISO37] norm: a) ISO 37-1 and b) ISO 37-2. Dimensions are in millimeters. Though not represented, both samples have a rectangular cross-section.

[1]Standard Test Methods for Vulcanized Rubber and Thermoplastic Elastomers-Tension.
[2]Rubber, vulcanized or thermoplastic - Determination of tensile stress-strain properties.

Provided that some of the samples are cured inside a magnetic field produced within a 82 mm air gap, there are restrictions regarding the length of the sample orienting the choice towards the ISO 37-2 dimensions (see Figure 2.1b). However, a 4 mm width might be too narrow for the markers that are done on the sample for video extensometry (see Chapter 3, Section 3.3.3) to be distant enough from the borders of the sample and hence to be free from edge effects. Thus, following the ISO 37-1 norm, the gage area and heads width of the ISO 37-2 norm are enlarged to 6 mm and 15 mm, respectively (as sketched in Figure 2.2a), in order to get a good compromise between the described restrictions and the need for a homogeneous state of strain and stress in the gage area of the sample during mechanical tensile tests. The sample thickness is set to the maximum of 3 mm.

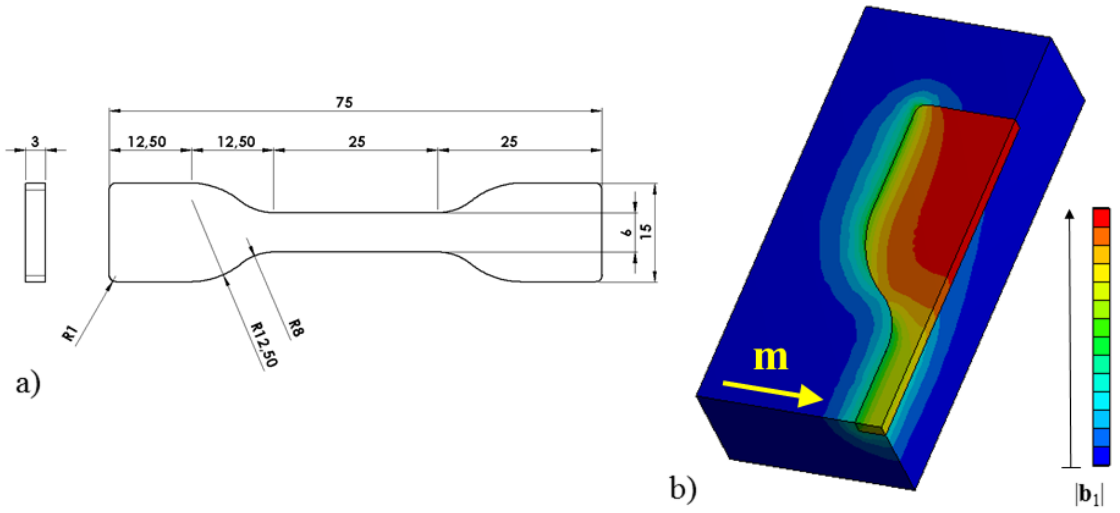

Figure 2.2: a) Dimensions, in millimeters, of the flat dog-bone sample ensuring a homogeneous state of stress in its gage area during mechanical tensile tests on MREs. b) 3D FEM simulations [ANSYS] showing the magnitude of the magnetic perturbation field $|\mathbf{b}_1|$ in a flat dog-bone magnetic sample magnetized ($\mathbf{m}$) transverse to its longitudinal axis.

However, as mentioned in the general introduction in Section 1.4.4, the shape of a body greatly influences the distribution of the total magnetic field $\mathbf{b}$ – even when submitted to a uniform external magnetic field $\mathbf{b}_0$. A numerical simulation, performed with the commercially available Finite Element Method (FEM) software [ANSYS] and reported in Figure 2.2b, shows that the magnetic perturbation field $\mathbf{b}_1$ (and thus $\mathbf{b}$ when the sample is magnetized by a uniform external magnetic field $\mathbf{b}_0$) is unfortunately not homogeneous in the gage area of the flat dog-bone sample suggested by the norm.

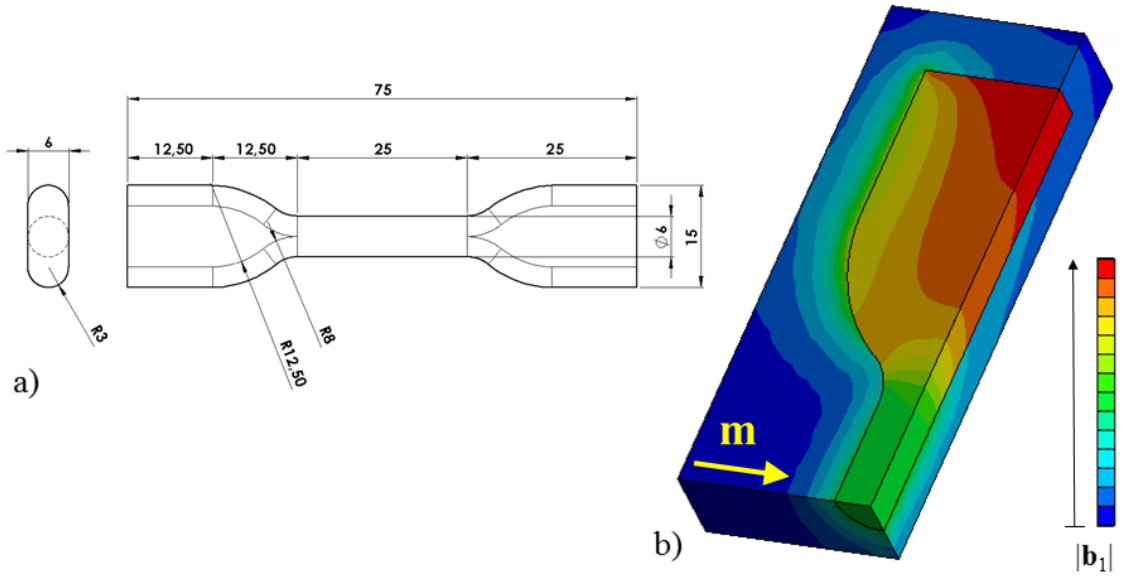

Figure 2.3: a) Dimensions, in millimeters, of the cylindrical dog-bone sample ensuring a homogeneous state of stress in its gage area during mechanical tensile tests on MREs. b) 3D FEM simulations [ANSYS] showing the magnitude of the magnetic perturbation field $|\mathbf{b}_1|$ in a cylindrical dog-bone magnetic sample magnetized ($\mathbf{m}$) transverse to its longitudinal axis: the magnetic response is now homogeneous in the gage area.

As a consequence, the design presented in Figure 2.2a is modified: we replaced the rectangular 3 *mm*-high cross-section by a 6 *mm*-diameter cylindrical one and increased the height of the heads to 6 *mm* though keeping them flat to simplify the design of the clamps (see Chapter 3, Section 3.3.2). The dimensions of this modified sample are presented in Figure 2.3a. On the one hand, having a cylindrical cross-section does not affect the homogeneity of the mechanical quantities in the gage area; cylindrical cross-sections are indeed commonly used for tensile testing in metals (ASTM E8/ISO 6892). On the other hand, the FEM simulation reported in Figure 2.3b now shows that the magnetic perturbation field $\mathbf{b}_1$ is homogeneous in the gage area of this cylindrical dog-bone sample when it is magnetized transverse to its longitudinal axis.

Though mechanical and magnetic quantities are homogeneous in the gage area of this modified sample (see Figure 2.3b), it still exhibits a non-homogeneous magnetic field $\mathbf{b}$ in its heads. As a matter of fact, only magnetic bodies of ellipsoidal (or as a subset, spherical) shapes can exhibit a homogeneous magnetic field $\mathbf{b}$ throughout their whole body (see Chapter 1, Section 1.4.4 and Figure 1.7). Though in mechanics, homogeneity is sufficient in the gage area to ensure proper material characteriza-

tion, we decided to verify experimentally whether this would also be the case when magneto-mechanical coupling is considered. Keeping the same design, the fabrication procedure is modified so that the sample's heads are replaced by non-magnetic 3D-printed plastic insets while only the cylindrical gage area is made of MRE and terminated at both ends by an ellipsoidal cap (see Figure 2.4a and further details in Section 2.3.3 dedicated to fabrication). A FEM simulation, reported in Figure 2.4b, shows that the magnetic perturbation field $\mathbf{b}_1$ is almost homogeneous in the nearly ellipsoidal MRE body of this modified sample.

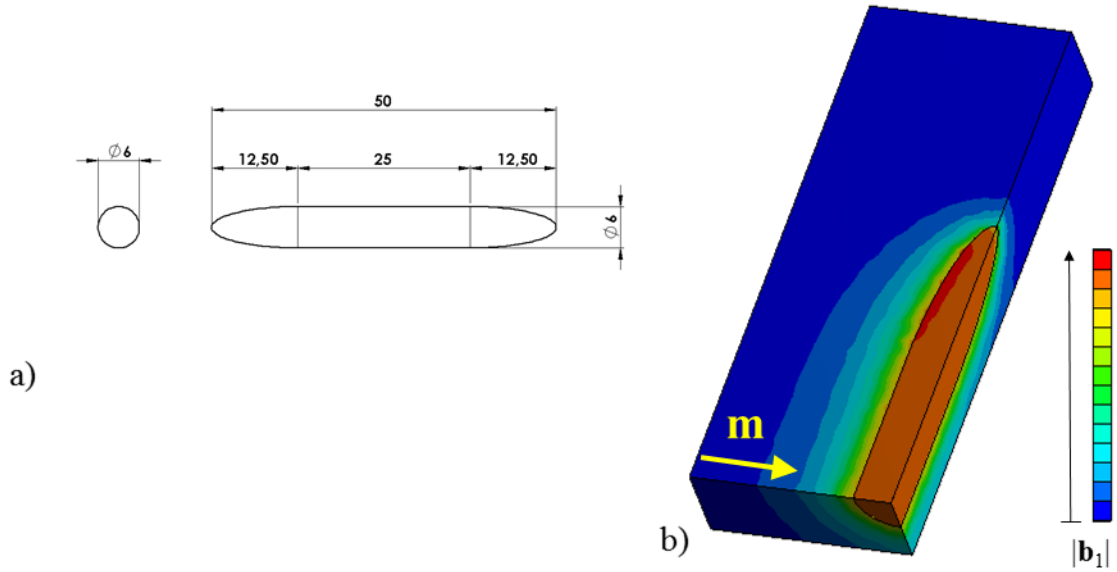

Figure 2.4: a) Dimensions, in millimeters, of the ellipsoidal part of the cylindrical dog-bone sample with nearly ellipsoidal MRE body and plastic heads. b) 3D FEM simulations [ANSYS] showing the magnitude of the magnetic perturbation field $|\mathbf{b}_1|$ in the nearly ellipsoidal MRE body: the magnetic response is almost homogeneous in the whole MRE part of the sample.

Two questions now have to be addressed:

1. Does this new design affect the mechanical response?
2. Does this modification actually impact the magneto-mechanical coupling?

To answer the first question, a purely mechanical test (after a precycling of 10 cycles) is performed on two pure silicone samples with either rectangular or cylindrical cross-section, and on two MRE samples with either a cylindrical dog-bone shape or a nearly ellipsoidal MRE body and plastic heads. The results are presented in Figure 2.5a and b, respectively. From the results of Figure 2.5a, it can be seen that both the flat and full cylindrical dog-bone samples exhibit almost the same mechan-

ical response up to large values of stretch, thus confirming as expected that both shapes are equally valid for mechanical testing. However, the results of Figure 2.5b show that the mechanical response of the cylindrical dog-bone sample with nearly ellipsoidal MRE body and plastic heads is only identical to the cylindrical dog-bone sample up to small stretch before showing a loss of stiffness past a stretch of approximately 1.1 due to debonding at the weak interface between the MRE body of the sample and the plastic heads. Hence, provided we remain below a 1.1 stretch, the latter sample safely yields a response that is representative of the material.

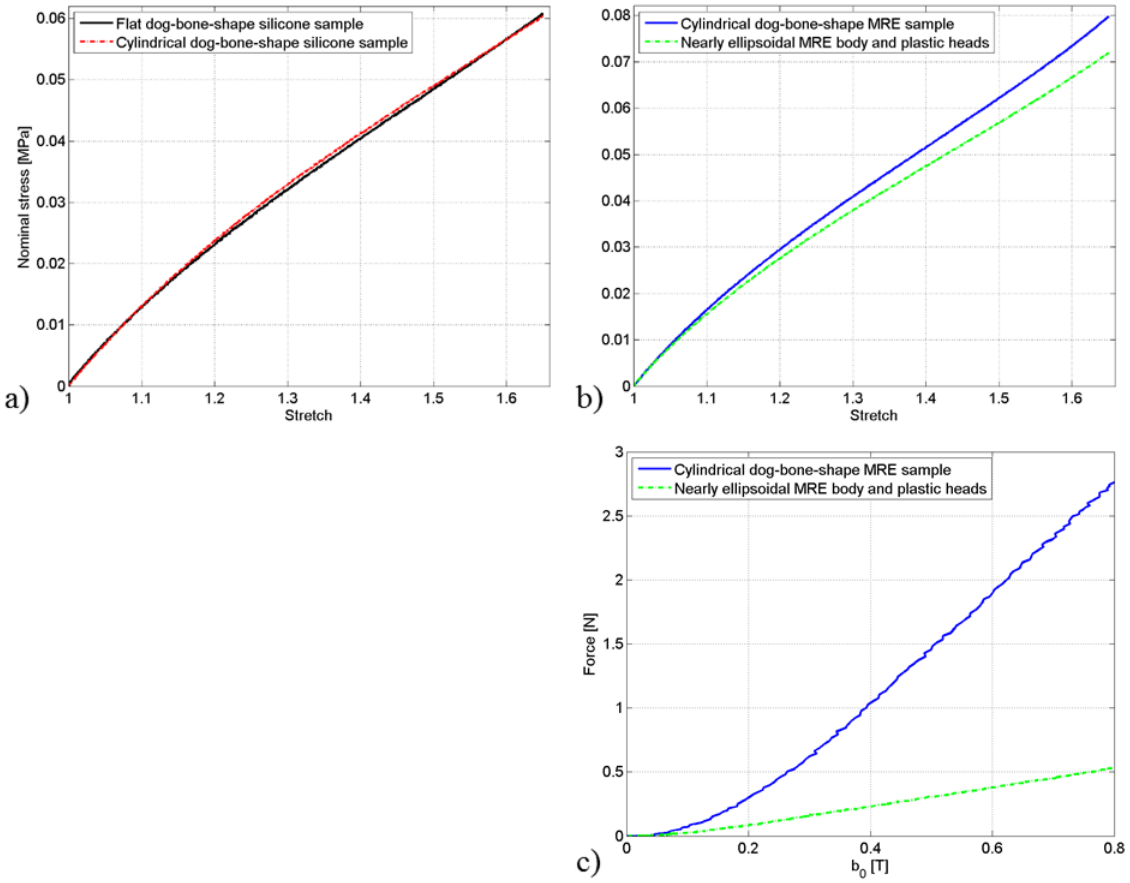

Figure 2.5: a) Mechanical response of a pure silicone sample for a flat dog-bone-shape sample and a cylindrical dog-bone-shape sample. b) Mechanical response of an isotropic MRE sample of identical particle content for a cylindrical dog-bone sample and a cylindrical dog-bone sample with nearly ellipsoidal MRE body and plastic heads. c) Force response under purely magnetic loading for the same samples as in b.

To answer the second question, the force response under purely magnetic loading (up to $\mathbf{b}_0 = 0.8\,T$) is monitored for two MRE samples – held fixed in the uniform

magnetic field applied transverse to their longitudinal axis – with either a cylindrical dog-bone shape or a nearly ellipsoidal MRE body and plastic heads thanks to the dedicated setup that will be described in detail in Chapter 3. The corresponding results are reported in Figure 2.5c. One sees that the force exerted by the sample is much higher in the case of the full cylindrical dog-bone sample than in the case of the dog-bone sample with nearly ellipsoidal MRE body[3] and plastic heads. This confirms the large contribution of the presence of magnetic field gradients within the MRE heads (see Figure 2.3b) to the whole magneto-mechanical response of the sample. In such a case the measurements would yield the response of a structure rather than that of the material.

As a conclusion, in order to perform a coupled magneto-mechanical testing of MREs, the full cylindrical dog-bone samples will be used for purely mechanical tests up to large deformations while the cylindrical dog-bone sample with nearly ellipsoidal MRE body and plastic heads will be used for coupled experiments provided that the corresponding stretch remains below the threshold identified earlier. Note that this threshold ($\pm 10\%$ nominal strain) is largely beyond the domain of small strains.

2.3 Materials and fabrication procedure

2.3.1 Materials selection

In the perspective of obtaining a material in which magneto-mechanical coupling is optimal (i.e. largest deformation produced by the smallest magnetic field) for a possible application in a tactile MRE interface, the selected matrix material is a very soft and stretchable silicone elastomer Ecoflex 00-20 from Smooth-On Inc., USA. This elastomer is a room temperature two-part addition-cured platinum-catalyzed system (RTV-2). According to the manufacturer, the obtained silicone has a Shore hardness of 00-20, an elongation at break of 845% and a density ρ_{sil} of 1,070 kg/m^3. It has a mixed viscosity of 3,000 cP [$cp = mPa.s$], which offers a good compromise between good dispersion when mixing, easy pouring and minimal settling of particles during accelerated curing.

The filler phase is carbonyl iron powder (CIP) SM from BASF Germany. This powder is made of spherical particles with a median diameter of 3.5 μm and contains up to 99.8% of Fe with low amounts of C, N and O. As soft iron is known to have

[3]Note that only a small contracting stretch of 0.991 at $\mathbf{b}_0 = 0.8\,T$ is observed in the case of the dog-bone sample with nearly ellipsoidal MRE body.

a low coercitivity and a magnetic saturation $\mu_0 m_s = 2.1\,T$ [Hay13], these particles are good candidates for MRE applications with optimal coupling. According to the manufacturer, the bulk density ρ_{bulk} is between 1,500 to 2,500 kg/m^3 in the form of powder, while the density of iron (as a solid metal) is 7,874 kg/m^3. The above-mentioned bulk density takes into account the presence of air gaps between particles when they occupy a given volume in the form of powder but this becomes irrelevant once the particles are mixed in the viscous liquid elastomer. Nevertheless, the density commonly considered in the MRE literature is taken either as the one of iron (e.g. [Schu14]) or slightly lower than that of iron (e.g. [Gor09]) – probably to account for the fact that minute air gaps can be retained between adjacent particles or between the particles and the elastomer chains. In practice during fabrication, the different elements of the compound are weighed and one actually works with m_P, m_A and m_B, that correspond to the mass of particles, Part A silicone and Part B catalyzer, respectively. In the chemistry and polymer literatures [Cie99, San13], the particles to silicone ratio is often expressed in Parts per Hundred Rubber [*phr*], which gives the mass of filler per hundred parts of raw compounded polymer mass ($phr = m_p / (m_A + m_B) * 100$). Hence, the CIP density ρ_{CIP} only comes into play to compute the corresponding particle volume fraction ϕ_{vol} as follows:

$$\phi_{vol} = \frac{\dfrac{m_P}{\rho_{CIP}}}{\dfrac{m_P}{\rho_{CIP}} + \dfrac{(m_A + m_B)}{\rho_{sil}}} = \left(\frac{100}{phr}\frac{\rho_{CIP}}{\rho_{sil}} + 1\right)^{-1}. \tag{2.1}$$

The particle volume fraction ϕ_{vol} is actually preferred in the mechanics community because it appears in the constitutive equations. However, considering the fact that it involves the equivalent density of CIP once dispersed in silicone, which might be sensitive to the chemistry of the elastomer matrix and possibly the mixing procedure, we will rather compare MRE composite samples on the basis of the particles to silicone ratio expressed in *phr* throughout this manuscript. The value taken for the density of CIP should be clearly stated if proper comparisons have to be made or if the volume fraction is needed as input for modeling.

2.3.2 Fabrication procedure

To fabricate pure silicone material, the elastomer (Part A) and the catalyzer (Part B) are first dispensed in a beaker in a one to one weight ratio thanks to a Sartorius

TE612 0.01 g-precision scale. In the case of MRE samples, the desired mass of particles is added to the polymer (Part A) and mixed by hand (using a spatula) to ensure a proper dispersion of the particles among the polymer chains before starting the polymerization of the network by adding the catalyzer (Part B). The obtained blend is then mixed thoroughly mechanically for three minutes with a large wing nut mounted on a drill rotating at 400 rpm in order to ensure a homogeneous dispersion of all constituents in the compound. This mixed compound is degassed at 1 $mbar$ for 8 minutes to eliminate any air entrapped during mixing and then poured by hand in a mold. The steps described above are conducted in less than 30 minutes, which is the so-called "pot lifetime" of the Ecoflex 00-20 elastomer, according to the manufacturer. Finally, curing is performed by heating the mold up to $100°C$, maintaining it at this temperature for 60 minutes and letting it cool down back to room temperature (see details in the next section). After this, the sample can be removed from the mold. Though this silicone can be cured at room temperature within $24h$, accelerating the curing process via heating has two advantages: lock particles in place quickly to avoid settling down during curing and reduce manufacturing time.

2.3.3 Molds and stands

In order to fabricate a sample of desired shape, dedicated molds are machined out of copper. This material is selected for its high thermal conductivity of 390 $W.m^{-1}K^{-1}$ so as to ensure optimized thermal exchanges through a significant thickness[4]. The negative half imprint of the cylindrical dog-bone sample described in Figure 2.3a is machined out of a pair of plates (each measuring 81 mm x 60 mm x 4.5 mm) thus providing a mold when assembled together. A detachable piece located next to the sample's heads provides clearance to fill the material into the mold along the sample's height and is reattached before curing (see Figure 2.6a). The molding process is realized with a 10 mL medical syringe centered by an apparatus above the opening (see Figure 2.6b).

When the full MRE cylindrical dog-bone sample (Figure 2.3a) needs to be fabricated, the MRE mixture is injected directly into this mold. When the cylindrical dog-bone

[4]It can also be mentioned incidentally that copper is very slightly diamagnetic (i.e. it creates a small magnetic field in opposition to the applied field) but its susceptibility is -1x10^{-5} [Hay13]. Another relevant comparison is with aluminum: it has a thermal conductivity of 237 $W.m^{-1}K^{-1}$ and is paramagnetic (i.e. it creates a small magnetic field in the direction of the applied field) with a susceptibility of 2.2x10^{-5} [Hay13]. In any case, such values of susceptibilities are so negligible, that under the maximum magnetic field of 0.8 T we can achieve, such a perturbation remains lower than that of the Earth magnetic field (between 25 and 65x10^{-6} T).

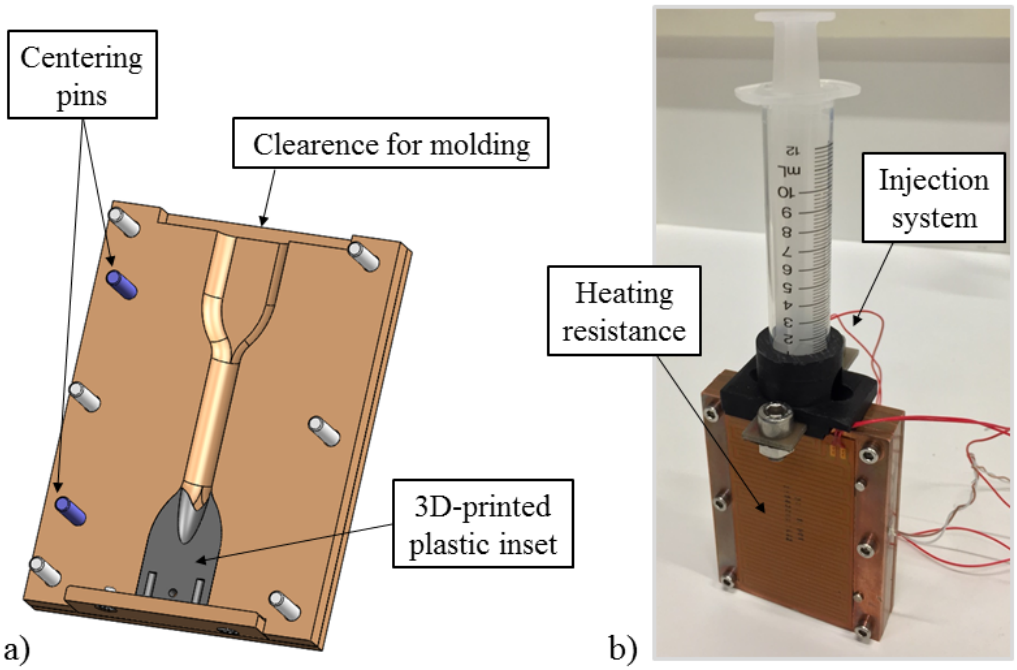

Figure 2.6: a) CAD drawing of the open mold (containing a sectional view of the lower 3D-printed plastic inset used for the fabrication of samples with nearly ellipsoidal MRE body). b) Picture of the mold assembled for the injection of the MRE material, showing the heating resistance of the external plate.

sample with nearly ellipsoidal MRE body and plastic heads (Figure 2.4a) needs to be fabricated, the lower 3D-printed plastic inset is first inserted, then the MRE mixture is injected, and finally the upper 3D-printed plastic inset is inserted. In order to obtain a non-magnetic heating system allowing to cure the sample while the mold is placed in an electromagnet in a repeatable fashion, the above-mentioned mold is sandwiched between two other copper plates (each measuring 81 mm x 60 mm x 3 mm) that bear, at the center of their external surface, a Minco HK5402 heating resistance covering an area of 76.2 mm x 41.9 mm (see Figure 2.6b). A thermocouple is inserted in one of the half imprint, close to the center of the sample, through a 1.5 mm-diameter hole terminated by a 0.7 mm-diameter and 2 mm-long hole where the sensitive tip of the thermocouple sits. The remaining air gap between the thermocouple wire and the hole is filled with thermally conductive paste. The selected thermocouple is of type T, hence providing a $0.5°C$ precision (in class 1) while being non-magnetic. It is connected to a temperature regulation system Statop 2415 (on/off PID regulation) that delivers current to the heating resistance following a desired heating schedule, here a rising rate of $10°C/min$ up

to 100°C and a dwelling time of 60 minutes.

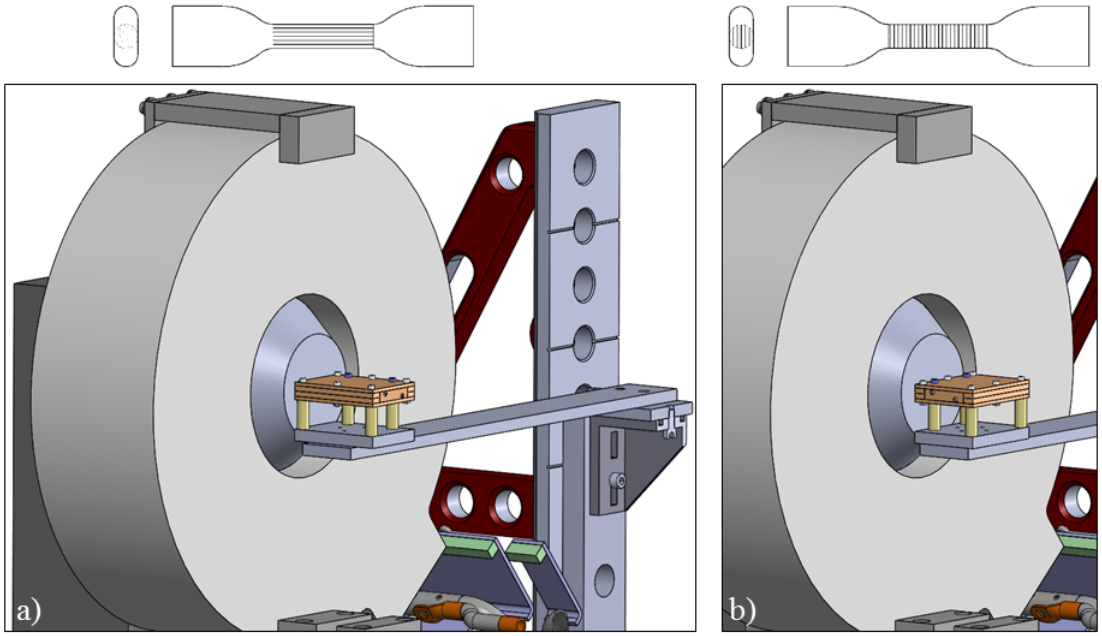

Figure 2.7: Schematics of the stand used to fabricate transversely isotropic samples (for clarity, one coil has been removed). a) Stand in the configuration yielding particle chains along the sample's longitudinal direction. b) Stand in the configuration yielding particle chains along the sample's transverse direction.

To fabricate transversely isotropic MRE samples, curing must be conducted under magnetic field. For curing – and the subsequent magneto-mechanical characterization – we use a two-coil electromagnet generating a nearly homogeneous field $\mathbf{b}_0 = 0.8\,T$ between two 90 mm-diameter poles separated by a 82 mm-air gap[5]. In this gap comes a removable aluminum plate maintained from outside of the magnet by a fixed bracket. Centering pins installed on this plate permit an easy and repeatable positioning of dedicated stands designed to hold the mold in place at the center of the magnetic field. These stands allow the fabrication of samples having chains of particles according to different orientations, namely along the sample's longitudinal direction so that chains are perpendicular to the field during the tests (Figure 2.7a, top), and along the sample's transverse direction (Figure 2.7b, top) so that chains are aligned with the field during the tests. In particular, the stand can be mounted in two perpendicular directions on the aluminum plate and yields the desired particle chain configurations (see Figure 2.7a and b). The tubular parts of the stand in contact with the copper mold are made of polyether ether ketone (PEEK) – a

[5]A more detailed description of the electromagnet is provided in Chapter 3, Section 3.3.

material having a very low thermal conductivity of 0.25 $W.m^{-1}K^{-1}$ while exhibiting good mechanical strength – so that the stand does not act as a heat sink.

2.4 Study of interfacial adhesion

In this section, the interfacial adhesion between the particles and the elastomer matrix for the MRE composites used in this work is addressed. We investigate how a pretreatment of the particles with a silane primer can modify the interfacial adhesion both from a microscopic and a macroscopic perspective and settle upon whether such pretreatment is needed in the rest of the study. More particularly, different MRE samples are prepared by modifying the surface of the CIP via silane primer treatment according to two procedures, prior to sample fabrication. These samples are then compared to a sample without particle treatment both under scanning electron microscope (SEM) and during macroscopic mechanical testing.

2.4.1 Samples preparation

As stated in Section 2.1, it has been suggested in previous MRE literature to coat the particles with a silane coupling agent in order to improve interfacial adhesion between the CIP fillers and the silicone elastomer matrix [Coq04, Coq06b, Wan06, Zha07, Fan10]. In this work, the tested coupling agent is the clear 1200 OS Primer from Dow Corning, USA. This silane-based primer contains a 5% non-volatile active content diluted in volatile siloxanes that need to evaporate before the two initially weakly bonding surfaces are put in contact with each other. The active content is octamethyltrisiloxane ($C_8H_{24}O_2Si_3$) in which the oxygen termination of the molecule is prone to bond with metals while the other end bonds to the silicone matrix.

Two procedures are followed to apply the primer onto the particles: either by spray-coating the particles with it or by stirring the particles in it. In the so-called "spray-coating" procedure, the particles are dispersed in a plastic container and sprayed with the primer using an airbrush while shaking the container. The particles are then air-dried for 45 minutes before being used in the sample fabrication procedure. In the "stirring" procedure, the iron particles are directly stirred in the silane primer dilution. The particle-primer mixture is then widely dispersed on a Teflon plate, rinsed out with ethanol and air-dried for 45 minutes before the particles are used in the fabrication procedure.

For this study of interfacial adhesion, different samples are fabricated:

Material		Pure silicone	Untreated MRE			Spray-coated MRE			Primer-stirred MRE	
Primer treatment on particles		N/A	None			Spray-coating method			Stirring method	
Particles to silicone ratio [phr]		N/A	21	140	210	21	140	210	21	210
SEM at rest		-	Fig. 2.11 a	-	See [Poes14]	Fig. 2.11 b	-	See [Poes14]	Fig. 2.11 c	See [Poes14]
SEM under tension		-	Fig. 2.12 a and d	-	See [Poes14]	Fig. 2.12 b and e	-	See [Poes14]	Fig. 2.12 c and f	See [Poes14]
Macroscopic cyclic tension	all cycles	Fig. 2.13	Fig. 2.14 a		Fig. 2.14 d	Fig. 2.14 b		Fig. 2.14 e	Fig. 2.14 c	Fig. 2.14 f
	stable hysteresis	Fig. 2.15	Fig. 2.15		Fig. 2.15					
	stable upload curve		Fig. 2.16 b	Fig. 2.16 b	Fig. 2.16 a Fig. 2.16 b	Fig. 2.16 b	Fig. 2.16 b	Fig. 2.16 a Fig. 2.16 b		Fig. 2.16 a

Table 2.1: List of samples fabricated for the interfacial adhesion study cross-referenced with the scale at which they were studied and reported data. (A dash in the cell means the experiment was not conducted, a blank cell means the corresponding data is not presented.)

- a pure silicone sample,
- transverse isotropic MRE samples without particle treatment,
- transverse isotropic MRE samples with silane treatment of the particles according to the "spray-coating" procedure,
- transverse isotropic MRE samples with silane treatment of the particles according to the "stirring" procedure.

MRE samples with very different particles to silicone ratio are studied: the lowest particles to silicone ratio of 21 *phr* is selected to permit a clear observation of the particles within the matrix of MRE samples under the microscope while higher particles to silicone ratios are also considered to investigate the macroscopic behavior of MREs likely to be used in engineering applications. Table 2.1 summarizes the samples fabricated in this study of interfacial adhesion and also details at what scale they were studied. In this table, we refer to our article regarding interfacial adhesion for results and curves that are not presented in this section for the sake of brevity.

In this preliminary study, the samples are casted in 24 mm x 24 mm x 4 mm copper molds and the magnetic field is applied with a coil-permanent magnet device, presented in Figure 2.8a and delivering a constant magnetic field of $\mathbf{b}_0 \approx 0.3T$ in the air gap. It caused the particles to align in chain-like structures in the direction of the field. The rest of the fabrication procedure is identical to the description made in Section 2.3.2. A finite element simulation with the Finite Element Method Magnetics

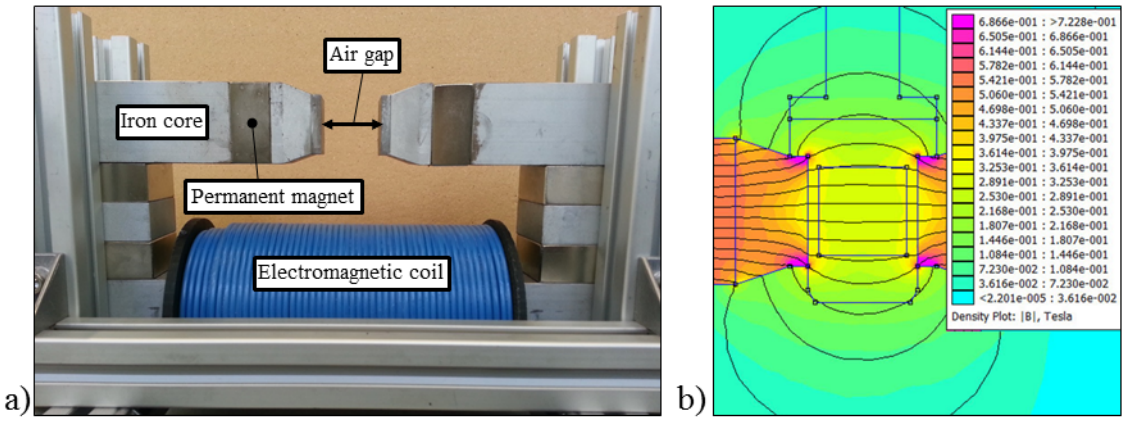

Figure 2.8: a) Coil-permanent magnet device used to create a magnetic field of $\mathbf{b}_0 \approx 0.3T$ during the curing of the samples. b) FEM simulation (plane, [FEMM]) showing the homogeneity of the magnetic flux $\mathbf{b}_0$ inside the air gap.

[FEMM] software shows that the applied magnetic field $\mathbf{b}_0$ is rather homogeneous in the zone where the samples were placed (see Figure 2.8b). However, the total magnetic field $\mathbf{b}$ within the sample is non homogeneous, especially at the corners, due to the parallelepipedic shape of the samples. Nevertheless, as the corners are to be maintained by clamps, this does not unduly affect the overall mechanical response of the samples in this preliminary comparative study.

2.4.2 Scanning electron microscopy

Microscopic scale investigations are conducted using an environmental Quanta 600 field emission gun (FEG) scanning electron microscope (SEM). Particles are first observed separately to evaluate how they were coated by the silane primer. Secondly, MRE samples are imaged at rest and under tension[6] to observe the effect of primer application at the local scale.

Observation of particles alone

The untreated particles, as well as the particles treated with primer according to both application methods ("stirring" and "spray-coating"), are investigated by SEM using a beam voltage of 5 kV and the Everhart-Thornley detector in high-vacuum

[6] An in-situ traction stage inside the SEM is used to pull on the MRE samples up to 140% nominal strain parallel to the particle chains, thus allowing to image the composites' microstructure at high deformation states.

mode. The corresponding images, obtained at two different magnifications, are presented in Figure 2.9.

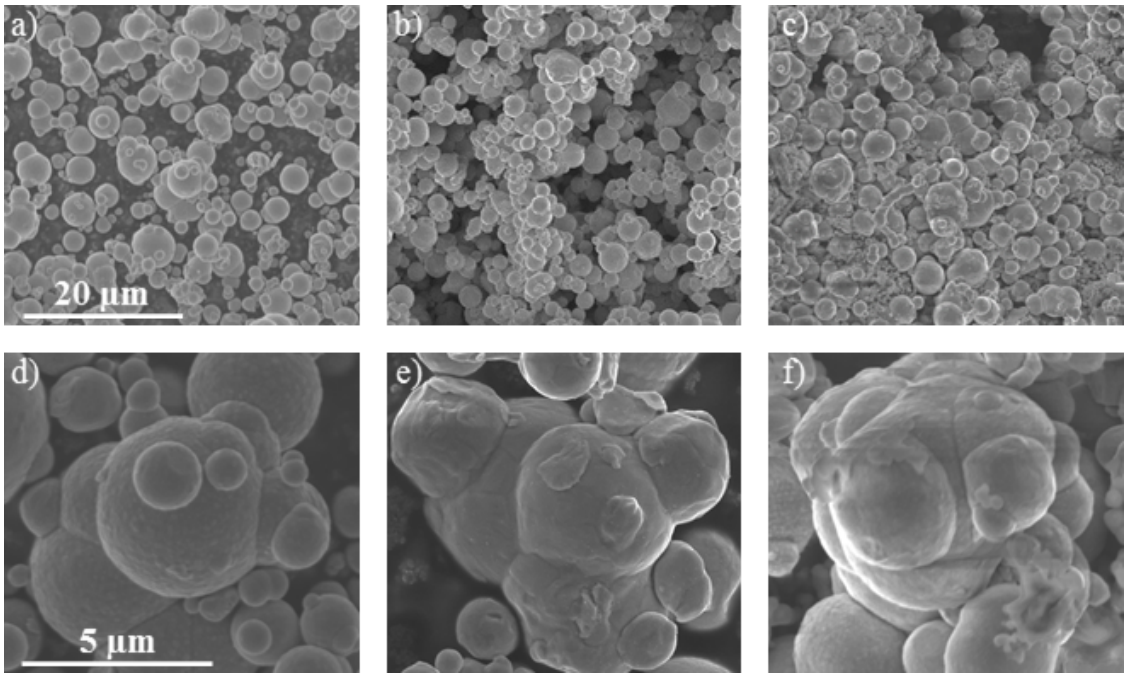

Figure 2.9: SEM micrographs of 3.5 μm median size carbonyl iron particles. Top: SEM micrographs (1,500×) of a) untreated particles, b) spray-coated particles and c) primer-stirred particles. Bottom: SEM micrographs (6,000×) of d) untreated particles, e) spray-coated particles and f) primer-stirred particles.

While the untreated (Figure 2.9a) and the spray-coated (Figure 2.9b) particles are rather loosely assembled, the primer-stirred particles (Figure 2.9c) are stuck together in irregular aggregates by the primer. The spray-coated particles tend to be covered homogeneously with a rather thin layer of primer (Figure 2.9e). In contrast, the majority of the primer-stirred particles are largely covered, though rather unevenly, by the silane primer treatment (Figure 2.9f).

Observation of MRE samples

SEM investigations of the MRE samples are then performed in low-vacuum mode with a chamber pressure of 130 Pa and environmental water vapor in order to limit charge phenomena during the imaging of such a low-conductivity material. In this case, a beam voltage of 10 kV and the back-scattered electron detector are used. Samples are cut across their thickness parallel to the chains of particles along the

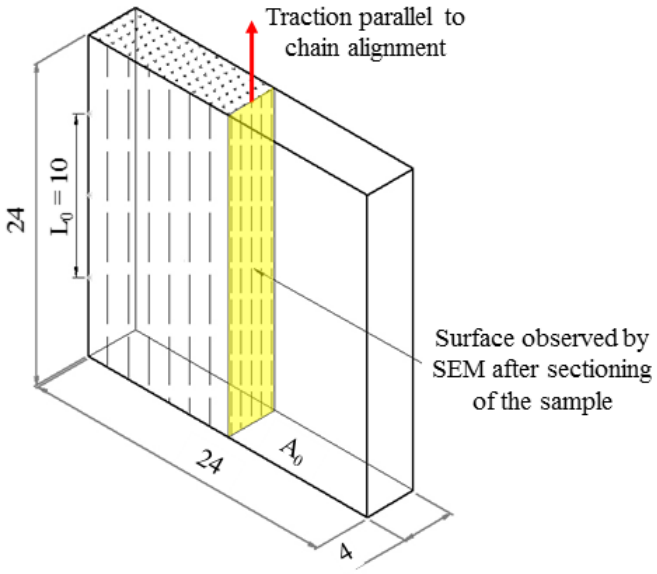

Figure 2.10: Sketch of the sample used in the interfacial adhesion study (dimensions in millimeters) and view of the surface observed in SEM investigations.

surface highlighted in Figure 2.10 and all observations are conducted on this cross-section.

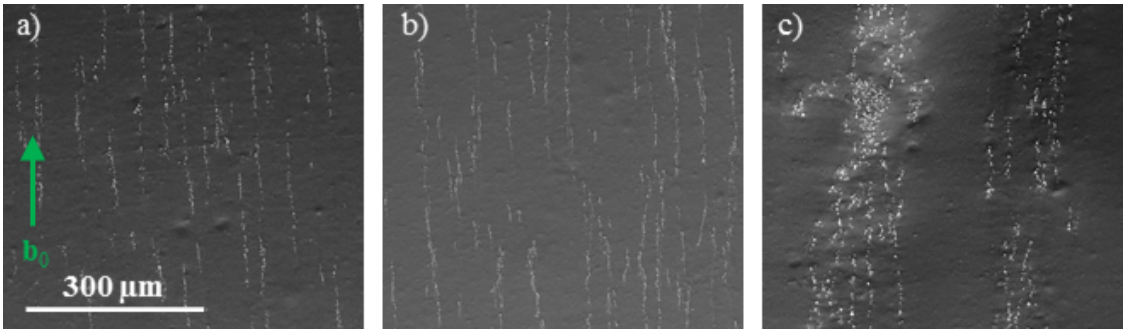

Figure 2.11: SEM micrographs (200×) of particle chain alignment in MRE samples with a particles to silicone ratio of 21 *phr*. The arrow indicates the direction of the magnetic field $\mathbf{b}_0$ during curing. a) Untreated MRE, b) spray-coated MRE and c) primer-stirred MRE.

SEM micrographs of 21 *phr* MREs with untreated, spray-coated and primer-stirred particles are first taken at rest to show the influence of the primer treatment on chain alignment. They are presented in Figure 2.11, where the silicone matrix appears as black background and the iron particles as white spots. There is no remarkable difference in chain alignment between the untreated (Figure 2.11a) and the spray-coated (Figure 2.11b) samples. In both cases, the particles cured under a magnetic

field $\mathbf{b}_0$ of 0.3 T are aligned in thin disconnected chains fairly homogeneously distributed in the matrix and spaced with small distances. In contrast, particle chains in the primer-stirred MRE (Figure 2.11c) create thick columns of irregular particle agglomerates separated by larger distances.

Next, 21 *phr* MREs with untreated, spray-coated and primer-stirred particles are pulled up to 2.4 nominal stretch along the chains direction thanks to an in-situ tensile stage inside the SEM. The composites microstructures along the sectioning surface are then imaged at high magnification, allowing to study the interfacial adhesion between the iron fillers and the silicone matrix under high deformation states at a very local scale. The corresponding images are presented in Figure 2.12. All samples in Figure 2.12a to c exhibit numerous large pore openings. The formation of these large pores is due to the initial damage that is caused by the scalpel cut in the matrix before loading and that is further enhanced by the strong irradiation under the 10 kV electron-beam. The fact that the large openings in the matrix are not due to mechanical stresses could be proven by observing a MRE sample that was previously cycled 12 times up to 2.5 nominal stretch outside of the SEM. This sample was then placed back in the SEM without any cutting performed, loaded up to a nominal stretch of 2.4 and imaged while paying attention to minimize the focus time: it did not show any large pore opening. Nevertheless, the initial damage of the matrix, along with the electron-beam induced deterioration of the material and the subsequent formation of pores under loading conditions, proved themselves useful to further investigate the interfacial adhesion between the iron fillers and the silicone matrix at a local scale.

High-magnification SEM micrographs of the samples loaded at 2.4 nominal stretch indeed show that the silicone matrix detaches from the particles without any remaining residues for the untreated MRE (Figure 2.12d). However, in the case of the spray-coated MRE, where the primer homogeneously covered the particles in a thin layer (Figure 2.9e), the matrix is still rather well attached to particles through wide strands covering nearly the whole particles (Figure 2.12e). In the case of the primer-stirred MRE, where the primer covered the particles less homogeneously and in a thicker layer (Figure 2.9f), the matrix still adheres to the primed surface but through much thinner and separate filaments (Figure 2.12f).

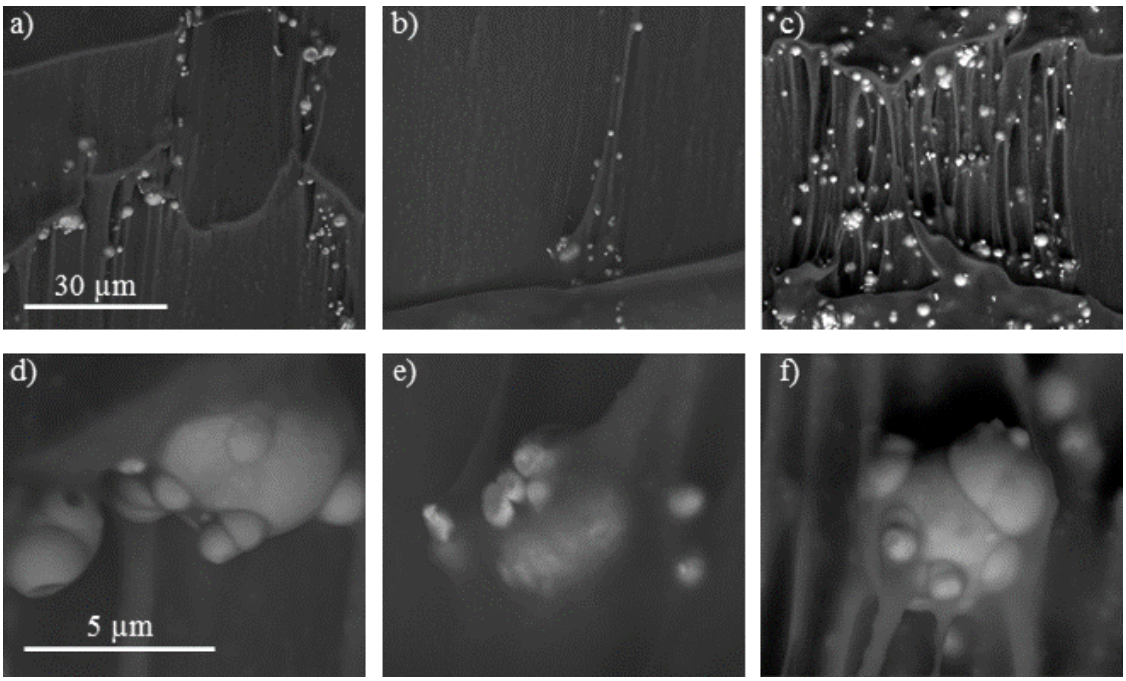

Figure 2.12: SEM micrographs showing the interfacial adhesion between the iron fillers and the silicone matrix in 21 *phr* MRE samples under a nominal stretch of 2.4. Note that samples are cut open, causing the opening of pores under tension, which is further promoted by electron irradiation. Top: SEM micrographs (1,500×) of a) untreated MRE, b) spray-coated MRE and c) primer-stirred MRE. Bottom: SEM micrographs (12,000×) of d) untreated MRE, e) spray-coated MRE and f) primer-stirred MRE.

2.4.3 Macroscopic mechanical tests

To investigate the effect of interfacial adhesion on the structural response of a sample, a pure silicone elastomer and MRE samples (particles to silicone ratios of 21 *phr*, 140 *phr* and 210 *phr*) are studied under cyclic tension at room temperature ($23°C$). In these preliminary experiments, the samples are maintained by grips attached to load cells mounted on step motors having an accuracy of less than $50\mu m$. The tensile force is thus measured by these 10 N load cells (Althen ALF328) with an accuracy of less than 50 mN. Ten sinusoidal loading/unloading cycles are performed in a displacement-controlled mode, up to a fixed amplitude of displacement corresponding to a maximum stretch of 2.5 and with an equivalent strain rate of $0.02\,s^{-1}$ (in the linear ramp). The tested samples, sketched in Figure 2.10, are initially unstrained before mechanical testing and are installed in the grips so that the initial sample length L_0 (and motor position) before loading is 10 mm. In what follows, results

are displayed as axial nominal stress – calculated as the ratio of the measured axial force to the cross-sectional area A_0 of the undeformed sample – versus axial stretch – calculated as the ratio of the current prescribed displacement of the motors to the sample initial length L_0. With regard to the shape of the samples in these preliminary experiments, we rather consider such plots as the axial structural response of the samples than as strictly representative of the material behavior.

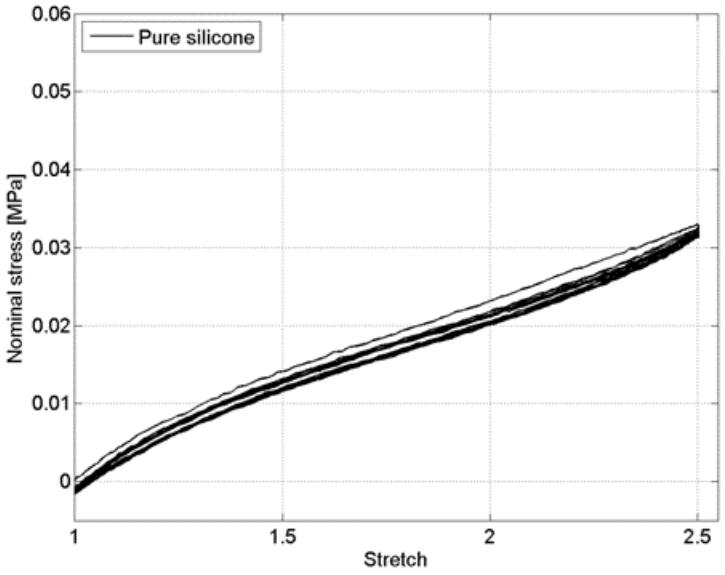

Figure 2.13: Structural response of the pure silicone sample submitted to cyclic tension at an equivalent strain rate of 0.02 s^{-1}.

The nominal stress-stretch response of the pure silicone elastomer is shown in Figure 2.13 while the nominal stress-stretch response of 21 *phr* and 210 *phr* MRE samples are shown in the top and bottom rows of Figure 2.14, respectively. The pure silicone elastomer shows a small difference in response between the first cycle and the following ones with only a very weak hysteresis. In the case of the 21 *phr* MRE samples, the nominal stress-stretch response of the first cycle differs significantly from the following cycles. The second cycle also differs from the following ones but less significantly. The large stress softening after the first cycle indeed diminishes with the following cycles to finally be negligible after about 6 cycles. The initial softening is comparable for the untreated MRE sample (Figure 2.14a) and the spray-coated MRE sample (Figure 2.14b) but more pronounced for the primer-stirred MRE sample (Figure 2.14c). After about 6 cycles, the stress-stretch responses are repeatable and only exhibit a weak hysteresis for all 21 *phr* MREs. For the 210 *phr* MRE samples, one can again observe a significant difference in the nominal stress-

stretch response between the first cycle and the following ones, which stabilizes after about 6 cycles though it still slightly oscillates around a stable average value. Compared to the untreated MRE (Figure 2.14d), the first cycle softening is remarkably larger for the spray-coated MRE (Figure 2.14e) and even larger for the primer stirred MRE (Figure 2.14f). Furthermore, for the stabilized curves, one observes an increase in stiffness between the primer-treated samples and the untreated MRE at large stretch.

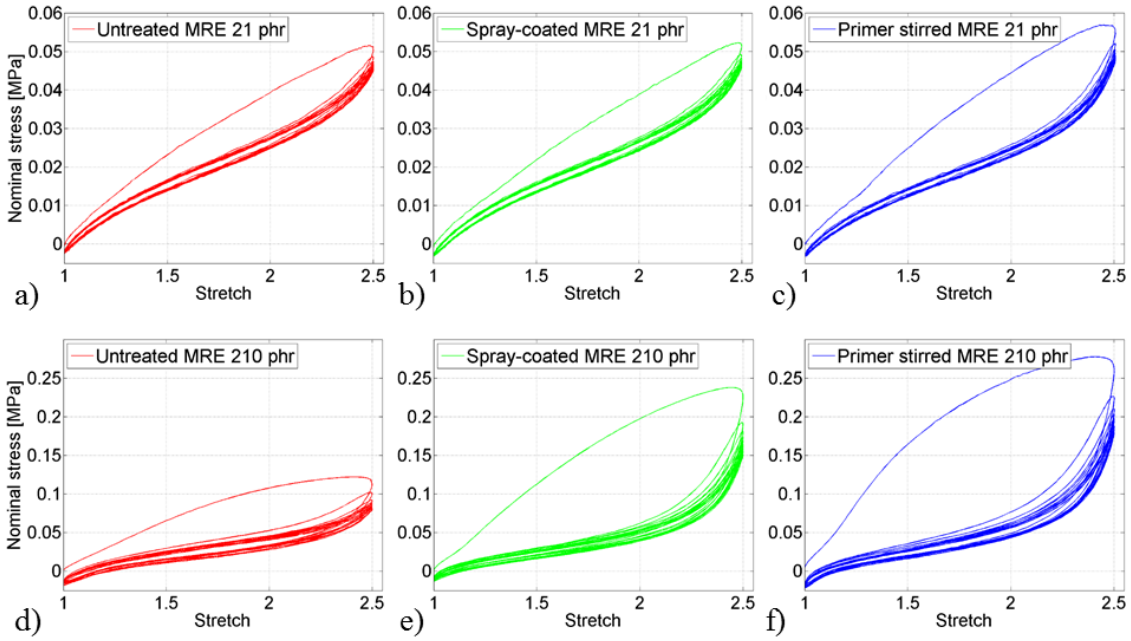

Figure 2.14: Structural response of the different MRE samples during cyclic tension parallel to the particle chains at an equivalent strain rate of 0.02 s^{-1}. Top: Particles to silicone ratio of 21 *phr* for a) untreated MRE, b) spray-coated MRE and c) primer-stirred MRE. Bottom: Particles to silicone ratio of 210 *phr* for d) untreated MRE, e) spray-coated MRE and f) primer-stirred MRE.

2.4.4 Discussion of results

The effect of the primer being first set aside, the responses of all particle-filled elastomers clearly show an initial softening known as Mullins effect [Mul57] and linked to the irreversible breaking or loosening of bonds between the filler particles and the macromolecular elastomer chains within the composite. The mechanical tests also highlight the influence of the particles to silicone ratio on the stiffness and the hysteretic dissipation in particle-filled elastomers. This can be easily seen by

comparing the stabilized hysteretic loop for the pure silicone, the 21 *phr* untreated MRE and the 210 *phr* untreated MRE, as reported in Figure 2.15. With a higher particles to silicone ratio, the stiffness of the material increases since the rigidity of the fillers is much higher than that of the matrix material. Furthermore, due to an increase of irreversible slip processes between the filler particles and a rearrangement in the polymer chain-network [Mie00], the width of both the initial and stabilized hysteresis increases with higher particles to silicone ratios.

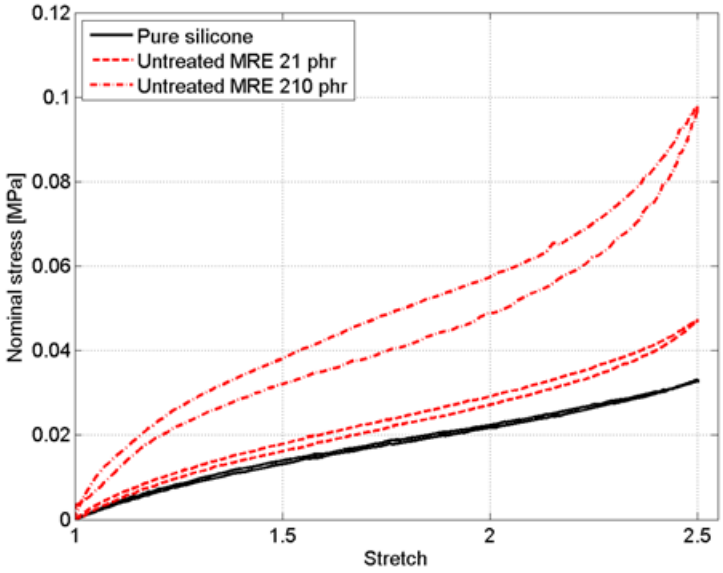

Figure 2.15: Stabilized hysteretic loop (shifted back to the origin) for pure silicone, 21 *phr* and 210 *phr* MRE samples.

The application of the primer also influences the stress-stretch response. Under fixed maximum stretch, a much larger hysteretic dissipation during the first cycle is observed for the primer treated samples (see Figure 2.14), especially at higher particles to silicone ratios. The primer application thus seems to create additional weak bonds between the polymer chains and the filler particles, which are destroyed during the first loading cycle.

In order to precisely compare the influence of the two primer treatments on the response of the composite, the stabilized loading curves for 210 *phr* MREs are reported in Figure 2.16a. There is no remarkable difference between the response of the untreated and the spray-coated MRE up to a nominal stretch of 1.8, after which the response of the spray-coated MRE is stiffer than that of the non-treated MRE. In contrast, the primer-stirred MRE shows an increased stiffness throughout the whole stabilized loading curve. It seems that the particle agglomerates seen previously un-

der SEM further increase the stiffness due to rubber entrapped in the filler network and an increased effective filler particles to silicone ratio [Wan99, Yat01, Leb02]. However, this way of applying the primer must be discarded in our case since it has the disadvantage of forming irregular particle agglomerates. Such a situation should be avoided in order to prevent field gradients during the application of a magnetic field and to ensure homogeneous material properties throughout the sample.

Finally, the effect of the primer, when applied by spraying, on the stiffness of the sample submitted to high stretch for different particles to silicone ratios is analyzed (see Figure 2.16b). For the low particles to silicone ratio, the effect of the primer treatment is nearly negligible on the macroscopic mechanical response of the corresponding sample as it only slightly increases the ultimate stiffness. In the case of the 140 *phr* and 210 *phr* MRE samples, the effect of the primer is only visible beyond a nominal stretch of 2 and 1.8, respectively. Hence, the spray-coated primer only enhances the MREs stiffness past a critical stretch threshold that increases as the particles to silicone ratio decreases. Beyond that critical stretch threshold, stronger bonds due to the primer application seem to prevent debonding of the particles from the matrix and lead to a stiffer macroscopic response. In the present study, since we will use particles to silicone ratios below 210 *phr* and remain under a nominal stretch of 1.8 (which still corresponds to large deformations), particles will not be primer-coated in order to reduce fabrication time.

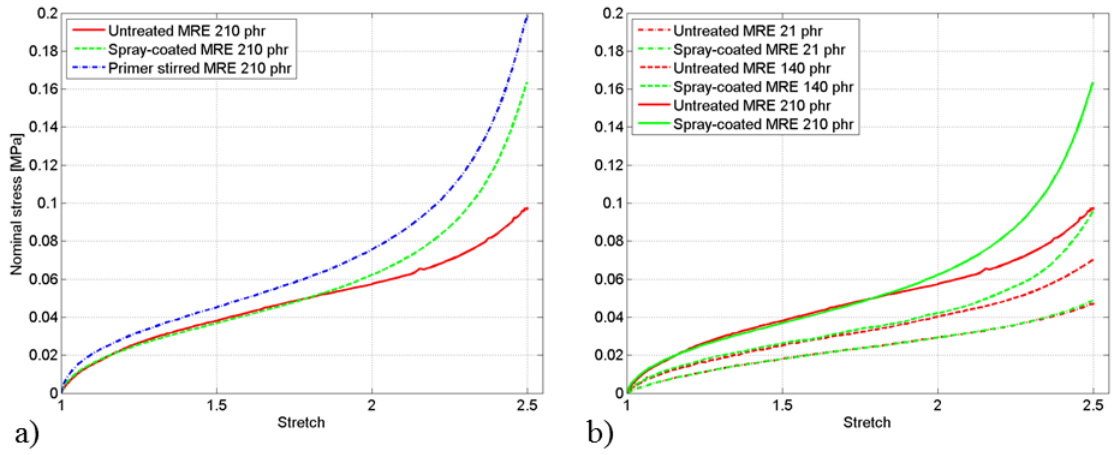

Figure 2.16: a) Stable loading curves (shifted back to the origin) for the 210 *phr* MREs with untreated particles, spray-coated particles and primer-stirred particles. b) Stable loading curves (shifted back to the origin) for untreated and spray-coated MRE samples exhibiting different particles to silicone ratios: 21 *phr*, 140 *phr* and 210 *phr*.

2.5 Conclusion

In this chapter, all aspects pertaining to the fabrication of the samples dedicated to the subsequent coupled magneto-mechanical characterization are presented. The design of a sample shape enabling to obtain both homogeneous mechanical and magnetic fields during magneto-mechanical loading is discussed. Material selection leads to the choice of a very soft silicone elastomer as the matrix and CIP 3.5 μm in average diameter as the fillers. The fabrication procedure is then detailed, from compounding to curing under magnetic fields in order to produce isotropic and two types of transversely isotropic samples for the subsequent coupled characterization. Finally, the interfacial adhesion between the iron fillers and the soft silicone matrix in MREs at high deformations is investigated. Spray-coating the particles with a silane primer prior to sample fabrication improves the macroscopic mechanical behavior, in terms of stiffness by preventing debonding of the particles from the matrix, though only above a critical stretch threshold that depends on the particles to silicone ratio. Hence, in the stretch and particles to silicone ratio ranges targeted in this work, particles will not be primer-coated so as to reduce the sample fabrication time.

Chapter 3

Magneto-mechanical characterization

This Chapter concerns the magneto-mechanical characterization of MREs. Therefore, in Section 3.1, the general theoretical framework for magneto-elastic continua is reviewed, and, in Section 3.2, the traction as well as the magnetic field response for the different test cases considered in this study are derived. In Section 3.3 the uniaxial tension setup for the magneto-mechanical testing of MREs is presented, followed by the experimental and parameter identification results in Section 3.4. The chapter closes by a conclusion in Section 3.5.

3.1 General theoretical framework

The present work uses the general continuum framework proposed by Kankanala and Triantafyllidis for isotropic MREs [Kan04] and extended to transversely isotropic MREs by Danas and Triantafyllidis [Dan12, Dan14]. The general theory is based on the assumption that there are no hysteretic or rate effects in the magneto-elastic solid, i.e. that there is no energy dissipation in a closed loading loop both in the strain and in the magnetization spaces. There are two equivalent ways of obtaining the coupled governing equations for a magneto-elastic solid:

- One approach is based on the variational method of continuum mechanics using a Lagrangian description. By minimizing the body's potential energy with respect to its independent variables, one obtains the appropriate mechanical as well as magnetic governing equations and boundary/interface conditions with respect to the undeformed, reference configuration. This method is particularly suitable for the numerical implementation of boundary value problems (BVPs). It will be described and used in Chapter 4.
- An alternative approach is the direct method of continuum mechanics that uses an Eulerian description. The coupled mechanical electro-magnetic nature of the theory is introduced through the energy balance law, in which an electro-

magnetic energy flux term is added to the standard mechanical and thermal flux terms. Balance laws for magnetism and mechanics are postulated on an arbitrary volume and, using the second law of thermodynamics, the governing equations of the magneto-elastic solid are derived in the deformed, current configuration. This method yields the traction response of the materials under investigation that will be identified with the help of experimental data. A brief recording of the main results of this approach for a self-contained presentation will be given in the following. For a detailed derivation, the reader is referred to the works of Kankanala, Danas and Triantafyllidis [Kan04, Dan12, Dan14] and the references therein. In particular, they demonstrate in [Kan04] that the variational and the direct methods are equivalent.

In what follows, the usual continuum mechanics conventions are employed, according to which all field quantities in small letters are associated with the current configuration while their counterparts in capital letters are associated with the reference configuration. In addition, scalars are denoted by normal-face letters δ, J, whereas vectors $\mathbf{u}$, $\mathbf{X}$ and tensors $\boldsymbol{\sigma}$, $\mathbf{F}$ are denoted by bold-face letters.

3.1.1 Governing equations

3.1.1.1 *Continuum kinematics*

To describe the motion and deformation of a magneto-elastic body in the three-dimensional Euclidean space with base vectors $\mathbf{e}_1$, $\mathbf{e}_2$ and $\mathbf{e}_3$, an undeformed, reference configuration $\mathcal{B}_0$, with boundary $\partial\mathcal{B}_0$, and a deformed, current configuration $\mathcal{B}$, with boundary $\partial\mathcal{B}$ are considered. These two configurations are related by a deformation function $\boldsymbol{\phi}$ which maps every point in the reference configuration $\mathbf{X} \in \mathcal{B}_0$ to a point in the current configuration $\mathbf{x} = \boldsymbol{\phi}(\mathbf{X}) \in \mathcal{B}$. The distance between these two points is described by the displacement field vector:

$$\mathbf{u}(\mathbf{X}) = \mathbf{x} - \mathbf{X}. \tag{3.1}$$

The deformation gradient $\mathbf{F}$ relative to the undeformed configuration $\mathcal{B}_0$ is then defined as the derivative of each component of the current $\mathbf{x}$ vector with respect to

each component of the reference $\mathbf{X}$ vector, and in relation with eq.(3.1) reads:

$$\mathbf{F} = \mathbf{x}\nabla = \mathbf{I} + \mathbf{u}\nabla, \quad J = \det \mathbf{F} > 0, \tag{3.2}$$

where $\nabla \equiv \partial(\,)/\partial\mathbf{X}$ denotes the reference gradient operator, $\mathbf{I}$ denotes the identity tensor and J is the Jacobian of the deformation. The second order tensor $\mathbf{F}$ is crucial in continuum mechanics as a measure of how an infinitesimal piece of material is stretched and rotated as the body evolves from its reference to its current configuration (see Figure 3.1).

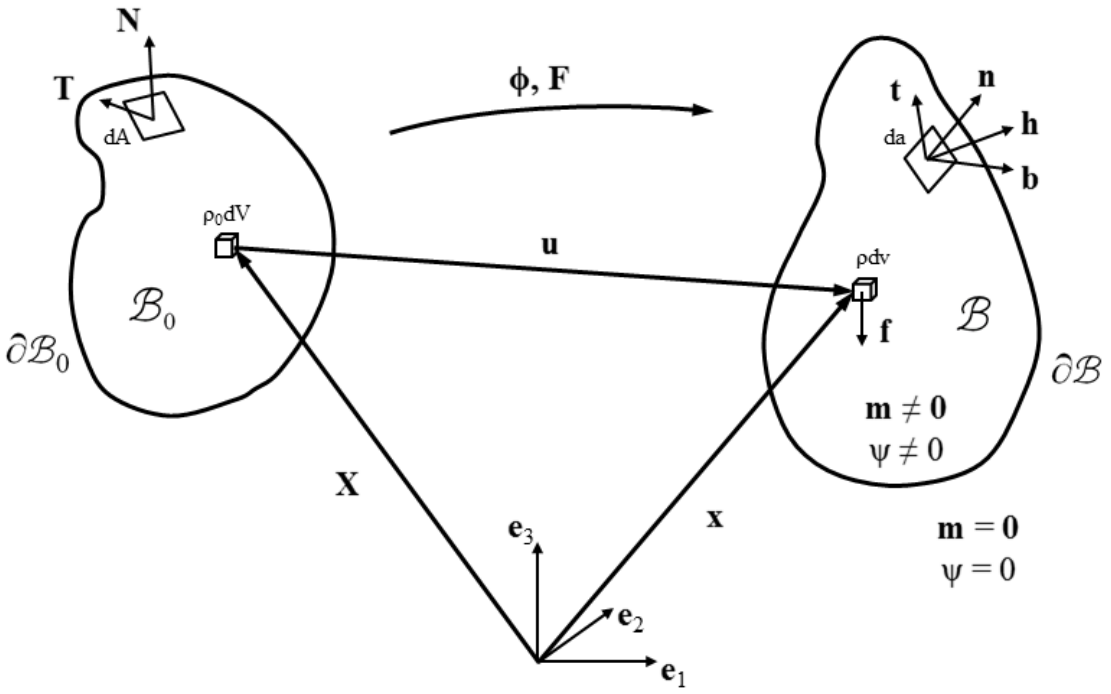

Figure 3.1: Summary schematic for the motion and deformation of an arbitrary magneto-elastic body $\mathcal{B}_0$ bounded by a closed surface $\partial\mathcal{B}_0$ in the undeformed, reference configuration into the deformed, current configuration $\mathcal{B}$, $\partial\mathcal{B}$ due to the combined action of mechanical loads and a magnetic field (defined in what follows).

3.1.1.2 *Magnetostatics*

We now consider that the deformed configuration arises due to the combined action of mechanical loads and a magnetic field. As introduced in Chapter 1, Section 1.4.2,

b, **h** and **m** are respectively the magnetic field, the **h**-field and the magnetization defined in this current configuration $\mathcal{B}$. They are related through the macroscopic constitutive relation $\mathbf{b} = \mu_0 (\mathbf{h} + \mathbf{m})$ with μ_0 the magnetic permeability in vacuum. From the no magnetic monopoles law and Gauss's divergence theorem, one obtains the point-wise governing equation for the magnetic field vector **b** and, in the case of a surface discontinuity in **b**, the interface discontinuity/boundary condition:

$$\nabla \cdot \mathbf{b} = 0, \quad \mathbf{n} \cdot [\![\mathbf{b}]\!] = 0, \quad \mathbf{x} \in \mathcal{B}, \tag{3.3}$$

where $\nabla \equiv \partial(\,)/\partial\mathbf{x}$ is the current gradient operator and $\nabla\cdot$ is the current divergence operator, **n** is the outward normal on the discontinuity surface in the current (deformed) configuration and $[\![f]\!] \equiv f_+ - f_-$ is the jump of the field quantity f evaluated at either side of the discontinuity surface[1]. The divergence of **b** equaling zero implies that there exist no magnetic monopoles. Furthermore, the interface condition states that the normal component of **b** is continuous at the boundary of two different media, while that of **h** is discontinuous.

From Ampère's circuit law of magnetostatics and Stoke's theorem, the point-wise governing equation for the **h**-field vector, and, in the case of a surface discontinuity in **h**, the interface discontinuity/boundary condition can be derived:

$$\nabla \times \mathbf{h} = \mathbf{j}, \quad \mathbf{n} \times [\![\mathbf{h}]\!] = \mathbf{0}, \quad \mathbf{x} \in \mathcal{B}, \tag{3.4}$$

where $\nabla\times$ is the current curl operator. In other words, the **h**-field curls around currents and, in the absence of an external current density $\mathbf{j} = \mathbf{0}$, the curl of **h** is equal to zero, as it can be assumed for the MRE materials under investigation. The interface condition for **h** then states that the tangential component of **h** is continuous, while that of **b** is discontinuous at the boundary of two different, non conducting media (surface current density equal to zero).

[1]The (+) subscript indicates the interior of the solid while the (-) subscript is used to indicate the surrounding space.

3.1.1.3 *Equilibrium, total stress and boundary traction*

Next, the equations of mechanical equilibrium in the presence of magneto-mechanical interactions in the current configuration $\mathcal{B}$ are considered. By the use of the so-called total Cauchy stress tensor $\boldsymbol{\sigma}$ as the extension of the Cauchy stress tensor in classical continuum mechanics, the point-wise governing equilibrium equation and the jump condition for the total stress have the simple form:

$$\nabla \cdot \boldsymbol{\sigma} + \rho \mathbf{f} = \mathbf{0}, \quad \mathbf{n} \cdot [\![\boldsymbol{\sigma}]\!] = \mathbf{t}, \quad \mathbf{x} \in \mathcal{B}, \tag{3.5}$$

where $\mathbf{f}$ is the mechanical body force per unit mass, ρ is the current material density and $\mathbf{t}$ is the mechanical surface traction per unit current area da. This symmetric total stress tensor $\boldsymbol{\sigma}$ is derived[2] adopting the direct method of continuum mechanics:

$$\boldsymbol{\sigma} = \boldsymbol{\sigma}^T = \rho \frac{\partial \psi}{\partial \mathbf{F}} \cdot \mathbf{F}^T + \mathbf{h}\mathbf{b} - \mu_0 \left(\mathbf{h} \cdot \mathbf{m} + \frac{1}{2} \mathbf{h} \cdot \mathbf{h} \right) \mathbf{I}, \tag{3.6}$$

together with the constitutive relation between the $\mathbf{h}$-field and the magnetization $\mathbf{m}$:

$$\mu_0 \mathbf{h} = \rho \frac{\partial \psi}{\partial \mathbf{m}}. \tag{3.7}$$

The new quantity $\psi(\mathbf{F}, \mathbf{m})$ introduced here is the free energy per unit mass (free energy density) depending on the deformation gradient tensor $\mathbf{F}$ and the current magnetization $\mathbf{m}$. As the magnetization is zero within the free space (unlike the $\mathbf{h}$-field or the magnetic field $\mathbf{b}$), this functional vanishes outside the material. Note that from this formulation based on the total stress derives the magnetic body force $-\mu_0 \mathbf{h} \cdot (\mathbf{m} \nabla)$. Furthermore, in vacuum ($\psi = 0$, $\mathbf{m} = \mathbf{0}$) the total stress is non-zero and gives as a result the expression of the well-known magnetostatic Maxwell stress tensor:

$$\boldsymbol{\sigma} = \boldsymbol{\sigma}^T = \mu_0 \left(\mathbf{h}\mathbf{h} - \frac{1}{2} \mathbf{h} \cdot \mathbf{h} \right) \mathbf{I}. \tag{3.8}$$

[2]The following notations are used: dyadic product $\mathbf{hb}$ (in index notation: $h_i b_j$) and contraction $\mathbf{h} \cdot \mathbf{m}$ (in index notation: $h_i m_i$, summation over the repeated index).

Given that experimentally we measure forces and have a better appreciation of the initial configuration $\mathcal{B}_0$, the first Piola-Kirchhoff stress tensor $\boldsymbol{\Pi}$ and the pseudo-traction vector $\mathbf{T}$ (current force $\mathbf{f}$ per unit reference area dA) are introduced as:

$$\boldsymbol{\sigma} = \frac{1}{J}\mathbf{F}\cdot\boldsymbol{\Pi}, \quad d\mathbf{f} = \mathbf{t}da = \mathbf{T}dA. \tag{3.9}$$

With the help of the corresponding transformations and jump conditions[3], the pseudo-traction vector is expressed as:

$$\mathbf{T} = \left\{\frac{\partial\left(\rho_0\psi\right)}{\partial\mathbf{F}} - \left[\frac{\partial\left(\rho_0\psi\right)}{\partial\mathbf{m}}\cdot\mathbf{m} + \frac{\mu_0 J}{2}\left(\mathbf{m}\cdot\mathbf{n}\right)^2\right]\mathbf{F}^{-T}\right\}\cdot\mathbf{N}. \tag{3.10}$$

where $\mathbf{N}$ is the reference counterpart of the outward normal $\mathbf{n}$ on the discontinuity surface in the current (deformed) configuration. Using the relationship between an infinitesimal volume element in the current configuration dv and in the reference configuration dV, the magnetic field response in terms of the reference density ρ_0 finally reads:

$$\mu_0\mathbf{h} = \frac{1}{J}\frac{\partial\left(\rho_0\psi\right)}{\partial\mathbf{m}}. \tag{3.11}$$

3.1.2 Free energy function for transversely isotropic MREs

The MRE composites considered in this study can be manufactured in the presence of a curing magnetic field causing the iron particles to form chain-like structures. Such samples require an anisotropic formulation for the free energy function $W\left(\mathbf{F},\mathbf{m},\widehat{\mathbf{N}}\right) \equiv \rho_0\psi$ depending on the deformation gradient tensor $\mathbf{F}$, the current magnetization vector $\mathbf{m}$ and the reference configuration particle-chain orientation unit vector $\widehat{\mathbf{N}}$. The free energy function W can be expressed in terms of invariants, i.e. scalar quantities that depend on the independent variables $\left(\mathbf{F},\mathbf{m},\widehat{\mathbf{N}}\right)$ and are invariant under objective coordinate transformations and material symmetry group transformations, rigid body displacements as well as rotations. It is a known result

[3] A detailed derivation of the traction response $\mathbf{T}$ is given in the Appendix, Section A.1. For an overview of the transformations of volume, surface and line elements, the reader is referred to eq.(4.7) in Chapter 4.

of representation theory, e.g. [Adk59, Adk60, Pip59, Zhe94], that a scalar function that depends on one symmetric rank-two tensor and two vector arguments is a function of the following ten independent invariants[4]:

$$\rho_0\psi = W\left(I_1, I_2, I_3, I_4, I_5, I_6, I_7, I_8, I_9, I_{10}\right), \tag{3.12}$$

$$I_1 = \operatorname{tr}\left(\mathbf{F}^T\cdot\mathbf{F}\right), \quad I_2 = \frac{1}{2}\left[I_1^2 - \operatorname{tr}\left(\mathbf{F}^T\cdot\mathbf{F}\right)^2\right], \quad I_3 = \det\left(\mathbf{F}^T\cdot\mathbf{F}\right), \tag{3.13}$$

$$I_4 = \widehat{\mathbf{N}}\cdot\mathbf{F}^T\cdot\mathbf{F}\cdot\widehat{\mathbf{N}}, \quad I_5 = \widehat{\mathbf{N}}\cdot\left(\mathbf{F}^T\cdot\mathbf{F}\right)^2\cdot\widehat{\mathbf{N}}, \tag{3.14}$$

$$I_6 = \mathbf{m}\cdot\mathbf{m}, \quad I_7 = \mathbf{m}\cdot\mathbf{F}\cdot\mathbf{F}^T\cdot\mathbf{m}, \quad I_8 = \mathbf{m}\cdot\left(\mathbf{F}\cdot\mathbf{F}^T\right)^2\cdot\mathbf{m}, \tag{3.15}$$

$$I_9 = \left(\mathbf{m}\cdot\mathbf{F}\cdot\widehat{\mathbf{N}}\right)^2, \quad I_{10} = \left(\mathbf{m}\cdot\mathbf{F}\cdot\widehat{\mathbf{N}}\right)\left(\mathbf{m}\cdot\mathbf{F}\cdot\mathbf{F}^T\cdot\mathbf{F}\cdot\widehat{\mathbf{N}}\right). \tag{3.16}$$

The characterization of MREs requires the determination of the free energy density function W to establish the macroscopic constitutive response of the material, whose parameters must then be determined by fitting experimental data. Very often, simplifications have to be made to allow identification from experiments, as it will be described in the next section.

[4]Notice the use of both the right Cauchy-Green tensor $\mathbf{F}^T\cdot\mathbf{F}$ and the left Cauchy-Green tensor $\mathbf{F}\cdot\mathbf{F}^T$ as quadratic measures of the stretch in the reference and current configuration, respectively.

3.2 Constitutive parameter identification

3.2.1 Reduced form of the free energy function

It is useful to reduce the complexity of the general form of the constitutive equations to identify the material behavior from experiments [Bus10, Dan12, Schu14]. In what follows, the working hypotheses are described. Overall, in addition to the incompressibility assumption (i.e. $I_3 = 1$), the invariants (I_2, I_5, I_8, I_{10}) exhibiting a higher order dependence on the deformation gradient $\mathbf{F}$ are not retained for simplicity since they mainly play a role at very high strains not considered in this work.

Let's first look at the invariants of eq.(3.13) corresponding to the mechanical response of an isotropic hyperelastic material:

$$I_1 = tr\left(\mathbf{F}^T\cdot\mathbf{F}\right), \quad I_2 = \frac{1}{2}\left[I_1^2 - tr\left(\mathbf{F}^T\cdot\mathbf{F}\right)^2\right], \quad I_3 = \det\left(\mathbf{F}^T\cdot\mathbf{F}\right) = J^2.$$

The elastomer composites under investigation being nearly incompressible, use is made of the incompressibility condition, namely $J = \det\mathbf{F} = 1 = I_3$. In this case the free energy density function W is considered to be independent of I_3. Furthermore, many successful models in rubber elasticity [Ste12, Hos13], as the prototype neo-Hookean model for example [Riv48], are independent of I_2. We also assume that W does not depend on this invariant for simplicity.

Next, we consider the set of invariants in eq.(3.14) related to the transverse isotropy, required by the presence of the particle chains ($\widehat{\mathbf{N}}$) for the purely mechanical case:

$$I_4 = \widehat{\mathbf{N}}\cdot\mathbf{F}^T\cdot\mathbf{F}\cdot\widehat{\mathbf{N}}, \quad I_5 = \widehat{\mathbf{N}}\cdot\left(\mathbf{F}^T\cdot\mathbf{F}\right)^2\cdot\widehat{\mathbf{N}}.$$

Motivated by recent results on fiber reinforced polymers (e.g. deBotton et al. [DeB06], who proposed a transversely isotropic counterpart of the isotropic neo-Hookean constitutive model), we make the hypothesis that the free energy density function W does not depend on I_5 for further simplicity.

The third set of invariants in eq.(3.15) is related to the isotropic magneto-mechanical response:

$$I_6 = \mathbf{m}\cdot\mathbf{m}, \quad I_7 = \mathbf{m}\cdot\mathbf{F}\cdot\mathbf{F}^T\cdot\mathbf{m}, \quad I_8 = \mathbf{m}\cdot\left(\mathbf{F}\cdot\mathbf{F}^T\right)^2\cdot\mathbf{m},$$

More specifically, I_6 accounts for the magnitude of the magnetization $\mathbf{m}$ in the material and will be included in the free energy density function W. The isotropic, magneto-elastic coupling is described by both invariants I_7 and I_8 but here we only retain I_7 and neglect the higher order terms carried in I_8.

The fourth set of invariants in eq.(3.16) introduces the combined dependence of the material's free energy density function W on magnetization, deformation and particle-chain orientation in the transversely isotropic case:

$$I_9 = \left(\mathbf{m}\cdot\mathbf{F}\cdot\widehat{\mathbf{N}}\right)^2, \quad I_{10} = \left(\mathbf{m}\cdot\mathbf{F}\cdot\widehat{\mathbf{N}}\right)\left(\mathbf{m}\cdot\mathbf{F}\cdot\mathbf{F}^T\cdot\mathbf{F}\cdot\widehat{\mathbf{N}}\right).$$

Again, only lower order terms, hence invariant I_9 will be retained in W to account for this interaction. Thus, the simplified energy density function depends on five invariants, while accounting for the magneto-mechanical interactions in transversely isotropic MREs:

$$\rho_0\psi = W\left(I_1, I_4, I_6, I_7, I_9\right). \tag{3.17}$$

The constitutive equations eq.(3.10) and eq.(3.11) require the calculation of $\partial W/\partial\mathbf{F}$ and $\partial W/\partial\mathbf{m}$, which in turn because of the chain rule of differentiation yield:

$$\frac{\partial W}{\partial\mathbf{F}} = \sum_i \frac{\partial W}{\partial I_i}\frac{\partial I_i}{\partial\mathbf{F}}, \quad \frac{\partial W}{\partial\mathbf{m}} = \sum_i \frac{\partial W}{\partial I_i}\frac{\partial I_i}{\partial\mathbf{m}}, \quad i = 1,4,6,7,9\ . \tag{3.18}$$

Consequently from eq.(3.18), we have to determine the first derivatives of the retained invariants with respect to the deformation gradient $\mathbf{F}$:

$$\frac{\partial I_1}{\partial\mathbf{F}} = 2\mathbf{F}, \quad \frac{\partial I_4}{\partial\mathbf{F}} = 2\mathbf{F}\cdot\left(\widehat{\mathbf{N}}\widehat{\mathbf{N}}\right), \tag{3.19}$$

$$\frac{\partial I_6}{\partial \mathbf{F}} = 0, \quad \frac{\partial I_7}{\partial \mathbf{F}} = 2\left(\mathbf{m}\mathbf{m}\right)\cdot\mathbf{F}, \quad \frac{\partial I_9}{\partial \mathbf{F}} = 2\left(\mathbf{m}\cdot\mathbf{F}\cdot\widehat{\mathbf{N}}\right)\mathbf{m}\widehat{\mathbf{N}}, \tag{3.20}$$

as well as their first derivatives with respect to the magnetization $\mathbf{m}$:

$$\frac{\partial I_1}{\partial \mathbf{m}} = 0, \quad \frac{\partial I_4}{\partial \mathbf{m}} = 0, \tag{3.21}$$

$$\frac{\partial I_6}{\partial \mathbf{m}} = 2\mathbf{m}, \quad \frac{\partial I_7}{\partial \mathbf{m}} = 2\mathbf{F}\cdot\mathbf{F}^{\mathbf{T}}\cdot\mathbf{m}, \quad \frac{\partial I_9}{\partial \mathbf{m}} = 2\left(\mathbf{m}\cdot\mathbf{F}\cdot\widehat{\mathbf{N}}\right)\mathbf{F}\cdot\widehat{\mathbf{N}}. \tag{3.22}$$

The experiments require the expression for the pseudo-traction response of eq.(3.10) that from eq.(3.18) - eq.(3.22) yields:

$$\begin{aligned}
\mathbf{T} &= 2\left[W_{,1}\mathbf{F} - \frac{p}{2}\mathbf{F}^{-T} + W_{,4}\mathbf{F}\cdot\left(\widehat{\mathbf{N}}\widehat{\mathbf{N}}\right)\right]\cdot\mathbf{N} \\
&+ 2\left[W_{,7}\left(\mathbf{m}\mathbf{m}\right)\cdot\mathbf{F} + W_{,9}\left(\mathbf{m}\cdot\mathbf{F}\cdot\widehat{\mathbf{N}}\right)\mathbf{m}\widehat{\mathbf{N}}\right]\cdot\mathbf{N} \\
&- 2\left[W_{,6}I_6\mathbf{F}^{-T} + W_{,7}I_7\mathbf{F}^{-T} + W_{,9}I_9\mathbf{F}^{-T}\right]\cdot\mathbf{N} \\
&- \frac{\mu_0}{2}\left[\left(\mathbf{m}\cdot\mathbf{n}\right)^2\mathbf{F}^{-T}\right]\cdot\mathbf{N},
\end{aligned} \tag{3.23}$$

where $W_{,i}$, often called response function, denotes the derivative of the free energy density function W with respect to the invariant I_i and the Lagrange multiplier p denotes the internal pressure (required by the incompressibility constraint: $J = \det\mathbf{F} = 1 = I_3$).

In the same way, the magnetic field response of eq.(3.11) becomes:

$$\mu_0\mathbf{h} = 2\left[W_{,6}\mathbf{m} + W_{,7}\mathbf{F}\cdot\mathbf{F}^{\mathbf{T}}\cdot\mathbf{m} + W_{,9}\left(\mathbf{m}\cdot\mathbf{F}\cdot\widehat{\mathbf{N}}\right)\mathbf{F}\cdot\widehat{\mathbf{N}}\right]. \tag{3.24}$$

As it can be easily seen, without the presence of a magnetic field inside a magnetic material ($\mathbf{h} = \mathbf{0}$ hence $\mathbf{m} = \mathbf{0}$) or when a magnetic field is present in the absence of a magnetic material for the field to act on ($\mathbf{h} \neq \mathbf{0}$ but $\mathbf{m} = \mathbf{0}$), eq.(3.23) reduces to the well known purely mechanical expressions. Similarly in the case of a non-

deformable magnetic material ($\mathbf{F} = \mathbf{I}$) the expressions of eq.(3.23) and eq.(3.24) reduce to their well known expressions from magnetostatics. In the general magneto-mechanical case, magnetically-induced stresses contribute to the response of the material, including both the combined dependence of the magnetization and the deformation (described by I_7, I_9) and induced Maxwell stresses at the boundary of the material (last term in eq.(3.23)). Finally, setting the unit particle-chain orientation vector $\widehat{\mathbf{N}}$ in the preferred direction allows to investigate the material response for transversely isotropic MRE composites, while setting $\widehat{\mathbf{N}} = \mathbf{0}$ only leaves the quantities related to an isotropic material.

3.2.2 Free energy density and response functions

Danas and Triantafyllidis [Dan14] proposed a compressible transversely isotropic free energy density function for MREs which will be adopted in this work (adjusted here for incompressibility with $J = 1$):

$$
\begin{aligned}
W\left(\mathbf{F}, \mathbf{m}, \widehat{\mathbf{N}}\right) &= \frac{G}{2}\left[C_1 \sum_{j=1}^{3} d_{1j}\left(I_1 - 3\right)^j\right] \\
&+ \frac{G}{2}\left[C_4 \sum_{j=2}^{4} d_{4j}\left(I_4 - 1\right)^j\right] \\
&+ \frac{G}{2}\left[C_6 \frac{I_6}{m_s^2} + C_{6s}\left\{\frac{1}{2}\ln\left[1 - \left(\frac{I_6}{m_s^2}\right)^2\right] + \frac{I_6}{m_s^2}\tanh^{-1}\left(\frac{I_6}{m_s^2}\right)\right\}\right] \\
&+ \frac{G}{2}\left[C_7 \frac{I_7}{m_s^2} + C_9 \frac{I_9}{m_s^2}\right],
\end{aligned}
\tag{3.25}
$$

By construction W as well as $\partial W/\partial \mathbf{F}$ and $\partial W/\partial \mathbf{m}$ vanish in the reference state corresponding to $I_1 = 3$, $I_4 = 1$ and $I_6 = I_7 = I_9 = 0$ since it is assumed to be stress- and magnetization-free. The free energy density function is further expressed with the help of the physical material parameters G $[Pa]$, the initial shear modulus and m_s $[A/m]$, the saturation magnetization of the material as well as the dimensionless material parameters C_i and d_{ij} to be determined by experiments. From this choice, the response functions that are the first derivatives of the energy function with respect to the corresponding invariants are given by:

$$W_{,1} = \frac{G}{2} C_1 \left[d_{11} + 2d_{12} \left(I_1 - 3 \right) + 3d_{13} \left(I_1 - 3 \right)^2 \right], \tag{3.26}$$

$$W_{,4} = \frac{G}{2} C_4 \left[2d_{42} \left(I_4 - 1 \right) + 3d_{43} \left(I_4 - 1 \right)^2 + 4d_{44} \left(I_4 - 1 \right)^3 \right], \tag{3.27}$$

$$W_{,6} = \frac{G}{2m_s^2} \left[C_6 + C_{6s} \tanh^{-1} \left(\frac{I_6}{m_s^2} \right) \right], \tag{3.28}$$

$$W_{,7} = \frac{G}{2m_s^2} C_7, \quad W_{,9} = \frac{G}{2m_s^2} C_9. \tag{3.29}$$

Note here as a special case, that a neo-Hookean material can be obtained for $C_1 = d_{11} = 1$ and all the other material parameters set to zero. Furthermore, a rigid linear magnetic material can be obtained for $C_6 \neq 0$, $C_{6s} = 0$ (accounting for the magnetic saturation) and $C_7 = C_9 = 0$ (accounting for the magneto-mechanical coupling). In this special case, the magnetic susceptibility of the material reads: $\chi = \mu_0 m_s^2 / \left(G C_6 \right)$.

3.2.3 Different test cases

In the uniaxial traction experiments presented in Section 3.4, the mechanical traction $\mathbf{T}$ is applied along the $\mathbf{e}_3$-axis of the sample, $T_3 \equiv T$, and the principal axes of deformation $\mathbf{F}$ as well as the applied field $\mathbf{h}$ are always aligned with a principal axis of the material (see Chapter 2, Section 2.2). Therefore, there are three independent equations of static equilibrium in the current and reference normal directions $\mathbf{n}_k = \mathbf{N}_k = \mathbf{e}_k$, $k = 1, 2, 3$, deducted from eq.(3.23). Additionally, in the experiments, $\mathbf{h}$ and $\mathbf{m}$ are always aligned with the $\mathbf{e}_1$-axis which from material orthotropy leads to one single equation relating the $\mathbf{h}$-field component $h_1 \equiv h$ and the magnetization component $m_1 \equiv m$ inside the material (all other components of the $\mathbf{h}$-field and the magnetization $\mathbf{m}$ vanish) deducted from eq.(3.24).

1. In the special cases of axisymmetry for the purely mechanical response (cases a and b in Figure 3.2), where the sample is either isotropic or has the particle-

chain direction $\widehat{\mathbf{N}}$ and the applied traction $\mathbf{T}$ both aligned with the $\mathbf{e}_3$-axis of the sample, the two radial principal stretches are equal. Hence, due to incompressibility: $\lambda_3 \equiv \lambda,\ \lambda_1 = \lambda_2 = 1/\sqrt{\lambda}$. Solving for the internal pressure p in a radial direction yields one expression for the traction response $T(\lambda)$.

2. In the purely mechanical case c (see Figure 3.2c), solving one equation in a stress-free normal direction (e.g. $\mathbf{e}_1$) for the internal pressure p and injecting it into the two other normal directions ($\mathbf{e}_2$ and $\mathbf{e}_3$) gives one expression for the relation between the principal stretch $\lambda_3 \equiv \lambda$ in traction direction and the principal stretch $\lambda_1 \equiv \bar{\lambda}$ in magnetic field direction and transverse to the applied traction while $\lambda_2 = 1/\left(\lambda\bar{\lambda}\right)$ due to incompressibility, and one expression for the traction response $T\left(\lambda, \bar{\lambda}\right)$.
3. In the magneto-mechanical cases d, e and f (see Figure 3.3), we obtain one expression for the relation between the principal stretches λ and $\bar{\lambda}$, one expression for the traction response $T\left(\lambda, \bar{\lambda}, m\right)$, and additionally one expression for the magnetic field response $h\left(\bar{\lambda}, m\right)$.

The expressions for the traction response T and the magnetic field response h are now derived for each case that is considered experimentally:

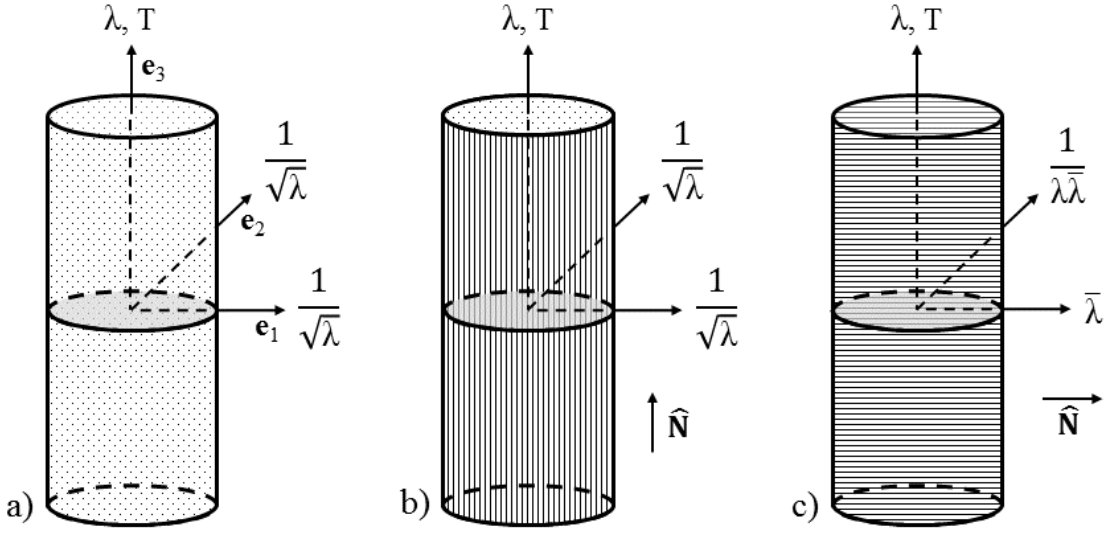

Figure 3.2: Schematic of the different test cases for the identification of the purely mechanical response T: a) isotropic MRE, b) transversely isotropic MRE with applied mechanical traction T along chain direction $\widehat{\mathbf{N}}$ and c) transversely isotropic MRE with applied mechanical traction T transverse to chain direction $\widehat{\mathbf{N}}$.

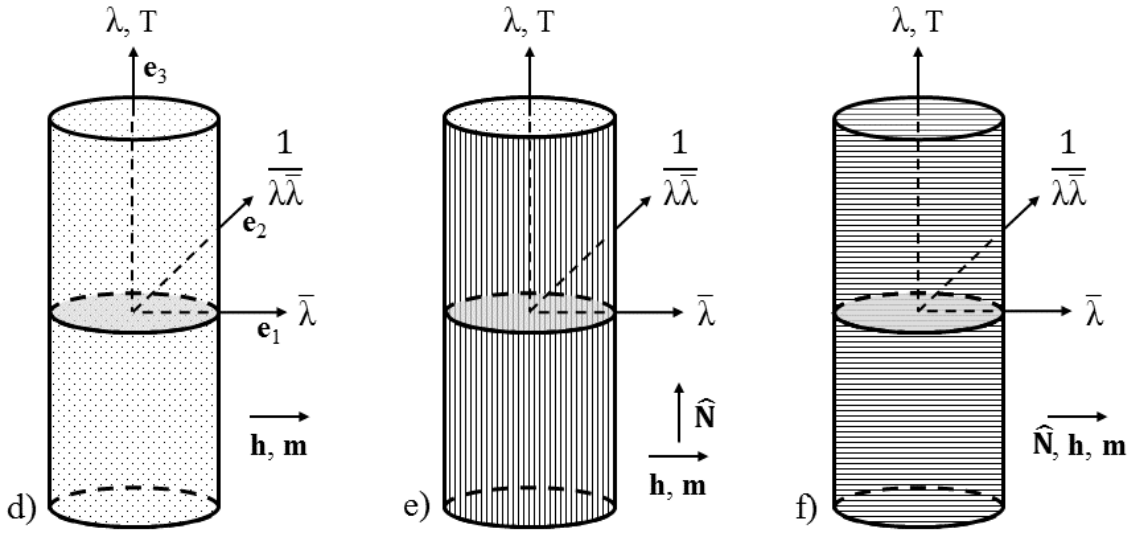

Figure 3.3: Schematic of the different test cases for the identification of the magneto-mechanical response T, h: d) isotropic MRE, e) transversely isotropic MRE with applied mechanical traction T along chain direction $\widehat{\mathbf{N}}$ and f) transversely isotropic MRE with applied mechanical traction T transverse to chain direction $\widehat{\mathbf{N}}$.

Purely mechanical response

a) Isotropic MRE:

$$\mathbf{T} = T\mathbf{e}_3,\ \mathbf{F} = \frac{1}{\sqrt{\lambda}}\mathbf{e}_1\mathbf{e}_1 + \frac{1}{\sqrt{\lambda}}\mathbf{e}_2\mathbf{e}_2 + \lambda\mathbf{e}_3\mathbf{e}_3:$$

$$T = 2W_{,1}\left(\lambda - \frac{1}{\lambda^2}\right). \tag{3.30}$$

b) Transversely isotropic MRE with traction along chain direction:

$$\mathbf{T} = T\mathbf{e}_3,\ \mathbf{F} = \frac{1}{\sqrt{\lambda}}\mathbf{e}_1\mathbf{e}_1 + \frac{1}{\sqrt{\lambda}}\mathbf{e}_2\mathbf{e}_2 + \lambda\mathbf{e}_3\mathbf{e}_3,\ \widehat{\mathbf{N}} = \mathbf{e}_3:$$

$$T = 2W_{,1}\left(\lambda - \frac{1}{\lambda^2}\right) + 2W_{,4}\lambda. \tag{3.31}$$

c) Transversely isotropic MRE with traction transverse to chain direction:

$$\mathbf{T} = T\mathbf{e}_3,\ \mathbf{F} = \bar{\lambda}\mathbf{e}_1\mathbf{e}_1 + \frac{1}{\lambda\bar{\lambda}}\mathbf{e}_2\mathbf{e}_2 + \lambda\mathbf{e}_3\mathbf{e}_3,\ \widehat{\mathbf{N}} = \mathbf{e}_1:$$

$$2W_{,1}\bar{\lambda}^2 + 2W_{,4}\bar{\lambda}^2 = 2W_{,1}\frac{1}{\left(\lambda\bar{\lambda}\right)^2}. \tag{3.32}$$

$$T = 2W_{,1}\left(\lambda - \frac{\bar{\lambda}^2}{\lambda}\right) - 2W_{,4}\frac{\bar{\lambda}^2}{\lambda}, \tag{3.33}$$

Magneto-mechanical response

d) Isotropic MRE:

$\mathbf{T} = T\mathbf{e}_3$, $\mathbf{F} = \bar{\lambda}\mathbf{e}_1\mathbf{e}_1 + \frac{1}{\lambda\bar{\lambda}}\mathbf{e}_2\mathbf{e}_2 + \lambda\mathbf{e}_3\mathbf{e}_3$, $\mathbf{h} = h\mathbf{e}_1$, $\mathbf{m} = m\mathbf{e}_1$:

$$2W_{,1}\bar{\lambda}^2 + 2W_{,7}\left(m\bar{\lambda}\right)^2 - \frac{\mu_0}{2}m^2 = 2W_{,1}\frac{1}{\left(\lambda\bar{\lambda}\right)^2}, \tag{3.34}$$

$$T = 2W_{,1}\left(\lambda - \frac{\bar{\lambda}^2}{\lambda}\right) - 2W_{,7}m^2\frac{\bar{\lambda}^2}{\lambda} + \frac{\mu_0}{2}m^2\frac{1}{\lambda}, \tag{3.35}$$

$$h = \frac{2}{\mu_0}\left(W_{,6} + W_{,7}\bar{\lambda}^2\right)m. \tag{3.36}$$

e) Transversely isotropic MRE with traction along chain direction:

$\mathbf{T} = T\mathbf{e}_3$, $\mathbf{F} = \bar{\lambda}\mathbf{e}_1\mathbf{e}_1 + \frac{1}{\lambda\bar{\lambda}}\mathbf{e}_2\mathbf{e}_2 + \lambda\mathbf{e}_3\mathbf{e}_3$, $\widehat{\mathbf{N}} = \mathbf{e}_3$, $\mathbf{h} = h\mathbf{e}_1$, $\mathbf{m} = m\mathbf{e}_1$:

$$2W_{,1}\bar{\lambda}^2 + 2W_{,7}\left(m\bar{\lambda}\right)^2 - \frac{\mu_0}{2}m^2 = 2W_{,1}\frac{1}{\left(\lambda\bar{\lambda}\right)^2}, \tag{3.37}$$

$$T = 2W_{,1}\left(\lambda - \frac{\bar{\lambda}^2}{\lambda}\right) + 2W_{,4}\lambda - 2W_{,7}m^2\frac{\bar{\lambda}^2}{\lambda} + \frac{\mu_0}{2}m^2\frac{1}{\lambda}, \tag{3.38}$$

$$h = \frac{2}{\mu_0}\left(W_{,6} + W_{,7}\bar{\lambda}^2\right) m. \tag{3.39}$$

f) Transversely isotropic MRE with traction transverse to chain direction: $\mathbf{T} = T\mathbf{e}_3$, $\mathbf{F} = \bar{\lambda}\mathbf{e}_1\mathbf{e}_1 + \frac{1}{\lambda\bar{\lambda}}\mathbf{e}_2\mathbf{e}_2 + \lambda\mathbf{e}_3\mathbf{e}_3$, $\widehat{\mathbf{N}} = \mathbf{e}_1$, $\mathbf{h} = h\mathbf{e}_1$, $\mathbf{m} = m\mathbf{e}_1$:

$$2W_{,1}\bar{\lambda}^2 + 2W_{,4}\bar{\lambda}^2 + 2W_{,7}\left(m\bar{\lambda}\right)^2 + 2W_{,9}\left(m\bar{\lambda}\right)^2 - \frac{\mu_0}{2}m^2 = 2W_{,1}\frac{1}{\left(\lambda\bar{\lambda}\right)^2}, \tag{3.40}$$

$$T = 2W_{,1}\left(\lambda - \frac{\bar{\lambda}^2}{\lambda}\right) - 2W_{,4}\frac{\bar{\lambda}^2}{\lambda} - 2W_{,7}m^2\frac{\bar{\lambda}^2}{\lambda} - 2W_{,9}m^2\frac{\bar{\lambda}^2}{\lambda} + \frac{\mu_0}{2}m^2\frac{1}{\lambda}, \tag{3.41}$$

$$h = \frac{2}{\mu_0}\left(W_{,6} + W_{,7}\bar{\lambda}^2 + W_{,9}\bar{\lambda}^2\right) m. \tag{3.42}$$

3.3 Magneto-mechanical characterization setup

To obtain the macroscopic behavior of different MRE samples under coupled magneto-mechanical loading, a uniaxial tension setup that can be integrated into a magnetic field is devised. This dedicated setup, whose overall schematic is given in Figure 3.4, is described in detail in what follows. To summarize, it consists of an electromagnet producing a homogeneous field within an air gap between its two poles. A tension setup, bringing the sample at the center of the air gap allows for the application of low rate cyclic tensile loadings on the MRE sample while monitoring in-situ mechanical and magnetic quantities.

3.3.1 Electromagnet

The electromagnet used in this study is custom-built by Bouhnik SAS and SigmaPhi, two French companies specialized in power electronics and coils systems. The electromagnet consists of two current conducting water-cooled copper coils mounted on a C-frame, each bearing in their center a truncated conical iron pole 90 mm in diameter, so as to concentrate a nearly homogeneous field across the 82 mm air

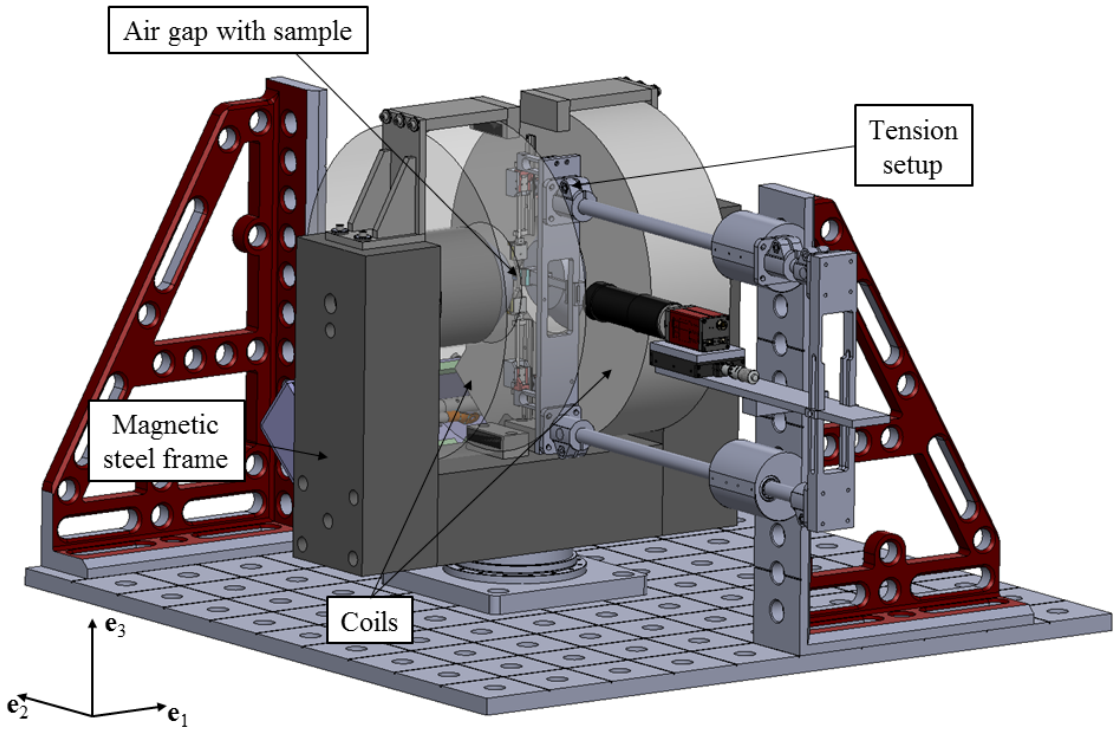

Figure 3.4: Overall schematic of the magneto-mechanical characterization setup.

gap between the two poles. The electromagnet is connected to a four-quadrant bipolar water-cooled power supply of $\pm 70\,V$ and $\pm 70\,A$ nominal voltage and intensity, respectively. Generation of the magnetic field is current-controlled (precision $\pm 50\,mA$) but can also be field-controlled when a probe measuring the magnetic field is installed within the air gap. The intensity delivered by the power supply can be varied either manually or through an analogic entry and yields a field $\mathbf{b}_0 = 0.8\,T$ at the center of the air gap for a current of 68 A. Values of the magnetic field homogeneity (difference $\triangle \mathbf{b}_0$ $[mT]$ from central field $\mathbf{b}_0 = \mu_0 \mathbf{h}_0 = 0.8\,T$ at 68 A) on the main axes at the decisive points within the air gap are reported in Figure 3.5 according to the manufacturer and verified by Hall probe measurements. In summary, the magnetic field $\mathbf{b}_0$ is almost homogeneous in the central zone of the air gap for all three directions ($\pm 1\,mT$ at $\pm 3\,mm$) and shows an increase in direction $\mathbf{e}_1$ ($+38\,mT$ at ± 25 mm) towards the poles as well as a decrease in direction $\mathbf{e}_2$ (-23 mT at $\pm 25\,mm$) and $\mathbf{e}_3$ ($-27\,mT$ at $+25\,mm$ and $-39\,mT$ at $-25\,mm$) towards the open space. Note that due to the shape of the frame (C-frame) there is a slight offset of the point of maximum magnetic field in positive direction $\mathbf{e}_3$.

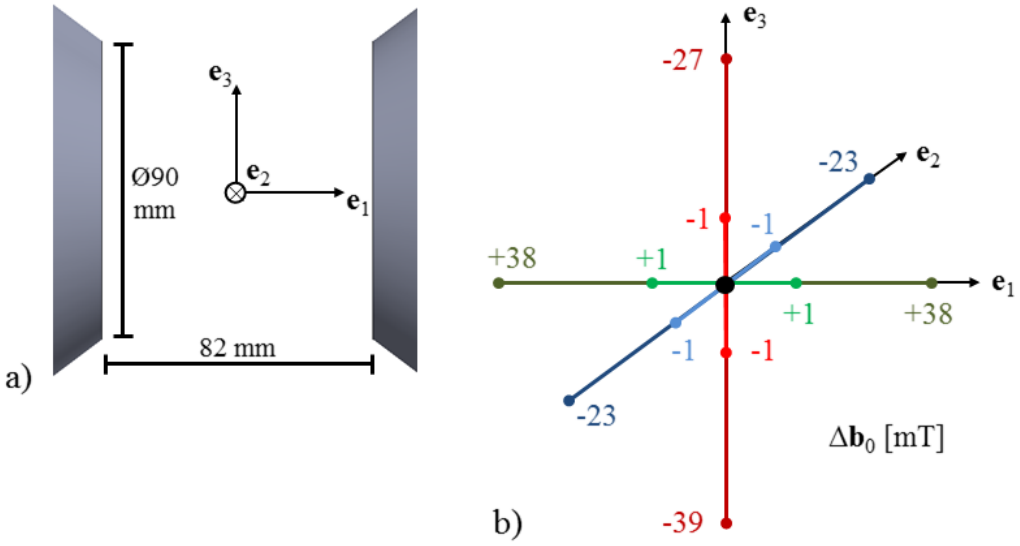

Figure 3.5: a) Sketch of the main axes centered within the poles of the magnet. b) Difference $\triangle \mathbf{b}_0$ $[mT]$ from central field $\mathbf{b}_0 = \mu_0 \mathbf{h}_0 = 0.8\,T$ at 68 A on the main axes at the decisive points within the air gap: central zone ($\pm 3\,mm$, light colored lines), long axis of the samples in curing positions ($\pm 25\,mm$, dark green and dark blue line), long axis of the sample in testing direction ($\pm 25\,mm$, dark red line).

3.3.2 Tension system

Symmetric tension is applied to the samples thanks to two linear Piezo LEGS motors from PiezoMotor installed in opposition. Piezoelectric materials have the advantage to be insensitive to magnetic fields and, per the needs of our application, these motors do not contain any ferromagnetic component that could perturb the applied magnetic field. Classical piezoelectric actuators are well known for providing nanometric to micrometric displacements while accommodating large loads; however, in these motors, the long-range motion of the axis is obtained by incremental steps through friction between the axis and piezo-operated driving legs. As a consequence, they can only bear very small loads. A brief sketch extracted from the operating manual and summarizing the Piezo LEGS "walking principle" is provided in Figure 3.6 for the interested reader. For the motors used in this setup, the maximum stroke is 80 mm and the recommended operating range is between 0 and 3 N with a stall load of 6.5 N (maximum available in non-magnetic version). Microsteps can be as low as 40 nm but because this technology cannot guarantee equal steps, especially under varying load, the motors have to be operated in a closed-control displacement loop. To this end, the axis of each motor is equipped with a laser-

engraved graduated glass ruler monitored by optical encoders; both provided by Renishaw (ATOM miniature encoder system). Once integrated in a LabVIEW (National Instruments) interface program developed at LMS, the whole system provides a resolution of 1 μm and a precision of $\pm 3\,\mu m$.

Each Piezo LEGS motor, along with its encoding system, is mounted at the sensitive end of a LCAE-600G single-point load cell from OMEGA (as seen in Figure 3.7). These load cells, generally used for scales and weighing platforms, are made of aluminum and have a maximum capacity of 6 N and a precision of $\pm 3\,mN$.

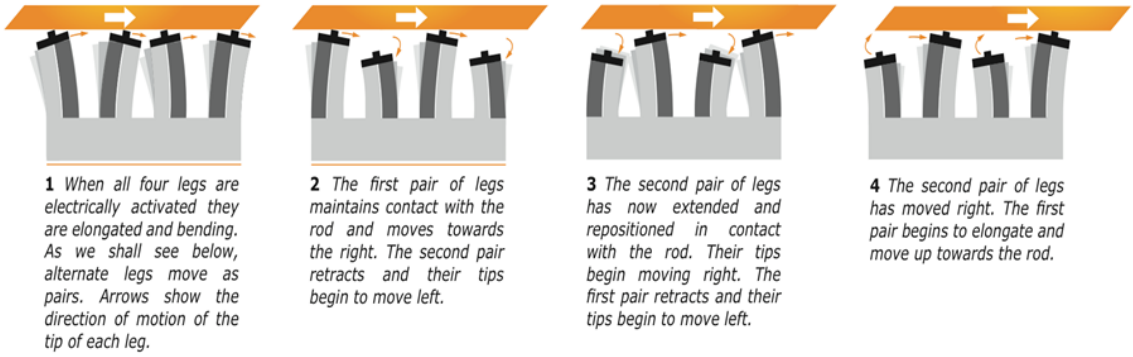

Figure 3.6: Schematic of the Piezo LEGS "walking principle" extracted from the operating manual provided by PiezoMotor.

At the end of the motor are attached custom-designed clamps that hold the sample during the test (see Figure 3.7 and Figure 3.8a). They consist of two aluminum plates; the first one is permanently fixed to the motor axis while the second one is free to slide up and down along two vertical guiding rods fixed along the normal axis of the first plate. Once the sample is installed in the clamps, the latter are pinched thanks to a spring system made of a brass thin plate and two bent screws. This spring-loading of the clamps maintains a constant gripping force on the head of the samples – that deform appreciably due to the large deformations they experience and the incompressibility of the material – and thus prevents slippage during tests.

Finally, this symmetric tension system is attached to an aluminum plate connected to two cylindrical arms gliding within two dry-friction bearings installed outside of the electromagnet, as can be seen in Figure 3.4 and in Figure 3.7. This allows to take the tension system in and out of the electromagnet for mounting the samples outside of the electromagnet prior to testing. With this tension system, mechanical tests can either be carried out in displacement-controlled or force-controlled modes.

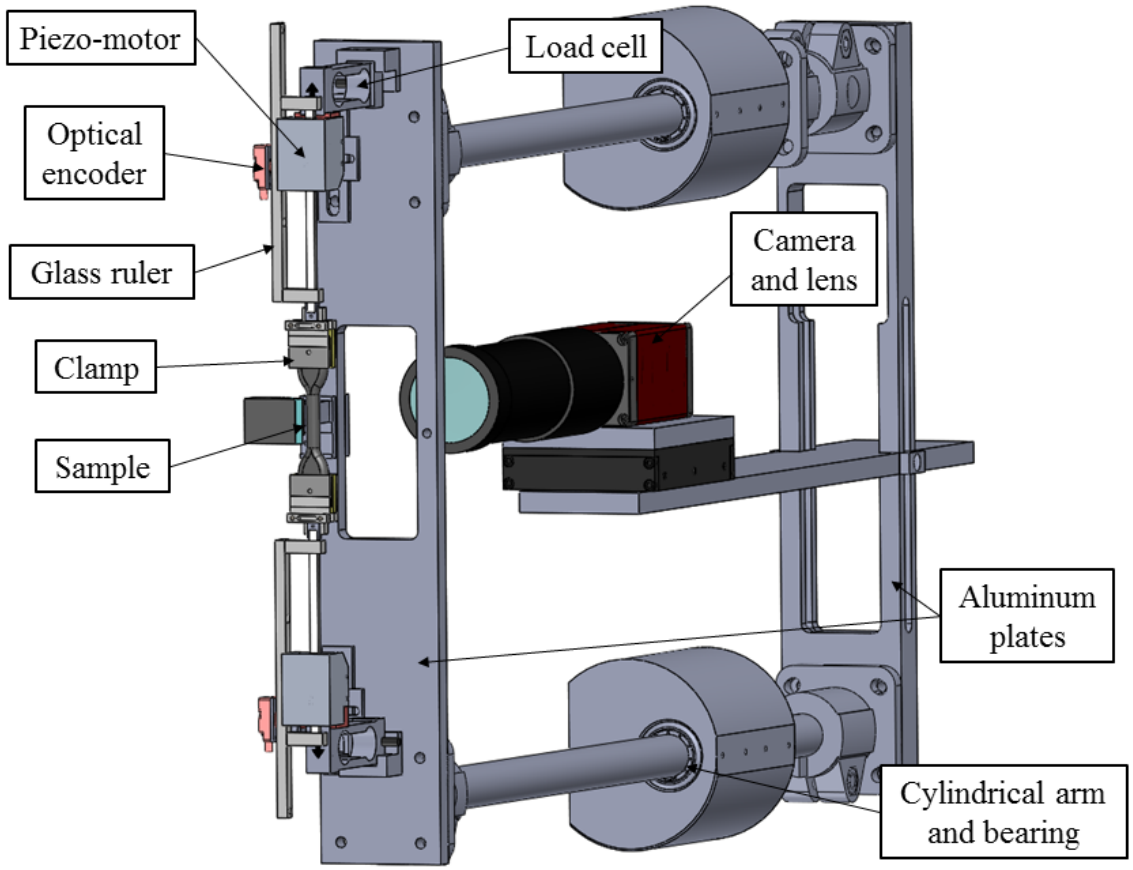

Figure 3.7: Schematic of the symmetric tensile setup showing the Piezo LEGS motors, the rulers and optical encoders, the load cells, the clamps and the sample. The setup holds a camera for optical diagnostics and can be taken in and out of the electromagnet for mounting the samples outside of the electromagnet prior to testing.

3.3.3 Mechanical diagnostics

Strains in the gage area of the samples are measured via non-contact video extensometry. To this end, a stand is attached perpendicularly to an aluminum plate mounted at the other end of the two cylindrical arms gliding within the bearings, opposite to the plate holding the tension system (see Section 3.3.2 and Figure 3.7). Note that a window was machined out of the plate holding the tensile system so as to provide the necessary clearance for optical access to the sample. A 5 Megapixels F-505B Pike CCD camera is installed on this stand and equipped with a 0.3× telecentric lens to take images of the sample during testing at a rate of 14.5 frames per second. In the configuration used for the study, the working distance is 173 mm, the field of view is 16 mm x 20 mm and the resolution is 12 μm/pixel while the depth of

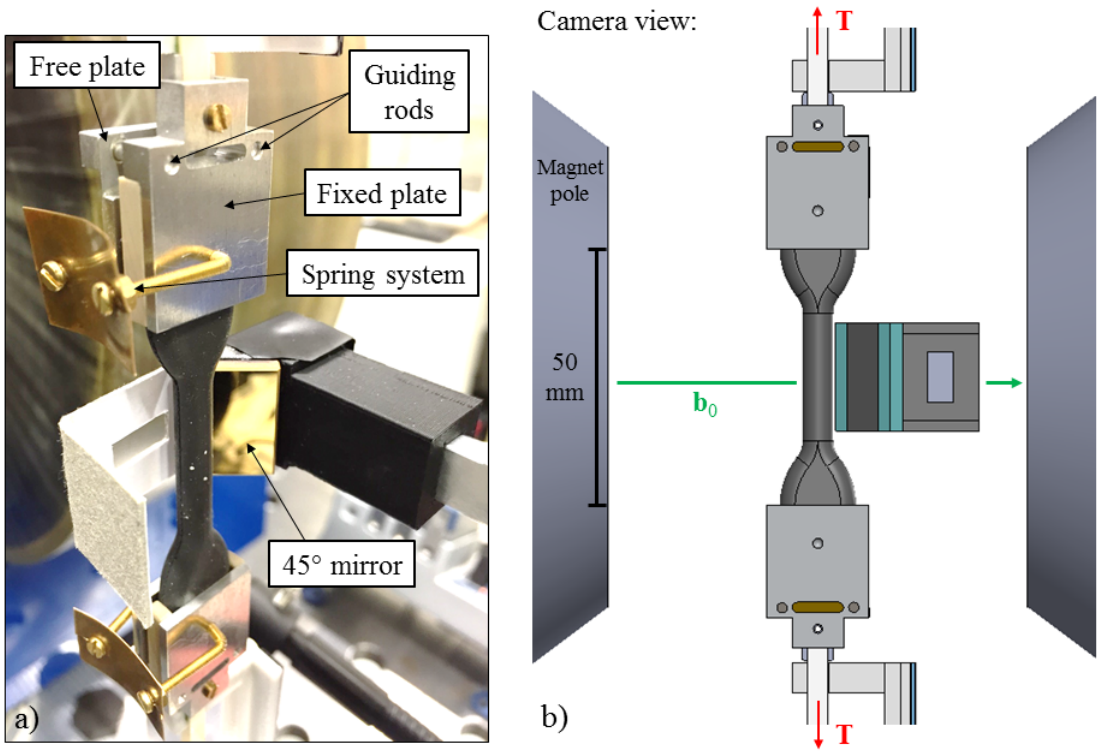

Figure 3.8: a) Picture of the setup especially showing the clamps systems holding the specimen, and the 45° mirror. b) Schematic of the sample held at the center of the electromagnet airgap, and of the 45° mirror from the camera vantage point.

field is 8 mm. For telecentric lenses, the magnification remains constant throughout the depth of field [Gro08], hence the out-of-plane movement of the sample due to its change in section during tension does not affect the tracking of material points located on the sample. Additionally, a mirror making a 45° angle with the camera CCD array is positioned next to the sample and reflects an image of its side (in the perpendicular plane to its front plane) towards the camera (see Figure 3.8). A single image thus contains a front view of the sample as well as a view of its side, which gives access to the strains along the three principal directions of the sample (Figure 3.8b). Note that once the optical components are installed and aligned, they stay in position since both the plate holding the tensile system and mirror, on the one hand, and the plate holding the camera, on the other hand, remain fixed (in relation to each other) when the whole system glides along the bearings.

To track the strains, markers[5] – consisting in black (for pure silicone samples) or

[5]For the lateral strain measurement, following the markers is preferred over borders detection as the most stable solution. In particular, along direction $\mathbf{e}_2$, the borders tend to bear slight

white (for MRE samples) acrylic paint dots applied with a sharp tip – are drawn onto the samples prior to testing, as represented in Figure 3.9. In particular, on the side of the sample facing the camera, two dots are drawn 6 *mm* apart at the center of the sample along its vertical axis (direction $\mathbf{e}_3$) and two dots are drawn 4 *mm* apart at the center of the sample along the corresponding transversal axis (direction $\mathbf{e}_1$). On the side of the sample facing the mirror, one dot is added so as to yield another pair of dots 4 *mm* apart at the center of the sample along the corresponding transversal axis (direction $\mathbf{e}_2$). A tracking algorithm implemented in LabVIEW follows in-situ the two vertical dots and the two pairs of lateral dots, thus giving access to the true (Eulerian) strain $\varepsilon = \ln(\lambda)$ along direction $\mathbf{e}_3$, $\mathbf{e}_1$ and $\mathbf{e}_2$, respectively (see Figure 3.9).

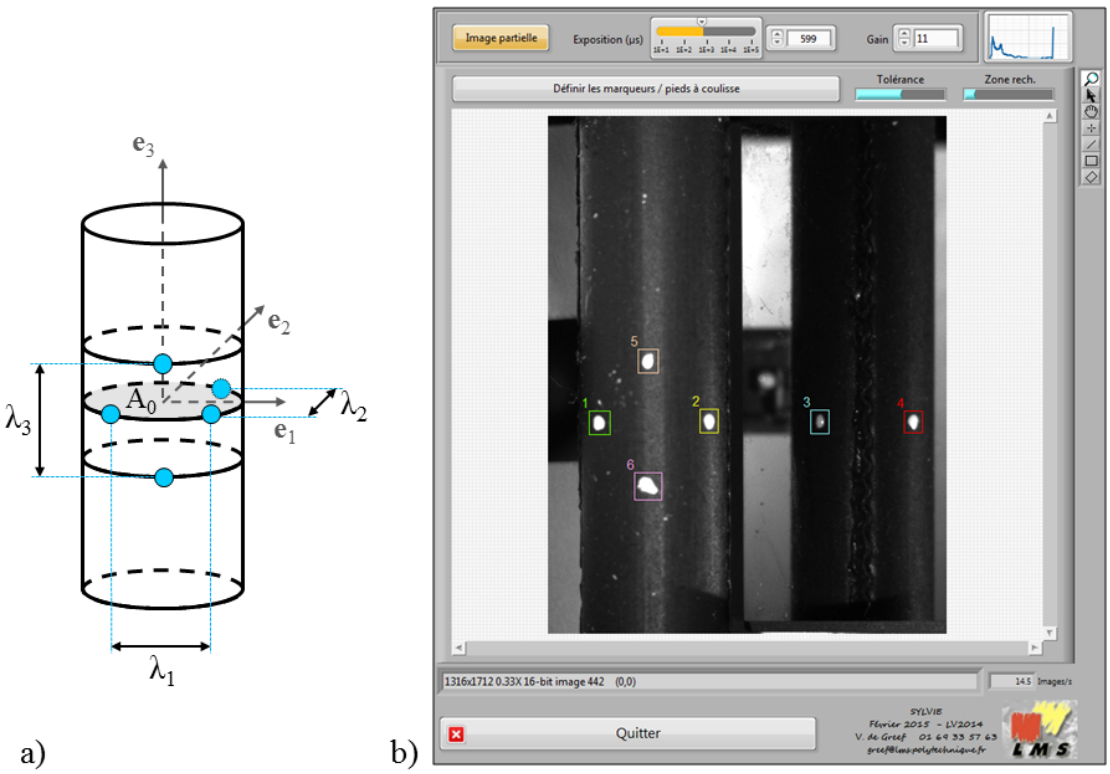

Figure 3.9: a) Schematic of the dots drawn on the sample and principal stretches. b) Image of the sample and its reflection in the 45° mirror showing the dots followed by the video extensometry system.

The force exerted on the sample during loading is measured by the two LCAE-600G single-point load cells from OMEGA mentioned in Section 3.3.2. The actual force is obtained by dividing by two the sum of the two voltage readings coming out

imperfections as they are along the junction of the two parts of the mold.

of the cells (calibration was performed by the manufacturer and was checked with calibrated weights before use).

3.3.4 Magnetic measurements

The magnetic material parameters have to be measured during sample deformation up to a high value of the magnetic field. A technique is thus needed enabling to carry out measurements at room temperature, on elastomeric cylindrical samples a few millimeters in diameter submitted to tension. Nearly all classical devices commonly used in physics laboratories exhibit limitations regarding at least one of the above-mentioned requirements [Czi06]. For example, the MOKE (Magneto-Optic Kerr Effect) technique, based on the change in polarization of a laser beam reflected on the sample as it becomes magnetized, is limited to metallic materials. The VSM (Vibrating-Sample Magnetometer) does not allow for measurements in tension because it requires the sample to vibrate. Faraday and Gouy scales, as well as devices based on torque tracking, are also incompatible with measurements in tension since the sample must be hanging and stress-free when the magnetic field is applied. One solution to overcome this problem is to measure the magnetic field around the sample at specific positions with the help of Hall probes while the sample is installed in the tensile system. This method, permitting in-situ magnetic measurements up to high magnetic fields, is used during this study and described in the next paragraph.

Measurements up to high magnetic fields

In-situ magnetic field measurements are carried out with transversal Hall probes. A Hall sensor consists in a thin semi-conductor. When a current is applied to the semi-conductor and the latter is placed within a magnetic field $\mathbf{b}$ so that the field lines are along its thickness, a voltage develops between the faces across the thickness. This phenomenon, known as the Hall effect, was reported by Edwin H. Hall in 1879 [Hal1879]. Because these sensors are sensitive to the magnetic field across their thickness, they need to be placed strictly perpendicular to the lines of the magnetic flux to be probed. Additionally, they need to be calibrated in reference to a known magnetic field. Two HGT-2010 Hall sensors from Lakeshore are used in this study. The sensitive semi-conductor is a 760 μm-thick square (2.28 mm x 2.28 mm) mounted at the end of a plastic stem. Both sensors are calibrated by placing them

at the center of the electromagnet where the same measurement can be done with the Hall probe given and calibrated by the electromagnet manufacturer, and they provide a precision of $\pm 1\%$ rdg at a range of $\pm 1\,T$ and stable temperature.

During coupled experiments, the fixed bracket behind the electromagnet (that also maintains the aluminum plate used during fabrication, see Chapter 2, Figure 2.7) is equipped with displacement stages holding two extension arms carrying each a Hall probe, as depicted in Figure 3.10a. One probe (named probe h) comes behind the sample at its center and can be adjusted along direction $\mathbf{e}_2$ to come nearly in contact with the sample. The second probe (named probe m) comes on the side of the sample and can be adjusted along directions $\mathbf{e}_1$ and $\mathbf{e}_2$. In both cases, the normal to the sensing element is along the applied magnetic field $\mathbf{b}_0$. Since the samples for the magnetic measurements have a nearly ellipsoidal MRE body (see Chapter 2, Section 2.2), the perturbation field $\mathbf{h}_1$ and the magnetization $\mathbf{m}$, hence the total magnetic field $\mathbf{b}$, are all nearly uniform within the material.

- Due to the continuity of the tangential component of $\mathbf{h}$, the Hall probe h placed at the back of the sample gives access to the total field $\mu_0\mathbf{h}$ $[T]$ inside the material (the externally applied field $\mathbf{h}_0$ plus the perturbation field $\mathbf{h}_1$, measured in air), since the contribution of the magnetization $\mathbf{m}$ vanishes at that point.

- Due to the continuity of the normal component of $\mathbf{b}$, the total magnetic field $\mathbf{b}$ $[T]$ inside the sample – now including the contribution of the total $\mathbf{h}$-field (measured at the back) plus the contribution of the magnetization $\mathbf{m}$ – is measured by the lateral Hall probe m, which then gives access to the magnetization $\mathbf{m}$ inside the sample.

The distribution of the magnetic field $\mathbf{b}$ in the airgap in the presence of a magnetic sample is sketched in Figure 3.10b (on the left) along with the positions of the h and m sensors relative to the sample. Additionally, the evolution of the magnetic field is sketched in Figure 3.10b (on the right) along direction $|\mathbf{e}_1|$ (bottom) and transverse to direction $|\mathbf{e}_2|$ (top) covering the discontinuity interface sample/air.

These probes are positioned by hand with the help of the camera to measure the magnetic quantities m and h within the sample when the latter is at rest. This can be done for different levels of the externally applied magnetic field up to a value of $\mathbf{b}_0 = \mu_0\mathbf{h}_0 = 0.8\,T$.

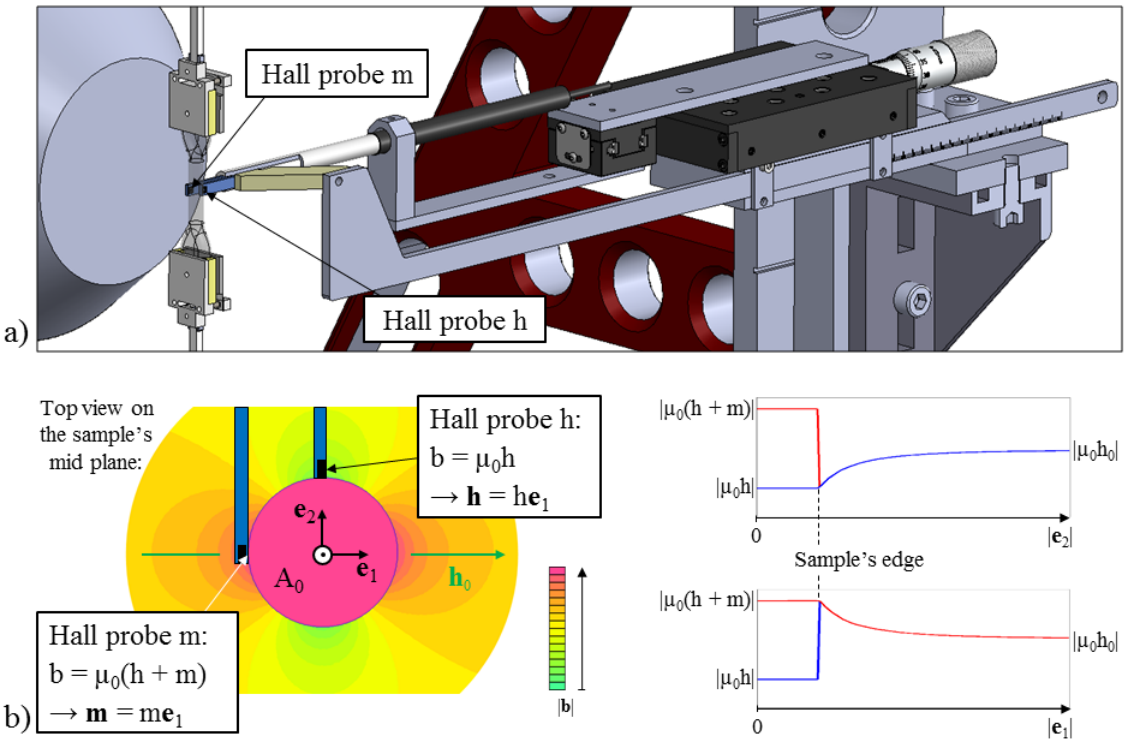

Figure 3.10: a) Stand coming from behind of the electromagnet and holding the two Hall probes h and m. b) On the left: FEM simulation (2D plane, [FEMM]) of the distribution of the magnetic field **b** in the airgap of an electromagnet in the presence of a magnetic sample of circular cross-section having a homogeneous magnetization **m**. On the right: evolution of the magnetic field **b** along direction $|\mathbf{e}_1|$ (bottom) and transverse to direction $|\mathbf{e}_2|$ (top) covering the discontinuity interface sample/air.

Initial susceptibility

However, since the sensitive elements of the Hall probes (in particular the element of Hall probe h, see Figure 3.10b) cannot be placed exactly at the discontinuity interface sample/air due to geometrical limitations, we decided to supplement the previously described measurements so as to correct the measurement's systematic error due to the probe position. To this end[6], temperature compensated high precision measurements of the initial volume susceptibility χ of the MRE samples are performed with the help of a susceptibilimeter (resolution: 10^{-6} $[-]$ SI). This technique consists in generating a known alternative low-intensity magnetic field in a coil. When a sample is placed at the center of the coil in the open cavity, it creates

[6]For the sake of brevity here, a discussion regarding the different approaches that could be taken is saved for Chapter 5.

a perturbation that affects the current in the coil and can be related to its initial susceptibility χ. In this study, the MS3/MS2G susceptibilimeter from Bartington is used. Its zone of measurement consists of a cylindrical gap (8.5 mm in diameter and 28 mm in height) in which one places a vial filled with the material to analyze (see Figure 3.11). Measurements are conducted on the materials and samples used in this study and the obtained values are reported Table 3.1.

Figure 3.11: Photograph of an MRE-filled vial to be placed in the open cavity (surrounded by the coil) of the Bartington MS2G sensor to determine the initial volume susceptibility χ of the material.

	silicone	CIP	isotropic 70 phr MRE	transversely isotropic 70 phr MRE with chains transverse to the magnetic field	transversely isotropic 70 phr MRE with chains along the magnetic field
$\chi\,[-]$	-11.9x10^{-6}	2.924	0.397	0.321	0.846

Table 3.1: Values of the initial volume susceptibility χ $[-]$ SI of the silicone matrix, the carbonyl iron particles (CIP) and the MRE samples used in this study, obtained from susceptibilimeter measurements (Bartington MS3/MS2G).

3.4 Experiments and parameter identification

In this work, experiments are conducted on three types of MRE samples shown in Figure 3.12 and listed below:

- isotropic 70 phr MRE
- transversely isotropic 70 phr MRE with chains along direction $\mathbf{e}_3$ (i.e. along the sample's axis and transverse to the magnetic field, if applied)
- transversely isotropic 70 phr MRE with chains along direction $\mathbf{e}_1$ (i.e. transverse to the sample's axis and along the magnetic field, if applied)

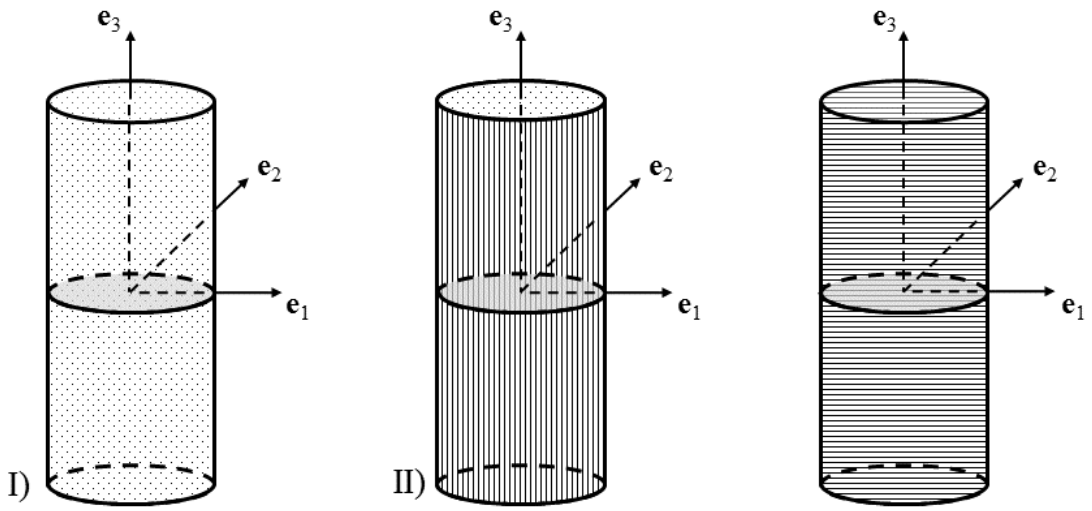

Figure 3.12: Schematics of the different types of MRE samples fabricated in this study. I) Isotropic MRE, II) transversely isotropic MRE with chains along direction $\mathbf{e}_3$ (i.e. along the sample's axis and transverse to the magnetic field, if applied) and transversely isotropic MRE with chains along direction $\mathbf{e}_1$ (i.e. transverse to the sample's axis and along the magnetic field, if applied).

Two types of tests are conducted and described in what follows:

- purely mechanical tests on MRE samples
- magneto-mechanical tests on MRE samples

3.4.1 Testing protocol

For all tests, a virgin sample of the material of interest is installed and aligned in the tensile setup with the help of the camera as the system is drawn out of the electromagnet. Once the clamps are in place, the setup is glided back inside the electromagnet and latched so that the sample lies exactly at the center of the magnet. At that stage the force applied on the sample as well as the strain are zero.

Purely mechanical tests

In the case of the purely mechanical tests, the sample is first pre-conditioned, which consists in submitting the sample to cyclic loading prior to the actual test in order to attain a stabilized behavior after an initial cyclic softening known as Mullins effect [Mul57]. The pre-cycling (10 cycles) is conducted in displacement-controlled mode, so that the relative displacement of the two piezo-motors oscillates between 0 and 30 mm following a sinus at a frequency of 0.01 Hz. Following the pre-conditioning, as the sample carries some residual strain, a relaxation time of 10 minutes is allowed before the motors are displaced to get the sample straight while keeping the force at 0 N. At this moment, the initial cross-section $A_0 = L_1 L_2 \pi/4$ is determined with the help of the camera, where L_1 and L_2 is the length of the sample in direction $\mathbf{e}_1$ and $\mathbf{e}_2$ in the gage area, respectively. The actual cyclic test (3 cycles) is then conducted in displacement-controlled mode, so that the relative displacement of the piezo-motors oscillates between 0 and 30 mm following a triangle at a frequency of 0.001 Hz (quasi-static).

Magneto-mechanical tests

In the case of the magneto-mechanical tests, the force is set and maintained at 0 N during the whole test, using the force-controlled mode to operate the motors. The magnetic field $\mathbf{b}_0$ is then cycled between 0 and 0.8 T (by varying the current between 0 and 68 A) in the same conditions than for the purely mechanical tests: 10 sinusoidal pre-cycles at a frequency of 0.01 Hz, followed by a relaxation time of 10 minutes, followed by 3 triangular test cycles at a frequency of 0.001 Hz (quasi-static). After these tests, again a relaxation time of 10 minutes is allowed before the in-situ magnetic field-related measurements are carried out manually with the Hall probes h and m (see Section 3.3.4). The probes are positioned by hand with the help of the camera to measure the magnetic quantities within the sample when the latter is at rest. This is done at current steps of 1 A up to a current of 68 A ($\mathbf{b}_0 = 0.8\,T$).

3.4.2 Experimental results

In this section, the experimental data obtained during the tests described in the previous section are presented and discussed. The plotted quantities are the nominal stress T_{ex}, stretches λ_{ex} along the principal directions $\mathbf{e}_1$, $\mathbf{e}_2$ and $\mathbf{e}_3$, the Jacobian

of the deformation J_{ex} as well as the magnetization m_{ex}, the magnetic field h_{ex} and the initial volume susceptibility χ_{ex}. The index "ex" is used to distinguish experimental quantities from their theoretical counterparts. In particular, the nominal stress T_{ex} $[MPa]$ is the experimental counterpart of the mechanical surface traction expressed in the theoretical sections[7] and is obtained by dividing the measured force f_{ex} $[N]$ by the sample's initial cross-section A_0 $[mm^2]$. The stretch λ_{ex} [-] corresponds to the variation of length divided by the initial probed length. As the in-situ extensometer returns results in true (Eulerian) strain ε, the following conversion is performed: $\lambda_{ex} = \exp(\varepsilon)$. Finally magnetic measurements from probes h and m both yield magnetic field data in $[T]$, and the initial volume susceptibility χ_{ex} obtained from susceptibilimeter measurements is given in SI units $[-]$.

Purely mechanical response

In what follows, we consider the loading part of the third cycle of testing (stabilized curves after material training/pre-cycling, see Chapter 2, Section 2.4.3). This data will be used for the subsequent characterization of the materials in Section 3.4.3.

In Figure 3.13, the principal stretches $\lambda_{1,ex}$, $\lambda_{2,ex}$ and $\lambda_{3,ex}$ are plotted together with J_{ex} as a function of the motor relative displacement. As predicted by theory, $\lambda_{1,ex} = \lambda_{2,ex}$ for the axisymmetric test cases a and b. When the particle chains are aligned transverse to the direction of traction $\mathbf{e}_3$, as in test case c, the contraction in the particle chain direction $\mathbf{e}_1$ is much smaller than along direction $\mathbf{e}_2$, as expected. The sample indeed exhibits the highest mechanical stiffness in the direction of the particle alignment, similar to what is classically observed in uni-directional fiber-reinforced composites.

To verify the incompressibility assumption, the Jacobian of the deformation $J_{ex} = \det \mathbf{F} = \lambda_{1,ex}\lambda_{2,ex}\lambda_{3,ex}$ is computed as the product of the three measured principal stretches during purely mechanical deformation and reported in Figure 3.13a through c. For every test case, J_{ex} exhibits almost the unit value for the whole range of deformation. The maximum deviation from the unit value (perfect incompressibility) for the three test cases a, b and c is, respectively: 0.0038, 0.0027 and 0.0197. Thus, the incompressibility assumption for the investigated MREs tends to be appropriate: there is no deformation of the particles (very high modulus compared to the silicone) in the nearly incompressible silicone matrix and there is minor

[7] In the considered cases, the nominal stress tensor as the transpose of the first Piola-Kirchhoff stress tensor are equal.

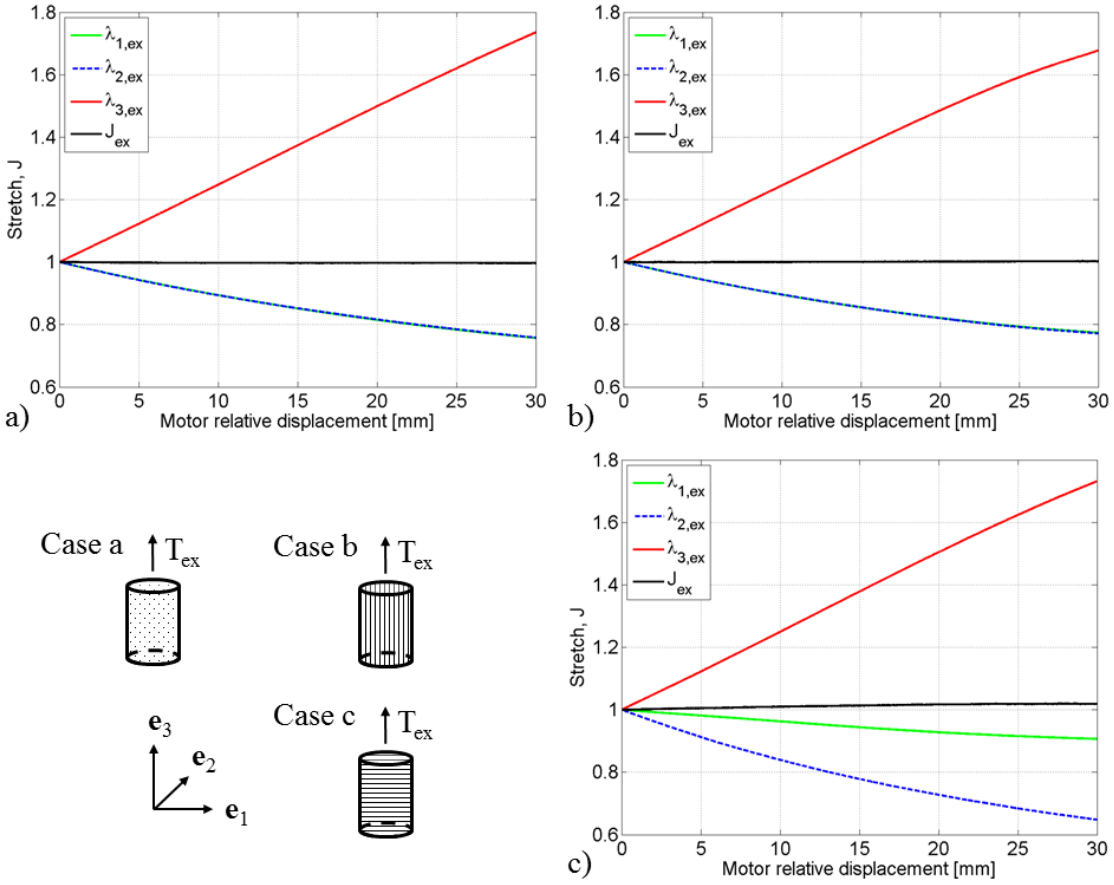

Figure 3.13: Principal stretches $\lambda_{1,ex}$, $\lambda_{2,ex}$, $\lambda_{3,ex}$ and the Jacobian of the deformation J_{ex} for a purely mechanical loading: a) isotropic 70 phr MRE, b) transversely isotropic 70 phr MRE with chains along direction $\mathbf{e}_3$ (i.e. along the sample's axis) and c) transversely isotropic 70 phr MRE with chains along direction $\mathbf{e}_1$ (i.e. transverse to the sample's axis).

interaction/debonding between the particles and the matrix for the investigated range of mechanical loading.

In Figure 3.14, the nominal stress T_{ex} is plotted as a function of the axial stretch $\lambda_{3,ex}$ for test cases a, b and c. When comparing the three tested samples with same particle content, the isotropic MRE (case a) shows the smallest stiffness for the whole range of deformation. While the responses of the two transversely isotropic samples are almost the same up to a stretch level of 1.15, the stiffness of sample b increases more significantly with an increasing stretch $\lambda_{3,ex}$. This behavior can be explained, when we consider the three-dimensional, nearly incompressible deformation state during the tension tests. On the one hand in case b, the mechanical traction is introduced along the particle chain orientation. For higher values of the applied

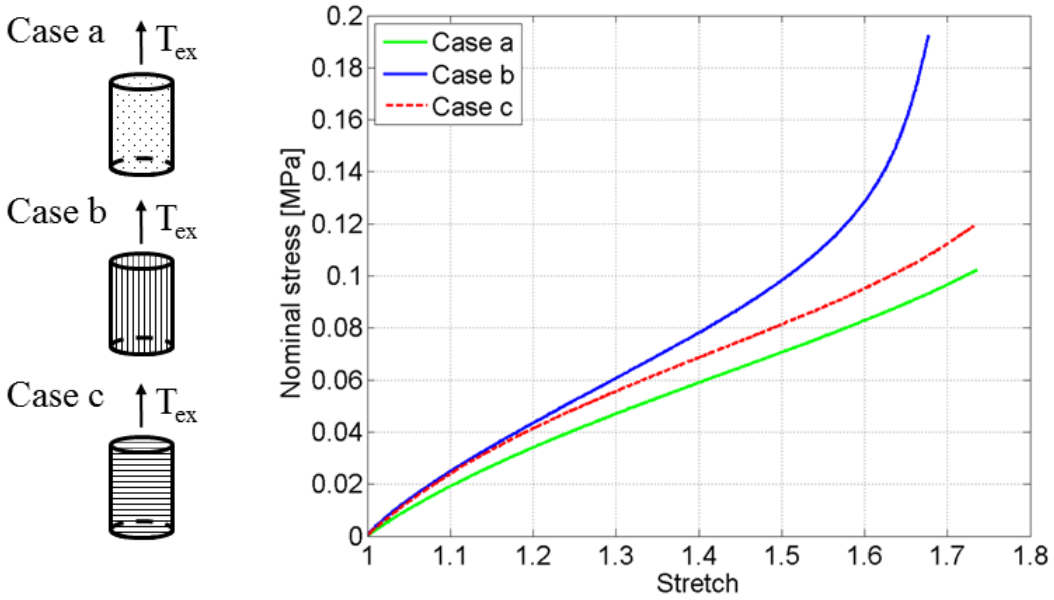

Figure 3.14: Purely mechanical loading curves for the isotropic 70 phr MRE (case a), the transversely isotropic 70 phr MRE with chains along direction $\mathbf{e}_3$ (i.e. along the sample's axis, case b) and the transversely isotropic 70 phr MRE with chains along direction $\mathbf{e}_1$ (i.e. transverse to the sample's axis, case c).

stretch, the individual particle chains approach each other due to the contraction in both directions $\mathbf{e}_1$ and $\mathbf{e}_2$, hence increasing the stiffness of the material. On the other hand in case c, the mechanical load is introduced transverse to the particle chain direction. The particles get closer along directions $\mathbf{e}_1$ and $\mathbf{e}_2$, probably resulting in the similar response for both cases b and c at lower stretch values (symmetric tension/compression response at low strains, compare to Figure 3.23). In particular, more resistance is offered along direction $\mathbf{e}_1$ (as the particles are already packed along the chains) than along direction $\mathbf{e}_2$ (where there is matrix material between the chains). This is clearly seen in Figure 3.13c where $1 > \lambda_{1,ex} > \lambda_{2,ex}$. However, due to a continuously imposed stretch in direction $\mathbf{e}_3$, the individual particle chains keep getting further from each other and eventually the "hardenings" obtained in directions $\mathbf{e}_1$ and especially $\mathbf{e}_2$ are less significant than the corresponding "hardenings" obtained when the chains are along the sample's axis (case b). Additionally, the higher deviation of J_{ex} in case c indicates that the particles in the chain are allowed to disperse more easily. Furthermore, note that for a given value of imposed displacement, the resulting stretches $\lambda_{3,ex}$ measured in the gage area of the sample are not equal for the three purely mechanical test cases: the stretch is slightly diminished by the stress transfer through the sample's head for a higher stiffness, in

particular when the tension is introduced in particle chain direction as in case b.

Magneto-mechanical response

- Test cycles

In what follows, the loading and in some cases the unloading part of the first cycle of testing (stabilized curves after material training/pre-cycling, see Chapter 2, Section 2.4.3) are plotted, and used for the subsequent characterization of the materials in Section 3.4.3.

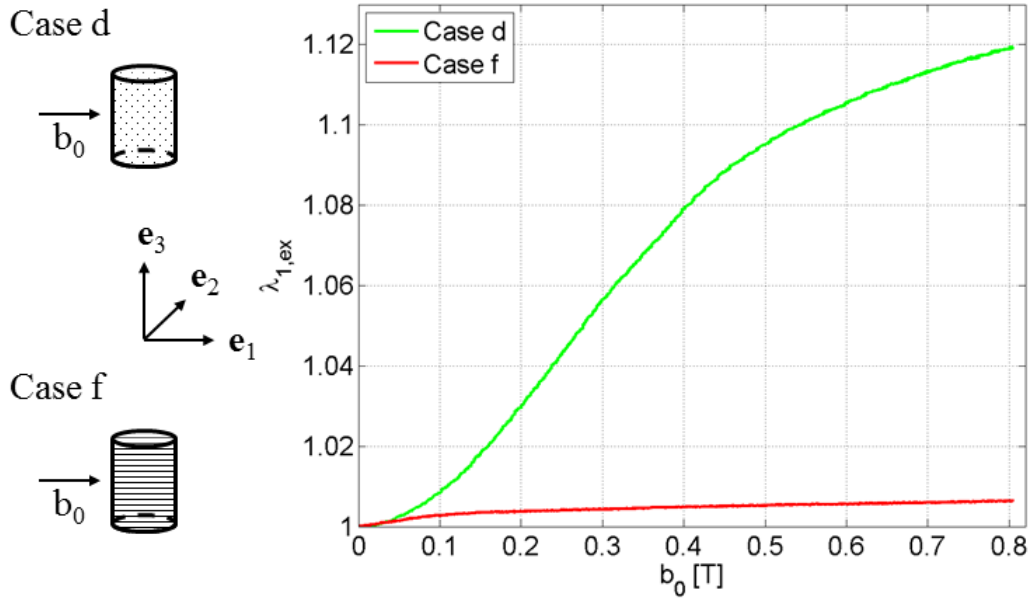

Figure 3.15: Principal stretch $\lambda_{1,ex}$ in samples subjected to purely magnetic loading (while the force is maintained at zero) for the isotropic 70 phr MRE (case d) and the transversely isotropic 70 phr MRE with chains along direction $\mathbf{e}_1$ (i.e. transverse to the sample's axis and along the applied magnetic field, case f).

In Figure 3.15, the principal stretch $\lambda_{1,ex}$ in direction $\mathbf{e}_1$ is plotted as a function of the corresponding externally applied magnetic field $\mathbf{b}_0$ for both test cases d and f (recall that the force is maintained at zero). Note that case e, in which the particle chains are aligned transverse to the applied field, is not presented here because this loading configuration is leading to a structural instability in the sample. This phenomenon will be discussed in more details at the end of the present section. In the isotropic case d, the sample is stretched in the direction of the field up to a level of 1.12 (12% strain) whereas in the transversely isotropic case f (Figure b) only a stretch of 1.0065 (0.65% strain) can be observed. This can be explained in the following way: both

samples want to expand in the magnetic field direction (and to contract transverse to the field due to incompressibility). In the isotropic case, the so-called shape effect due to Maxwell stresses at the interface enhances the magnetic susceptibility and is predominant, the magnetic particle dipoles try to re-arrange themselves accordingly. Once approaching the saturation (compare to Figure 3.20b and Figure 3.21b), this effect becomes less significant. In the transversely isotropic case f, the initial shape of the sample is equal to case d and Maxwell stresses at the sample/air interface again would tend to expand the sample in magnetic field direction $\mathbf{e}_1$. But this time, the particles are already structured in their preferred arrangement since the particle chains have already formed to enhance the magnetic susceptibility of the sample during curing. Hence the magnetic susceptibility is already nearly optimal[8] (the sample might have some residual stress from being constrained in the mold) and one can only notice a small deformation to further enhance it.

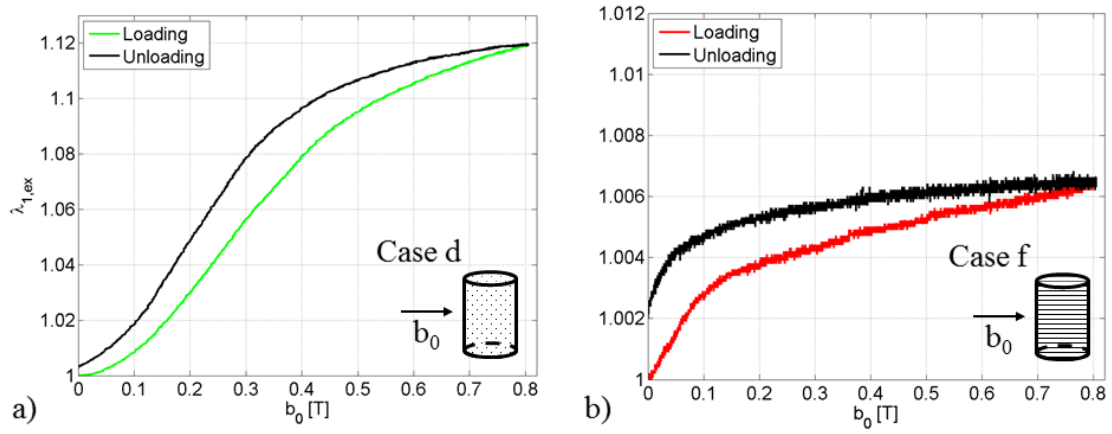

Figure 3.16: Principal stretch $\lambda_{1,ex}$ in samples subjected to purely magnetic loading and unloading (while the force is maintained at zero): a) isotropic 70 phr MRE (case d), b) transversely isotropic 70 phr MRE with chains along direction $\mathbf{e}_1$ (i.e. transverse to the sample's axis and along the applied magnetic field, case f).

An interesting phenomenon can also be observed when looking at the unloading part of these curves (not used for the parameter identification). Therefore, in Figure 3.16, the loading and unloading behavior of the principal stretch $\lambda_{1,ex}$ is plotted as a function of the magnetic field $\mathbf{b}_0$ applied in direction $\mathbf{e}_1$ for both test cases d and f. A magnetic remanence stretch – vanishing during the 10 minutes relaxation time

[8]Note that the sample is cured in the horizontal position whereas it is tested in the vertical position. Thus, the slight asymmetry of the applied field due to the C-frame of the electromagnet will slightly influence the material response.

allowed after material training and testing – can be observed. The iron particles probably carry some amount of remanence magnetization, although not detectable in the precision of the Hall probe measurements, which leads to a magnetic remanence stretch (as similarly observed by Abramchuk et al. [Abr07] as well as Danas and Triantafyllidis [Dan12]). Both MRE samples maintain the configuration obtained by applying the magnetic field in some amount even when the magnetic field is decreased, since the magnetic field seen by the composite is increased due to the remanence magnetization in the unloading part.

In Figure 3.17, the principal stretches $\lambda_{1,ex}$, $\lambda_{2,ex}$, $\lambda_{3,ex}$ are plotted as a function of the magnetic field $\mathbf{b}_0$ applied in direction $\mathbf{e}_1$ for both test cases d and f. The force is also plotted on a secondary axis (with the same scale minus 1 N enhancing the noise and its peaks due to the vibrations of the unit that cools the electromagnet). Hence one can see that the two dents on $\lambda_{2,ex}$ and $\lambda_{3,ex}$ curves in Figure 3.17b are correlated to these external vibrations.

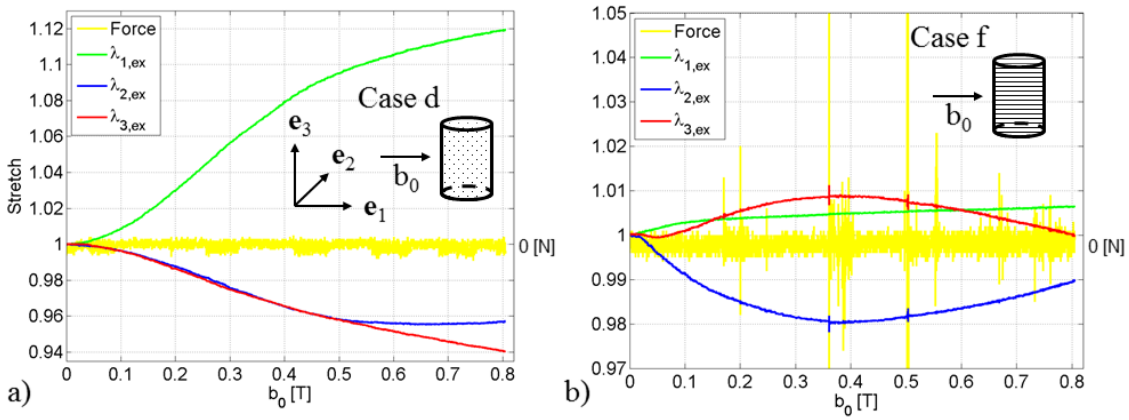

Figure 3.17: Principal stretches $\lambda_{1,ex}$, $\lambda_{2,ex}$, $\lambda_{3,ex}$ in samples subjected to purely magnetic loading (while the force is maintained at zero): a) isotropic 70 phr MRE (case d), b) transversely isotropic 70 phr MRE with chains along direction $\mathbf{e}_1$ (i.e. transverse to the sample's axis and along the applied magnetic field, case f).

If one refers to the incompressible behavior[9], the expansion $\lambda_{1,ex}$ in the magnetic field direction $\mathbf{e}_1$ (as seen in Figure 3.15) should be expected to induce a contraction ($\lambda_{2,ex}$, $\lambda_{3,ex}$) transverse to the magnetic field direction $\mathbf{e}_1$. This behavior can be observed in the isotropic case d (see Figure 3.17a): the isotropic sample contracts almost symmetrically along its cross-section, though, at higher magnetic field (and thus at

[9]The maximum deviation of J_{ex} from the unit value (perfect incompressibility) for the test cases d and f is, respectively: 0.0072 and 0.0065.

higher strain), the contraction in direction $\mathbf{e}_3$ becomes larger than the contraction along direction $\mathbf{e}_2$. This could be attributed to the following contributions:

1. As reported in Figure 3.5b, the non-uniformity of the externally applied magnetic field $\mathbf{b}_0$ seen by the long axis of the sample is higher than the slight non-uniformity seen by the short axis of the sample (cross-section). The particles (together with the matrix) are displaced towards the higher magnitude of the field at the center of the electromagnet, thus contracting the sample mainly in $\mathbf{e}_3$. This effect emerges clearly when the dominant shape effect is fading out approaching saturation magnetization but the externally applied magnetic field further increases.
2. As reported in Chapter 2, Figure 2.4, a slight internal magnetic field non-uniformity can be observed in the nearly ellipsoidal MRE sample for the magneto-mechanical tests at the junction of the cylindrical MRE body with the elliptical MRE caps and additionally could influence the experimental material response.
3. Probably at higher magnetic field-induced expansion $\lambda_{1,ex}$, the MRE sample does not remain an ellipsoid of revolution (see for instance Brown [Bro66] or Raikher and Stolbov [Rai03]), and non-uniform internal magnetic fields are developed.
4. Also mechanical effects probably come into play at higher strains as the contraction along the short axis of the sample saturates earlier than along its long axis, and, additionally, the radial deformation of the elliptical MRE cap is restrained by its plastic casing (3D-printed plastic head).

In the transversely isotropic case f (see Figure 3.17b), the behavior is even more complex. During purely magnetic loading, a competition between the shape effect, the local position of the particles relative to each other and magnetic field non-uniformities can be observed. Maxwell stresses at the sample/air interface tend to expand the sample in the magnetic field direction $\mathbf{e}_1$ and thus to contract the sample transverse to the field due to incompressibility. However, compared to the isotropic case, the mechanical stiffness is enhanced in chain-direction $\mathbf{e}_1$ and diminished transverse to chain direction, i.e. along $\mathbf{e}_2$ (see paragraph: Purely mechanical response). Hence, the contraction in $\mathbf{e}_2$ has a larger amplitude than the expansion in $\mathbf{e}_1$ and $\lambda_{3,ex}$ seems to be guided due to incompressibility. Predominantly and counter-acting to this shape effect, the particles tend to stay in their preferred configuration obtained during curing. At maximum applied field $\mathbf{b}_0 = 0.8\,T$ the magnetic particles want

to get to the same positions as cured and the three principal stretches almost come back to the unit value. Magnetic field non-uniformities, as in the isotropic case d, probably play a predominant role in direction $\mathbf{e}_3$, especially for high magnetic fields.

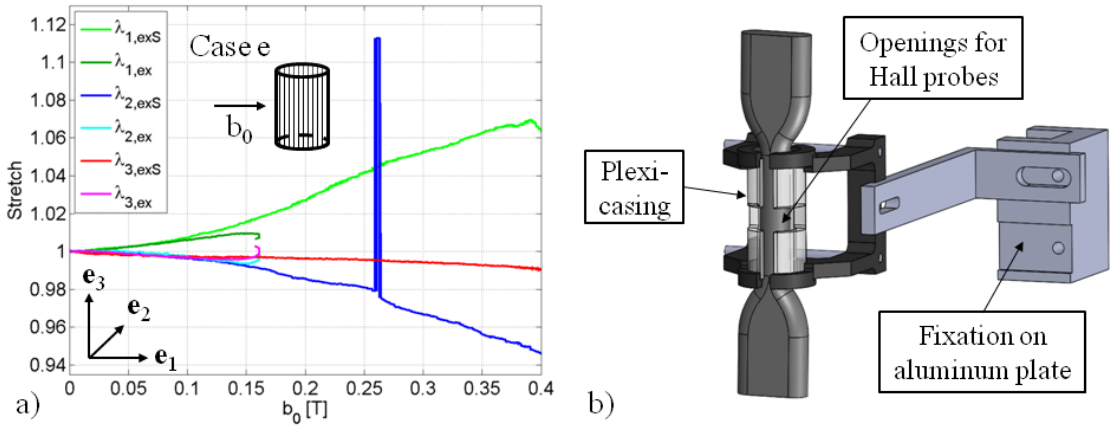

Figure 3.18: a) Principal stretches $\lambda_{1,ex}$, $\lambda_{2,ex}$, $\lambda_{3,ex}$ for the transversely isotropic 70 phr MRE with chains along direction $\mathbf{e}_3$ (i.e. along the sample's axis and transverse to the applied magnetic field, case e) subjected to purely magnetic loading (while the force is maintained at zero). The subscript "S" denotes experiments where a Plexiglass-casing is used to stabilize the sample. b) Schematic of the sample held at the center of the electromagnet airgap and the Plexiglass-casing stabilizing the sample (compare to Figure 3.7).

Finally, test case e, where the magnetic field is applied transverse to the particle-chain direction, is discussed. In this case, structural instabilities – not observed in the whole range of applied magnetic fields $\mathbf{b}_0$ in the two other cases – develop even at low applied fields. One can indeed notice in Figure 3.18a that the principal stretches $\lambda_{1,ex}$, $\lambda_{2,ex}$ and $\lambda_{3,ex}$ diverge around $\mathbf{b}_0 = 0.15T$. In the experimental setup, the MRE samples are held with their long axis perpendicular to the field. If the samples were to hang free, they would align their longest axis $\mathbf{e}_3$ to the magnetic field direction $\mathbf{e}_1$, like a compass needle. However, for cases d and f, the magnetic torques are not strong enough to reach the onset of bifurcation whereas in case e, supported by the transverse alignment of the chains and thus a higher susceptibility along the chains, this instable point can be reached earlier. Therefore, a Plexiglass-casing (allowing to follow the markers and lubrified with silicone oil to let the sample slide freely, see Figure 3.18b,) is installed around the sample to prevent it from buckling. This allowed to expand the range of probing of the material response up to an applied magnetic field $\mathbf{b}_0 = 0.4T$, as illustrated through the principal stretches $\lambda_{1,exS}$, $\lambda_{2,exS}$

and $\lambda_{3,exS}$ plotted in Figure 3.18a. Note that the peak on the $\lambda_{2,exS}$ curve corresponds to a brief loss of the markers as in some configurations, the Plexiglass-casing disturbs the detection.

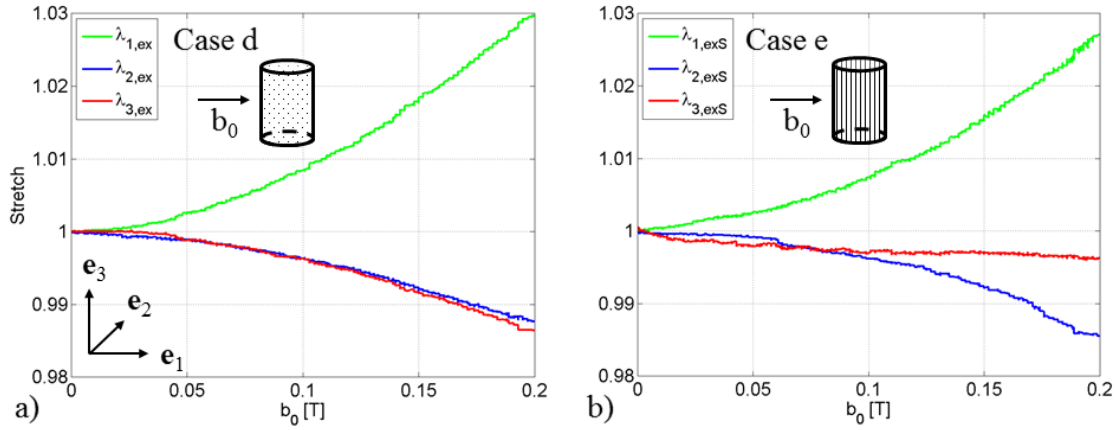

Figure 3.19: Principal stretches $\lambda_{1,ex}$, $\lambda_{2,ex}$, $\lambda_{3,ex}$ in samples subjected to purely magnetic loading (while the force is maintained at zero): a) isotropic 70 phr MRE (case d), b) transversely isotropic 70 phr MRE with chains along direction $\mathbf{e}_3$ (i.e. along the sample's axis and transverse to the applied magnetic field, case e).

In Figure 3.19, the principal stretches $\lambda_{1,ex}$, $\lambda_{2,ex}$, $\lambda_{3,ex}$ are plotted as a function of the magnetic field $\mathbf{b}_0$ applied in direction $\mathbf{e}_1$ for both test cases d and e (case e when stabilized with Plexiglass-casing)[10]. It is remarkable that a very similar response can be observed for both samples. Maxwell stresses at the sample/air interface expand the samples in the magnetic field direction $\mathbf{e}_1$ to enhance the susceptibility and the samples contract transverse to the field due to incompressibility. And, as predicted by theory (see eq.(3.38)), there is no contribution of I_9, which means that the magnetic effect of the particle chains does not play a role in the traction response of test case e. Furthermore, the overall lower deformation in the transversely isotropic case e as compared to the isotropic case d can be attributed to the overall higher stiffness of the field-structured material, whereas the mechanical effect of the particle chains diminishes the contraction in direction $\mathbf{e}_3$ as compared to the contraction in direction $\mathbf{e}_2$ in test case e.

[10]In this latter case, the maximum deviation of J_{ex} from the unit value is 0.0175.

- m-h response

Because the Hall probes need to be positioned by hand at each field increment (applied current steps of 1 A up to a value of 68 $A \mathrel{\widehat{=}} \mathbf{b}_0 = 0.8\,T$), the magnetic field measurements were conducted separately and are presented in this section. Since the sensitive elements of the Hall probes (in particular the element of Hall probe h, see Section 3.3.4 and Figure 3.10b) cannot be placed exactly at the discontinuity interface sample/air due to geometrical limitations, the measurement's systematic error due to the probe position needs to be corrected.

As a first solution, this correction is performed by shifting upwards the raw experimental m-h curves for test cases d and f (Hall probe measures in Figure 3.20a and Figure 3.21a) to match their initial slope with the temperature-compensated high-precision measurements of the initial volume susceptibility χ_{ex} of the MRE samples performed with the help of a susceptibilimeter (Bartington MS3/MS2G, resolution: 10^{-6} $[-]$ SI). These initial susceptibility results, reported in Section 3.3.4, Table 3.1, are plotted in Figure 3.20a and Figure 3.21a for test cases d and f as the red dotted slopes, respectively. The shift to obtain the corrected m-h curves for test cases d and f is performed in the following way:

1. On the one hand, the data of probe h – obtained by searching for the minimum of $\mu_0 h$ – needs a larger amplitude of correction since the center of the sensitive element of probe h can only be placed at 1.14 mm from the interface. Therefore, the data of probe h at each current increment is lowered by an increasing value, that slightly saturates at high current, as shown by the red curve in Figure 3.20b and Figure 3.21b.
2. On the other hand, the data of probe m – obtained by searching for the maximum of $\mu_0\,(h + m)$ – only needs a slight correction since the center of the sensitive element of probe m can almost be placed at the interface though slight imperfection at the borders of the samples are present. Therefore, the data of probe m at each current increment is increased by an increasing value, that slightly saturates at high current, as shown by the green curve in Figure 3.20b and Figure 3.21b.

Finally, the measured value of the initial susceptibility χ_{ex} is taken up to a magnetic field $\mu_0 h = 0.1\,T$ to cancel out the noise of the Hall probe measures at small values of the magnetic field. The final m-h curves after these corrections are plotted as solid lines in Figure 3.20a for test case d and in Figure 3.21a for test case f.

The corrections are supplemented by the observation in the MRE literature that

experimental values of the saturation magnetization $m_{s,MRE,ex}$ (see for instance [Kal05, Dan12]) tend to be lower than theoretically predicted. Indeed, the saturation magnetization of (isotropic and transversely isotropic) MREs $m_{s,MRE}$ at high magnetic fields is usually predicted as (see for instance [Mar00, Mar06, Schu14]):

$$\mu_0 m_{s,MRE} = \phi_{vol} \mu_0 m_{s,Fe} \; [T] \,, \tag{3.43}$$

where ϕ_{vol} is the particle volume fraction, 8.7% in the case of 70 phr MRE[11], and $\mu_0 m_{s,Fe}$ is the saturation magnetization of bulk iron, 2.1 T [Hay13]. The theoretically predicted value of the saturation magnetization for the 70 phr MREs investigated in this study is plotted for comparison as the blue line in Figure 3.20a and Figure 3.21a: one can also observe in the experimental data that the saturation tends to strive for a lower value than theoretically predicted.

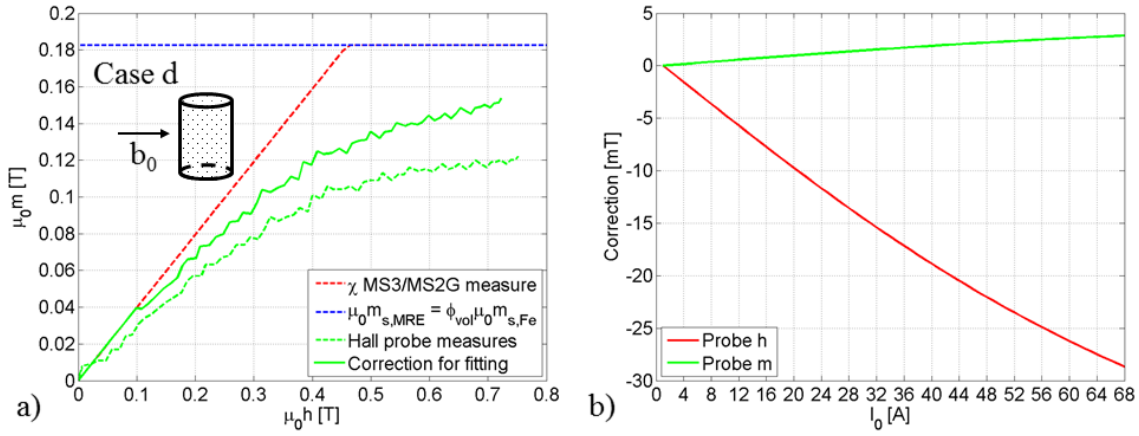

Figure 3.20: Isotropic 70 phr MRE (case d): a) Experimental and corrected data for the magnetic response. b) Charts/values of the correction applied to probe h and m experimental data.

In test case e, the MRE sample shows instabilities and the measurements up to high magnetic fields are not reliable: due to the Plexiglass-casing stabilizing the sample it is difficult to place the sensitive elements of the Hall probes properly, even with the help of the camera.

[11] For the conversion of phr values into ϕ_{vol} see Chapter 2, eq.(2.1), $\rho_{sil} = 1,070\, kg/m^3$ is used for the density of the silicone matrix (according to the manufacturer) and the density of iron (as a solid metal) is used for the density of the MRE filler particles $\rho_{CIP} = 7,874\, kg/m^3$.

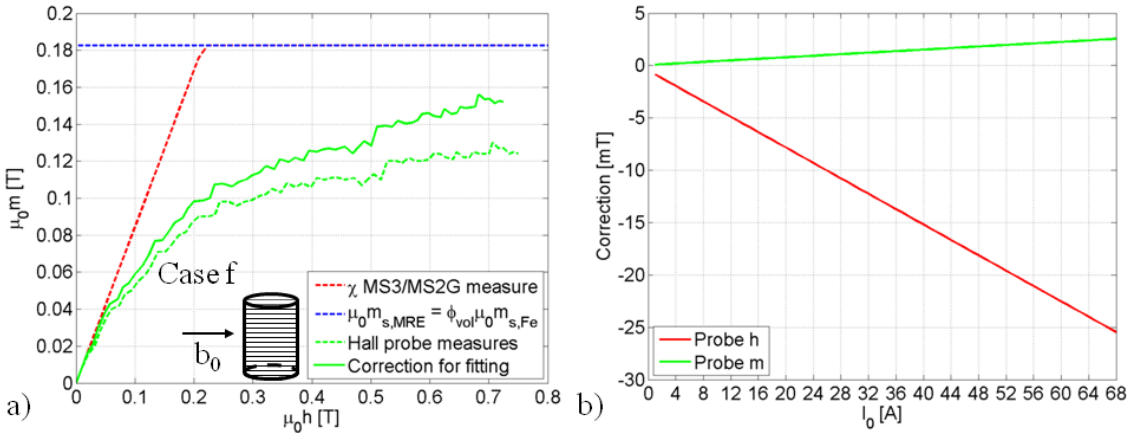

Figure 3.21: Transversely isotropic 70 phr MRE with chains along direction $\mathbf{e}_1$ (i.e. transverse to the sample's axis and along the applied magnetic field, case f): a) Experimental and corrected data for the magnetic response. b) Charts/values of the correction applied to probe h and m experimental data.

3.4.3 Parameter identification results

All the ingredients have been assembled to identify the material parameters of the response functions for each invariant in use in isotropic and transversely isotropic MRE continua. For the magneto-mechanical experimental data sets, e.g. $\left(T_{ex}, h_{ex}, m_{ex}, \lambda_{ex}, \bar{\lambda}_{ex}\right)$ with $ex = 1, ..., n$ measurement points, and the corresponding constitutive response T and h depending on the material parameters $\mathbf{p}$, the solution $\mathbf{p}^*$ is determined on the basis of a least-squares optimization method [Ogd04]. In the present work, the MATLAB routine *fminsearch*[12] is used to find the minimum of the unconstrained multi-variable functions (see details in what follows) based on a derivative-free Nelder-Mead simplex algorithm as described in Lagarias et al. [Lag98]. A summary of the identified material parameters is given in Table 3.2.

Purely mechanical response

First, we start with the purely mechanical case presented in Figure 3.2a. There is one constitutive equation eq.(3.30) for the traction response T to determine the constants related to I_1 for isotropic MREs by fitting the corresponding nominal

[12]Maximum number of function evaluations and iteration steps, respectively: $MaxFunEvals = 3000$, $MaxIter = 3000$; termination tolerance on the function and step value, respectively: $TolFun = 1e^{-8}$, $TolX = 1e^{-12}$.

stress-stretch upload curve (T_{ex}, λ_{ex}), where the subscript a refers to case a:

$$\min_{\mathbf{p}} \sum_{ex} \left\| T\left(\lambda_{ex}, \mathbf{p}\right) - T_{ex} \right\|_a^2 . \tag{3.44}$$

This objective function to be minimized is the squared 2-Norm of the residuals between predictions of the constitutive equation and the experimental data with the following material parameters:

$$\mathbf{p} = \left[G, C_1 = 1, d_{11} = 1, d_{12}, d_{13}\right]_a . \tag{3.45}$$

As a first check of the determined solution $\mathbf{p}^*$, the relative error is reported according to:

$$err_a T = \frac{\left| T\left(\lambda_{ex}, \mathbf{p}^*\right) - T_{ex} \right|_a}{\max\left\{T_{\lambda_{ex}=1.1}, T_{ex}\right\}_a}, \tag{3.46}$$

where $T_{\lambda_{ex}=1.1}$ is the measured nominal stress at a stretch of 1.1 so as to avoid division by small values of T_{ex} when the stretches are close to 1 [Ogd04]. Since a starting guess for the model parameters is required as input, different sets of possible start parameters have been tried to minimize the relative error. The parameter identification results are shown in Figure 3.22. For the whole range of deformation, the experimental data can be fitted very well, showing a relative error of less than 5%.

While the error in the fit could have been further diminished by increasing the order of the response function $W_{,1}$, the predicted response for various deformation modes would become no longer realistic. In particular, the biaxial tension response either increases or decreases in an extreme fashion. Choosing an order 3 function ($j = 1...3$ for I_1 in eq.(3.25)) leads to a reasonable prediction of the material behavior in uniaxial tension/compression, plane shear and biaxial tension for higher values of strains, as seen in Figure 3.23 (compare to Figure 6.6 on page 180 in [Schu14]): higher principal stresses for biaxial tension than for plane shear and for uniaxial tension are predicted; uniaxial compression and tension behave symmetrically at lower strains whereas the compression response has a higher amplitude at higher

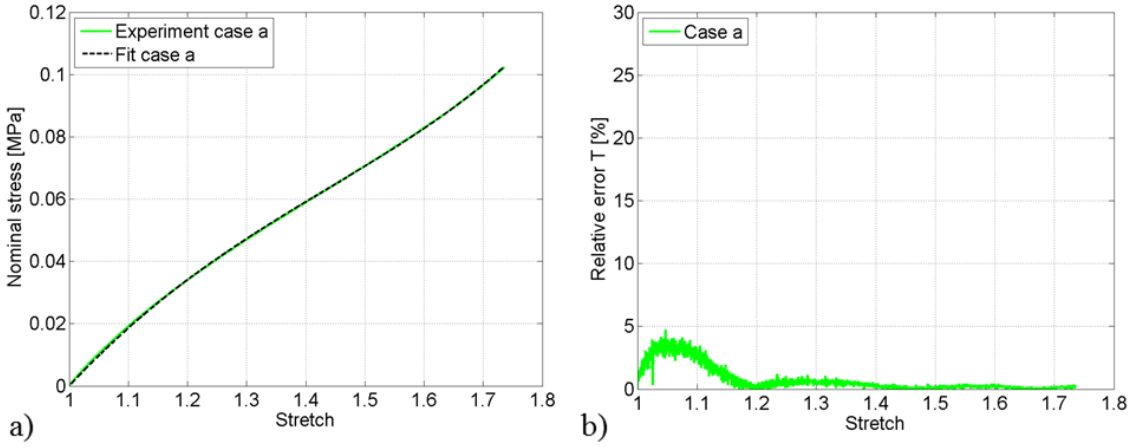

Figure 3.22: Case a for the isotropic 70 phr MRE: a) Purely mechanical loading curve and least-squares fit. b) Relative error in the fit.

strains.

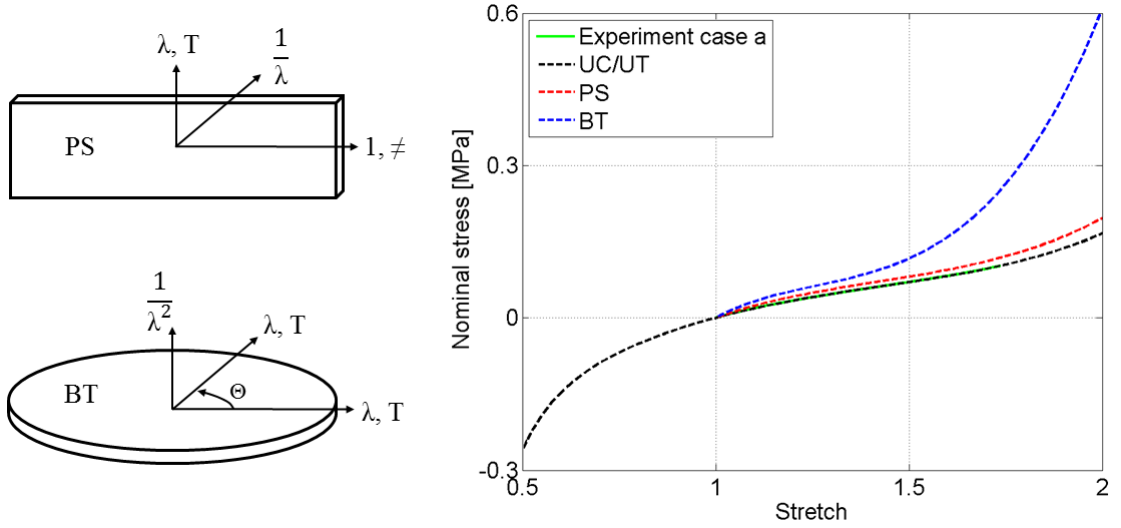

Figure 3.23: Case a: Predicted response T of the isotropic 70 phr MRE for uniaxial tension/compression (UT/UC), plane shear (PS) and biaxial tension (BT) for values of λ between 0.5 and 2.

In the case of the transversely isotropic MRE samples as described in Figure 3.2b and c, there are two constitutive equations for T and experimental stress-stretch curves for either $\widehat{\mathbf{N}} = \mathbf{e}_3$, eq.(3.31) or $\widehat{\mathbf{N}} = \mathbf{e}_1$, eq.(3.33), respectively, to determine

the constants related to I_1 and I_4:

$$\min_{\mathbf{p}} \sum_{ex} \left(\|T(\lambda_{ex}, \mathbf{p}) - T_{ex}\|_b^2 + \left\| T\left(\lambda_{ex}, \bar{\lambda}_{ex}, \mathbf{p}\right) - T_{ex} \right\|_c^2 \right). \tag{3.47}$$

This objective function to be minimized is then the sum of the squared 2-Norms from each experimental data set with the following shared material parameters:

$$\mathbf{p} = [G, C_1 = 1, d_{11} = 1, d_{12}, d_{13}, C_4, d_{42} = 1, d_{43}, d_{44}]_{b/c}\,, \tag{3.48}$$

and the relative errors, respectively:

$$err_bT = \frac{|T(\lambda_{ex}, \mathbf{p}^*) - T_{ex}|_b}{\max\{T_{\lambda_{ex}=1.1}, T_{ex}\}_b}, \quad err_cT = \frac{\left|T\left(\lambda_{ex}, \bar{\lambda}_{ex}, \mathbf{p}^*\right) - T_{ex}\right|_c}{\max\{T_{\lambda_{ex}=1.1}, T_{ex}\}_c}. \tag{3.49}$$

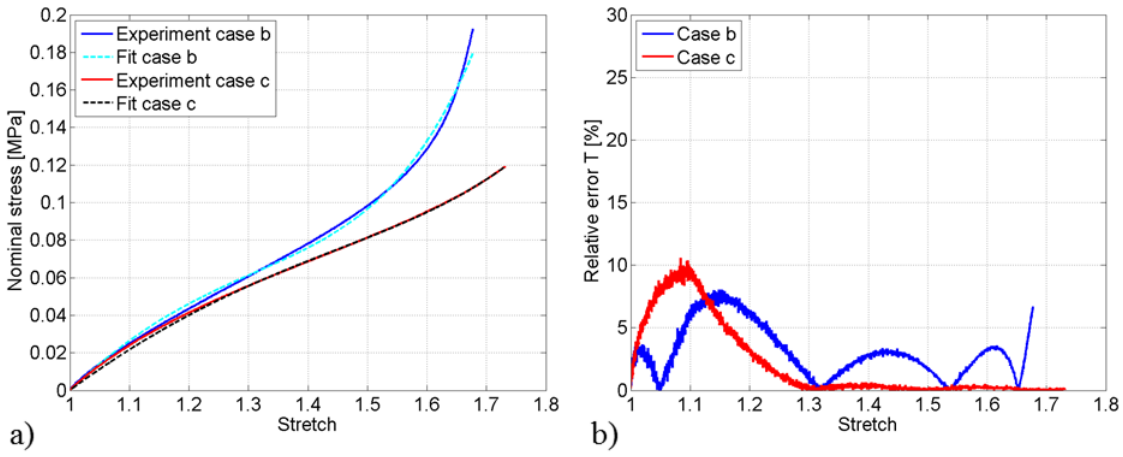

Figure 3.24: Case b and c for the transversely isotropic 70 phr MRE samples: a) Purely mechanical loading curves and least-squares fit. b) Relative errors of the fit.

The combination of the different test cases for the transversely isotropic MRE material provides unique solutions for the model parameters at the expense of a reduction in the quality of the fit. As seen in Figure 3.24, the relative error is increased but stays below a value of 10 percent. Especially the initial steep slope – as already observed to a lower amount in the isotropic case a, Figure 3.22 – is not accurately

represented by the material model, which has been observed previously in the work of Schubert [Schu14].

Magneto-mechanical response

Next, we proceed with the magneto-mechanical case keeping the purely mechanical constants found in the previous section. For the isotropic MRE, the deformation response at $T = 0$ for magnetic loading eq.(3.35) together with the constitutive equation for the magnetic field h eq.(3.36) allow to find the material parameters related to I_6 and I_7 :

$$\underset{\mathbf{p}}{min} \sum_{ex} \left(\left\| T\left(\lambda_{ex}, \bar{\lambda}_{ex}, m_{ex}, \mathbf{p}\right) - T_{ex} \right\|_d^2 + \left\| h\left(\bar{\lambda}_{ex}, m_{ex}, \mathbf{p}\right) - h_{ex} \right\|_d^2 \right), \tag{3.50}$$

with shared material parameters:

$$\mathbf{p} = \left[\mathbf{p}_a^*, m_s, C_6, C_{6s}, C_7\right]_d, \tag{3.51}$$

and the relative errors, respectively:

$$err_d T = \frac{\left| T\left(\lambda_{ex}, \bar{\lambda}_{ex}, m_{ex}, \mathbf{p}^*\right) - T_{ex} \right|_d}{\max\left\{T_{\lambda_{ex}=1.1}, T_{ex}\right\}_d}, \quad err_d h = \frac{\left| h\left(\bar{\lambda}_{ex}, m_{ex}, \mathbf{p}^*\right) - h_{ex} \right|_d}{\max\left\{h_{0.1\,T}, h_{ex}\right\}_d}, \tag{3.52}$$

where $T_{\lambda_{ex}=1.1}$ is the equivalent nominal stress at a stretch λ of 1.1 from case a and $h_{0.1\,T}$ is the measured magnetic field $\mu_0 h_{ex} = 0.1\,T$. The parameter identification results are shown in Figure 3.25 and in Figure 3.26. The additional information leads to a further loss in the quality of the fit but the relative error stays below an acceptable value of 20%.

In the case of the transversely isotropic MRE material (case f)[13], the deformation response at $T = 0$ for magnetic loading eq.(3.41) together with the constitutive equation for the magnetic field h, eq.(3.42), allow to find the material parameters

[13]Due to experimental errors/ instabilities in test case e (particle chains perpendicular to the applied magnetic field), only test case f is used to identify the material parameters for the transversely isotropic 70 phr MRE material.

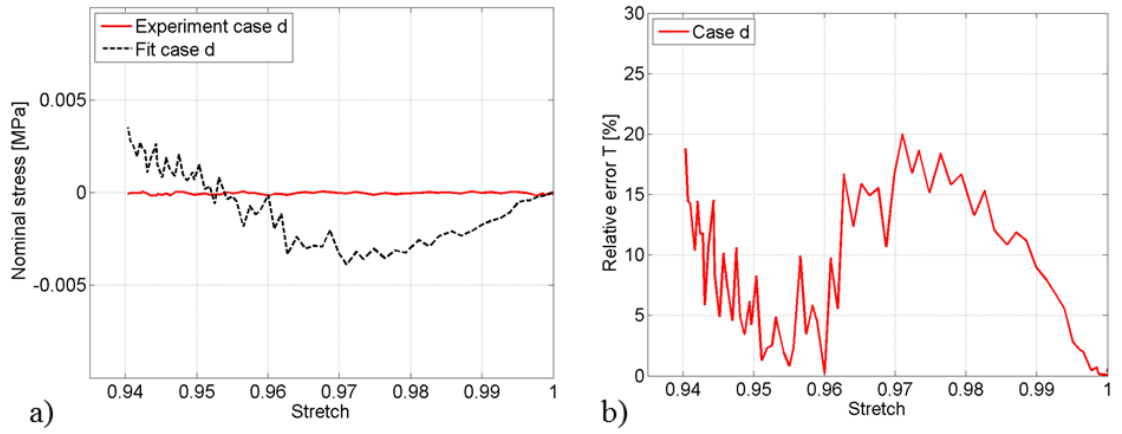

Figure 3.25: Case d for the isotropic 70 phr MRE: a) Deformation response at $T = 0$ for magnetic loading and least-squares fit. b) Relative error in the fit.

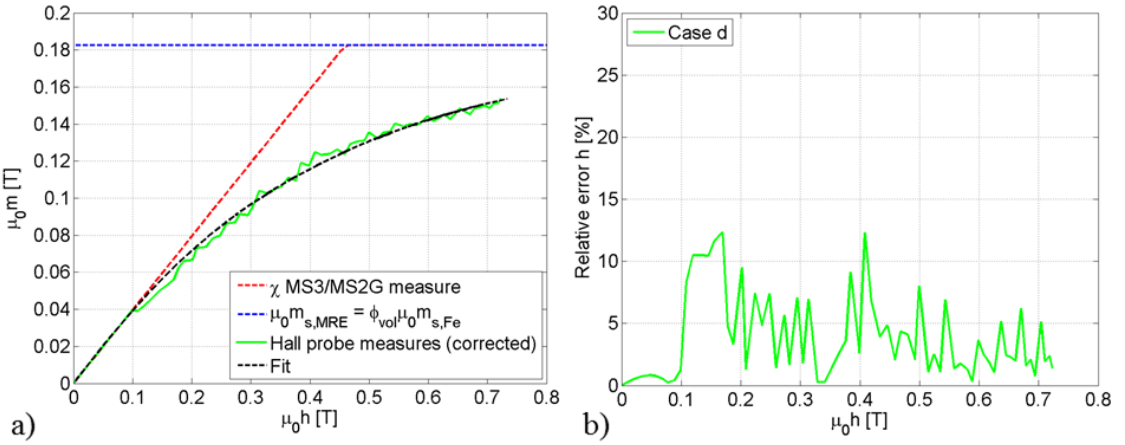

Figure 3.26: Case d for the isotropic 70 phr MRE: a) Magnetic response and least-squares fit. b) Relative error in the fit.

related to I_6, I_7 and I_9 :

$$\min_{\mathbf{p}} \sum_{ex} \left(\left\| T\left(\lambda_{ex}, \bar{\lambda}_{ex}, m_{ex}, \mathbf{p}\right) - T_{ex} \right\|_f^2 + \left\| h\left(\bar{\lambda}_{ex}, m_{ex}, \mathbf{p}\right) - h_{ex} \right\|_f^2 \right), \tag{3.53}$$

with shared material parameters:

$$\mathbf{p} = \left[\mathbf{p}_{b/c}^*, m_s, C_6, C_{6s}, C_7, C_9 \right]_f, \tag{3.54}$$

and the relative errors, respectively:

$$err_f T = \frac{\left| T\left(\lambda_{ex}, \bar{\lambda}_{ex}, m_{ex}, \mathbf{p}^*\right) - T_{ex} \right|_f}{\max\left\{T_{\lambda_{ex}=1.1}, T_{ex}\right\}_f}, \quad err_f h = \frac{\left| h\left(\bar{\lambda}_{ex}, m_{ex}, \mathbf{p}^*\right) - h_{ex} \right|_f}{\max\left\{h_{0.1\,T}, h_{ex}\right\}_f}, \tag{3.55}$$

where $T_{\lambda_{ex}=1.1}$ is the equivalent nominal stress at a stretch λ_{ex} of 1.1 from case c and $h_{0.1\,T}$ is the measured magnetic field $\mu_0 h_{ex} = 0.1\,T$. The parameter identification results are shown in Figure 3.27 and in Figure 3.28.

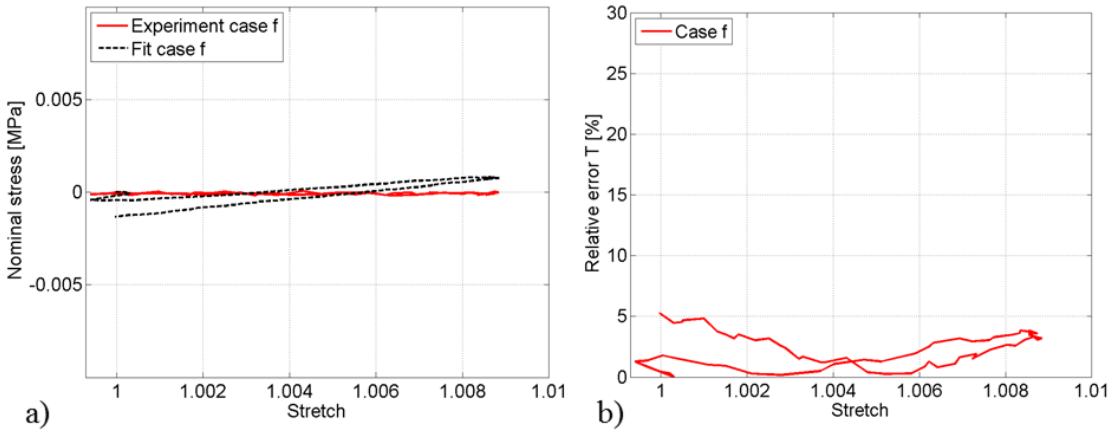

Figure 3.27: Case f for the transversely isotropic 70 phr MRE: a) Deformation response at $T = 0$ for magnetic loading and least-squares fit. b) Relative error in the fit.

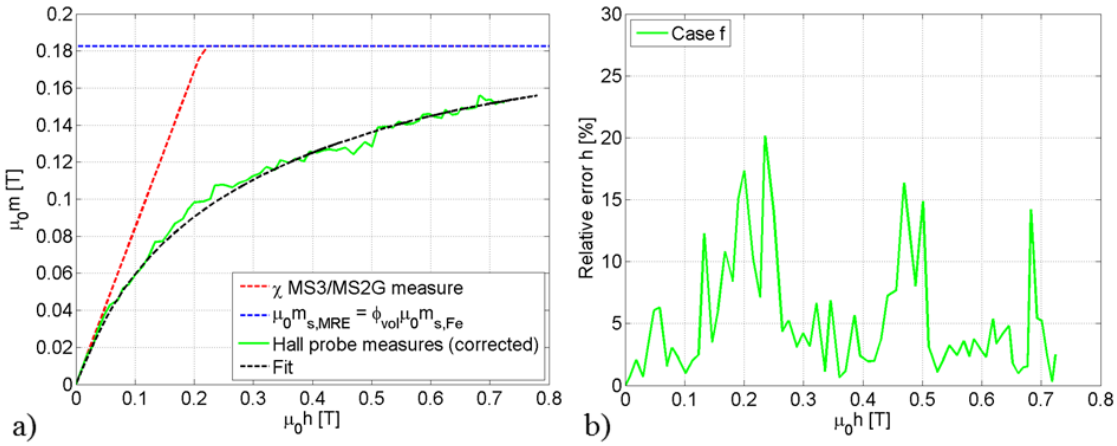

Figure 3.28: Case f for the transversely isotropic 70 phr MRE: a) Magnetic response and least-squares fit. b) Relative error in the fit.

As a first check on the obtained material parameters the predictions of the initial susceptibility are compared to the corresponding measurements in Figure 3.29 and predict the material behavior very well. The highest susceptibility can be observed in the transversely isotropic case when the particle chains are aligned with the applied magnetic field (case f) whereas the susceptibility is importantly diminished when the particle chains are aligned transverse to the applied magnetic field (case e). The initial susceptibility of the isotropic MRE (case d) material lies in between these extreme behaviors. Finally, a summary of the identified material parameters is given in Table 3.2.

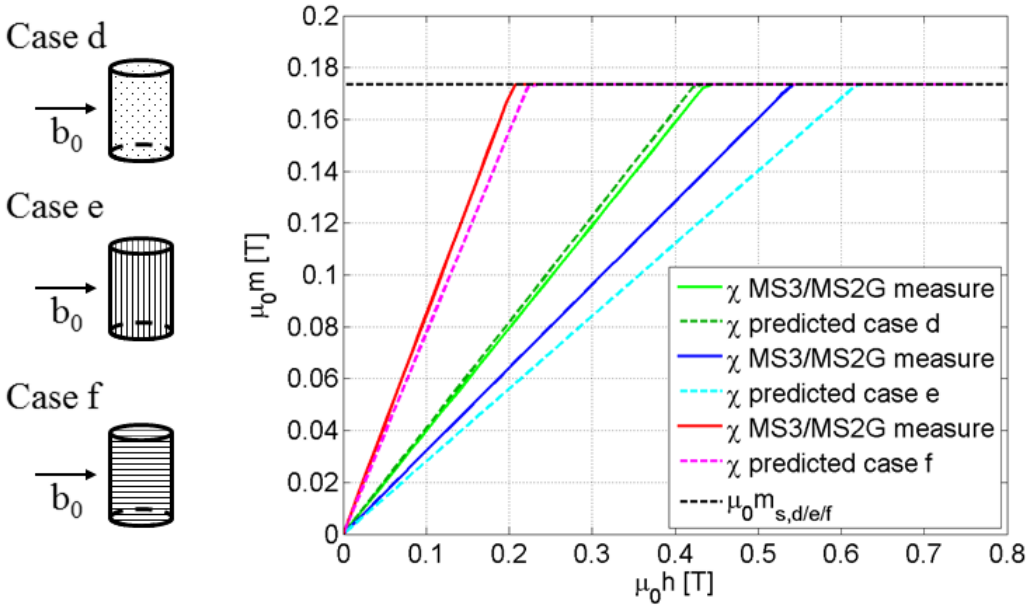

Figure 3.29: Predicted initial volume susceptibility $\chi[-]$ SI for the isotropic 70 phr MRE (case d), the transversely isotropic 70 phr MRE with chains along direction $\mathbf{e}_3$ (i.e. along the sample's axis and transverse to the applied magnetic field, case e) and the transversely isotropic 70 phr MRE with chains along direction $\mathbf{e}_1$ (i.e. transverse to the sample's axis and along the applied magnetic field, case f) compared to the corresponding measurements.

	G [Pa]	C_1	d_{11}	d_{12}	d_{13}	C_4	d_{42}	d_{43}	d_{44}
I	6.818e+04	1	1	-0.0649	0.0546	-	-	-	-
II	1.001e+05	1	1	-0.1802	0.0855	0.0014	1	-47.65	30.69

	m_s [A/m]	C_6	C_{6s}	C_7	C_9
I	1.3810e+5	1.1438	0.8456	-0.2838	-
II	1.3810e+5	0.1904	0.7909	0.6640	-0.5456

Table 3.2: Summary of the identified material parameters: isotropic 70 phr MRE (I) and transversely isotropic 70 phr MRE (II).

3.5 Conclusion

In this chapter, all aspects pertaining to the coupled magneto-mechanical characterization dedicated to the subsequent numerical implementation are presented. The general continuum framework proposed by Kankanala and Triantafyllidis for isotropic MREs [Kan04] and extended to transversely isotropic MREs by Danas and Triantafyllidis [Dan12, Dan14] is reviewed and the magneto-mechanically coupled traction as well as the magnetic field responses are developed for the material's constitutive characterization. Next, an entirely novel testing apparatus is devised to slide in place between the poles of a powerful electromagnet that allows simultaneous mechanical and magnetic field measurements using optical techniques for strain measurement and Hall probes for magnetic ones. The experimental data obtained during magneto-mechanical tensile testing is discussed and shows the complex, highly coupled phenomena that can be observed in MRE material testing. Finally, the material parameters of isotropic and transversely isotropic MREs are identified on the basis of a multi-variable functions least-squares fit.

Chapter 4

Numerical implementation

4.1 Introduction

Based on previous developments for coupled electromagnetic-mechanical processes in the books by Brown [Bro66] and Kovetz [Kov00], Kankanala and Triantafyllidis [Kan04] proposed a fully coupled variational formulation for finite strain magneto-elasticity. By minimizing the model's generalized potential energy with respect to its independent variables, one obtains the appropriate mechanical as well as magnetic governing equations and boundary/interface conditions. Since – except for some trivial geometries – analytical solutions cannot generally be derived due to strong non-linearities in the governing equations, this approach provides a powerful technique for generating finite element (FE) approximations. Hence the approach is used in Danas and Triantafyllidis [Dan14] to develop numerical solutions for two-dimensional boundary value problems (BVPs) in MREs. In the present study, this framework is extended to the axisymmetric space corresponding to the considered tactile MRE device. To achieve this, the axisymmetric problem of a simple MRE disk subjected to a spatially localized magnetic field generated by an electromagnetic coil is implemented. The numerical results are then compared to experimental data collected on the corresponding prototype (see Figure 4.1).

Therefore, in Section 4.2, the variational framework is presented and applied to solve the BVP at hand. The numerical FE implementation is developed by deriving the axisymmetric force vectors and stiffness matrices needed for a standard FEM code in Section 4.3 and the problem's geometry and boundary conditions are defined in Section 4.4. The results of the simulation then are analyzed in Section 4.5 and compared to the experimental data obtained with the corresponding prototype in Section 4.6. Finally, concluding remarks are given in Section 4.7.

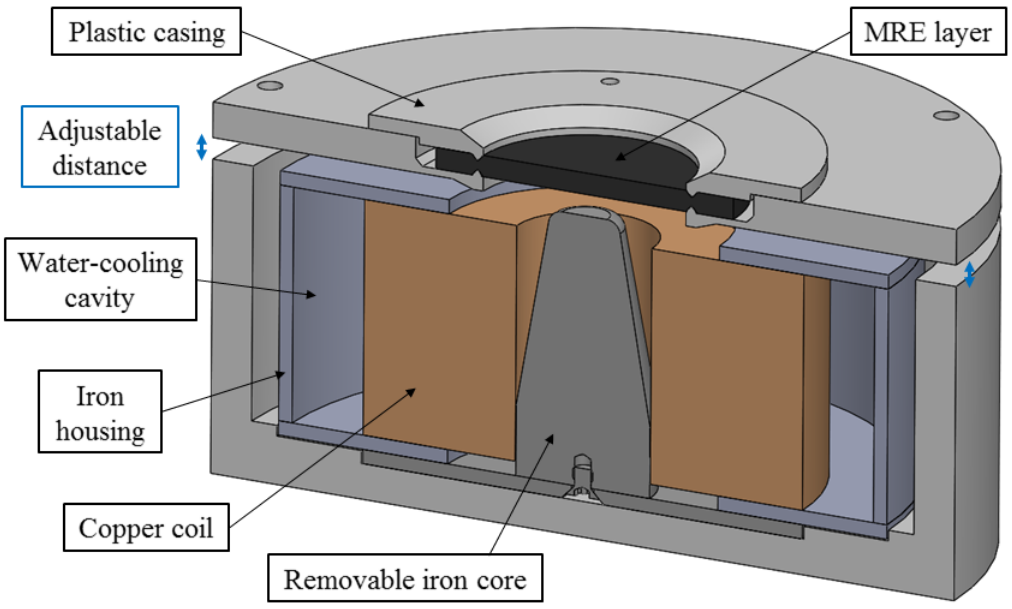

Figure 4.1: Schematic (cross-section view along a symmetry plane) of a simple MRE layer placed on top of an electromagnetic coil.

4.2 Total Lagrangian variational formulation of the fully-coupled magneto-mechanical problem

The general variational framework for magneto-elasticity is reviewed and extended to the case of non-uniform applied magnetic fields in this section. For simplicity (and without loss in generality) kinetic energy and thermal effects are ignored as in the previous chapters[1].

4.2.1 General framework for a non-uniform applied magnetic load

4.2.1.1 *Total potential energy in the current configuration*

In contrast to finite elasticity, a magneto-elastic solid not only stores energy inside the volume V it occupies but its presence also changes the magnetic field of the free space around it. The total energy $\mathcal{E}$ of the system (solid occupying V plus surrounding free space $\mathbb{R}^3$) is then defined as the sum of the solid's free energy contribution (as introduced in Chapter 3, Section 3.1) plus the magnetic energy contribution of

[1] Quasi-static approximation and fixed temperature.

the entire space:

$$\mathcal{E} = \int_V \rho\psi dv + \int_{\mathbb{R}^3} \frac{\mu_0}{2} (\mathbf{h}\cdot \mathbf{h})\, dv, \tag{4.1}$$

where ρ is the current material density, $\psi(\mathbf{F}, \mathbf{m})$ is the free energy per unit mass (free energy density) and μ_0 is the magnetic permeability in vacuum. The $\mathbf{h}$-field can be expressed in terms of the magnetic field $\mathbf{b}$ and the magnetization $\mathbf{m}$ as follows:

$$\mathbf{h} = \frac{\mathbf{b}}{\mu_0} - \mathbf{m} \tag{4.2}$$

Since the magnetic field $\mathbf{b}$ is always divergence-free ($\nabla\cdot \mathbf{b} = 0$), it can be re-expressed as the curl of some vector field. This allows to define the magnetic vector potential $\mathbf{a}$ according to:

$$\mathbf{b} = \nabla \times \mathbf{a}. \tag{4.3}$$

To find the potential energy $\mathcal{P}$ of the system, one has to subtract the contribution of the external work $\mathcal{W}$ of the applied loads from the total energy $\mathcal{E}$ stored in the system:

$$\mathcal{P} = \mathcal{E} - \mathcal{W}. \tag{4.4}$$

The external work $\mathcal{W}$ thus includes the contribution of a non-uniform, externally applied magnetic load by means of a time-independent electric current density $\mathbf{j}$ throughout the volume of a coil (see for instance Thomas and Triantafyllidis [Tho09]), as well as the contribution of the mechanical body force $\mathbf{f}$ and the applied mechanical surface traction $\mathbf{t}$:

$$\mathcal{W} = \int_V (\mathbf{j}\cdot \mathbf{a} + \rho\mathbf{f}\cdot \mathbf{u})\, dv + \int_{\partial V} \mathbf{t}\cdot \mathbf{u} da. \tag{4.5}$$

Then, the potential energy $\mathcal{P}$ of the system in the current configuration reads:

$$\begin{aligned}\mathcal{P} &= \int_V (\rho\psi - \mathbf{j}\cdot\mathbf{a} - \rho\mathbf{f}\cdot\mathbf{u})\, dv + \\ &\int_{\mathbb{R}^3} \frac{1}{2\mu_0}\left[(\mathbf{b}-\mu_0\mathbf{m})\cdot(\mathbf{b}-\mu_0\mathbf{m})\right] dv - \int_{\partial V} \mathbf{t}\cdot\mathbf{u}\, da,\end{aligned} \tag{4.6}$$

where the **h**-field has been re-written in terms of the magnetic field **b** and the magnetization **m** by use of eq.(4.2).

4.2.1.2 *Transformation of the field variables in the reference configuration*

However, a total Lagrangian formulation of this problem in the reference configuration is advantageous as the starting point for the present numerical FE algorithm. In a total Lagrangian method, all calculations at each stage of the loading history are referred to the undeformed geometry which is meshed once and for all, independently of the (often large) deformations that are induced by loading. Moreover, for the coupled magneto-mechanical problem at hand to account for Maxwell stresses, it is convenient to use a Full Lagrangian formulation. Therefore, the kinematic relations from continuum mechanics eq.(4.7) relating volume elements (dv, dV), oriented surface elements (da, dA with outward normal **n**, **N**) and oriented line elements (dl, dL with tangent vector **s**, **S**) in the current and reference configuration, respectively, are used to transform the field variables in the reference configuration:

$$dv = JdV, \quad \mathbf{n}da = J\mathbf{N}\cdot\mathbf{F}^{-1}dA, \quad \mathbf{s}dl = \mathbf{F}\cdot\mathbf{S}dL, \quad J \equiv \det\mathbf{F}. \tag{4.7}$$

This leads to the relation between the current density ρ and the reference density ρ_0 of the solid:

$$\rho = \frac{\rho_0}{J}, \tag{4.8}$$

as well as to the relation between the current and the reference electric current

density $\mathbf{j}$, $\mathbf{J}$:

$$\mathbf{j} = \frac{1}{J}\mathbf{J}\cdot\mathbf{F}^T. \tag{4.9}$$

Moreover, the current magnetic field $\mathbf{b}$ is replaced by its reference configuration counterpart, denoted $\mathbf{B}$, according to[2]:

$$\mathbf{b} = \frac{1}{J}\mathbf{F}\cdot\mathbf{B} \tag{4.10}$$

and again, since the reference magnetic field $\mathbf{B}$ is always divergence-free ($\nabla\cdot\mathbf{B} = 0$), it can be re-expressed as the curl of the reference magnetic vector potential $\mathbf{A}$ according to:

$$\mathbf{B} = \nabla\times\mathbf{A}, \tag{4.11}$$

and related to the current magnetic vector potential $\mathbf{a}$ by:

$$\mathbf{a} = \mathbf{F}^{-T}\cdot\mathbf{A} \tag{4.12}$$

Consequently, the potential energy takes the following form in the reference configuration in which all field variables are functions of $\mathbf{X}$:

$$\begin{aligned}\mathcal{P} \;=\; & \int_V (\rho_0\psi - \mathbf{J}\cdot\mathbf{A} - \rho_0\mathbf{f}\cdot\mathbf{u})\,dV + \\ & \int_{\mathbb{R}^3} \frac{J}{2\mu_0}\left[\left(\frac{1}{J}\mathbf{F}\cdot\mathbf{B} - \mu_0\mathbf{m}\right)\cdot\left(\frac{1}{J}\mathbf{F}\cdot\mathbf{B} - \mu_0\mathbf{m}\right)\right]dV - \int_{\partial V}\mathbf{T}\cdot\mathbf{u}\,dA,\end{aligned} \tag{4.13}$$

where capital $\mathbf{T}$ is the mechanical pseudo-traction on the reference boundary (current force per unit reference area). Finally, it is helpful to recall that the deformation

[2]For a detailed derivation, see for instance Appendix A in [GalPhD12].

gradient $\mathbf{F}$ can be expressed with the help of the displacement field, which will be solved later on:

$$\mathbf{F} = \mathbf{I} + \mathbf{u}\nabla. \tag{4.14}$$

4.2.1.3 *Variational principle (in the reference configuration)*

Among all admissible independent fields respecting the essential boundary conditions, the ones that satisfy the equilibrium equations also render the potential energy $\mathcal{P}$ an extremum. The principal solution is therefore obtained by considering arbitrary variations δ of the potential energy with respect to its three independent fields, namely:

$$\mathbf{q} = [\mathbf{u}, \mathbf{A}, \mathbf{m}]\,. \tag{4.15}$$

Extremizing the potential energy then implies that the first variation of $\mathcal{P}$ is equal to zero:

$$\delta\mathcal{P}\left(\mathbf{u}, \mathbf{A}, \mathbf{m}\right) = \mathcal{P}_{,\mathbf{u}}\delta\mathbf{u} + \mathcal{P}_{,\mathbf{A}}\delta\mathbf{A} + \mathcal{P}_{,\mathbf{m}}\delta\mathbf{m} = 0. \tag{4.16}$$

In the above expressions, $\mathcal{P}_{,\mathbf{q}}\delta\mathbf{q}$ denote the first Frechet derivatives of the potential energy $\mathcal{P}$ with respect to the independent variables $\mathbf{q}$. This relation, in view of eq.(4.14) and eq.(4.11), can be re-written as:

$$\delta\mathcal{P}\left(\mathbf{u}, \mathbf{A}, \mathbf{m}\right) = \mathcal{P}_{V,\mathbf{F}} : \delta\mathbf{F} + \mathcal{P}_{V,\mathbf{B}} \cdot \delta\mathbf{B} + \mathcal{P}_{V,\mathbf{m}} \cdot \delta\mathbf{m} = 0, \tag{4.17}$$

where $\mathcal{P}_{V,\mathbf{F}}$, $\mathcal{P}_{V,\mathbf{B}}$, and $\mathcal{P}_{V,\mathbf{m}}$ (notation including the volume integrals) are the first derivatives of the potential energy $\mathcal{P}$ with respect to $\mathbf{F}$, $\mathbf{B}$, and $\mathbf{m}$, respectively, and the following connections between $\delta\mathbf{F}$, $\delta\mathbf{B}$ and $\delta\mathbf{u}$, $\delta\mathbf{A}$ apply:

$$\delta\mathbf{F} = \delta\mathbf{u}\nabla, \quad \delta\mathbf{B} = \nabla \times \delta\mathbf{A} \quad . \tag{4.18}$$

It is not in the scope of this work to detail the full derivation and the results of the aforementioned variations are just given in the following[3]. The corresponding Euler-Lagrange equations are Newton's and Maxwell's equations in the reference configuration, which can be shown to coincide with their current configuration counterparts obtained independently by the direct approach. Vanishing of the variation of the potential energy with respect to the displacement field yields:

$$\mathcal{P}_{,\mathbf{u}}\delta\mathbf{u} = 0 \quad \Longrightarrow \quad \nabla\cdot\boldsymbol{\Pi} + \rho_0\mathbf{f} = \mathbf{0},\ \mathbf{X}\in V,\ \mathbf{N}\cdot[\![\boldsymbol{\Pi}]\!] = \mathbf{T},\ \mathbf{X}\in\partial V, \tag{4.19}$$

where $\boldsymbol{\Pi} = J\mathbf{F}^{-1}\cdot\boldsymbol{\sigma}$ is the total first Piola-Kirchhoff stress tensor and $\boldsymbol{\sigma}$ the total Cauchy stress tensor (both carrying magnetic and mechanical contributions). Next, vanishing of the variation of the potential energy with respect to the magnetic vector potential results in Ampère's differential equation and boundary/interface condition in the reference configuration:

$$\mathcal{P}_{,\mathbf{A}}\delta\mathbf{A} = 0 \quad \Longrightarrow \quad \nabla\times\mathbf{H} = \mathbf{J},\ \mathbf{X}\in\mathbb{R}^3,\ \mathbf{N}\times[\![\mathbf{H}]\!] = \mathbf{0},\ \mathbf{X}\in\partial V, \tag{4.20}$$

where $\mathbf{H} = \mathbf{h}\cdot\mathbf{F}$ is the magnetic field in the reference configuration. Finally, we consider the vanishing of the variation of the potential energy with respect to the magnetization $\mathbf{m}$, which gives the constitutive relation:

$$\mathcal{P}_{,\mathbf{m}}\delta\mathbf{m} = 0 \quad \Longrightarrow \quad \mu_0\mathbf{h} = \rho\frac{\partial\psi}{\partial\mathbf{m}},\ \mathbf{X}\in V. \tag{4.21}$$

To complete the formulation, reference configuration charge conservation and interface condition:

$$\nabla\cdot\mathbf{J} = 0,\ \mathbf{X}\in V, \quad \mathbf{N}\cdot[\![\mathbf{J}]\!] = 0,\ \mathbf{X}\in\partial V, \tag{4.22}$$

[3]The interested reader is referred to the articles of Kankanala, Thomas and Triantafyllidis [Kan04, Kan08, Tho09].

as well as the Coulomb gauge and interface condition:

$$\nabla\cdot \mathbf{A} = 0,\ \mathbf{X}\in V,\quad \mathbf{N}\cdot[\![\mathbf{A}]\!] = 0,\ \mathbf{X}\in \partial V, \tag{4.23}$$

are imposed separately to uniquely determine $\mathbf{J}$ and $\mathbf{A}$, respectively.

4.2.2 Framework for the prototype device simulation

For the envisaged practical application, a general magneto-mechanical element (MRE disk and iron core/housing), the specific case of a time-independent current density through a coil element as well as an air element can be deducted from the general framework and implemented for the axisymmetric case.

Magneto-mechanical bodies

The potential energy of a magneto-mechanical body occupying a volume V (MRE disk and iron core/housing) takes the following form in the reference configuration:

$$\mathcal{P}_V = \int_V \left(\rho_0\psi + \frac{J}{2\mu_0}\left\|\frac{1}{J}\mathbf{F}\cdot\mathbf{B} - \mu_0\mathbf{m}\right\|^2\right) dV, \tag{4.24}$$

where $\|A\|^2 = A_iA_i$ is the standard Euclidean norm. Note that the contribution of the mechanical surface traction $\mathbf{T}$ is dropped[4] at this point since we do not apply mechanical traction in the simulation of the haptic surface prototype. Furthermore, gravitational effects are ignored, assuming that gravity is weak compared to the magnetic forces. The MRE composites in question exhibit near incompressibility, showing almost zero volume change under load, hence a Poisson's ratio of approximately 0.5. This incompressibility constraint means that finite element codes can model these types of materials only if they have special element formulations which are able to describe this type of particular behavior. A possibility to overcome the problem is to introduce the bulk modulus $K\,[Pa]$ in the free energy density function $W = \rho_0\psi$ and set it large in comparison to the initial shear modulus: $K = 100 * G$.

[4] In the case of, mechanical loads can be directly imposed as either displacement or force boundary conditions in the FEM code.

This solves the mathematical problem in the finite element analysis[5] and leads to $J = det\mathbf{F} \approx 1$. The free energy density function W accounting for (slight) compressibility effects then reads (see Danas and Triantafyllidis [Dan14]):

$$\begin{aligned} W\left(\mathbf{F},\mathbf{m},\widehat{\mathbf{N}}\right) &= \frac{K}{2}\left(J-1\right)^2 + \frac{G}{2}\left[C_1\sum_{j=1}^{3} d_{1j}\left(J^{-\frac{2}{3}}I_1 - 3\right)^j\right] \\ &+ \frac{G}{2}\left[C_4\sum_{j=2}^{4} d_{4j}\left(J^{-\frac{2}{3}}I_4 - 1\right)^j\right] \\ &+ \frac{G}{2}\left[C_6\frac{I_6}{m_s^2} + C_{6s}\left\{\frac{1}{2}\ln\left[1-\left(\frac{I_6}{m_s^2}\right)^2\right] + \frac{I_6}{m_s^2}\tanh^{-1}\left(\frac{I_6}{m_s^2}\right)\right\}\right] \\ &+ \frac{G}{2}\left[C_7\frac{I_7}{m_s^2} + C_9\frac{I_9}{m_s^2}\right]. \end{aligned} \tag{4.25}$$

Within this framework, both an isotropic MRE disk with $\rho_0\psi = W_I\left(I_1, I_3, I_6, I_7\right)$ as well as a transversely isotropic MRE disk with $\rho_0\psi = W_{II}\left(I_1, I_3, I_4, I_6, I_7, I_9\right)$ as determined in Chapter 3[6] can be included. Rigid materials such as iron, $\rho_0\psi = W_{Iron}\left(I_1, I_3, I_6\right)$, are modeled by using a high enough shear modulus G as compared to the MRE material itself (i.e. $G_{Iron} \sim 1000\, G_{MRE}$).

Coil

The non-uniform magnetic load is introduced with the help of a time-independent current density $\mathbf{J}$ through a coil, whereas the magnetization $\mathbf{m}$ is set to zero (copper is assumed non magnetic). The potential energy can then be expressed as:

$$\mathcal{P}_V = \int_V \left(\rho_0\psi - \mathbf{J}\cdot\mathbf{A} + \frac{1}{2\mu_0 J}\left\|\mathbf{F}\cdot\mathbf{B}\right\|^2\right) dV. \tag{4.26}$$

The free energy density function $\rho_0\psi = W_{Coil}\left(I_1, I_3\right)$ is the energy density of the

[5] Note however that larger values of $K > 500 * G$ could lead to volumetric locking of the elements and in that case a hybrid (probably constant pressure) formulation needs to be used instead. Nevertheless, in the present study, the simple compressible formulation is found to be sufficiently accurate and simple to implement.

[6] Note that for the experimentally derived free energy density function W in Chapter 3 the incompressibility condition ($I_3 = J^2 = 1$) is used for analytical simplicity.

copper coil metal, set rigid, $\mathbf{F} \approx \mathbf{I}$, by a high enough shear modulus G as compared to the MRE material itself (i.e. $G_{Coil} \sim 1000\, G_{MRE}$).

Air

Finally, the potential energy for the air that guides but does not contribute to the magnetic field reads:

$$\mathcal{P}_V = \int_V \left(\rho_0 \psi + \frac{1}{2\mu_0 J} \left\| \mathbf{F} \cdot \mathbf{B} \right\|^2 \right) dV, \tag{4.27}$$

with a free energy function $\rho_0 \psi = W_{Air}\left(I_1, I_3\right) \approx 0$. To control the air mesh and to deal with the zero energy of the air respectively, a penalty type energy[7] obtained from numerical considerations is used.

4.3 Axisymmetric FEM formulation

The finite element method (FEM) is a numerical discretization technique designed to obtain approximate numerical solutions to BVPs and thus to predict the response of physical systems subjected to external loads. A structure is idealized as many small, discrete surfaces (in 2D) or volumes (in 3D) called finite elements (FE), which are connected at nodes. The global equations are obtained through a complex assembly of elements to a global model based on the elements connectivity. The initial nonlinear problem is resolved using an incremental approach via a standard Newton-Raphson procedure, as discussed below. This allows for the solution of the initial Euler-Lagrange equations using the above described weak formulations. More specifically, let $\mathbf{f}$ be a vector function, often called force vector, that is differentiable with respect to its independent variables $\mathbf{q}$, where $\mathbf{q} = [\delta\mathbf{u}, \delta\mathbf{A}, \delta\mathbf{m}]$. The variational principle leads, after a finite element discretization, to seeking the vector of unknown nodal degrees of freedom by solving a system of equations of the form:

$$\mathbf{f}\left(\mathbf{q}\right) = \mathbf{0}.$$

[7] W_{Air} is set to zero and the displacement of the air nodes is connected to the displacement of the closest material node (MRE, iron, coil).

The Newton-Raphson method, solving the variation equations involving non-linearities, is based on the first-order Taylor expansion of the global force vector about the previous iterate, set to zero:

$$\mathbf{f}^{[k+1]} \approx \mathbf{f}^{[k]} + \triangle\mathbf{q}^{[k]} \cdot \mathbf{K}^{[k]} = \mathbf{0}.$$

The correction $\triangle\mathbf{q}^{[k]}$ that defines the current approximation $\mathbf{q}^{[k+1]}$ is:

$$\triangle\mathbf{q}^{[k]} = \mathbf{q}^{[k+1]} - \mathbf{q}^{[k]},$$

where the so-called tangent stiffness matrix $\mathbf{K}^{[k]}$ at the previous iterate $\mathbf{q}^{[k]}$ is:

$$\mathbf{K}^{[k]} = \left.\frac{\partial \mathbf{f}}{\partial \mathbf{q}}\right|_{\mathbf{q}^{[k]}}.$$

The implementation of the Newton-Raphson algorithm for a nonlinear system of equations is summarized as (see for instance, Bonnet et al. [Bon14]):

1. Initialization:

(i) Choose $\mathbf{q}^{[0]} = \mathbf{0}$ and tolerance ϵ;

(ii) Compute initial force vector $\mathbf{f}^{[0]} \equiv \mathbf{f}\left(\mathbf{q}^{[0]}\right)$;

2. For $k = 0, 1, \ldots$ (Newton-Raphson increment)

(i) Compute stiffness matrix $\mathbf{K}^{[k]}$;

(ii) Update the iterate $\mathbf{q}^{[k+1]} = \mathbf{q}^{[k]} - \left(\mathbf{K}^{[k]}\right)^{-1} \cdot \mathbf{f}^{[k]}$.

(iii) Compute new force vector $\mathbf{f}^{[k+1]} = \mathbf{f}\left(\mathbf{q}^{[k+1]}\right)$;

(iiii) Convergence test: $\left\|\mathbf{f}^{[k+1]}\right\| \leq \epsilon \left\|\mathbf{f}^{[0]}\right\|$?;

If yes: STOP, $\mathbf{q} = \mathbf{q}^{[k+1]}$, next load increment.

If no, do $k = k + 1$ and return to 2(i).

In the standard Newton-Raphson method (see Figure 4.2) the stiffness matrix is re-assembled at each iteration of each load increment in the process. The computational expense for models with a large number of degrees of freedoms, and a large number of loading increments can therefore be considerable. However, in the

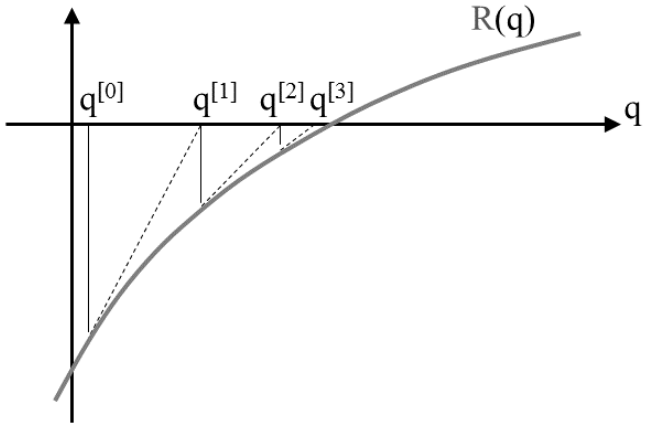

Figure 4.2: Scalar nonlinear equation $R(q)$: principle of the standard Newton-Raphson solution scheme [Bon14].

neighborhood of the solution, the Newton-Raphson method has a quadratic convergence and few correction iterations are usually required [MSC10, MSC14, Bon14]. In what follows, the numerical techniques which are implemented as user elements in the finite element program [FEAP] are described.

4.3.1 Discretized variational principle

One can discretize the magneto-elastic problem by dividing the total volume V of the system to discrete finite volume elements by:

$$V = \sum_e V_e, \tag{4.28}$$

with V_e denoting the volume of each element. The total potential energy $\mathcal{P}_V$ of the system is then the sum of the potential energies of all elements:

$$\mathcal{P}_V = \sum_e \mathcal{P}_{V_e}, \tag{4.29}$$

with $\mathcal{P}_{V_e}$ denoting the potential energy of each element. This allows for the definition

of the element force vector $\mathbf{f}_{V_e}$ conjugate to the element vector of unknowns $\delta\mathbf{q}_e$:

$$\mathbf{f}_{V_e} \equiv \left[\mathcal{P}_{V_e,\mathbf{F}}, \mathcal{P}_{V_e,\mathbf{B}}, \mathcal{P}_{V_e,\mathbf{m}}\right], \quad \delta\mathbf{q}_e = \left[\delta\mathbf{u}, \delta\mathbf{A}, \delta\mathbf{m}\right]. \tag{4.30}$$

where $\mathcal{P}_{V_e,\mathbf{F}}$, $\mathcal{P}_{V_e,\mathbf{B}}$, and $\mathcal{P}_{V_e,\mathbf{m}}$ are the first derivatives of the potential energy $\mathcal{P}_{V_e}$ with respect to $\mathbf{F}$, $\mathbf{B}$, and $\mathbf{m}$, respectively (see eq.(4.17)). Solving the problem with numerical algorithms requires also the consideration of the second derivatives of the potential energy $\mathcal{P}_{V_e}$ with respect to $\mathbf{F}$, $\mathbf{B}$, and $\mathbf{m}$. Similarly, the elementary stiffness matrix $\mathbf{K}_{V_e}$ is then defined by:

$$\mathbf{K}_{V_e} \equiv \begin{bmatrix} \mathcal{P}_{V_e,\mathbf{FF}} & \mathcal{P}_{V_e,\mathbf{FB}} & \mathcal{P}_{V_e,\mathbf{Fm}} \\ & \mathcal{P}_{V_e,\mathbf{BB}} & \mathcal{P}_{V_e,\mathbf{Bm}} \\ symm & & \mathcal{P}_{V_e,\mathbf{mm}} \end{bmatrix}. \tag{4.31}$$

Following the introduction in Section 4.3, the above definitions give the discrete equilibrium equations for each element e at Newton-Raphson increment $[k+1]$:

$$\mathbf{f}_{V_e} \cdot \delta\mathbf{q}_e + \triangle\mathbf{q}_e \cdot \mathbf{K}_{V_e} \cdot \delta\mathbf{q}_e = \mathbf{0}. \tag{4.32}$$

In what follows, we set the magnetization vector $\mathbf{m}$ constant per element. The magnetization does not need to satisfy any continuity between connecting elements, i.e. the magnetization in each element is not coupled to the magnetization in a neighboring element. The static condensation argument therefore eliminates all degrees of freedom associated with $\mathbf{m}$ [Ala08]. This is a convenient way to deal with the nodes at the interfaces between elements having a different magnetization $\mathbf{m}$. By solving eq.(4.32) for the correction of the magnetization $\triangle\mathbf{m}$:

$$\triangle\mathbf{m} = -\left(\mathcal{P}_{V_e,\mathbf{m}} + \triangle\mathbf{F} : \mathcal{P}_{V_e,\mathbf{Fm}} + \triangle\mathbf{B} \cdot \mathcal{P}_{V_e,\mathbf{Bm}}\right) \cdot \left(\mathcal{P}_{V_e,\mathbf{mm}}\right)^{-1}, \tag{4.33}$$

one easily gets the new, condensed force vector $\mathbf{f}_{V_e}$ and stiffness matrix $\mathbf{K}_{V_e}$ conjugate

to the new, condensed element vector of unknowns $\delta\mathbf{q}_e$:

$$\mathbf{f}_{V_e} = \begin{bmatrix} \mathcal{P}_{V_e,\mathbf{F}} - \mathcal{P}_{V_e,\mathbf{m}} \cdot (\mathcal{P}_{V_e,\mathbf{mm}})^{-1} \cdot \mathcal{P}_{V_e,\mathbf{mF}} \\ \mathcal{P}_{V_e,\mathbf{B}} - \mathcal{P}_{V_e,\mathbf{m}} \cdot (\mathcal{P}_{V_e,\mathbf{mm}})^{-1} \cdot \mathcal{P}_{V_e,\mathbf{mB}} \end{bmatrix}, \quad \delta\mathbf{q}_e = [\delta\mathbf{u}, \delta\mathbf{A}], \tag{4.34}$$

$$\mathbf{K}_{V_e} = \tag{4.35}$$

$$\begin{bmatrix} \mathcal{P}_{V_e,\mathbf{FF}} - \mathcal{P}_{V_e,\mathbf{Fm}} \cdot (\mathcal{P}_{V_e,\mathbf{mm}})^{-1} \cdot \mathcal{P}_{V_e,\mathbf{mF}} & \mathcal{P}_{V_e,\mathbf{FB}} - \mathcal{P}_{V_e,\mathbf{Fm}} \cdot (\mathcal{P}_{V_e,\mathbf{mm}})^{-1} \cdot \mathcal{P}_{V_e,\mathbf{mB}} \\ symm & \mathcal{P}_{V_e,\mathbf{BB}} - \mathcal{P}_{V_e,\mathbf{Bm}} \cdot (\mathcal{P}_{V_e,\mathbf{mm}})^{-1} \cdot \mathcal{P}_{V_e,\mathbf{mB}} \end{bmatrix}.$$

4.3.2 Axisymmetric space

Implementing the variational formulation for axisymmetric problems significantly simplifies the formulation. Structure and loading are assumed rotationally symmetric about the Z-direction, which implies that no field depends on the Θ coordinate and the description of the problem is reduced to the (R, Z) space (see Figure 4.3).

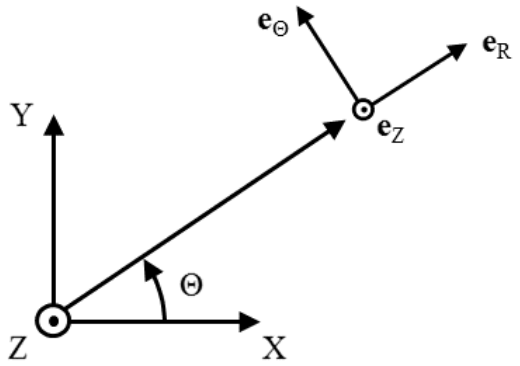

Figure 4.3: Axisymmetric space (view on a plane of constant Z): (R, Θ, Z) are reference configuration cylindrical coordinates with respective cylindrical unit vectors $\mathbf{e}_R$, $\mathbf{e}_\Theta$, and $\mathbf{e}_Z$. For the case currently of interest follows $r = R + u_R$, $\theta = \Theta$, $z = Z + u_Z$, and $\mathbf{e}_r = \mathbf{e}_R$, $\mathbf{e}_\theta = \mathbf{e}_\Theta$, $\mathbf{e}_z = \mathbf{e}_Z$, whereas (r, θ, z) are current configuration cylindrical coordinates with respective cylindrical unit vectors $\mathbf{e}_r$, $\mathbf{e}_\theta$, and $\mathbf{e}_z$.

The displacement field $\mathbf{u}$ at any point $\mathbf{X}(R, Z)$ for a two-dimensional mesh in the reference configuration is then:

$$\mathbf{u}(R, Z) = \begin{bmatrix} u_R(R, Z) \\ 0 \\ u_Z(R, Z) \end{bmatrix}. \tag{4.36}$$

In the axisymmetric situation, any radial displacement u_R automatically induces a constant strain in the circumferential direction $\mathbf{e}_\Theta$. Therefore, the deformation gradient expressed in cylindrical coordinates in the case of axisymmetric deformation can be written in matrix form as:

$$\mathbf{F} = \mathbf{I} + \mathbf{u}\boldsymbol{\nabla} = \begin{bmatrix} 1 + \dfrac{\partial u_R}{\partial R} & 0 & \dfrac{\partial u_R}{\partial Z} \\ 0 & 1 + \dfrac{u_R}{R} & 0 \\ \dfrac{\partial u_Z}{\partial R} & 0 & 1 + \dfrac{\partial u_Z}{\partial Z} \end{bmatrix}. \tag{4.37}$$

Recalling the definition of the magnetic induction with the help of the magnetic vector potential according to $\mathbf{B} = \nabla \times \mathbf{A}$, only the azimuthal component of $\mathbf{A} = [0, A_\Theta, 0]$ is left non-zero. From this definition, the magnetic induction $\mathbf{B}$ in cylindrical coordinates becomes:

$$\mathbf{B}(R, Z) = \begin{bmatrix} B_R \\ 0 \\ B_Z \end{bmatrix} = \begin{bmatrix} -\dfrac{\partial A_\Theta}{\partial Z} \\ 0 \\ \dfrac{1}{R}\dfrac{\partial (R\, A_\Theta)}{\partial R} \end{bmatrix} = \begin{bmatrix} -\dfrac{\partial A_\Theta}{\partial Z} \\ 0 \\ \dfrac{A_\Theta}{R} + \dfrac{\partial A_\Theta}{\partial R} \end{bmatrix}. \tag{4.38}$$

As a consequence, the problem's independent variables reduce to three (after static condensation of the magnetization variables m_R and m_Z as discussed earlier in this

chapter) and the new element vector of unknowns $\delta\mathbf{q}_e$ is readily given by:

$$\delta\mathbf{q}_e = [\delta u_R, \delta u_Z, \delta A_\Theta]\,. \tag{4.39}$$

In the framework of the coil element, again only the azimuthal component of the driving electric current density[8] $\mathbf{J} = [0, J_\Theta, 0]$ is non-zero:

$$J_\Theta = \frac{I_0}{h\,\ln\left(\dfrac{d_e}{d_i}\right) R}, \tag{4.40}$$

where I_0 is the total applied current, h, d_e and d_i are the coil's height (along $\mathbf{e}_Z$), outer diameter and inner diameter (along $\mathbf{e}_R$), respectively. The total applied current (magnitude) I_0 is the load parameter for the incremental Newton-Raphson procedure.

With this formulation in place, it is straightforward to show that the separately imposed charge conservation (eq.4.22) as well as the Coulomb gauge condition (eq.4.23) and the associated interface conditions in the reference configuration are satisfied as a result of axisymmetry, that is:

$$\nabla\cdot\mathbf{J} = 0,\ \mathbf{X}\in V,\quad \mathbf{N}\cdot[\![\mathbf{J}]\!] = 0,\ \mathbf{X}\in\partial V,$$

and:

$$\nabla\cdot\mathbf{A} = 0,\ \mathbf{X}\in V,\quad \mathbf{N}\cdot[\![\mathbf{A}]\!] = 0,\ \mathbf{X}\in\partial V.$$

4.3.3 FEM implementation

Shape functions and their derivatives

The flexibility in treating arbitrary geometrical configurations and loadings is achieved by representing the analysis domain as a collection of isoparametric elements of

[8] The reference field is equal to the current counterpart, since the coil is assumed rigid and does not deform.

simple shape on each of which the unknown fields[9] are approximated by means of polynomial shape functions. The displacement and the displacement gradient approximation (as well as the corresponding variations δ) in terms of the shape function matrix $\boldsymbol{\mathcal{S}}_{\mathbf{u}}$, the derivative matrix $\boldsymbol{\mathcal{D}}_{\mathbf{u}}$ and the nodal displacement vector $\mathbf{u}^{(N)}$ with nodes (N) are:

$$\mathbf{u} \approx \boldsymbol{\mathcal{S}}_{\mathbf{u}} \cdot \mathbf{u}^{(N)}, \quad \mathbf{u}\boldsymbol{\nabla} \approx \boldsymbol{\mathcal{D}}_{\mathbf{u}} \cdot \mathbf{u}^{(N)}, \tag{4.41}$$

$$\delta\mathbf{u} \approx \boldsymbol{\mathcal{S}}_{\mathbf{u}} \cdot \delta\mathbf{u}^{(N)}, \quad \delta\mathbf{u}\boldsymbol{\nabla} \approx \boldsymbol{\mathcal{D}}_{\mathbf{u}} \cdot \delta\mathbf{u}^{(N)}. \tag{4.42}$$

Analogically, the magnetic vector potential and the potential gradient approximation (as well as the corresponding variations δ) in terms of the shape function matrix $\boldsymbol{\mathcal{S}}_{A_\Theta}$, the derivative matrix $\boldsymbol{\mathcal{D}}_{A_\Theta}$ and the nodal magnetic vector potential $\mathbf{A}_\Theta^{(N)}$ read:

$$A_\Theta \approx \boldsymbol{\mathcal{S}}_{A_\Theta} \cdot \mathbf{A}_\Theta^{(N)}, \quad A_\Theta\boldsymbol{\nabla} \approx \boldsymbol{\mathcal{D}}_{A_\Theta} \cdot \mathbf{A}_\Theta^{(N)}, \tag{4.43}$$

$$\delta A_\Theta \approx \boldsymbol{\mathcal{S}}_{A_\Theta} \cdot \delta\mathbf{A}_\Theta^{(N)}, \quad \delta A_\Theta\boldsymbol{\nabla} \approx \boldsymbol{\mathcal{D}}_{A_\Theta} \cdot \delta\mathbf{A}_\Theta^{(N)}. \tag{4.44}$$

We will consider that the same shape functions of a four-node bi-linear quadrilateral element (with nodes $(N) = (1), (2), (3), (4)$, see Figure 4.4) will be used to interpolate all nodal unknowns:

$$\mathcal{S}^{(1)}(\xi_R, \xi_Z) = \frac{1}{4}(1 - \xi_R)(1 - \xi_Z), \tag{4.45}$$

$$\mathcal{S}^{(2)}(\xi_R, \xi_Z) = \frac{1}{4}(1 + \xi_R)(1 - \xi_Z),$$

[9] In the axisymmetric case discussed here, all the independent variables, the non zero displacement components δu_R and δu_Z and the non-zero magnetic vector potential component δA_Θ, are continuous functions of the space variables R and Z.

$$\mathcal{S}^{(3)}\left(\xi_R,\xi_Z\right)=\frac{1}{4}\left(1+\xi_R\right)\left(1+\xi_Z\right),$$

$$\mathcal{S}^{(4)}\left(\xi_R,\xi_Z\right)=\frac{1}{4}\left(1-\xi_R\right)\left(1+\xi_Z\right),$$

just as their derivatives with respect to the isoparametric coordinates (ξ_R,ξ_Z):

$$\mathcal{D}^{(1)}_{\xi_R}=\frac{\partial\mathcal{S}^{(1)}}{\partial\xi_R}=-\frac{1}{4}\left(1-\xi_Z\right),\quad \mathcal{D}^{(1)}_{\xi_Z}=\frac{\partial\mathcal{S}^{(1)}}{\partial\xi_Z}=-\frac{1}{4}\left(1-\xi_Z\right), \tag{4.46}$$

$$\mathcal{D}^{(2)}_{\xi_R}=\frac{\partial\mathcal{S}^{(2)}}{\partial\xi_R}=\quad\frac{1}{4}\left(1-\xi_Z\right),\quad \mathcal{D}^{(2)}_{\xi_Z}=\frac{\partial\mathcal{S}^{(2)}}{\partial\xi_Z}=-\frac{1}{4}\left(1+\xi_Z\right),$$

$$\mathcal{D}^{(3)}_{\xi_R}=\frac{\partial\mathcal{S}^{(3)}}{\partial\xi_R}=\quad\frac{1}{4}\left(1+\xi_Z\right),\quad \mathcal{D}^{(3)}_{\xi_Z}=\frac{\partial\mathcal{S}^{(3)}}{\partial\xi_Z}=\quad\frac{1}{4}\left(1+\xi_Z\right),$$

$$\mathcal{D}^{(4)}_{\xi_R}=\frac{\partial\mathcal{S}^{(4)}}{\partial\xi_R}=-\frac{1}{4}\left(1+\xi_Z\right),\quad \mathcal{D}^{(4)}_{\xi_Z}=\frac{\partial\mathcal{S}^{(4)}}{\partial\xi_Z}=\quad\frac{1}{4}\left(1-\xi_Z\right).$$

These bi-linear elements are appropriate since the potential energy involves only up to first derivatives of continuous functions of the independent variables. Furthermore, note that, by choosing quadrilateral elements, the deformation gradient does not have to be constant throughout the element.

The isoparametric mapping equations relate a point expressed in the global coordinate system (R,Z) with its local (isoparametric) coordinates (ξ_R,ξ_Z) according to:

$$R=\sum_{(N)=(1)}^{(4)}\mathcal{S}^{(N)}\left(\xi_R,\xi_Z\right)R^{(N)},\quad Z=\sum_{(N)=(1)}^{(4)}\mathcal{S}^{(N)}\left(\xi_R,\xi_Z\right)Z^{(N)}. \tag{4.47}$$

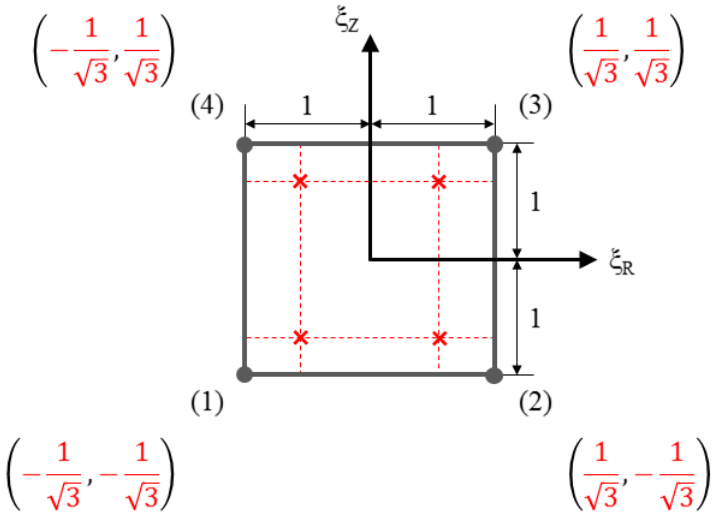

Figure 4.4: Four-node bi-linear quadrilateral element used within this study. The coordinates in red designate the positions of the integration points (IP) for the numerical integration described in Section 4.3.3.

To avoid calculating the inverse map $\xi_R(R,Z)$ and $\xi_Z(R,Z)$, one computes the derivatives of the shape functions in the domain of the parent element (R,Z) in the following way, using chain rule:

$$\begin{bmatrix} \dfrac{\partial \mathcal{S}^{(N)}(\xi_R,\xi_Z)}{\partial \xi_R} \\ \dfrac{\partial \mathcal{S}^{(i)}(\xi_R,\xi_Z)}{\partial \xi_Z} \end{bmatrix} = \underbrace{\begin{bmatrix} \dfrac{\partial R}{\partial \xi_R} & \dfrac{\partial Z}{\partial \xi_R} \\ \dfrac{\partial R}{\partial \xi_Z} & \dfrac{\partial Z}{\partial \xi_Z} \end{bmatrix}}_{\mathcal{J}} \begin{bmatrix} \dfrac{\partial \mathcal{S}^{(N)}(R,Z)}{\partial R} \\ \dfrac{\partial \mathcal{S}^{(i)}(R,Z)}{\partial Z} \end{bmatrix}, \tag{4.48}$$

and we define the local-to-global transformation $(\xi_R,\xi_Z) \rightarrow (R,Z)$ by:

$$\mathcal{J} = \begin{bmatrix} \sum\limits_{(N)=(1)}^{(4)} \dfrac{\partial \mathcal{S}^{(N)}}{\partial \xi_R} R^{(N)} & \sum\limits_{(N)=(1)}^{(4)} \dfrac{\partial \mathcal{S}^{(N)}}{\partial \xi_R} Z^{(N)} \\ \sum\limits_{(N)=(1)}^{(4)} \dfrac{\partial \mathcal{S}^{(N)}}{\partial \xi_Z} R^{(N)} & \sum\limits_{(N)=(1)}^{(4)} \dfrac{\partial \mathcal{S}^{(N)}}{\partial \xi_Z} Z^{(N)} \end{bmatrix} \equiv \begin{bmatrix} \mathcal{J}_{\xi_R R} & \mathcal{J}_{\xi_R Z} \\ \mathcal{J}_{\xi_Z R} & \mathcal{J}_{\xi_Z Z} \end{bmatrix}, \tag{4.49}$$

where $\boldsymbol{\mathcal{J}}$ is the so-called Jacobian mapping matrix[10]. As a next step one easily gets the inverse Jacobian matrix $\boldsymbol{\mathcal{J}}^{-1}$ for the inverse mapping $(R, Z) \rightarrow (\xi_R, \xi_Z)$:

$$\boldsymbol{\mathcal{J}}^{-1} = \frac{1}{\det \boldsymbol{\mathcal{J}}} \begin{bmatrix} \mathcal{J}_{\xi_Z Z} & -\mathcal{J}_{\xi_R Z} \\ -\mathcal{J}_{\xi_Z R} & \mathcal{J}_{\xi_R R} \end{bmatrix} \equiv \begin{bmatrix} \mathcal{J}_{R\xi_R} & \mathcal{J}_{Z\xi_R} \\ \mathcal{J}_{R\xi_Z} & \mathcal{J}_{Z\xi_Z} \end{bmatrix}, \tag{4.50}$$

where the determinant of the Jacobian mapping matrix $\det \boldsymbol{\mathcal{J}}$ must be positive for a valid one-to-one mapping:

$$\det \boldsymbol{\mathcal{J}} = \mathcal{J}_{\xi_R R}\mathcal{J}_{\xi_Z Z} - \mathcal{J}_{\xi_R Z}\mathcal{J}_{\xi_Z R} > 0. \tag{4.51}$$

Numerical integration

To calculate the elementary volume integrals, one also needs to map them from the global (R, Z) to the local coordinate system (ξ_R, ξ_Z). In the axisymmetric situation, the element's volume integral can be expressed as:

$$\int_{V_e} f(R, Z)\, dV = 2\pi \int_{A_e} f(R, Z)\, R dA, \tag{4.52}$$

where the (incremental) area dA is mapped to the local coordinate system with the help of the determinant of the Jacobian mapping matrix:

$$dA = dR dZ = \det \boldsymbol{\mathcal{J}}\, d\xi_R d\xi_Z. \tag{4.53}$$

Hence the mapping of the elementary volume integral finally reads:

$$\int_{V_e} f(R, Z)\, dV = 2\pi \int_{-1}^{1}\int_{-1}^{1} f(\xi_R, \xi_Z)\, R \det \boldsymbol{\mathcal{J}}\, d\xi_Z d\xi_R. \tag{4.54}$$

[10]The reader must not confuse the Jacobian mapping matrix $\boldsymbol{\mathcal{J}}$ with the scalar Jacobian of the deformation $J = \det \mathbf{F}$ and the electric current density $\mathbf{J} = [0, J_\Theta, 0]$.

A numerical 2x2 Gauss integration rule[11] is then applied with four integration points (IP) (see Figure 4.4) and with Gauss weights $W_{IP} = 1$:

$$\int_{-1}^{1}\int_{-1}^{1} f\left(\xi_R, \xi_Z\right) d\xi_R d\xi_Z \approx \sum_{IP=1}^{4} W_{IP} f_{IP} \tag{4.55}$$

Approximation of the force vector and the stiffness matrix

The formulation is now set to approximate the force vector with the help of the gradient matrix $\boldsymbol{\mathcal{G}}$ (defined next). In the special case of a coil element the magnetic loading is introduced at this point (matrix $\boldsymbol{\mathcal{S}}$ defined next) and $J_\Theta = 0$ for all other elements:

$$\mathbf{f}_{V_e} \approx \int_{V_e} \left(\boldsymbol{\mathcal{G}}^T \cdot \mathbf{f}_e - J_\Theta \boldsymbol{\mathcal{S}}^T\right) dV. \tag{4.56}$$

Similarly, the approximation of the elementary stiffness matrix[12] can be found:

$$\mathbf{K}_{V_e} \approx \int_{V_e} \boldsymbol{\mathcal{G}}^T \cdot \mathbf{K}_e \cdot \boldsymbol{\mathcal{G}} dV. \tag{4.57}$$

Evaluating the developed quantities for the numerical solution in two dimensions, the nodal unknowns $\delta\mathbf{q}_e^{(N)}$ are written as:

$$\delta\mathbf{q}_e^{(N)} \equiv \begin{bmatrix} \delta u_R^{(N)} \\ \delta u_Z^{(N)} \\ \delta A_\Theta^{(N)} \end{bmatrix}, \ (N) = (1), (2), (3), (4). \tag{4.58}$$

The gradient matrix $\boldsymbol{\mathcal{G}}$ is the essential element of the code. It relates the non-zero entries of the axisymmetric deformation gradient $\mathbf{F}$ as well as the non-zero

[11] This integration rule is exact for a product of two cubic polynomials (polynomials of degree 3) or less.

[12] For the sake of brevity here, the coefficients of $\mathbf{f}_e$ and $\mathbf{K}_e$ are given in the Appendix, Section A.2.

components of the axisymmetric magnetic field vector $\mathbf{B}$ in terms of the global unknowns $\delta\mathbf{q}_e$ to the nodal unknowns $\delta\mathbf{q}_e^{(N)}$:

$$\begin{bmatrix} F_{RR}-1 \\ F_{RZ} \\ F_{ZR} \\ F_{ZZ}-1 \\ F_{\Theta\Theta}-1 \\ B_R \\ B_Z \end{bmatrix} = \begin{bmatrix} \dfrac{\partial u_R}{\partial R} \\ \dfrac{\partial u_R}{\partial Z} \\ \dfrac{\partial u_Z}{\partial R} \\ \dfrac{\partial u_Z}{\partial Z} \\ \dfrac{u_R}{R} \\ -\dfrac{\partial A_\Theta}{\partial Z} \\ \dfrac{A_\Theta}{R}+\dfrac{\partial A_\Theta}{\partial R} \end{bmatrix} = \boldsymbol{\mathcal{G}} \cdot \begin{bmatrix} \delta\mathbf{q}_e^{(1)} \\ \delta\mathbf{q}_e^{(2)} \\ \delta\mathbf{q}_e^{(3)} \\ \delta\mathbf{q}_e^{(4)} \end{bmatrix}. \tag{4.59}$$

As an assembly of shape functions and their local derivatives the gradient matrix $\boldsymbol{\mathcal{G}}$ is then defined as:

$$\boldsymbol{\mathcal{G}} \equiv \left[\begin{array}{cccc} \boldsymbol{\mathcal{S}}\boldsymbol{\mathcal{J}}^{-1}\boldsymbol{\mathcal{D}}^{(1)} & \boldsymbol{\mathcal{S}}\boldsymbol{\mathcal{J}}^{-1}\boldsymbol{\mathcal{D}}^{(2)} & \boldsymbol{\mathcal{S}}\boldsymbol{\mathcal{J}}^{-1}\boldsymbol{\mathcal{D}}^{(3)} & \boldsymbol{\mathcal{S}}\boldsymbol{\mathcal{J}}^{-1}\boldsymbol{\mathcal{D}}^{(4)} \end{array} \right], \tag{4.60}$$

where:

$$\boldsymbol{\mathcal{S}}\boldsymbol{\mathcal{J}}^{-1}\boldsymbol{\mathcal{D}}^{(N)} = \tag{4.61}$$

$$\begin{bmatrix} \mathcal{J}_{R\xi_R}\mathcal{D}^{(N)}_{\xi_R} + \mathcal{J}_{Z\xi_R}\mathcal{D}^{(N)}_{\xi_Z} & 0 & 0 \\ \mathcal{J}_{R\xi_Z}\mathcal{D}^{(N)}_{\xi_R} + \mathcal{J}_{Z\xi_Z}\mathcal{D}^{(N)}_{\xi_Z} & 0 & 0 \\ 0 & \mathcal{J}_{R\xi_R}\mathcal{D}^{(N)}_{\xi_R} + \mathcal{J}_{Z\xi_R}\mathcal{D}^{(N)}_{\xi_Z} & 0 \\ 0 & \mathcal{J}_{R\xi_Z}\mathcal{D}^{(N)}_{\xi_R} + \mathcal{J}_{Z\xi_Z}\mathcal{D}^{(N)}_{\xi_Z} & 0 \\ \frac{\mathcal{S}^{(N)}}{R} & 0 & 0 \\ 0 & 0 & -\mathcal{J}_{R\xi_Z}\mathcal{D}^{(N)}_{\xi_R} - \mathcal{J}_{Z\xi_Z}\mathcal{D}^{(N)}_{\xi_Z} \\ 0 & 0 & \frac{\mathcal{S}^{(N)}}{R} + \mathcal{J}_{R\xi_R}\mathcal{D}^{(N)}_{\xi_R} + \mathcal{J}_{Z\xi_R}\mathcal{D}^{(N)}_{\xi_Z} \end{bmatrix},$$

for nodes $(N) = (1), (2), (3), (4)$.

Finally, the matrix $\boldsymbol{\mathcal{S}}$ in the special case of a coil element as an assembly of shape functions is defined as:

$$\boldsymbol{\mathcal{S}} \equiv \begin{bmatrix} 0 & 0 & \mathcal{S}^{(1)} & 0 & 0 & \mathcal{S}^{(2)} & 0 & 0 & \mathcal{S}^{(3)} & 0 & 0 & \mathcal{S}^{(4)} \end{bmatrix}. \tag{4.62}$$

4.4 Problem geometry/mesh, initial/boundary conditions and material parameters

In this Section, the geometry/mesh and initial/boundary conditions of the problem are defined and the appropriate material parameters are given. The considered system is implemented as an assembly of different user elements derived from the framework for non-uniform magnetic fields depending on their magnetic and mechanical properties (Section 4.2.2). The geometry definition and meshing is done with the finite element grid generator Gmsh [GMSH] and prepared for input into [FEAP] with a user-built FORTRAN code. The geometry as well as an exemplary mesh of the prototype device are shown in the following Figures, as two kind of investigations were carried out during this study, either without (Figure 4.5) or with a tapered iron core (Figure 4.6) placed at the center of the coil (height h: 33 mm, outer diameter d_e: 65 mm, inner diameter d_i: 20 mm) that is surrounded by an iron housing (see Figure 4.10). In both cases, an MRE disk (3 mm in thickness, 44 mm in diameter) is held on top of the coil at its center, either 3 mm above the upper face of the coil or 3 mm above the upper face of the iron core, when the latter is

installed.

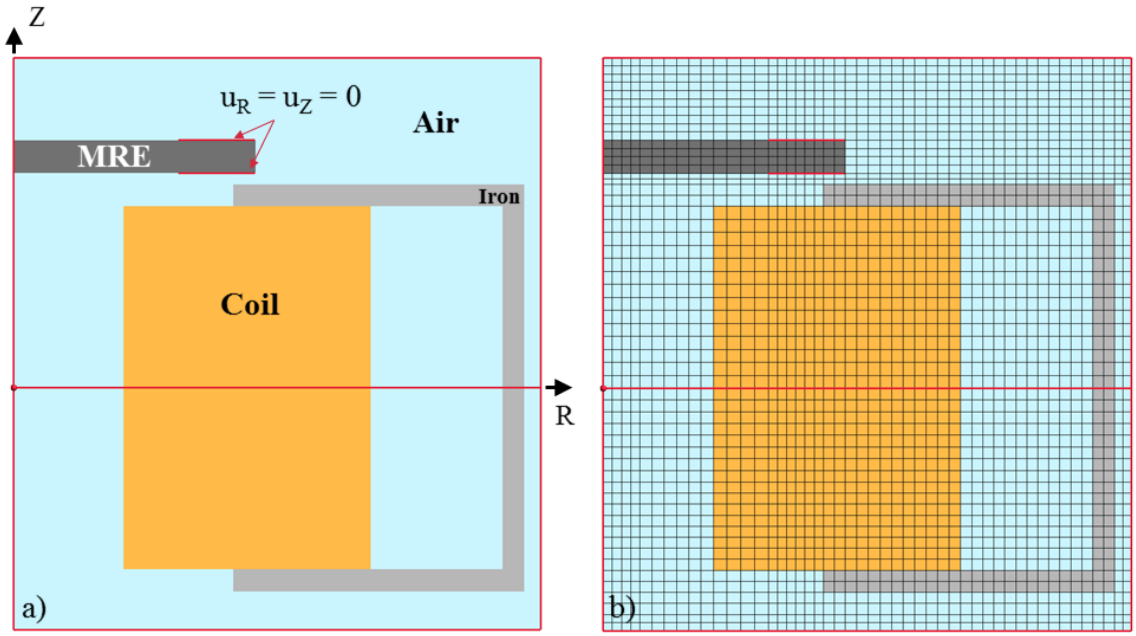

Figure 4.5: Case of a prototype device without a tapered iron core at the center of the coil. Schematic of a) the geometry and b) the finite element mesh.

To complete the implementation the initial and boundary conditions are needed. The initially unloaded problem:

$$\mathbf{u} = \mathbf{0}, \quad \mathbf{A} = \mathbf{0}\, at\, I_0 = 0, \tag{4.63}$$

is driven by the coil's total input electric current I_0. The essential boundary conditions for $\mathbf{u}$ are:

$$u_R = 0, \quad u_Z = 0, \tag{4.64}$$

at the outer top and bottom edges, where the MRE is clamped over 7 mm (see Figure 4.1, red lines on the top and bottom surface of the MRE layer in Figure 4.5 and Figure 4.6), as well as:

$$u_Z = 0\, at\, Z = 0, \tag{4.65}$$

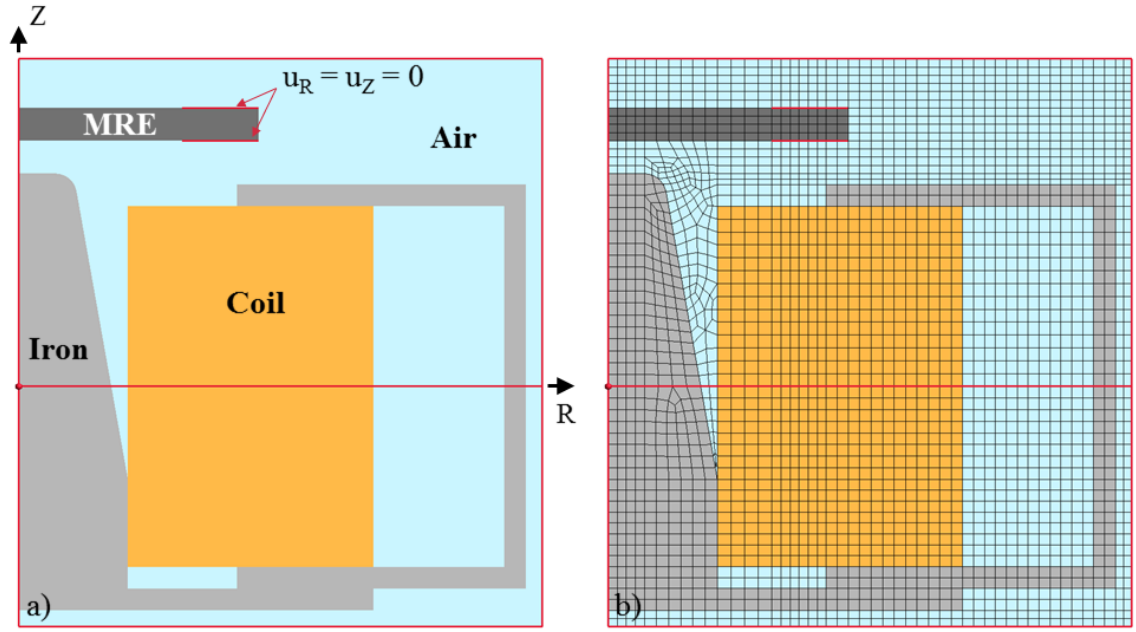

Figure 4.6: Case of a prototype device with a tapered iron core at the center of the coil. Schematic of a) the geometry and b) the finite element mesh.

to fix the system in the axisymmetric space. Furthermore, axisymmetry implies that the azimuthal component of the magnetic vector potential vanishes at the axis of rotational symmetry:

$$A_\Theta = 0 \; at \; R = 0. \tag{4.66}$$

Additionally, the magnetic field decays to zero at infinity which is implemented by applying $A_\Theta = 0$ at the outer edges of the system[13]:

$$A_\Theta \to 0 \; as \; R^2 + Z^2 \to \infty. \tag{4.67}$$

Finally, the material parameters for the elements in use have to be defined. The parameters for both isotropic (I) and transversely isotropic (II) MRE elements are

[13] Since the magnetic flux is kept by the surrounding iron casing inside the region of interest shown in Figure 4.5 and Figure 4.6, only a small region of meshed air next to the iron material – expanded by a coarser meshed air region on the lower and upper face of the coil in the case without iron core and on the upper face of the coil in the case with iron core – proved to be sufficient to let the magnetic field decay to zero.

extracted from the material characterization carried out in Chapter 3 and are summarized in Table 4.1a, whereas $K = 100 * G$, respectively. Furthermore, the parameters of the iron and coil elements are summarized in Table 4.1b, whereas $K = 10 * G$ and all other material parameters not displayed are set to zero, respectively. For the air elements, the energy is set to zero and the displacement of the air nodes is connected to the displacement of the closest material node (MRE, iron, coil).

a)	G [Pa]	C_1	d_{11}	d_{12}	d_{13}	C_4	d_{42}	d_{43}	d_{44}
I	6.818e+04	1	1	-0.0649	0.0546	-	-	-	-
II	1.001e+05	1	1	-0.1802	0.0855	0.0014	1	-47.65	30.69

	m_s [A/m]	C_6	C_{6s}	C_7	C_9
I	1.3810e+5	1.1438	0.8456	-0.2838	-
II	1.3810e+5	0.1904	0.7909	0.6640	-0.5456

b)	K [Pa]	G [Pa]	C_1	d_{11}	m_s [A/m]	C_6	C_{6s}
Iron	1e+10	1e+9	1	1	1.4516e+5	1.2415	1.1119
Coil	1e+10	1e+9	1	1	-	-	-

Table 4.1: Summary of the material parameters used for the FEM simulations: a) isotropic 70 phr MRE (I) and transversely isotropic 70 phr MRE (II). b) Iron core and housing (Iron), and copper coil (Coil).

4.5 Simulation results

In this section, the axisymmetric simulation results of the response of the isotropic 70 phr MRE disk subjected to the spatially localized magnetic field of a copper coil – either without or with an iron core installed at its center – are presented. The line and field plots are achieved with the analysis and visualization application [PARAVIEW]. Two problems nevertheless remain:

1. The model is appropriate to represent the behavior of the MRE material, but cannot deal yet with the extreme magnetic response of the iron material: the steep slope of the susceptibility that, at low values of the magnetic field, rapidly turns into saturation causes the Newton-Raphson scheme to collapse. As a first solution, the value of the initial susceptibility is reduced and the lower resulting fields are compensated by applying an unrealistic high input

current.

2. The complex geometry of the problem causes the air mesh to collapse, when the MRE material moves. Since the energy of the air elements is set to zero with the help of a penalty function, their displacement is connected to the displacement of the nearest material element. The air nodes next to the deforming MRE material move with the same amount and crash into the air elements ($\det \boldsymbol{\mathcal{J}} < 0$) that are fixed with the rigid environment (copper coil, iron core). Therefore, the maximum possible displacement of the MRE disk is linked to the element size: the finer the mesh, the less the MRE disk is allowed to move. A fine mesh however is needed to accurately model the distribution of the magnetic field, a vicious circle.

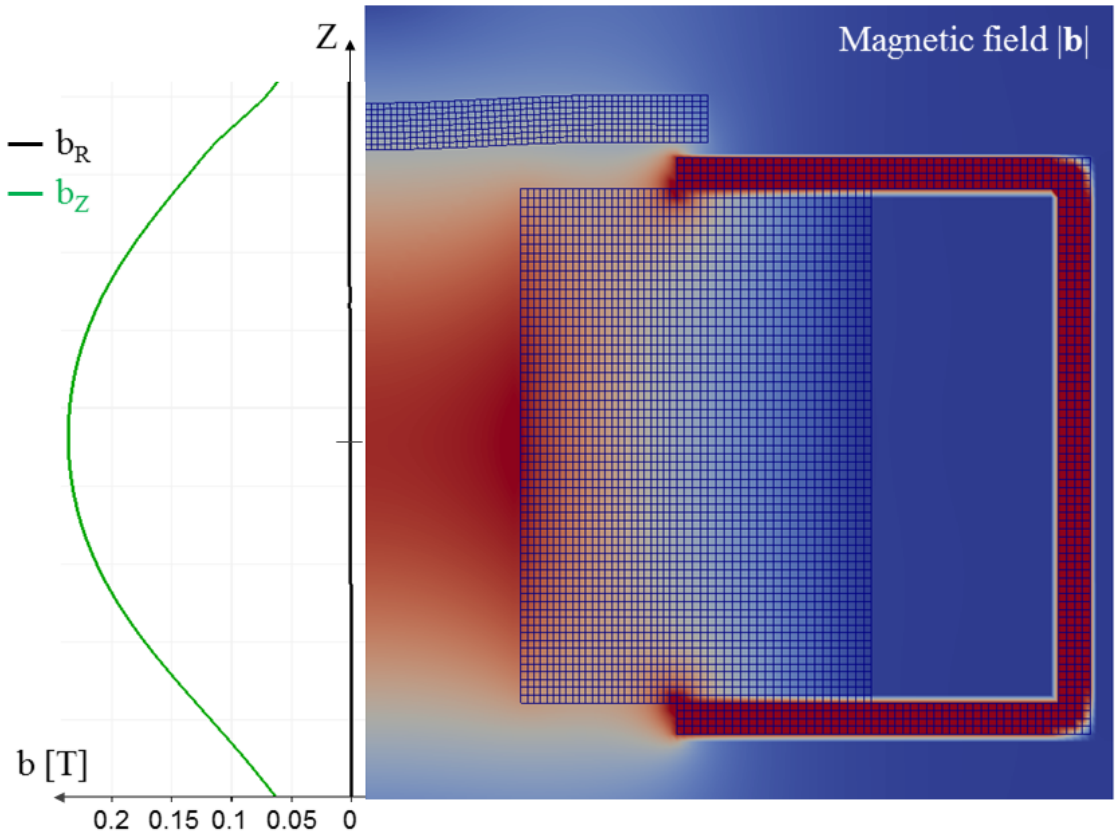

Figure 4.7: Case without iron core: magnetic field components b_z and b_R as a function of the vertical symmetry axis Z of the system (on the left). Distribution of the magnitude of the magnetic field $\mathbf{b}$ in the region of interest (on the right).

Case without iron core

In Figure 4.7, the magnetic field components b_z and b_R are plotted as a function of the vertical symmetry axis Z of the system and the distribution of the magnetic field $\mathbf{b}$ is shown in the region of interest for the case without the iron core. The simulation represents very well the externally applied magnetic field of the coil. The Z-component of the applied field is highest at the center of the coil and diminishes approaching the top and bottom faces. On the Z-axis, the radial component of the magnetic field b_R vanishes, as predicted by theory. The magnetic field is further guided by the surrounding iron casing wherein the magnetic field reaches the maximum values. The presence of the MRE disk only slightly enhances the magnetic field due to its low susceptibility.

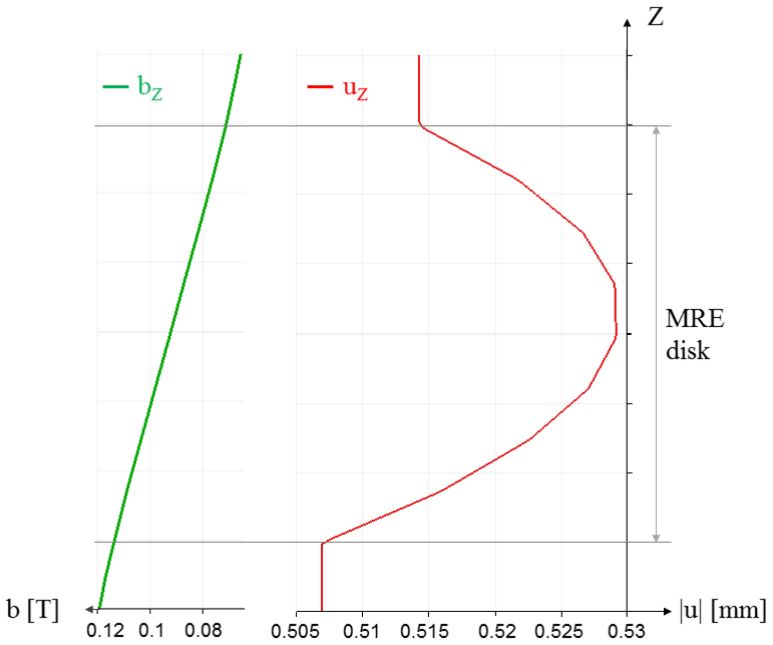

Figure 4.8: Case without iron core: magnetic field component b_z (on the left) and displacement component u_Z (on the right) as a function of the vertical symmetry axis Z of the system in the region where the MRE disk is placed.

However, the mechanically soft MRE disk – fixed at the outer edges – is attracted by the field gradient towards the center of the coil. In Figure 4.8, the magnetic field component b_z and the displacement component u_Z are plotted as a function of the vertical symmetry axis Z of the system in the region where the MRE disk is placed. For an input current intensity $I_0 = 80 * 20\ A$, corresponding to a magnetic field of 237 mT at the center of the coil, the maximum displacement $u_Z = 0.53\ mm$ of the

MRE disk is reached before the mesh collapses in this configuration. It is interesting that the MRE disk thereby slightly gets compressed upon the action of the gradient field.

Case with iron core

In Figure 4.9, the magnetic field components b_z and b_R are plotted as a function of the vertical symmetry axis Z of the system and the distribution of the magnetic field $\mathbf{b}$ is shown in the region of interest for the case with the iron core. The latter greatly enhances the magnetic flux throughout the system's magnetic circuit and directs the magnetic field towards the center of the MRE disk. Thus, a 7.5× lower input current is needed ($I_0 = 10.625 * 20\ A$, corresponding to to a magnetic field of 187 mT at the top of the iron core on the symmetry axis Z) to provoke the same displacements towards the center of the coil as observed in the case without the iron core.

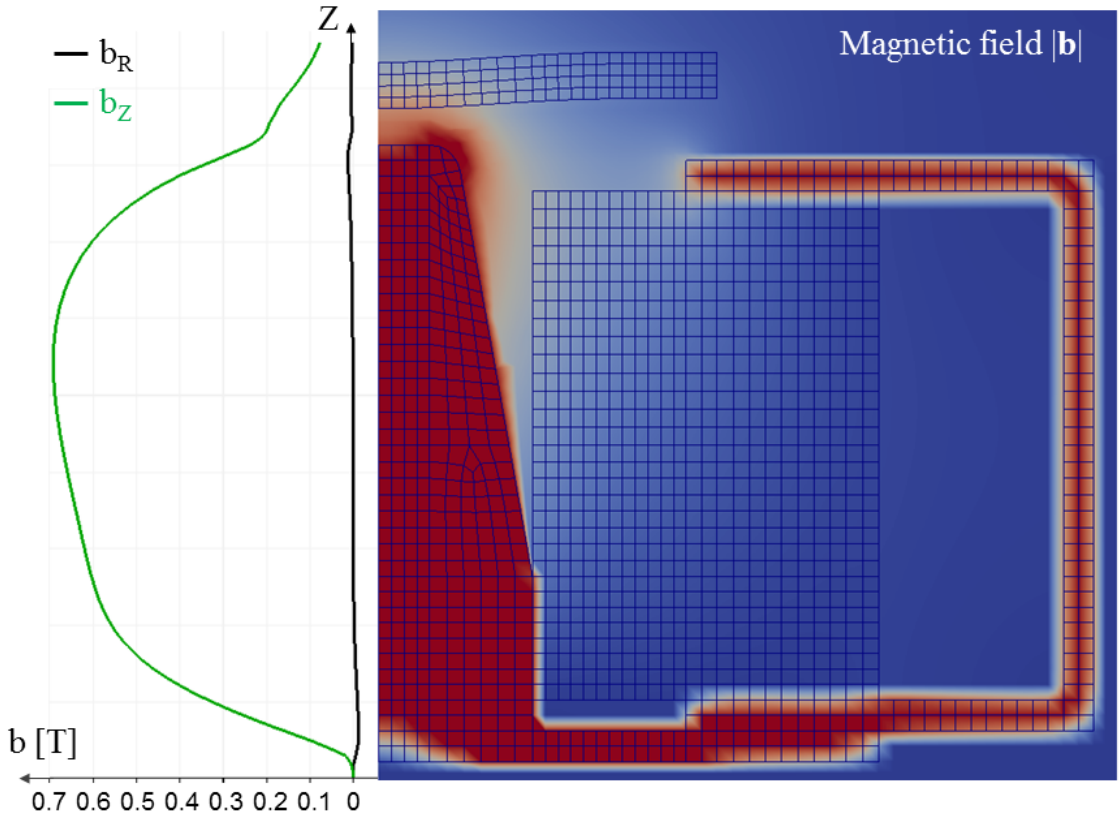

Figure 4.9: Case with iron core: magnetic field components b_z and b_R as a function of the vertical symmetry axis Z of the system (on the left). Distribution of the magnitude of the magnetic field $\mathbf{b}$ in the region of interest (on the right).

The case of transversely isotropic MREs with particle chains aligned in the plane of the disk is not an axisymmetric configuration, whereas numerical issues still prevent the case of transversely isotropic MREs with particle chains aligned along the thickness of the disk, i.e along direction Z, to converge.

4.6 Experimental validation

In this section, the haptic interface prototype (see Figure 4.1) that serves both as a proof of concept for the corresponding MRE application and as a benchmark for the validation of the axisymmetric simulations performed in the previous section is described.

4.6.1 Haptic surface prototype

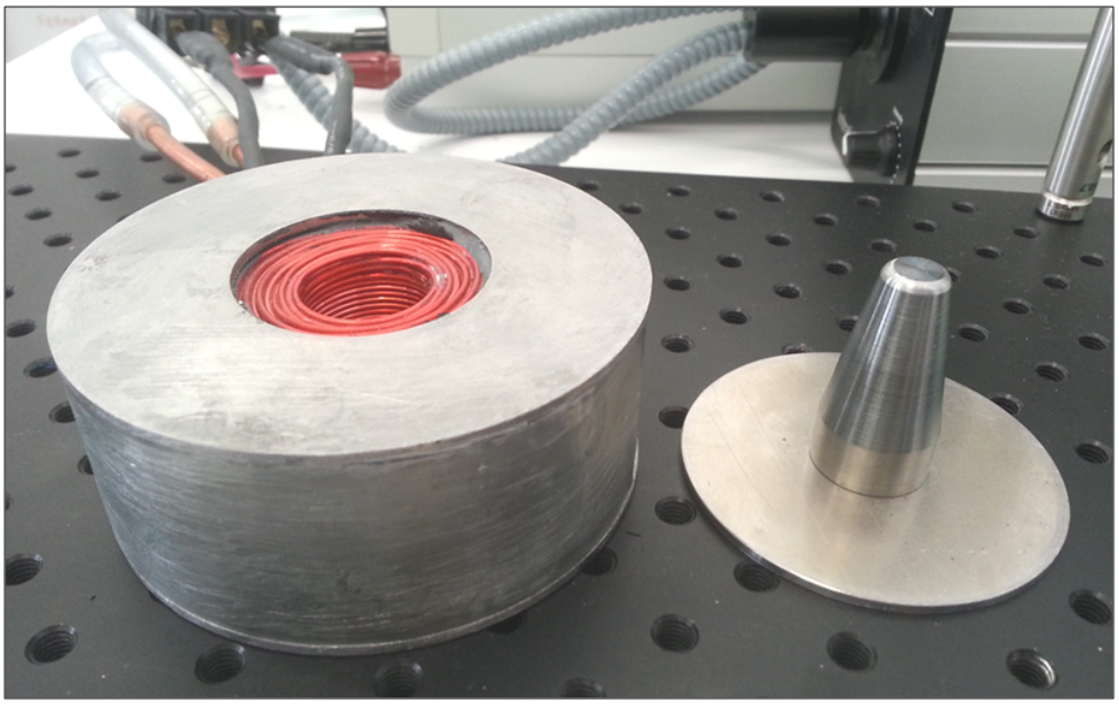

Figure 4.10: Photograph showing the coil encased in a pure iron housing (on the left) and the iron core that can be placed at its center to enhance the generated magnetic field (on the right).

Magnetic coil

The magnetic field is generated by an electromagnetic coil manufactured by the Caylar company, France. The coil itself is powered by a 20 V-20 A source. The winding is made of copper 1.2 mm in diameter and contains 360 turns. This coil is surrounded by a pure iron housing allowing extra space for water to circulate and cool down the system. Here water is supplied via a simple connection to a tap. A tapered pure iron core can be installed at the center of the coil to enhance the intensity of the magnetic field at the location where the MRE layer is to be installed. A schematic of the prototype as well as a photograph of the electromagnetic coil and its tapered pure iron core are provided in Figure 4.1 and Figure 4.10, respectively.

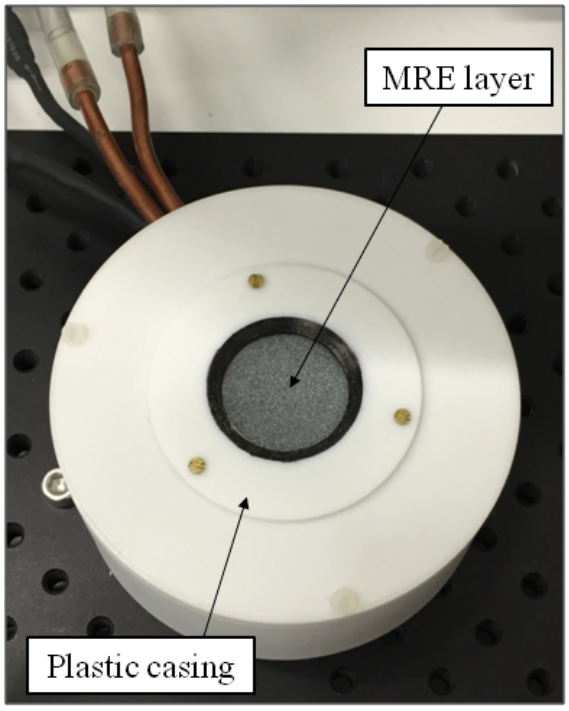

Figure 4.11: Photograph of the final prototype device showing the electromagnetic coil within an overall plastic casing and the MRE disk with applied speckle pattern installed on top of the coil at its center.

This coil is inserted in a 3D-printed plastic casing that enables to place and then clamp an MRE disk (at different height positions) on top of the coil at its center. The diameter of the disk within the clamp is then 30 mm. A photograph of the final prototype with an MRE disk installed is shown in Figure 4.11.

MRE disk

The MRE disks used within this prototype are manufactured following the technique described in Chapter 2, Section 2.3. To yield an MRE disk 3 mm in thickness and 44 mm in diameter, a mold corresponding to the negative imprint of the disk is machined out of copper and inserted between the copper heating plates. Isotropic samples are obtained by curing the samples in the absence of a magnetic field while transversely isotropic samples are obtained by curing the samples within the electromagnet described in Chapter 3, Section 3.3. Dedicated stands are used to obtain chains aligned either in the plane of the disk (so-called parallel disk) or along the thickness of the disk (so-called transverse disk).

4.6.2 Experiments

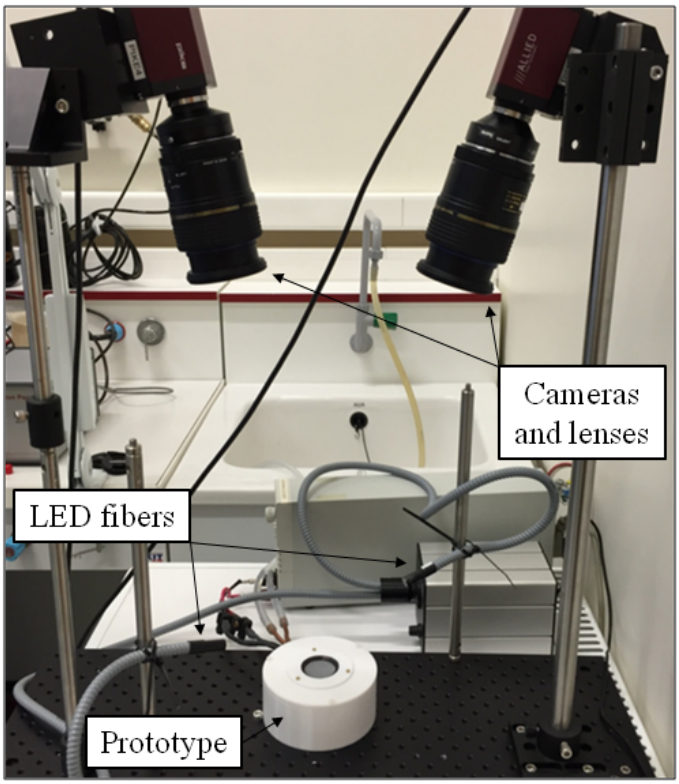

Figure 4.12: 3D-DIC experimental setup used to access the displacements of the MRE disks under increasing magnetic field generated within the prototype.

In the objective of cross-validating the numerical simulations performed earlier while studying the effect of the material microstructure on the disk's response to a

magnetic field, three types of 70 phr MRE disks are tested within the prototype: isotropic, parallel and transverse. Tests are carried out either without or with the tapered iron core placed at the center of the coil. The MRE disk is then installed so as to maintain a vertical gap of 3 mm with either the coil or the iron core, respectively. During each test, an increasing current intensity is applied to the electromagnetic coil (thus yielding an increasing magnetic field) while the deformation of the layer is monitored in-situ by 3D Digital Image Correlation (3D-DIC) using a Correlated Solutions software. When the iron core is not installed, the maximum current intensity applied to the electromagnetic coil is 20 A whereas when the iron core is installed, the maximum applied intensity is 3 A, as beyond this threshold the layers are entering in contact with the core (despite the spacer installed to elevate the disk).

Pertaining to the requirements of DIC [Sut09], a random speckle pattern is applied onto the MRE layer thanks to white spray paint (the sample itself constituting a dark background). The MRE layer is lit symmetrically at low incidence by LED optical fibers to obtain proper contrast without reflections when the surface deforms. The deforming MRE layer is then imaged by two Pike 505-B cameras equipped with Tamron lenses and installed symmetrically on both sides of the prototype so as to form an angle with its normal (see Figure 4.12). A calibration of the system with a normalized target permits the Correlated Solutions 3D-DIC software to locate the cameras in space and relate the displacements of the speckle pattern of the initially flat surface to the displacement of the layer in the three-dimensional space.

4.6.2.1 Experimental results

In Figure 4.13, the vertical position at the center of the upper surface of the disk is plotted as a function of the applied current intensity for each test case. Additionally, the vertical displacement profiles of the upper surface along the cross-section of a symmetry plane are plotted for all tested MRE disks in Figure 4.14 for the maximum current intensity applied (20 A without the iron core, 3 A with the iron core). For these curves, a null vertical position is considered when the disk is at rest with no magnetic field applied and the origin of the axis for the position along the cross-section is taken at the center of the disk.

As predicted by the FEM simulations (7.5× lower input current for same displacements, when the iron core is installed), Figure 4.13 readily shows the interest of installing the iron core in the prototype as much larger vertical displacements are

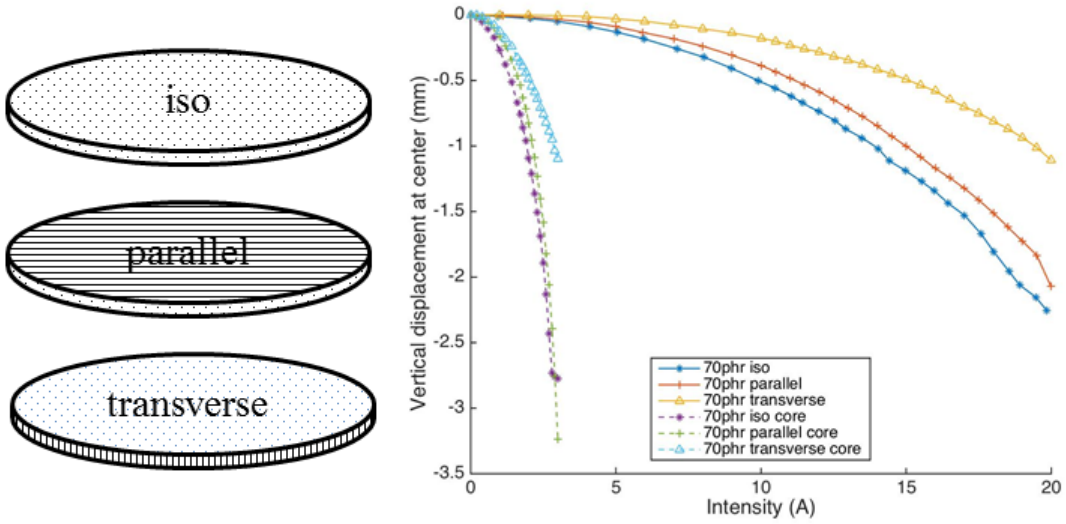

Figure 4.13: Vertical displacement at center of the disk as a function of the current intensity for all tested MRE disks.

obtained with a much lower applied current (6.67× lower input current for same displacements, 3 A compared to 20 A), hence magnetic field. This is particularly interesting for applications in which the current is supplied by batteries, e.g. mobile devices.

From Figure 4.14, it appears that the "most efficient" material for the considered haptic application is the transversely isotropic one with the chains along the thickness of the disk, i.e perpendicular to the magnetic field gradient on the symmetry axis towards the center of the coil. Indeed, it consistently exhibits larger displacements than both the other transversely isotropic material and the isotropic material for a given magnetic field/applied current. This material is then followed by the isotropic material and the transverse isotropic one with the chains along the plane of the disk, i.e. along the magnetic field gradient on the symmetry axis towards the center of the coil. These results are consistent with the material behavior observed in the magneto-mechanical experiments of Chapter 3, Section 3.4.2. As far as the transversely isotropic sample is concerned, large displacements are recorded through a structural instability. The fact that the particle chains are perpendicular to the applied field generates large local effects leading overall to large displacements and to structural instability depending on the configuration of the test. In the case of the disk, this instability is not an issue and on the contrary, it leads to the largest vertical displacements.

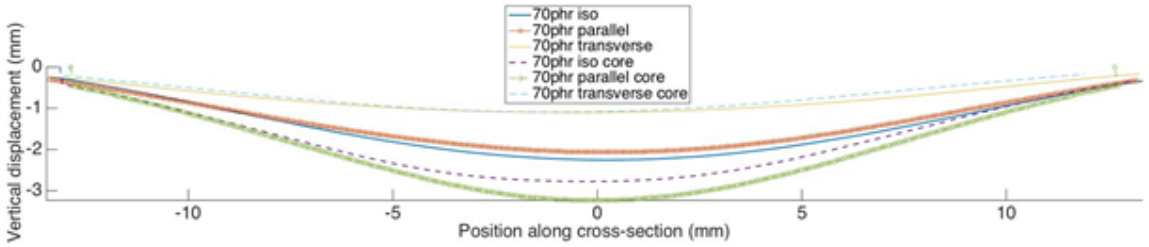

Figure 4.14: Vertical displacement profiles along the cross-section for all tested MRE disks.

The isotropic results can be further used to compare to the numerical simulations. As shown in Figure 4.15, the simulated shape of the MRE Disks follows the experimental trend. Note the local magnetic field concentration with the help of the iron core at the center of the MRE disk. The displacements of the disk tend to be strongly underestimated (by a factor 20, probably due to the coarse mesh in this case) when the iron core is installed and slightly overestimated (by a factor 2, fine mesh) when the iron core is removed.

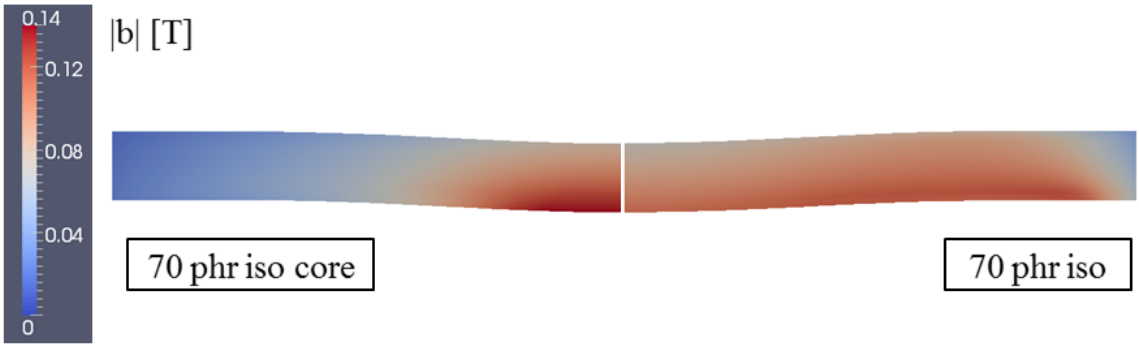

Figure 4.15: FEM simulations: distribution of the magnitude of the magnetic field $\mathbf{b}$ in the isotropic MRE Disks with (on the right) or without the iron core installed (on the left) at a displacement $u_Z = 0.53\,mm$, respectively.

4.7 Conclusion

In this chapter, all aspects pertaining to the numerical implementation of the material model to solve the boundary value problem at hand are presented. A novel formulation of the coupled magneto-mechanical variational principle for a non-uniform applied magnetic field, using displacement, magnetic vector potential and magneti-

zation as independent variables, is developed, which models the MRE disk, the iron core and housing, the copper coil and the surrounding air gaps. Next, the corresponding FEM discretization is derived in detail. Finally, some simulation results are presented and supplemented by experimental results obtained from the corresponding prototype device as a first proof of concept for a haptic interface MRE application: for a given magnetic field, the material yielding the largest displacements is the transversely isotropic one with chains perpendicular to the magnetic field. An isotropic material also gives larger displacements than a transversely isotropic material with chains along the magnetic field direction. Last but not least, it is shown that large displacements can be obtained with smaller applied currents when the field of the electromagnet is concentrated through an iron core, thus opening the possibility of designing compact haptic devices.

Chapter 5

Conclusion and future work

5.1 Conclusion

The present work pertains to a new class of active materials, namely magneto-rheological elastomers (MREs). These are composites consisting of a rubber matrix impregnated by micron-sized ferromagnetic particles. The mechanical properties of the resulting composites are altered by the application of external magnetic fields. Due to their coupled magneto-mechanical response, MREs are of great interest to engineering applications, while their novelty has opened many fundamental questions in solid mechanics. This doctoral thesis is a combined experimental and theoretical study of the macroscopic response of MREs that includes sample testing, characterization and the modeling of an MRE device. An extensive literature survey is presented in Chapter 1 before introducing the motivation of the present study, which is to characterize the behavior of MREs with a main focus on their coupled magneto-mechanical response up to large strains and under high magnetic fields. Such characterization is indeed crucial to obtain a phenomenological material model to be implemented in numerical analysis.

The thesis continues with Chapter 2 that deals with the fabrication of samples. Since sample testing occurs under combined mechanical and magnetic fields, the geometry of the sample has to ensure uniformity of both strain and magnetization. This is achieved by an entirely novel almost elliptical design attached to special, non-magnetic grips. The magnetic field uniformity is verified by full field calculations of the corresponding boundary value problem. The fabrication of samples, the influence of curing conditions and iron particle surface treatment is also discussed in Chapter 2, where combined SEM observations and mechanical testing results of different types of specimens are presented. In particular, it is shown, that a chemical particle surface treatment prior to sample fabrication improves the macroscopic mechanical behavior, in terms of stiffness by preventing debonding of the particles from the

matrix, though only above a critical stretch threshold that depends on the particles to silicone ratio. Additionally, the MRE specimens can be cured in the presence of strong magnetic fields, leading to the formation of particle chain structures and thus to an overall anisotropic composite.

The presentation continues in Chapter 3 that discusses the novel magneto-mechanical testing setup as well as the material's constitutive characterization, based on the tests results. An entirely novel testing apparatus has been built to slide in place between the poles of a powerful electromagnet that allows simultaneous mechanical and magnetic field measurements using optical techniques for strain measurement and Hall probes for magnetic ones. Stress, all three principal stretches and magnetic measures during magneto-mechanical loading allowed to get a deeper understanding of the complex phenomena inherent to these novel, nearly incompressible materials. On the one hand, purely mechanical loading tests showed the stiffening effect in field-structured MREs compared to their isotropic counterparts. Similar to what is classically observed in uni-directional fiber-reinforced composites, the investigated materials exhibited the highest mechanical stiffness in the direction of the particle alignment, though this effect mainly comes into play at higher deformations beyond a strain of 20%. On the other hand, purely magnetic loading tests showed the complex, highly magneto-mechanically coupled deformation behavior of isotropic and transversely isotropic MREs. Maxwell stresses at the solid/air interface lead to an expansion in applied magnetic field direction in the case of isotropic – maximum deformations of 12% at an externally applied uniform magnetic field of $\mathbf{b}_0 = 0.8\,T$ have been observed in this case – and field structured MREs, with particle chains aligned transverse to the applied field. However, when the magnetic field is applied along the direction of the particle chains, the particles try to keep their preferred configuration obtained during curing and only an expansion of 0.6% has been observed at an externally applied uniform magnetic field of $\mathbf{b}_0 = 0.8\,T$. Note also that in the case of field-structured MREs, with particle chains aligned perpendicular to the applied field, structural instabilities – not observed in the whole range of applied magnetic fields $\mathbf{b}_0$ in the two other cases – develop even at a low applied field of $\mathbf{b}_0 = 0.15\,T$.

A continuum description for the constitutive law that allows for finite strains and accounts for anisotropy is used to model the material at hand. Although this law in its most general form depends on 10 invariants, a reduced but still complicated version is considered in this work. Using the data of the experimental coupled char-

acterization, the material parameters of the coupled constitutive law for isotropic and transversely isotropic MREs could be successfully identified with maximum relative errors of 20%, thus suggesting that a more complex material model could be beneficial, especially in the case of transversely isotropic MREs.

Finally Chapter 4 pertains to the modeling of a prototype device that subjects the above-described MREs to a non-uniform magnetic field. The goal is to compare experimental results, i.e. the vertical displacement of an MRE disk induced by a local magnetic field, to results of the numerical (FEM) calculations of the corresponding boundary value problem which uses the experimentally produced constitutive description of the MRE disks. A novel formulation of the coupled magneto-mechanical variational principle is presented, which models the MRE disk, the iron core and housing, the coil and the surrounding air gaps, and the corresponding axisymmetric FEM discretization is derived in detail. First simulation results for isotropic MRE disks are presented and compared to experimental results from the new prototype device. Predicted by FEM, the interest of concentrating the field locally with the help of the iron core is also shown experimentally, as a much lower current input, hence magnetic field, is needed to provoke much higher deformations. Additional experimental results for transversely isotropic MRE disks are also presented and underline the importance of the materials microstructure. Indeed, the material yielding the largest displacements is the transversely isotropic one with chains perpendicular to the magnetic field.

5.2 Future work

This work covered numerous aspects regarding MREs: fabrication, experimental characterization, constitutive parameters identification and numerical modeling. It brought new answers but also uncovered difficulties specifically linked to the coupled magneto-mechanical behavior of MREs thus suggesting several avenues for future work in this domain.

The design of the sample could be further improved by using molds produced with fabrication techniques like 3D CNC machining or metallic 3D printing to obtain an actual ellipsoid in 3D. Additionally, further tests to improve the adhesion between the sample's MRE body and the plastic heads need to be done. Appropriate surface agents and different plastic materials can be evaluated when a new 3D-printer acquired arrives at the lab. This would allow magneto-mechanical tests under pre-

strains. Furthermore, concerning the fabrication of the samples dedicated to the subsequent coupled magneto-mechanical characterization with the developed setup, different MRE materials should be tested. First of all, various particle contents and their influence on the magneto-mechanical coupling shall be evaluated. Additionally, like mentioned in the general introduction, a variety of different matrix (softer and harder, as well as various material formulations) and particle materials (size and geometry, hard magnetic particles) could be tested to characterize their aptitude for the envisioned applications.

Concerning the constitutive modeling, first of all, the equations have to be further developed to allow additional checks with the obtained material parameters. Also the principal stretches could be predicted as well as the behavior for different deformation modes in the more complex cases. Obtaining extra experimental data for various deformation modes seems to be very complicated and it can be questioned if it even is possible to achieve uniform field distributions in strain and magnetization space for uniaxial compression, shear, biaxial tension, ... Additionally the testing configuration in uniaxial tension with the applied field along the longest axis of the devised sample could give interesting results but further major developments of the testing apparatus would therefore be needed. Furthermore, more complex material models – also taking into account the higher order invariants and introducing multiplicative dependencies of the free energy density function on the invariants – will further enhance the parameter identification especially in the context of transversely isotropic MREs. In a more distant perspective, the time-dependent material behavior (and thus relaxation, creep, stress recovery and fatigue experiments) as well as the temperature-dependent behavior (and thus the integration of heating/cooling systems into the testing apparatus) will also be important extensions for the existing model.

Next, the magnetic measurements need to be more precise to obtain enhanced results on the coupled magneto-mechanical response and magnetic hysteresis phenomena beyond the quasi-static responses observed in this study. The Hall probe system could be updated with further electronics and design developments. The Hall probes installed can only measure the magnetic quantities at rest and must be corrected when the sample deforms. A perspective would be to mount these probes on automated stages controlled in real-time according to the change in section of the sample that is followed by in-situ video extensometry. An alternative way to measure the internal $\mathbf{h}$-field and the samples magnetization $\mathbf{m}$ during deformation

without displacing the Hall probes is possible with an analytical solution (but could not yet be brought to an end up to now): more specifically, the distances between the probes and the sample change but because these distances are measured in-situ and there exists an analytical solution for the decay of the magnetic fields away from an elliptical sample, one could more properly correct the measured fields to obtain the magneto-mechanically coupled response within the deforming sample. As an alternative approach, measurements of the change of the magnetic flux throughout the cross-section of a measurement-coil when an MRE sample is present or not (working principle of a susceptibilimeter) proved to give precise results and could be extended to measure the (initial) susceptibility of the deforming MRE material.

Concerning the FEM simulations of the axisymmetric BVP at hand, further developments of the code are needed to analyze isotropic and transversely isotropic materials and to appropriately capture the behavior of the iron material (probably with a Langevin model, [GalPhD12]). By providing manual or automatic facilities to reconstruct the mesh when the original one becomes highly distorted could further improve the FE modeling of large deformation applications with complex geometries. In a broader perspective, extending this analysis to a 3D setting would prove useful to model all presented cases, which cannot be modeled with an axisymmetric model, and also would allow a simultaneous experimental-numerical approach for the MRE material parameter identification.

Regarding the development of haptic devices such as a tactile MRE interface, the prototype results show an optimal coupling in the case of the transversely isotropic MREs with the particle chains aligned perpendicular to the magnetic field, and the interest to play with the MRE microstructure to provoke local instabilities with compass effect. Furthermore, non-uniform spatially localized magnetic fields and structural instabilities – in addition to a deformable matrix material and controlled in an adequate geometrical and loading configuration – turned out to provoke high deformations at smaller applied magnetic fields.

Finally, the phenomenological/experimental approach during this study has brought new answers and new questions on the way to a better understanding of the highly coupled behavior of these novel materials. Further experiments together with the tools of homogenization theory and micro models are required in order to better explain what is actually going on inside MREs during fabrication as well as in operation. Advancing the presented concept, one comes to a conclusion that, as soon as structure engineering of MREs, similar to that of meta-materials, would

become possible, this would enable synthesis of MREs, whose magneto-deformation is pre-planned both in sign and amplitude [Sto11].

A Appendix

A.1 Derivation of the traction response

In this Section, the derivation of the traction response in Chapter 3, eq.(3.10) is detailed. Let double square brackets define the jump in the enclosed field quantity inside to the outside of the body. More specifically, $[\![f]\!] \equiv f_+ - f_-$ is the difference of the field quantity f evaluated at either side of the discontinuity surface, called jump of the field quantity, where the (+) subscript indicates the interior of the solid while the (-) subscript is used to indicate the surrounding space. Then, in the absence of surface currents, the magnetic fields must satisfy the jump conditions:

$$\mathbf{n} \cdot [\![\mathbf{b}]\!] = 0, \tag{A.1}$$

and:

$$\mathbf{n} \times [\![\mathbf{h}]\!] = \mathbf{0}, \tag{A.2}$$

where $\mathbf{n}$ is the outward normal on the discontinuity surface in the current (deformed) configuration. Since the discontinuity surface coincides with the boundary of the solid, on the material side:

$$\psi_+ = \psi, \quad \mathbf{m}_+ = \mathbf{m}, \tag{A.3}$$

whereas on the free space side:

$$\psi_- = 0, \quad \mathbf{m}_- = \mathbf{0}. \tag{A.4}$$

Using this information plus the interface conditions for the magnetic field $\mathbf{b}$ together with the macroscopic constitutive relation $\mathbf{b} = \mu_0 (\mathbf{h} + \mathbf{m})$:

$$\mathbf{n} \cdot [\![\mathbf{b}]\!] = \mathbf{n} \cdot (\mathbf{b}_+ - \mathbf{b}_-) = \mathbf{n} \cdot (\mathbf{h}_+ - \mathbf{h}_- + \mathbf{m}) \mu_0 = 0, \tag{A.5}$$

one gets the relation for the jump of the $\mathbf{h}$-field:

$$\mathbf{n} \cdot [\![\mathbf{h}]\!] = -\mathbf{m} \cdot \mathbf{n}, \tag{A.6}$$

which combined with eq.A.2 yields:

$$[\![\mathbf{h}]\!] = -\mathbf{n} (\mathbf{n} \cdot \mathbf{m}) . \tag{A.7}$$

The mechanical surface traction $\mathbf{t}$ (current mechanical force $\mathbf{f}$ per unit current area da), is obtained from the jump of the total Cauchy stress tensor $\boldsymbol{\sigma}$ by:

$$\mathbf{n} \cdot [\![\boldsymbol{\sigma}]\!] = \mathbf{t}. \tag{A.8}$$

Therefore, the jump quantities related to the contributions in the total Cauchy stress tensor, eq.(3.6), are evaluated separately. The jump quantity related to the free energy density contribution by using eq.$(A.3)_1$ and eq.$(A.4)_1$ reads:

$$\left[\!\!\left[\frac{\partial (\rho\psi)}{\partial \mathbf{F}} \cdot \mathbf{F}^T \right]\!\!\right] \cdot \mathbf{n} = \left(\frac{\partial (\rho\psi_+)}{\partial \mathbf{F}} \cdot \mathbf{F}^T - \frac{\partial (\rho\psi_-)}{\partial \mathbf{F}} \cdot \mathbf{F}^T \right) \cdot \mathbf{n} = \left(\frac{\partial (\rho\psi)}{\partial \mathbf{F}} \cdot \mathbf{F}^T \right) \cdot \mathbf{n}. \tag{A.9}$$

The jump of $\mathbf{hb}$ together with eq.(A.1) gives:

$$[\![\mathbf{hb}]\!] \cdot \mathbf{n} = \mathbf{0}. \tag{A.10}$$

Furthermore, by using eq.$(A.3)_2$ and eq.$(A.4)_2$ one obtains:

$$\mathbf{n}\cdot\left[\!\left[-\mu_0\left(\mathbf{h}\cdot\mathbf{m}\right)\mathbf{I}\right]\!\right]=-\mu_0\left(\mathbf{h}_+\cdot\mathbf{m}_+-\mathbf{h}_-\cdot\mathbf{m}_-\right)\mathbf{I}\cdot\mathbf{n}=-\mu_0\left(\mathbf{h}_+\cdot\mathbf{m}\right)\mathbf{n}. \tag{A.11}$$

Finally, with the help of eq.(A.7) one gets:

$$\mathbf{n}\cdot\left[\!\left[-\frac{\mu_0}{2}\left(\mathbf{h}\cdot\mathbf{h}\right)\mathbf{I}\right]\!\right]=-\frac{\mu_0}{2}\left(\mathbf{m}\cdot\mathbf{n}\right)^2\mathbf{n}. \tag{A.12}$$

Hence, respecting eq.(A.8) - eq.(A.12) the mechanical surface traction $\mathbf{t}$ is expressed as:

$$\mathbf{t}=\left[\frac{\partial\left(\rho\psi\right)}{\partial\mathbf{F}}\cdot\mathbf{F}^T\right]\cdot\mathbf{n}-\mu_0\left[\mathbf{h}_+\cdot\mathbf{m}+\frac{1}{2}\left(\mathbf{m}\cdot\mathbf{n}\right)^2\right]\mathbf{n}. \tag{A.13}$$

Using the first Piola-Kirchhoff stress tensor $\boldsymbol{\Pi}$ and the pseudo-traction vector $\mathbf{T}$ (current mechanical force $\mathbf{f}$ per unit reference area dA):

$$\boldsymbol{\Pi}=J\boldsymbol{\sigma}\cdot\mathbf{F}^{-T},\quad \mathbf{T}dA=\mathbf{t}da=d\mathbf{f}, \tag{A.14}$$

as well as the relation between the current density ρ and the reference density ρ_0 of the solid:

$$\rho=\frac{\rho_0}{J}, \tag{A.15}$$

and the magnetic field response eq.(3.11) expressed in terms of the reference density ρ_0:

$$\mu_0\mathbf{h}_+=\frac{1}{J}\frac{\partial\left(\rho_0\psi\right)}{\partial\mathbf{m}}, \tag{A.16}$$

the pseudo-traction vector $\mathbf{T}$ eq.(3.10) can be written as:

$$\mathbf{T} = \left\{ \frac{\partial \left(\rho_0 \psi\right)}{\partial \mathbf{F}} - \left[\frac{\partial \left(\rho_0 \psi\right)}{\partial \mathbf{m}} \cdot \mathbf{m} + \frac{\mu_0 J}{2} \left(\mathbf{m} \cdot \mathbf{n}\right)^2 \right] \mathbf{F}^{-T} \right\} \cdot \mathbf{N}, \tag{A.17}$$

where $\mathbf{N}$ is the reference counterpart of the outward normal $\mathbf{n}$ on the discontinuity surface in the current (deformed) configuration.

A.2 Coefficients of the force vector and the stiffness matrix

In this Section, the coefficients of the force vector $\mathbf{f}_e$ and the stiffness matrix $\mathbf{K}_e$ for the numerical implementation of the BVP in Chapter 4 are detailed:

$$\mathbf{f}_e = \begin{bmatrix} \mathcal{P}_{e,\mathbf{F}} - \mathcal{P}_{e,\mathbf{m}} \cdot \left(\mathcal{P}_{e,\mathbf{mm}}\right)^{-1} \cdot \mathcal{P}_{e,\mathbf{mF}} \\ \\ \mathcal{P}_{e,\mathbf{B}} - \mathcal{P}_{e,\mathbf{m}} \cdot \left(\mathcal{P}_{e,\mathbf{mm}}\right)^{-1} \cdot \mathcal{P}_{e,\mathbf{mB}} \end{bmatrix}, \tag{A.18}$$

$$\mathbf{K}_e = \tag{A.19}$$

$$\begin{bmatrix} \mathcal{P}_{e,\mathbf{FF}} - \mathcal{P}_{e,\mathbf{Fm}} \cdot \left(\mathcal{P}_{e,\mathbf{mm}}\right)^{-1} \cdot \mathcal{P}_{e,\mathbf{mF}} & \mathcal{P}_{e,\mathbf{FB}} - \mathcal{P}_{e,\mathbf{Fm}} \cdot \left(\mathcal{P}_{e,\mathbf{mm}}\right)^{-1} \cdot \mathcal{P}_{e,\mathbf{mB}} \\ \\ symm & \mathcal{P}_{e,\mathbf{BB}} - \mathcal{P}_{e,\mathbf{Bm}} \cdot \left(\mathcal{P}_{e,\mathbf{mm}}\right)^{-1} \cdot \mathcal{P}_{e,\mathbf{mB}} \end{bmatrix}.$$

Therefore, the first as well as the second order derivatives of the potential energy $\mathcal{P}_e$ of the general framework for a non-uniform applied magnetic load derived in Chapter 4, Section 4.2.1 with respect to the independent variables $\mathbf{F}$, $\mathbf{B}$, $\mathbf{m}$ are considered:

$$\mathcal{P}_e = W - \mathbf{J} \cdot \mathbf{A} + \frac{J}{2\mu_0} \left\| \frac{1}{J} \mathbf{F} \cdot \mathbf{B} - \mu_0 \mathbf{m} \right\|^2, \tag{A.20}$$

where $\|A\|^2 = A_i A_i$ is the standard Euclidean norm.

First order derivatives of the potential energy $\mathcal{P}_e$ with respect to $\mathbf{F}$, $\mathbf{B}$, $\mathbf{m}$

Using standard indicial notation in Cartesian coordinates, the first order derivative of the potential energy $\mathcal{P}_e$ with respect to the deformation gradient $\mathbf{F}$ reads:

$$\begin{aligned} \mathcal{P}_{e,\mathbf{F}} = \frac{\partial \mathcal{P}_e}{\partial F_{ij}} &= \frac{\partial W}{\partial F_{ij}} - \frac{1}{2\mu_0 J} \left\| \mathbf{F} \cdot \mathbf{B} - \mu_0 \mathbf{m} \right\|^2 F_{ji}^{-1} \\ &+ \frac{1}{\mu_0 J} \left(F_{ir} B_r - \mu_0 m_i \right) B_j, \end{aligned} \tag{A.21}$$

where use has been made of the following results (see for instance [Pet12]):

$$\frac{\partial J^{-1}}{\partial F_{ij}} = -J^{-2} \frac{\partial J}{\partial F_{ij}} = -J^{-1} F_{ji}^{-1}. \tag{A.22}$$

Next, the first order derivative of the potential energy $\mathcal{P}_e$ with respect to the reference magnetic field $\mathbf{B}$ gives:

$$\mathcal{P}_{e,\mathbf{B}} = \frac{\partial \mathcal{P}_e}{\partial B_i} = \frac{1}{\mu_0 J} \left(F_{rk} B_k - \mu_0 m_r \right) F_{ri}. \tag{A.23}$$

Furthermore, the first order derivative of the potential energy $\mathcal{P}_e$ with respect to the current magnetization $\mathbf{m}$ is:

$$\mathcal{P}_{e,\mathbf{m}} = \frac{\partial \mathcal{P}_e}{\partial m_i} = \frac{\partial W}{\partial m_i} - \frac{1}{J} \left(F_{ir} B_r - \mu_0 m_i \right). \tag{A.24}$$

Second order derivatives of the potential energy $\mathcal{P}_e$ with respect to $\mathbf{F}$, $\mathbf{B}$, $\mathbf{m}$

The second order derivatives of the potential energy $\mathcal{P}_e$ with respect to $\mathbf{F}$, $\mathbf{B}$ and $\mathbf{m}$ are evaluated by direct derivation of relations (A.21), (A.23) and (A.24), such that:

$$\begin{aligned}\mathcal{P}_{e,\mathbf{FF}} = \frac{\partial^2 \mathcal{P}_e}{\partial F_{ij} \partial F_{kl}} &= \frac{\partial^2 W}{\partial F_{ij} \partial F_{kl}} + \frac{1}{2\mu_0 J} \left\| \mathbf{F} \cdot \mathbf{B} - \mu_0 \mathbf{m} \right\|^2 \left(F^{-1}_{lk} F^{-1}_{ji} + F^{-1}_{jk} F^{-1}_{li} \right) \\ &- \frac{1}{\mu_0 J} \left(F_{ks} B_s - \mu_0 m_k \right) B_l F^{-1}_{ji} \\ &- \frac{1}{\mu_0 J} F^{-1}_{lk} \left(F_{im} B_m - \mu_0 m_i \right) B_j \\ &+ \frac{1}{\mu_0 J} \delta_{ik} B_l B_j,\end{aligned} \tag{A.25}$$

where δ_{ik} is the Kronecker delta.

$$\begin{aligned}\mathcal{P}_{e,\mathbf{FB}} = \frac{\partial^2 \mathcal{P}_e}{\partial F_{ij} \partial B_k} &= \frac{1}{\mu_0 J} \left[F_{ik} B_j + \left(F_{in} B_n - \mu_0 m_i \right) \delta_{jk} \right] \\ &- \frac{1}{\mu_0 J} \left[\left(F_{pk} F_{pr} B_r - \mu_0 m_s F_{sk} \right) F^{-1}_{ji} \right],\end{aligned} \tag{A.26}$$

$$\mathcal{P}_{e,\mathbf{Fm}} = \frac{\partial^2 \mathcal{P}_e}{\partial F_{ij} \partial m_k} = \frac{\partial^2 W}{\partial F_{ij} \partial m_k} + \frac{1}{J} \left(F_{kr} B_r - \mu_0 m_k \right) F^{-1}_{ji} - \frac{1}{J} \delta_{ik} B_j, \tag{A.27}$$

$$\mathcal{P}_{e,\mathbf{BB}} = \frac{\partial^2 \mathcal{P}_e}{\partial B_i \partial B_j} = \frac{1}{\mu_0 J} F_{ki} F_{kj}, \tag{A.28}$$

$$\mathcal{P}_{e,\mathbf{Bm}} = \frac{\partial^2 \mathcal{P}_e}{\partial B_i \partial m_j} = -\frac{1}{J} F_{ji}, \tag{A.29}$$

$$\mathcal{P}_{e,\mathbf{mm}} = \frac{\partial^2 \mathcal{P}_e}{\partial m_i \partial m_j} = \frac{\partial^2 W}{\partial m_i \partial m_j} + \frac{\mu_0}{J} \delta_{ij}. \tag{A.30}$$

First and second order derivatives of the free energy density function W with respect to $\mathbf{F}$ and $\mathbf{m}$

The above equations also need the evaluation of the first order derivatives of the free energy density function W defined in Chapter 4, eq.(4.25), with respect to $\mathbf{F}$ and $\mathbf{m}$:

$$\frac{\partial W}{\partial F_{ij}} = \sum_P \frac{\partial W}{\partial I_P} \frac{\partial I_P}{\partial F_{ij}}, \tag{A.31}$$

$$\frac{\partial W}{\partial m_i} = \sum_P \frac{\partial W}{\partial I_P} \frac{\partial I_P}{\partial m_i}, \tag{A.32}$$

with $P = 1, 3, 4, 6, 7, 9$. Using standard chain rule, the second order derivatives are similarly found to be:

$$\frac{\partial^2 W}{\partial F_{ij} \partial F_{kl}} = \sum_P \sum_Q \frac{\partial^2 W}{\partial I_P \partial I_Q} \frac{\partial I_P}{\partial F_{ij}} \frac{\partial I_Q}{\partial F_{kl}} + \sum_P \frac{\partial W}{\partial I_P} \frac{\partial^2 I_P}{\partial F_{ij} \partial F_{kl}}, \tag{A.33}$$

$$\frac{\partial^2 W}{\partial F_{ij} \partial m_k} = \sum_P \sum_Q \frac{\partial^2 W}{\partial I_P \partial I_Q} \frac{\partial I_P}{\partial F_{ij}} \frac{\partial I_Q}{\partial m_k} + \sum_P \frac{\partial W}{\partial I_P} \frac{\partial^2 I_P}{\partial F_{ij} \partial m_k}, \tag{A.34}$$

$$\frac{\partial^2 W}{\partial m_i \partial m_j} = \sum_P \sum_Q \frac{\partial^2 W}{\partial I_P \partial I_Q} \frac{\partial I_P}{\partial m_i} \frac{\partial I_Q}{\partial m_j} + \sum_P \frac{\partial W}{\partial I_P} \frac{\partial^2 I_P}{\partial m_i \partial m_j}, \tag{A.35}$$

with $P = Q = 1, 3, 4, 6, 7, 9$.

First and second order derivatives of the free energy density function W with respect to the invariants

Next, the first order derivatives of the free energy density function $W_{,P} = \partial W / \partial I_P$ with respect to the invariants in use[1] are evaluated:

[1] See Chapter 3, Section 3.2.1, and: $I_3 = J = \det \mathbf{F}$.

$$W_{,1} = \frac{G}{2} C_1 J^{-\frac{2}{3}} \left[d_{11} + 2d_{12} \left(J^{-\frac{2}{3}} I_1 - 3 \right) + 3d_{13} \left(J^{-\frac{2}{3}} I_1 - 3 \right)^2 \right], \tag{A.36}$$

$$\begin{aligned} W_{,3} &= K (J-1) \\ &- \frac{G}{3} C_1 J^{-\frac{5}{3}} I_1 \left[d_{11} + 2d_{12} \left(J^{-\frac{2}{3}} I_1 - 3 \right) + 3d_{13} \left(J^{-\frac{2}{3}} I_1 - 3 \right)^2 \right] \\ &- \frac{G}{3} C_4 J^{-\frac{5}{3}} I_4 \left[2d_{42} \left(J^{-\frac{2}{3}} I_4 - 1 \right) + 3d_{43} \left(J^{-\frac{2}{3}} I_4 - 1 \right)^2 + 4d_{44} \left(J^{-\frac{2}{3}} I_4 - 1 \right)^3 \right], \end{aligned} \tag{A.37}$$

$$W_{,4} = \frac{G}{2} C_4 J^{-\frac{2}{3}} \left[2d_{42} \left(J^{-\frac{2}{3}} I_4 - 1 \right) + 3d_{43} \left(J^{-\frac{2}{3}} I_4 - 1 \right)^2 + 4d_{44} \left(J^{-\frac{2}{3}} I_4 - 1 \right)^3 \right], \tag{A.38}$$

$$W_{,6} = \frac{G}{2m_s^2} \left[C_6 + C_{6s} \tanh^{-1} \left(\frac{I_6}{m_s^2} \right) \right], \tag{A.39}$$

$$W_{,7} = \frac{G}{2m_s^2} C_7, \quad W_{,9} = \frac{G}{2m_s^2} C_9, \tag{A.40}$$

as well as the second order derivatives of the free energy density function $W_{,PQ} = \partial^2 W / \partial I_P \partial I_Q$ with respect to the invariants in use:

$$W_{,11} = G C_1 J^{-\frac{4}{3}} \left[d_{12} + 3d_{13} \left(J^{-\frac{2}{3}} I_1 - 3 \right) \right], \tag{A.41}$$

$$
\begin{aligned}
W_{,13} &= -\frac{G}{3}C_1 J^{-\frac{5}{3}}\left[d_{11}-6d_{12}+27d_{13}\right] \\
&\quad -\frac{G}{3}C_1 J^{-\frac{5}{3}}\left[4\left(d_{12}-9d_{13}\right)J^{-\frac{2}{3}}I_1\right] \\
&\quad -\frac{G}{3}C_1 J^{-\frac{5}{3}}\left[9d_{13}J^{-\frac{4}{3}}I_1^2\right],
\end{aligned}
\tag{A.42}
$$

$$
\begin{aligned}
W_{,33} &= K \\
&+ \frac{G}{3}J^{-\frac{8}{3}}\left\{\frac{5}{3}\left[C_1\left(d_{11}-6d_{12}+27d_{13}\right)I_1+C_4\left(-2d_{42}+3d_{43}-4d_{44}\right)I_4\right]\right\} \\
&+ \frac{G}{3}J^{-\frac{8}{3}}\left\{\frac{14}{3}J^{-\frac{2}{3}}\left[C_1\left(d_{12}-9d_{13}\right)I_1^2+C_4\left(d_{42}-3d_{43}+6d_{44}\right)I_4^2\right]\right\} \\
&+ \frac{G}{3}J^{-\frac{8}{3}}\left\{9J^{-\frac{4}{3}}\left[C_1 d_{13}I_1^3+C_4\left(d_{43}-4d_{44}\right)I_4^3\right]\right\} \\
&+ \frac{G}{3}J^{-\frac{8}{3}}\left\{\frac{44}{3}J^{-2}C_4 d_{44}I_4^4\right\},
\end{aligned}
\tag{A.43}
$$

$$
\begin{aligned}
W_{,43} &= -\frac{G}{3}C_4 J^{-\frac{5}{3}}\left[2d_{42}\left(2J^{-\frac{2}{3}}I_4-1\right)\right] \\
&\quad -\frac{G}{3}C_4 J^{-\frac{5}{3}}\left[3d_{43}\left(J^{-\frac{2}{3}}I_4-1\right)\left(3J^{-\frac{2}{3}}I_4-1\right)\right] \\
&\quad -\frac{G}{3}C_4 J^{-\frac{5}{3}}\left[4d_{44}\left(J^{-\frac{2}{3}}I_4-1\right)^2\left(4J^{-\frac{2}{3}}I_4-1\right)\right],
\end{aligned}
\tag{A.44}
$$

$$
W_{,44} = GC_4 J^{-\frac{4}{3}}\left[d_{42}+3d_{43}\left(J^{-\frac{2}{3}}I_4-1\right)+6d_{44}\left(J^{-\frac{2}{3}}I_4-1\right)^2\right], \tag{A.45}
$$

$$
W_{,66} = GC_{6s}\frac{1}{2\left(m_s^4-I_6^2\right)}. \tag{A.46}
$$

***First and second order derivatives of the invariants with respect to* $\mathbf{F}$ *and* $\mathbf{m}$**

Furthermore, we have to determine the first order derivatives of the invariants with respect to the deformation gradient $\mathbf{F}$:

$$\frac{\partial I_1}{\partial F_{ij}} = 2F_{ij}, \tag{A.47}$$

$$\frac{\partial I_3}{\partial F_{ij}} = I_3 F^{-1}_{ji}, \tag{A.48}$$

$$\frac{\partial I_4}{\partial F_{ij}} = 2\widehat{N}_j F_{ip} \widehat{N}_p, \tag{A.49}$$

$$\frac{\partial I_7}{\partial F_{ij}} = 2m_i F_{sj} m_s, \tag{A.50}$$

$$\frac{\partial I_9}{\partial F_{ij}} = 2\left(m_p F_{pq} \widehat{N}_q\right) m_i \widehat{N}_j, \tag{A.51}$$

as well as the second order derivatives of the invariants with respect to the deformation gradient $\mathbf{F}$:

$$\frac{\partial I_1}{\partial F_{ij} \partial F_{kl}} = 2\delta_{ik}\delta_{jl}, \tag{A.52}$$

$$\frac{\partial I_3}{\partial F_{ij} \partial F_{kl}} = I_3 \left(F^{-1}_{lk} F^{-1}_{ji} - F^{-1}_{jk} F^{-1}_{li}\right), \tag{A.53}$$

$$\frac{\partial I_4}{\partial F_{ij} \partial F_{kl}} = 2\delta_{ik} \widehat{N}_j \widehat{N}_l, \tag{A.54}$$

$$\frac{\partial I_7}{\partial F_{ij}\partial F_{kl}} = 2m_i\delta_{jl}m_k, \tag{A.55}$$

$$\frac{\partial I_9}{\partial F_{ij}\partial F_{kl}} = 2m_i\widehat{N}_j m_k\widehat{N}_l. \tag{A.56}$$

Then, we have to determine the first order derivatives of the invariants with respect to the magnetization $\mathbf{m}$:

$$\frac{\partial I_6}{\partial m_i} = 2m_i, \tag{A.57}$$

$$\frac{\partial I_7}{\partial m_i} = 2F_{iq}F_{sq}m_s, \tag{A.58}$$

$$\frac{\partial I_9}{\partial m_i} = 2\left(m_p F_{pq}\widehat{N}_q\right)F_{ir}\widehat{N}_r. \tag{A.59}$$

as well as the second order derivatives of the invariants with respect to the magnetization $\mathbf{m}$:

$$\frac{\partial^2 I_6}{\partial m_i\partial m_j} = 2\delta_{ij}, \tag{A.60}$$

$$\frac{\partial^2 I_7}{\partial m_i\partial m_j} = 2F_{ik}F_{jk}, \tag{A.61}$$

$$\frac{\partial^2 I_9}{\partial m_i\partial m_j} = 2F_{iq}\widehat{N}_q F_{jr}\widehat{N}_r. \tag{A.62}$$

And finally, the second order derivatives of the invariants with respect to the defor-

mation gradient **F** and the magnetization **m** are found to be:

$$\frac{\partial^2 I_7}{\partial F_{ij} \partial m_k} = 2m_i F_{kj} + 2\delta_{ik} F_{sj} m_s, \tag{A.63}$$

$$\frac{\partial^2 I_9}{\partial F_{ij} \partial m_k} = 2\left[F_{kq}\widehat{N}_q m_i \widehat{N}_j + \left(m_p F_{pq}\widehat{N}_q\right)\delta_{ik}\widehat{N}_j\right]. \tag{A.64}$$

Bibliography

[ANSYS] ANSYS Inc. ANSYS R15 multiphysics, December 2013.

[Abr07] S. Abramchuk, E. Kramarenko, G. Stepanov, L.V. Nikitin, G. Filipcsei, A.R. Khokhlov, and M. Zrinyi. Novel highly elastic magnetic materials for dampers and seals: Part I. preparation and characterization of the elastic materials. *Polymers for Advanced Technologies*, 18:883–890, 2007.

[Adk59] J.E. Adkins. Symmetry relations for orthotropic and transversely isotropic materials. *Archive for Rational Mechanics and Analysis*, 4(1):193–213, 1959.

[Adk60] J.E. Adkins. Further symmetry relations for transversely isotropic materials. *Archive for Rational Mechanics and Analysis*, 5(1):263–274, 1960.

[Ala08] C.R. Alavala. *Finite element methods: basic concepts and applications.* PHI Learning, New Dehli, 2008.

[Als07] Th. Alshuth, M. Ramspeck, R.H. Schuster, B. Halbedel, and F. Zschunke. Magnetorheologische elastomere: Einfluss der partikelausrichtung auf die schaltbarkeit. *Kautschuk Gummi Kunststoffe*, (September 2007):448–455, 2007.

[Ant11] P.S. Antonel, G. Jorge, O.E. Perez, A. Butera, and A.G. Leyva. Magnetic and elastic properties of $CoFe_2O_4$-polydimethylsiloxane magnetically oriented elastomer nanocomposites. *Journal of Applied Physics*, 110(043920):1–8, 2011.

[Aus11] G. Ausanio, C.L. Hison, V. Iannotti, L. Lanotte, and L. Lanotte. Magneto-piezoresistance in elastomagnetic composites. *Journal of Applied Physics*, 110(063903):1–5, 2011.

[Aus14] G. Ausanio, V. Iannotti, E. Ricciardi, L. Lanotte, and L. Lanotte. Magneto-piezoresistance in magnetorheological elastomersfor magnetic induction gradient or position sensors. *Sensors and Actuators A*, 205:235–239, 2014.

[Bel02] C. Bellan and G. Bossis. Field dependence of viscoelastic properties of mr elastomers. *Journal of Modern Physics B*, 16(17 & 18):2447–2453, 2002.

[Ber00] J.S. Bergström and M.C. Boyce. Large strain time-dependent behavior of filled elastomers. *Mechanics of Materials*, 32(11):627–644, 2000.

[Ber12] A. Bergander, J. Lozada, T. Pössinger, and S. Roselier. EP 2504607 A2. Translatably and rotably semi-active device, 2012.

[Bic11] I. Bica. Magnetoresistor sensor with magnetorheological elastomers. *Journal of Industrial and Engineering Chemistry*, 17:83–89, 2011.

[Boc12] A. Boczkowska and S. Awietjan. *Microstructure and properties of magnetorheological elastomers*, chapter 6, pages 147–180. InTech, 2012.

[Boeh01] J. Böhm. *Der Payneeffekt: Interpretation und Anwendung in einem neuen Materialgesetz für Elastomere.* PhD thesis, University of Regensburg, 2001.

[Boes07] H. Böse. Viscoelastic properties of silicone-based magnetorheological elastomers. *Journal of Modern Physics B*, 21(29):4790–4797, 2007.

[Boes09] H. Böse and R. Röder. Magnetorheological elastomers with high variability of their mechanical properties. *Journal of Physics: Conference Series*, 149(012090):1–6, 2009.

[Boes12] H. Böse, R. Rabindranath, and J. Ehrlich. Soft magnetorheological elastomers as new actuators for valves. *Journal of Intelligent Material Systems and Structures*, 23(9):989–994, 2012.

[Bol11] C. Bolzmacher, G. Changeon, V. Plaud, S. Roselier, J. Lozada, and M. Hafez. Tactile refreshable screen based on magneto-rheological fluids for map exploration and navigation tasks. *SPIE Proceedings*, 8066, 2011.

[Bon14] M. Bonnet, A. Frangi, and C. Rey. *The Finite Element Method in Solid Mechanics.* McGraw-Hill Education, Milano, 2014.

[Bor01] L. Borcea and O. Bruno. On the magneto-elastic properties of elastomer-ferromagnet composites. *Journal of the Mechanics and Physics of Solids*, 49:2877–2919, 2001.

[Bor12] T. Borbath, S. Günther, D.Y. Borin, Th. Gundermann, and S. Odenbach. X-ray micro-tomographic analysis of magnetic field-induced

phase transitions in magnetorheological elastomers. *Smart Materials and Structures*, 21(105018):1–7, 2012.

[Bos01] G. Bossis, C. Abbo, S. Cutillas, S. Lacis, and C. Metayer. Electroactive and electrostructured elastomers. *Journal of Modern Physics B*, 15(6 & 7):564–573, 2001.

[Bro12] A.L. Browne and N.L. Johnson. US 0266417 A1. Active material based fasteners including cable ties and twist ties, 2012.

[Bro66] W.F. Brown. *Magnetoelastic Interactions*. Springer New York, 1966.

[Bus07] R. Bustamante. *Mathematical modelling of non-linear magneto- and electro-active rubber-like materials*. PhD thesis, University of Glasgow, 2007.

[Bus08] R. Bustamante, A. Dorfmann, and R.W. Ogden. On variational formulations in nonlinear magnetoelastostatics. *Mathematics and Mechanics of Solids*, 13:725–745, 2008.

[Bus10] R. Bustamante. Transversely isotropic nonlinear magneto-active elastomers. *Acta Mechanica*, 210:183–214, 2010.

[Cam10] F.C. Campbell. *Structural Composite Materials*. ASM International, 2010.

[Car00] J.D. Carlson and M.R. Jolly. MR fluid, foam and elastomer devices. *Mechatronics*, 10:555–569, 2000.

[Car01] J.D. Carlson. US 6296088 B1. Magnetorheological fluid seismic damper, 2001.

[Cha94] D.J. Charlton, J. Yang, and K.K. Teh. A review of methods to characterize rubber elastic behavior for use in finite element analysis. *Rubber Chemistry and Technology*, 67(3):481–503, 1994.

[Che07] L. Chen, X.L. Gong, W.Q. Jiang, J.J. Yao, H.X. Deng, and W.H. Li. Investigation on magnetorheological elastomers based on natural rubber. *Journal of Materials Science*, 42:5483–5489, 2007.

[Che91] D.X. Chen, J.A. Brug, and R.B. Goldfarb. Demagnetizing factors for cylinders. *IEEE Transactions on Magnetics*, 27(4):3601–3619, 1991.

[Chen07] L. Chen, X.L. Gong, and W.H. Li. Microstructures and viscoelastic properties of anisotropic magnetorheological elastomers. *Smart Materials and Structures*, 16, 2007.

[Cie99] A. Ciesielski. *An Introduction to Rubber Technology*. Rapra Technology Ltd, Shrewsbury, 1999.

[Coq04] E. Coquelle. *Propriétés élastiques et viscoélastiques de matériaux composites adaptifs*. PhD thesis, University of Nice Sophia-Antipolis, 2004.

[Coq06a] E. Coquelle and G. Bossis. Mullins effect in elastomers filled with particles aligned by a magnetic field. *International Journal of Solids and Structures*, 43:7659–7672, 2006.

[Coq06b] E. Coquelle, G. Bossis, D. Szabo, and F. Giulieri. Micromechanical analysis of an elastomer filled with particles organized in chain-like structure. *Journal of Materials Science*, 41(18):5941–5953, 2006.

[Cre01] C. Creton, J. Hooker, and K.R. Shull. Bulk and interfacial contributions to the debonding mechanisms of soft adhesives: extension to large strains. *Langmuir*, 17:4948–4954, 2001.

[Cri09] R.J. Crist. US 7584685 B2. Active vibrational damper, 2009.

[Czi06] H. Czichos, T. Saito, and L. Smith. *Handbook of Materials Measurement Methods*. Springer Science+Business Media, Berlin, 2006.

[Dan12] K. Danas, S.V. Kankanala, and N. Triantafyllidis. Experiments and modeling of iron-particle-filled magnetorheological elastomers. *Journal of the Mechanics and Physics of Solids*, 60:120–138, 2012.

[Dan14] K. Danas and N. Triantafyllidis. Instability of a magnetoelastic layer resting on a non-magnetic substrate. *Journal of the Mechanics and Physics of Solids*, 69:67–83, 2014.

[Dav99] L.C. Davis. Model of magnetorheological elastomers. *Journal of Applied Physics*, 85(6):3348–3351, 1999.

[DeB06] G. DeBotton, I. Hariton, and E. Socolsky. Neo-hookean fiber-reinforced composites in finite elasticity. *Journal of the Mechanics and Physics of Solids*, 54:533–559, 2006.

[Dek83] M.E.J. Dekkers and D. Heikens. The effect of interfacial adhesion on the tensile behavior of polystyrene-glass-bead composites. *Jounal of Applied Polymer Science*, 28:3809–3815, 1983.

[Dia09] J. Diani, B. Fayolle, and P. Gilormini. A review on the Mullins effect. *European Polymer Journal*, 45:601–602, 2009.

[Dig08] G. Diguet, E. Beaugnon, and J.Y. Cavaillé. From dipolar interactions

of a random distribution of ferromagnetic particles to magnetostriction. *Journal of Magnetism and Magnetic Materials*, 321:396–401, 2008.

[Dig10] G. Diguet. *Huge magnetostriction of magneto-rheological composite*. PhD thesis, University of Grenoble, 2010.

[Dor03] A. Dorfmann and R.W. Ogden. Magnetoelastic modelling of elastomers. *European Journal of Mechanics - A/Solids*, 22(4):497–507, 2003.

[Dor04] A. Dorfmann and R.W. Ogden. A constitutive model for the Mullins effect with permanent set in particle-reinforced rubber. *International Journal of Solids and Structures*, 41:1855–1878, 2004.

[Dor05] A. Dorfmann and R.W. Ogden. Some problems in nonlinear magnetoelasticity. *Zeitschrift für angewandte Mathematik und Physik ZAMP*, 56(4):718–745, 2005.

[Due00] T.A. Duenas and G.P. Carman. Large magnetostrictive response of Terfenol-D resin composites. *Journal of Applied Physics*, 87(9):4696–4701, 2000.

[Eli02] L.D. Elie and J.M. Ginder. EP 0784163 B1. Variable stiffness bushing using magnetorheological elastomers, 2002.

[FEAP] R.L. Taylor. Feap - finite element analysis program version 8.3, March 2011.

[FEMM] D.C. Meeker. FEMM - finite element method magnetics version 4.2, November 2013.

[Fan10] Y.C. Fan, X.L. Gong, W.Q. Jiang, W. Zhang, B. Wei, and W.H. Li. Effect of maleic anhydride on the damping property of magnetorheological elastomers. *Smart Materials and Structures*, 19(055015):1–8, 2010.

[Fan11] Y.C. Fan, X.L. Gong, S.H. Xuan, W. Zhang, J. Zheng, and W.Q. Jiang. Interfacial friction damping properties in magnetorheological elastomers. *Smart Materials and Structures*, 20(035007):1–8, 2011.

[Far04a] M. Farshad and A. Benine. Magnetoactive elastomer composites. *Polymer Testing*, 23:347–353, 2004.

[Far04b] M. Farshad and M. Le Roux. A new active noise abatement barrier system. *Polymer Testing*, 23:855–860, 2004.

[Far05] M. Farshad and M. Le Roux. Compression properties of magnetostrictive polymer composite gels. *Polymer Testing*, 24:163–168, 2005.

[Fu08] S.Y. Fu, X.Q. Feng, B. Lauke, and Y.W. Mai. Effects of particle size, particle/matrix interface adhesion and particle loading on mechanical properties of particulate-polymer composites. *Composites: Part B*, 39:933–961, 2008.

[GMSH] C. Geuzaine and J.F. Remacle. Gmsh version 2.8.5: a three-dimensional finite element mesh generator with built-in pre- and post-processing facilities, September 2014.

[Gal12] E. Galipeau and P. Ponte Castañeda. The effect of particle shape and distribution on the macroscopic behavior of magnetoelastic composites. *International Journal of Solids and Structures*, 49:1–17, 2012.

[Gal13a] E. Galipeau and P. Ponte Castañeda. A finite-strain constitutive model for magnetorheological elastomers: Magnetic torques and fiber rotations. *Journal of the Mechanics and Physics of Solids*, 61:1065–1090, 2013.

[Gal14] E. Galipeau, S. Rudykh, G. DeBotton, and P. Ponte Castañeda. Magnetoactive elastomers with periodic and random microstructures. *International Journal of Solids and Structures*, 51:3012–3024, 2014.

[GalPhD12] E. Galipeau. *Non-linear homogenization of magnetorheological elastomers at finite strain*. PhD thesis, University of Pennsylvania, 2012.

[Gen12] A.N. Gent. *Engineering with Rubber*. Carl Hanser Verlag, Munich, 2012.

[Gen84] A.N. Gent and B.K. Park. Failure processes in elastomers at or near a rigid spherical inclusion. *Journal of Materials Science*, 19:1947–1956, 1984.

[Gin00] J.M. Ginder, M.E. Nichols, L.D. Elie, and S.M. Clark. Controllable-stiffness components based on magnetorheological elastomers. *Smart Structures and Materials*, 3985:418–425, 2000.

[Gin02] J.M. Ginder, S.M. Clark, W.F. Schlotter, and M.E. Nichols. Magnetostrictive phenomena in magnetorheological elastomers. *Journal of Modern Physics B*, 16(17 & 18):2412–2418, 2002.

[Gin99] J.M. Ginder, M.E. Nichols, L.D. Elie, and J.L. Tardiff. Magnetorhe-

ological elastomers: properties and applications. *SPIE Proceedings*, 3675:131–138, 1999.

[Gon05] X.L. Gong, X.Z. Zhang, and P.Q. Zhang. Fabrication and characterization of isotropic magnetorheological elastomers. *Polymer Testing*, 24:669–676, 2005.

[Gon07] X.L. Gong, L. Chen, and J.F. Li. Study of utilizable magnetorheological elastomers. *Journal of Modern Physics B*, 21(29):4875–4882, 2007.

[Gor09] S.R. Gorodkin, R.O. James, and W.I. Kordonski. Magnetic properties of carbonyl iron particles in magnetorheological fluids. *Journal of Physics: Conference Series*, 149(012051):1–4, 2009.

[Gro08] H. Gross, F. Blechinger, and B. Achtner. *Handbook of Optical Systems*. Wiley-VCH, Berlin, 2008.

[Gua08] X.C. Guan, X.F. Dong, and J.P. Ou. Magnetostrictive effect of magnetorheological elastomer. *Journal of Magnetism and Magnetic Materials*, 320:158–163, 2008.

[Gue12] D. Günther, D.Y. Borin, S. Günther, and S. Odenbach. X-ray microtomographic characterization of field-structured magnetorheological elastomers. *Smart Materials and Structures*, 21(015005):1–7, 2012.

[Guy94] M. Guyot. *Mesure des paramètres magnétiques fondamentaux des matériaux ferromagnétiques ou ferrimagnétiques*, chapter Rappels sur les paramètres fondamentaux du magnétisme, pages 5–24. CNRS Formation, Meudon, 1994.

[Hab06] G. Habenicht. *Kleben*. Springer Heidelberg, Berlin, 2006.

[Hal1879] E.H. Hall. On a new action of the magnet on electric currents. *American Journal of Mathematics*, 2(3):287–292, 1879.

[Har06] J.A. Harvey. *Smart Materials. In Mechanical Engineers' Handbook*, volume 1. Wiley, 3rd edition, 2006.

[Hay13] W.M. Haynes. *CRC Handbook of Chemistry and Physics*. CRC Press, Florida, 2013.

[Hos13] M. Hossain and P. Steinmann. More hyperelastic models for rubber-like materials: consistent tangent operators and comparative study. *Journal of the Mechanical Behavior of Materials*, 22(1-2):27–50, 2013.

[Hu05] Y. Hu, Y.L. Wang, X.L. Gong, X.Q. Gong, X.Z. Zhang, W.Q. Jiang,

P.Q. Zhang, and Z.Y. Chen. New magnetorheological elastomers based on polyurethane/si-rubber hybrid. *Polymer Testing*, 24(3):324–329, 2005.

[ISO37] ISO 37. Rubber, vulcanized or thermoplastic - determination of tensile stress-strain properties, 2011.

[Jan10] Y. Jansen, T. Karrer, and J. Borchers. Mudpad: tactile feedback and haptic texture overlay for touch surfaces. *Proceedings of the ACM International Conference on Interactive Tabletops and Surfaces*, pages 11–14, 2010.

[Jol96] M.R. Jolly, J.D. Carlson, B.C. Munoz, and T.A. Bullions. The magnetoviscoelastic response of elastomer composites consisting of ferrous particles embedded in a polymer matrix. *Journal of Intelligent Material Systems and Structures*, 7:613–622, 1996.

[Kal05] M. Kallio. *The elastic and damping properties of magnetorheological elastomers*. PhD thesis, Tampere University of Technology, 2005.

[Kal11] J. Kaleta, M. Krolewicz, and D. Lewandowski. Magnetomechanical properties of anisotropic and isotropic magnetorheological composites with thermoplastic elastomer matrices. *Smart Materials and Structures*, 20(085006):1–13, 2011.

[Kan04] S.V. Kankanala and N. Triantafyllidis. On finitely strained magnetorheological elastomers. *Journal of the Mechanics and Physics of Solids*, 52:2869–2908, 2004.

[Kan07] S.V. Kankanala. *On finitely strained magnetoelastic solids*. PhD thesis, University of Michigan, 2007.

[Kan08] S.V. Kankanala and N. Triantafyllidis. Magnetoelastic buckling of a rectangular block in plane strain. *Journal of the Mechanics and Physics of Solids*, 56:1147–1169, 2008.

[Kar13] L. Kari. *Magneto-sensitive elastomers - theory and applications*, chapter Constitutive Models for Rubber VIII Chapter 2, pages 13–18. CRC Press 2013, 2013.

[Kim14] M.S. Kim, K.M. Yang, S.H. Lee, J.H. Yoon, U.C. Jeong, I.H. Yang, and J.E. Oh. US 8844914 B2. Variable differential mount apparatus using magnetorheological elastomer, 2014.

[Koo12] J.H. Koo, A. Dawson, and H.J. Jung. Characterization of actuation

properties of magnetorheological elastomers with embedded hard magnetic particles. *Journal of Intelligent Material Systems and Structures*, 23(9):1049–1054, 2012.

[Kov00] A. Kovetz. *Electromagnetic Theory*. Oxford, New York, 2000.

[Kyu12] K.U. Kyung, J.U. Lee, S. Park, H. Prahlad, and P. von Guggenberg. Flexible visio-haptic display. *Haptics: Perception, Devices, Mobility, and Communication*, 7283:206–209, 2012.

[Lag98] J.C. Lagarias, J.A. Reeds, M.H. Wright, and P.E. Wright. Convergence properties of the nelder-mead simplex method in low dimensions. *SIAM Journal on Optimization*, 9(1):112–147, 1998.

[Lan03] L. Lanotte, G. Ausanio, C. Hison, V. Iannotti, and C. Luponio. The potentiality of composite elastic magnets as novel materials for sensors and actuators. *Sensors and Actuators A*, 106:56–60, 2003.

[Lan04] L. Lanotte, G. Ausanio, C. Hison, V. Iannotti, C. Luponio, and C. Luponio Jr. State of the art and development trends of novel nanostructured elastomagnetic composites. *Journal of Optoelectronics and Advanced Materials*, 6(2):523–532, 2004.

[Leb02] J.L. Leblanc. Rubber-filler interactions and rheological properties in filled compounds. *Progress in Polymer Science*, 27:627–687, 2002.

[Lee11] C.H. Lee and M.G. Jang. Virtual surface characteristics of a tactile display using magneto-rheological fluids. *Sensors*, 11(3):2845–2856, 2011.

[Leg08] L. Léger and C. Creton. Adhesion mechanisms at soft polymer interfaces. *Philosophical Transactions of the Royal Society A*, 366:1425–1442, 2008.

[Lem91] E. Lemaire, C. Paparoditis, and G. Bossis. Yield stresses in magnetic suspensions. *Progress in Colloid & Polymer Science*, 84:425–427, 1991.

[Li08] W.H. Li and X.Z. Zhang. Research and applications of mr elastomers. *Recent Patents on Mechanical Engineering*, 1:161–166, 2008.

[Lok04] M. Lokander. *Performance of magnetorheological rubber materials*. PhD thesis, KTH Stockholm, 2004.

[MSC10] MSC-Software. Whitepaper. Nonlinear finite element analysis of elastomers, 2010.

[MSC14] MSC-Software. Whitepaper. Introductory guide to nonlinear analysis, 2014.

[Mar00] J.E. Martin, E. Venturini, J. Odinek, and R.A. Anderson. Anisotropic magnetism in field-structured composites. *Physical Review E*, 61(3):2818–2830, 2000.

[Mar04] J.E. Martin, E. Venturini, G.L. Gulley, and J. Williamson. Using triaxial magnetic fields to create high susceptibility particle composites. *Physical Review E*, 69(021508):1–15, 2004.

[Mar06] J.E. Martin, R.A. Anderson, D. Read, and G. Gulley. Magnetostriction of field-structured magnetoelastomers. *Physical Review E*, 74(051507):1–17, 2006.

[Mar13] P.R. Marur. US 0087985 A1. Magneto-rheological elastomer-based vehicule suspension, 2013.

[Mar98] J.E. Martin, R.A. Anderson, and C.P. Tigges. Simulation of the athermal coarsening of composites structured by a uniaxial field. *Journal of Chemical Physics*, 108(9):3765–3787, 1998.

[Mie00] C. Miehe and J. Keck. Superimposed finite elastic-viscoelastic-plastoelastic stress response with damage in filled rubbery polymers. Experiments, modelling and algorithmic implementation. *Journal of the Mechanics and Physics of Solids*, 48:323–365, 2000.

[Moo68] F.C. Moon and Y.H. Pao. Magnetoelastic buckling of a thin plate. *Journal of Applied Mechanics*, 35(1):53–58, 1968.

[Mor09] K. Morozov, M. Shliomis, and H. Yamaguchi. Magnetic deformation of ferrogel bodies: procrustes effect. *Physical Review E*, 79(040801):1–4, 2009.

[Mul57] L. Mullins and N.R. Tobin. Theoretical model for the elastic behavior of filler-reinforced vulcanized rubbers. *Rubber Chemistry and Technology*, 30(2):555–571, 1957.

[Ogd04] R.W. Ogden, G. Saccomandi, and I. Sgura. Fitting hyperelastic models to experimental data. *Computational Mechanics*, 34(6):484–502, 2004.

[Ogd11] R.W. Ogden. *Mechanics and electrodynamics of magneto- and electroelastic materials*, volume 527, chapter Magnetostatics: from basic principles to nonlinear interactions in deformable media, pages 107–152. Springer Vienna, 2011.

[Osb45] J.A. Osborne. Demagnetizing factors of the general ellipsoid. *Physical Review*, 67(11&12):351–357, 1945.

[PARAVIEW] U. Ayachit. The ParaView guide: a parallel visualization application, 2015.

[Pei04] P. Peignot and K. Rhodes. Choosing a silicone adhesive and treatment system. *Medical Device Technology*, 15(3):22–24, 2004.

[Pet12] K.B. Petersen and M.S. Pedersen. The matrix cookbook. 2012.

[Pip59] A.C. Pipkin and R.S. Rivlin. The formulation of constitutive equations in continuum physics. I. *Archive for Rational Mechanics and Analysis*, 4(1):129–144, 1959.

[Pon11] P. Ponte Castañeda and E. Galipeau. Homogenization-based constitutive models for magnetorheological elastomers at finite strain. *Journal of the Mechanics and Physics of Solids*, 59:194–215, 2011.

[Rab48] J. Rabinow. The magnetic fluid clutch. *Transactions of the American Institute of Electrical Engineers*, 67(2):1308–1315, 1948.

[Rai03] Y.L. Raikher and O.V. Stolbov. Magnetodeformational effect in ferrogel samples. *Journal of Magnetism and Magnetic Materials*, 258-259:477–479, 2003.

[Rai08] Y.L. Raikher, O.V. Stolbov, and G.V. Stepanov. Deformation of a circular ferroelastic membrane in a uniform magnetic field. *Technical Physics*, 53(9):1169–1176, 2008.

[Ram04] J. Ramier. *Comportement mécanique d'élastomères chargés, influence de l'adhésion charge-polymère, influence de la morphologie*. PhD thesis, University of Lyon, 2004.

[Rig83] Z. Rigbi and L. Jilken. The response of an elastomer filled with soft ferrite to mechanical and magnetic influences. *Journal of Magnetism and Magnetic Materials*, 37:267–276, 1983.

[Riv48] R.S. Rivlin. Large elastic deformations of isotropic materials. i. fundamental concepts. *Philosophical Transactions of the Royal Society A*, 240(822):459–490, 1948.

[Sai1855] A.J.C.B. Saint-Venant. Mémoire sur la torsion des prismes. *Mémoires Divers Savants*, 14:233–560, 1855.

[San13] M. Sangermano, P. Allia, P. Tiberto, G. Barrera, F. Bondioli, N. Florini, and M. Messori. Photo-cured epoxy networks functionalized

with Fe_3O_4 generated by non-hydrolytic sol-gel process. *Macromolecular Chemistry and Physics*, 214(4):508–516, 2013.

[Sat89] M. Sato and Y. Ishii. Simple and approximate expressions of demagnetizing factors of uniformly magnetized rectangular rod and cylinder. *Journal of Applied Physics*, 66(2):983–985, 1989.

[Sax13] P. Saxena, M. Hossain, and P. Steinmann. A theory of finite deformation magneto-viscoelasticity. *International Journal of Solids and Structures*, 50:3886–3897, 2013.

[Sche07] N. Scheerbaum, D. Hinz, O. Gutfleisch, K.H. Müller, and L. Schultz. Textured polymer bonded composites with Ni-Mn-Ga magnetic shape memory particles. *Acta Materialia*, 55:2707–2713, 2007.

[Schu13] G. Schubert, P. Harrison, and Z. Guo. The behaviour of magnetorheological elastomers under equi-biaxial tension. In *19th International Conference on Composite Materials*, 2013.

[Schu14] G. Schubert. *Manufacture, characterisation and modelling of magnetorheological elastomers*. PhD thesis, University of Glasgow, 2014.

[She04] Y. Shen, M.F. Golnaraghi, and G.R. Heppler. Experimental research and modeling of magnetorheological elastomers. *Journal of Intelligent Material Systems and Structures*, 15:27–35, 2004.

[Shi95] T. Shiga, A. Okada, and T. Kurauchi. Magnetroviscoelastic behavior of composite gels. *Journal of Applied Polymer Science*, 58(4):787–792, 1995.

[Ste07] G.V. Stepanov, S.S. Abramchuk, D.A. Grishin, L.V. Nikitin, E.Y. Kramarenko, and A.R. Khokhlov. Effect of a homogeneous magnetic field on the viscoelastic behavior of magnetic elastomers. *Polymer*, 48:488–495, 2007.

[Ste12] P. Steinmann, M. Hossain, and G. Possart. Hyperelastic models for rubber-like materials: consistent tangent operators and suitability for Treloar's data. *Archive of Applied Mechanics*, 82(9):1183–1217, 2012.

[Ste13] G.V. Stepanov, E.Y. Kramarenko, and D.A. Semerenko. Magnetodeformational effect of the magnetoactive elastomer and its possible applications. *Journal of Physics: Conference Series*, 412(012031):1–4, 2013.

[Sto11] O.V. Stolbov, Y.L. Raikher, and M. Balasoiu. Modelling of magne-

todipolar striction in soft magnetic elastomers. *Soft Matter*, 7:8484–8487, 2011.

[Sun08] T.L. Sun, X.L. Gong, W.Q. Jiang, J.F. Li, Z.B. Xu, and W.H. Li. Study on the damping properties of magnetorheological elastomers based on cis-polybutadiene rubber. *Polymer Testing*, 27(4):520–526, 2008.

[Sut09] M.A. Sutton, J.J. Orteu, and H.W. Schreier. *Image Correlation for Shape, Motion and Deformation Measurements*. Springer Science+Business Media, New York, 2009.

[Tho09] J.D. Thomas and N. Triantafyllidis. On electromagnetic forming processes in finitely strained solids: Theory and example. *Journal of the Mechanics and Physics of Solids*, 57:1391–1416, 2009.

[Tho13] F. Thorsteinsson, I. Gudmundsson, and C. Lecomte. US 0060349 A1. Prosthetic and orthotic devices having magnetorheological elastomer spring with controllable stiffness, 2013.

[Var05] Z. Varga, G. Filipcsei, and M. Zrinyi. Smart composites with controlled anisotropy. *Polymer*, 46:7779–7787, 2005.

[Var06] Z. Varga, G. Filipcsei, and M. Zrinyi. Magnetic field sensitive functional elastomers with tunable elastic modulus. *Polymer*, 47:227–233, 2006.

[Vic02] J. de Vicente, G. Bossis, S. Lacis, and M. Guyot. Permeability measurements in cobalt ferrite and carbonyl iron powders and suspensions. *Journal of Magnetism and Magnetic Materials*, 251:100–108, 2002.

[Vid07] F. Vidal-Verdu and M. Hafez. Graphical tactile displays for visually-impaired people. *IEEE Transactions on Neural Systems and Rehabilitation Engineering*, 15(1):119–130, 2007.

[Wal14] B. Walter, P. Saxena, J.P. Pelteret, J. Kaschta, D.W. Schubert, and P. Steinmann. Magneto-sensitive elastomers: an experimental point of view. *Proceedings in Applied Mathematics and Mechanics*, 14:403–404, 2014.

[Wan06] Y.L Wang, Y. Hu, L. Chen, X.L. Gong, W.Q. Jiang, P.Q. Zhang, and Z.Y. Chen. Effects of rubber/magnetic particle interactions on the performance of magnetorheological elastomers. *Polymer Testing*, 25(2):262–267, 2006.

[Wan99] M.J. Wang. The role of filler networking in dynamic properties of filled rubber. *Rubber Chemistry and Technology*, 72:430–448, 1999.

[Wei10] B. Wei, X.L. Gong, and W.Q. Jiang. Influence of polyurethane properties on mechanical performances of magnetorheological elastomers. *Journal of Applied Polymer Science*, 116:771–778, 2010.

[Yat01] F. Yatsuyanagi, N. Suzuki, M. Ito, and H. Kaidou. Effects of secondary structure of fillers on the mechanical properties of silica filled rubber systems. *Polymer*, 42:9523–9529, 2001.

[Yin06] H.M. Yin, L.Z. Sun, and J.S. Chen. Magneto-elastic modeling of composites containing chain-structured magnetostrictive particles. *Journal of the Mechanics and Physics of Solids*, 54:975–1003, 2006.

[Zha07] X.Z. Zhang, X.L. Gong, P.Q. Zhang, and W.H. Li. Existence of bound-rubber in magnetorheological elastomers and its influence on material properties. *Chinese Journal of Chemical Physics*, 20(2):173–179, 2007.

[Zhe94] Q.S. Zheng. Theory of representations for tensor functions - a unified invariant approach to constitutive equations. *Applied Mechanics Reviews*, 47(11):545–587, 1994.

[Zri96] M. Zrinyi, L. Barsi, and A. Büki. Deformation of ferrogels induced by nonuniform magnetic fields. *J. Chem. Physics*, 104(21):8750–8756, 1996.

[Zri97] M. Zrinyi, L. Barsi, and A. Büki. Ferrogel: a new magneto-controlled elastic medium. *Polymer Gels and Networks*, 5:415–427, 1997.

[Zub12] A.Y. Zubarev. On the theory of the magnetic deformation of ferrogels. *Soft Matter*, 8:3174–3179, 2012.

Abstract: Experimental Characterization, Modeling and Simulation of Magneto-Rheological Elastomers

In this thesis, we study a class of active materials named Magneto-Rheological Elastomers (MREs) with a main focus on their coupled magneto-mechanical response up to large strains and up to high magnetic fields. With the purpose of achieving a coupled characterization of MREs behavior for the design of haptic interface devices, this work encompasses experimental, theoretical and numerical developments.

The first part of this work is dedicated to aspects pertaining to sample fabrication. Isotropic and magnetic field-cured MREs, composed of soft silicone rubber and micrometric carbonyl iron powder, are manufactured using a reliable and repeatable process. A special sample geometry is designed in order to obtain both homogeneous mechanical and magnetic fields during the coupled-field characterization. The interfacial adhesion between the iron fillers and the silicone matrix in MREs submitted to large deformations is investigated and a critical strain threshold is identified beyond which a primer treatment of the particles is needed to prevent debonding between the particles and the matrix.

The second part of this thesis focuses on the coupled magneto-mechanical characterization of MREs and involves both theoretical and experimental developments. Based on the general theoretical framework for transversely isotropic magneto-elastic continua proposed by Kankanala, Danas and Triantafyllidis [Kan04, Dan12, Dan14], the coupled magneto-mechanical constitutive laws for both isotropic and anisotropic MREs are used to determine experimentally the corresponding constitutive model's material parameters. The actual characterization of MREs is conducted thanks to a specially designed and novel experimental setup allowing tensile tests up to large strains and under high magnetic fields. The experimental data thus obtained provide the constitutive models for the isotropic and anisotropic MREs needed as input for the subsequent numerical simulations.

The third part of this work pertains to the experiments, modeling and numerical calculations for boundary value problems corresponding to the design of a haptic interface prototype. A coupled variational formulation for a non-uniform applied magnetic field, using displacement, magnetic vector potential and magnetization as independent variables, is proposed and subsequently applied to the solution of the boundary value problem of an MRE layer subjected to the spatially localized magnetic field produced by an electromagnetic coil. The axisymmetric problem is solved numerically using finite element analysis. The device has been built and experimental results are compared to numerical simulations, thus providing a benchmark for the validation of the axisymmetric simulations as well as a proof of concept for the design of haptic interface applications.

Résumé : Caractérisation Expérimentale, Modélisation et Simulation des Elastomères Magnéto-Rhéologiques

Cette thèse porte sur une classe de matériaux actifs nommés Elastomères Magnéto-Rhéologiques (EMR) et en particulier sur leur réponse magnéto-mécanique en grandes déformations et en présence de champs magnétiques élevés. Dans l'objectif d'aboutir à une caractérisation couplée du comportement des EMR pour permettre le design d'interfaces haptiques, ce travail comporte des développements expérimentaux, théoriques et numériques.

La première partie de ce travail s'intéresse aux aspects liés à la fabrication des échantillons. Des EMR isotropes et structurés par l'application d'un champ magnétique pendant la fabrication, composés d'une matrice de silicone mou et de particules de fer doux micrométriques, sont fabriqués de façon précise et répétable. Un échantillon dédié est également développé afin d'obtenir simultanément des champs mécaniques et magnétiques homogènes dans celui-ci lors de la caractérisation couplée. La question de l'adhésion interfaciale entre les particules de fer doux et la matrice de silicone est également étudiée pour des EMR soumis à de grandes déformations et un seuil de déformation critique est identifié, au-delà duquel un traitement chimique des particules devient nécessaire pour éviter la décohésion entre les particules et la matrice.

La seconde partie de cette thèse couvre la caractérisation magnéto-mécanique couplée des EMR et comporte des développement numériques et expérimentaux. S'appuyant sur le cadre théorique général des solides magnéto-élastiques continus isotropes transverses proposé par Kankanala, Danas and Triantafyllidis [Kan04, Dan12, Dan14], les lois de comportement magnéto-mécaniques couplées pour des EMR isotropes et anisotropes sont utilisées pour obtenir expérimentalement les jeux de paramètres matériaux du modèle de comportement correspondant. La caractérisation expérimentale est réalisée grâce à un dispositif dédié et original permettant de mener des essais de traction uniaxiale en grandes déformations et sous champs magnétiques élevés. Les données expérimentales ainsi obtenues fournissent les modèles de comportement des EMR isotropes et anisotropes nécessaires pour pouvoir mener ensuite des simulations numériques.

La troisième partie de ce travail concerne les expériences, la modélisation et les simulations numériques de problèmes aux limites correspondant au design d'un prototype d'interface haptique. Une formulation variationnelle couplée pour un champ magnétique non uniforme, utilisant le déplacement, le vecteur potentiel magnétique et la magnétisation comme variables indépendantes, est proposée et appliquée pour obtenir la solution d'un problème aux limites pour une couche d'EMR soumise à un champ localisé produit par une bobine électromagnétique. Le problème axisymétrique est résolu par éléments finis. Un prototype d'interface haptique a été développé et les résultats expérimentaux sont comparés aux simulations numériques, servant ainsi à la fois de validation expérimentale pour les simulations éléments finis axisymétriques mais aussi de preuve de concept pour l'application technologique correspondante.